UNIVERSITY OF OXFORD

DEPARTMENT OF ENGINEERING SCIENCE

Laser writing of graphitic structures inside CVD diamond

Marta KRÜGER

Jesus College

A thesis submitted for the degree of

Doctor of Philosophy

March 1, 2025

Abstract

Laser writing of graphitic structures inside CVD diamond

Marta KRÜGER

Diamond is the strongest and the hardest material known and possess scientifically attractive characteristics. Currently, diamond is not only extracted from the Earth but also can be fabricated in a laboratory. The advantage of synthetic industrial diamond is that it can be manufactured in unlimited quantities and its features might be tailored with respect to a particular application. Diamond is used in a variety of industries and research areas. Diamond possesses high thermal conductivity, is resistant to irradiation and suits perfectly to the harsh environments. It surpasses the properties of other counter semiconductor materials, including Si and GaAs, on several electrical figures of merit. Moreover, due to its extreme strength, diamond exhibits high resistance to scratches and breakages. Thanks to these excellent material properties, diamond devices already find application in sensing in harsh environments for detection of rradiation. Additionally, diamond-based devices possess potential application in other areas, such as electrochemistry, quantum technology and biomedicine. However, advanced manufacturing methods are needed to make effective devices from this challenging substrate. Laser writing with ultrashort pulsed lasers is an effective method for fabrication of structures in three dimensions inside transparent materials. This thesis explores optimisation of laser writing for conductive graphite-based structures inside synthetic diamond substrates and shows routes towards effective diamond devices.

Whilst laser writing of conductive structures in synthetic diamond has been demonstrated for more than ten years, much work is still needed to optimise the process conditions for devices, understand the laser written

structures, and explore new applications. This thesis presents a variety of advances in ultrashort pulsed laser graphitisation of diamond supported by adaptive optics, providing progress towards exploitation of diamond's extraordinary characteristics and implementation of diamond devices into current working systems.

This thesis focuses on laser written conductive columns that pass vertically through a diamond wafer. An all-carbon device was designed and laser written for characterisation of the electrical properties of the fabricated structures, without post-processing or metallisation. This architecture allows rapid testing of devices all manufactured using the same material. A detailed study was conducted to examine the relationship between laser pulse repetition rate and resistance of laser fabricated graphitic columns. This analysis reveals a surprisingly narrow laser fabrication window with pulse repetition rate, ranging from 200 Hz to 2 kHz, when graphitic wires showed consistent ohmic conductivity. Furthermore, it was demonstrated through varying laser writing speed that the delivered laser dose (defined as number of pulses per distance) is critical in the formation of conductive graphitic pathways.

Novel concepts of advanced laser writing are demonstrated to enable fabrication of new devices. It is shown that overwriting of laser generated columns using different pulse repetition rates can modify electrical properties. Particularly, an initially ohmic conductive column can be overwritten with a high pulse repetition rate laser to create a structure showing an asymmetric barrier potential, with diode-like behaviour. It is also shown how a holographic laser process can be used to generate multiple columns simultaneously by splitting the laser beam up into many foci. This can be useful for scaling of devices to large numbers of columns. Finally, functional diamond devices are described that were developed in collaboration and rely upon the advances in laser graphitisation developed in the thesis, for applications in

power electronics and detection of high energy particles.

A variety of methods are presented for evaluating laser written columns, aside from just electrical properties. Quantitative polarising optical microscopy is demonstrated as an effective way to visualise strain induced by the laser written features. Measurements are given showing the stress generated around graphitic columns and important considerations raised. These techniques are especially important for the design of future photonic devices, such as optical waveguides, that operate based upon refractive index modulation arising from strain.

Acknowledgements

First and foremost, I would like to thank my supervisors, Dr Patrick Salter and Professor Martin Booth for their support, guidance and encouragement throughout this research process. Your expertise and patience have been instrumental in shaping this work, and I am very thankful for the countless hours you have dedicated to my development as a scholar.

I also extend my gratitude to the EPSRC and Opsydia Ltd for funding this project. I would like to thank all the team members of Opsydia, who supported me during my studies. I am very thankful to my industrial supervisor, Lewis Fish and Dr. Simon Henley, Dr. David Myles and Dr. Phil Diggle for countless discussions, constructive feedback and insightful suggestions that have improved the quality of this work.

I owe a special debt of gratitude to my colleagues and friends in the Dynamic Optics and Photonics Group. The countless stimulating discussions have made this journey not only bearable but enjoyable. I am particularly thankful to Dr. Chao He, Dr. Ravi Shivaraman and Dr. Mohan Wang for their support and constant encouragement. Thank you for your guidance and assistance on my journey of studying laser writing.

I am incredibly grateful to everyone who has contributed to my journey. Thank you for helping me achieve this significant milestone.

Publications

Krueger, M., Salter P., Booth M., Parallel laser fabrication of electrically conductive graphitic columns in diamond *(This article is based upon work from Chapter 5 (Optics Express. 32. 46578-46585))*.

Krueger, M., Salter, P., Booth, M.J Influence of pulse repetition rates on electrical properties of laser-written conductors in diamond. *(This article is based upon work from Chapter 4 (ACS Nano. 2024 Jan 30;18(4):2861-2871))*.

Mali, M. et al., Latest results from the RD42 collaboration on the radiation tolerance of polycrystalline diamond detectors. *(Nuclear Instruments and Methods in Physics Research Section A: Accelerators, Spectrometers, Detectors and Associated Equipment, Volume 1062, 2024 - Part of Chapter 7 is based on this work)*.

Salter, P. S., Villar, M.P., Lloret, F., Reyes, D.F., **Krueger, M.**, Henderson, C.S, Araujo, D., Jackman, R.B Laser Engineering Nanocarbon Phases within Diamond for Science and Electronics. *(ACS Nano 2024, 18, 4, 2861–2871 - Part of Chapter 4 is based on this work)* .

Walny, R. et al., Progress in Diamond Detector Development. *(Volume 420 - 10th International Workshop on Semiconductor Pixel Detectors for Particles and Imaging (Pixel2022) - New Pixel Materials and Configurations, May 2023 - Part of Chapter 7 is based on this work)*.

Krueger, M., Salter, P., Booth, M.J. Laser processing and electrical analysis of embedded graphitic wires in diamond. *(Frontiers in Ultrafast Optics: Biomedical, Scientific, and Industrial Applications XXIII, Proc. of SPIE Vol. 12411, January 2023 - Part of Chapter 4 is based on this work)*.

Henderson, C., Watkins, R., **Krueger, M.**, Jonasson, E., Salter, P., Jackman, R.B. All carbon diodes laser written in diamond *(January 2023 – Part of Chapter 7 is based on this work (submitted))*.

Conference Presentations

De Beers 73rd Diamond Conference

Oxford-September 2023 (Oral presentation)

”Laser processing and electrical analysis of embedded graphitic wires in diamond at different pulse repetition rates”

Frontiers in Ultrafast Optics: Biomedical, Scientific and Industrial Applications XXIII, SPIE, Photonics West Conference

San Francisco-January 2023 (Oral Presentation)

”Laser processing and electrical analysis of embedded graphitic wires in diamond”

University of Oxford Photonics Day

Oxford-September 2022 (Poster)

”Laser processing and electrical analysis of embedded graphitic wires in diamond at different pulse repetition rates”

De Beers 72nd Diamond Conference

Coventry-September 2022 (Poster)

”Electrical analysis of laser written graphitic structures in diamond”

De Beers 71st Diamond Conference

Coventry-September 2021 (Oral presentation)

”Analysis of laser written graphitic structures in diamond ”

De Beers 70th Diamond Conference

Coventry-September 2020 (Poster)

”Polarized light imaging of laser written microstructures in diamond”

Patents

”DIAMOND-BASED ELECTRICAL COMPONENT” Salter, Kruger, Booth, Jackman, Henderson; UK PATENT APPLICATION NUMBER 2303700.5; March 2023

Awards

”Meyricke Graduate Scholarship”, Jesus College

Contents

List of Figures

List of Tables

List of Abbreviations

AO	**A**daptive **O**ptics
DLW	**D**irect **L**aser **W**riting
CVD	**C**hemical **V**apour **D**eposition
CW	**C**ontinuous **W**ave
FIB	**F**ocused **I**on **B**eam
FWHM	**F**ull **W**idth **H**alf **M**aximum
HPHT	**H**igh **P**ressure **H**igh **T**emperature
LC-SLM	**L**iquid **C**rystal **S**patial **L**ight **M**odulator
NA	**N**umerical **A**perture
NV	**N**itrogen **V**acancy
NCN	**N**ano **C**arbon **N**etwork
PL	**P**hotoluminescence
PRR	**P**ulse **R**epetition **R**ate
RIM	**R**efracrive **I**ndex **M**ismatch
SEM	**S**canning **E**lectron **M**icroscopy
TEM	**T**ransmission **E**lectron **M**icroscopy
SLM	**S**patial **L**ight **M**odulator

Chapter 1

Diamond as an engineering material

1.1 Introduction

Since ancient times, diamonds have been known as the most precious gemstones on Earth. This brilliant gemstone was and still is associated with wealth and special occasions. Therefore, diamond as the world's most famous gemstone is mostly associated with the jewellery industry. However, this precious jewel is also interesting from a scientific perspective and is known as a very versatile engineering material used for cutting tools and abrasives. Its rarity and remarkable range of physical properties make it the world's most popular and sought-after gemstone. As a result, a lab-grown diamond market has emerged. Thus, this thesis primarily focuses on improving the properties of devices fabricated in industrial diamond.

1.2 Diamond structure

Diamond is a naturally occurring mineral, which is composed of carbon atoms, which are arranged tetrahedrally (see figure 1.1).

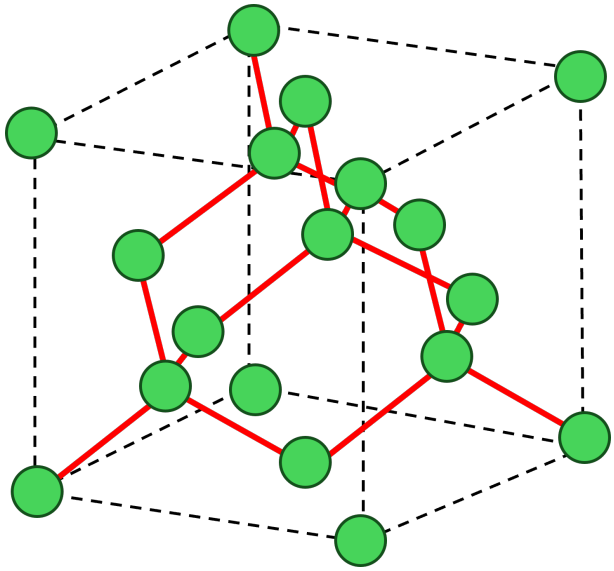

FIGURE 1.1: Diamond lattice structure, carbon (C) atoms (black dots) arranged tetrahedrally in a 3D structure, based on [1].

In that configuration each carbon atom is covalently bonded to four other carbon atoms. Each carbon atom shares one of its outer electrons with each of other carbon atoms. This sharing of electrons results in a force between each pair of atoms, thus a bond holds them tightly together. The carbon-carbon bonds ensure the regular arrangement of the atoms, which form a unit cell of a crystal structure, i.e. a basic structure unit. These units are periodically repeated in three dimensions. Owing to the tetrahedral arrangement of atoms, diamond exhibits a strong, rigid, and three-dimensional structure, which is the foundation of its unique characteristics.

1.3 Properties of diamond

Diamond exhibits extreme physical and chemical properties unmatched by any other material. It has the highest thermal conductivity, the highest stiffness and low thermal expansion coefficient, is chemically inert, radiation hard, optically transparent from the ultraviolet (UV) to the infrared (IR) and possesses extreme hardness and wear resistance [2, 3]. These extraordinary characteristics make it an attractive material, which finds use in variety of applications.

Natural diamond serves not only as a valuable gem, but is also exploited as a heat spreader, an abrasive, etc. [4, 5]. According to the above properties, diamond is considered as an engineering material for many other potential applications. However, the scarcity of natural diamond resulted in a demand for laboratory synthesized diamond. Moreover, it was proved that laboratory grown diamonds exhibit the same chemical, optical and physical properties as mined ones [6, 7]. Although diamond is made from 99.95% carbon, it also contains some impurities, e.g. trace elements, which are often called defects [8]. Atoms of other elements, e.g. nitrogen or boron, might be present in diamond's structure as a result of the growing process or be introduced in to the structure on purpose, e.g. to functionalize the material. The carbon atoms are often replaced by atoms of the chosen element. It is known that the presence and amount of trace elements have an impact on the colour and performance of the diamond crystal. Apart from extra elements, substitutional impurities, e.g. nitrogen, phosphorus, silicon, diamond also possess some crystallographic defects. The most common crystallographic defects present in both natural and synthetic diamond are dislocations, interstitials, and vacancies. The controllable implementation of impurities is known as doping, which is used in synthetic diamond growth processes to improve performance and material properties. Doping diamond is challenging due

to its rigid atomic structure. Although diamond is non-conductive, it is currently possible to alter its properties to act as a semiconductor via controllable doping. Addition of phosphorus and boron to the diamond structure makes it either a n-type or p-type semiconductor, respectively. Currently, silicon is the most common semiconductor applied in electronic technology. However, the continuous demand for high capacity power devices with low losses requires alternative materials. As a result both gallium nitride (GaN) and silicon carbide (SiC) are applied in high power electronics to potentially replace silicon-based devices. The thermal conductivity of diamond together with its electrical field resistance are far greater than those of silicon and alternatives (see table 1.1).

Property / Material	**Silicon (Si)**	**Silicon Carbide (SiC)**	**Gallium Nitride (GaN)**	**Diamond**
Band Gap (eV)	1.11	3.26	3.39	5.47
Breakdown Field E_c (MV/cm)	0.3	3.5	3.4	10.0
Electron Mobility (cm^2/Vs)	1500	800	900	2200
Thermal Conductivity (W/cm·K)	1.5	4.9	2.0	22

TABLE 1.1: Properties of diamond compared with other semiconductors, based on [9].

High thermal conductivity enables efficient heat transfer, and high electrical field resistance reduces the power conversion losses. Having these characteristics, diamond becomes an attractive semiconductor material for electronic devices in power transmission, electric vehicles, etc. Therefore, further study and development of diamond doping is necessary. Doping diamond to obtain p-type semiconductor is already well established. The most common dopant is boron. Obtaining the n-type diamond semiconductor is still quite challenging, however, there are elements, that could be applied to

form this type of a semiconductor, for example nitrogen or phosphorus [10]. Figure 1.2 presents the atomic structure of diamond and diamond doped with phosphorus.

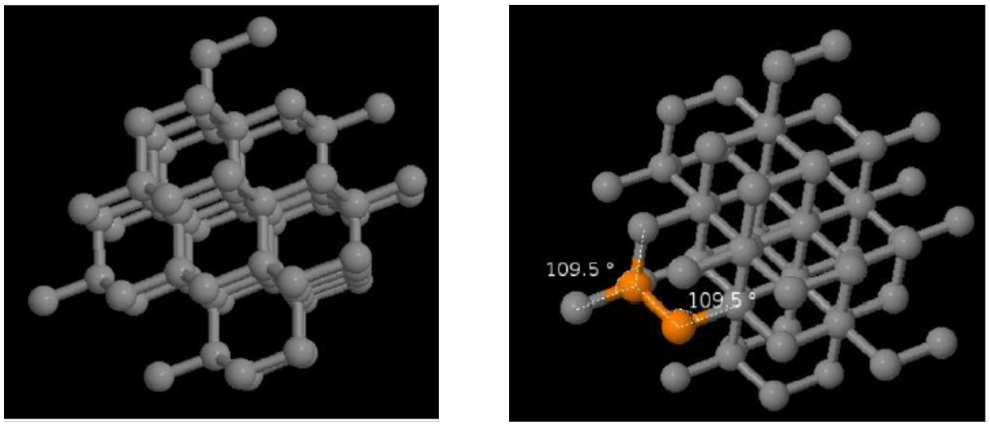

FIGURE 1.2: AIMPRO software simulation of atomic structure of pure diamond (left) and diamond with a phosphorus pair (right).

It was already demonstrated that doping of diamond to form both n-type and p-type semiconductors is possible, including formation of a p-n junction [11]. Figure 1.3 presents the schematic of a band diagram of diamond.

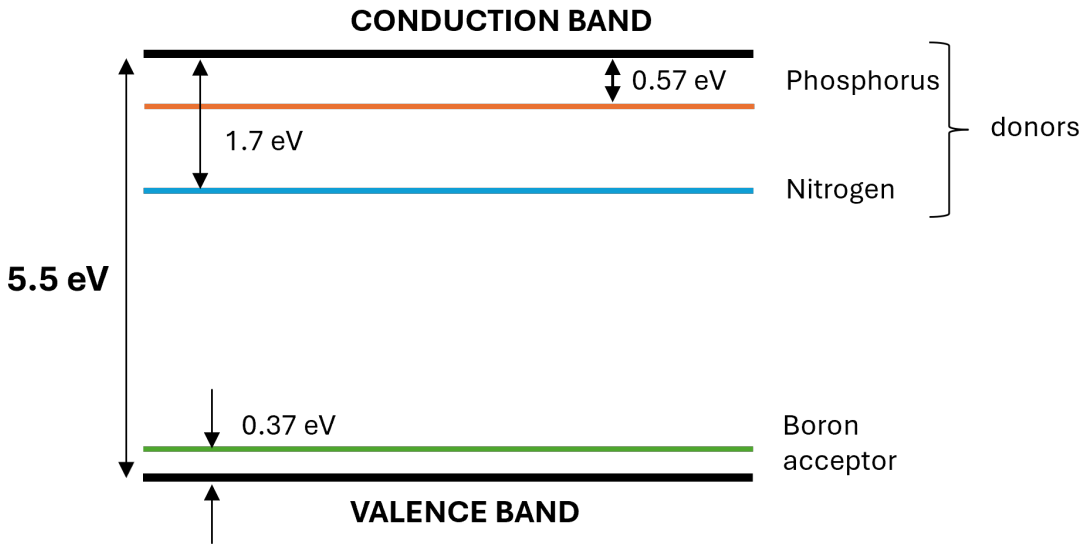

FIGURE 1.3: Energy band diagram of diamond, based on [12].

The wide energy band gap, i.e. 5.5 eV, of intrinsic diamond offers high electrical insulating properties. However, when both p-type and n-type

electrical conductivity are well managed, diamond can be used as a semiconductor for high temperature environments. Although, no satisfactory n-type doping has been established yet. The small lattice constant of diamond means incorporation of impurities for doping is difficult. Phosphor can be used, but is still at a relatively deep energy level. Improving doping techniques for diamond would result in fabrication of novel next-generation electronic devices.

1.4 Classification of diamonds

Diamonds can be classified according to the amount of chemical impurities. Most natural diamonds (95%) contain nitrogen as the main impurity and are distinguished as type Ia diamonds. They normally vary from near-colourless to light yellow. Nitrogen atoms in this case are present as pairs or small groups called aggregates (clusters). Type Ib diamonds are very rare. Here nitrogen is present mainly in the form of single substitutional atoms. These diamonds are often bright yellow in colour. Type II diamonds contain negligible amount of nitrogen. Among all diamonds, IIa diamonds are considered as chemically the purest, i.e. with no significant amount of nitrogen or boron impurities. They are rare and usually colourless, but they can also be grey, light brown or light pink. Diamonds containing boron impurities are classified as IIb diamonds. The trace element boron is responsible for their blue or greyish blue colour [13]. The Gemological Institute of America and other groups have created tools to distinguish types of diamond. In a laboratory setting, the identification of diamond is based on the detection of chemical imperfections in the atomic structure. Therefore, knowledge of diamond type is important for gemologists, who determine whether the investigated diamond is natural or synthetic. Natural diamonds are found in all types: Ia, Ib, IIa and IIb (see figure 1.4). However, HPHT diamonds can only be Ib, IIa

and IIb, whereas CVD diamonds are only IIa and IIb [13].

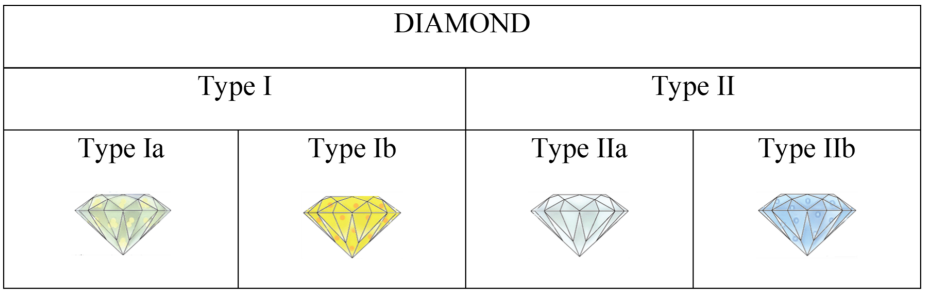

FIGURE 1.4: Diamond classification, based on [26].

1.5 Fabrication methods of synthetic diamonds

Natural diamonds are formed from millions of years of geological pressure and now are extracted from mines deep in Earth. Currently, it is possible to reproduce the conditions resent in the Earth's mantle in laboratory chambers. There are several techniques available that imitate the natural diamond growing environment, i.e. high pressure, and high temperature. It is reported that around 50% of mined diamonds are not of gemstone quality and are used for industrial purposes only. The rarity and unique combination of features of diamond accelerated the development of synthetic diamond acquisition. The first synthetic diamonds were produced in the 1950s for industrial uses by General Electric [14]. Currently, synthetic diamonds have approached gem quality and are being used in the jewellery industry as a less expensive alternative to mined diamonds. The most common method imitating the natural diamond growth environment is high-pressure high-temperature (HPHT). Another known method of growing industrial diamond is chemical vapour deposition (CVD). Figure 1.5 illustrates different synthesis methods according to the phase diagram of carbon.

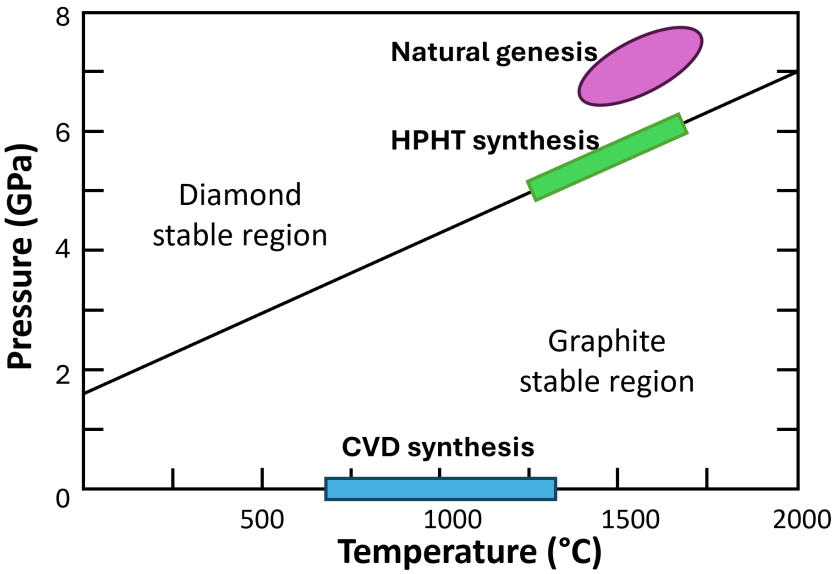

FIGURE 1.5: Different methods of diamond synthesis, based on [15].

Usually, an artificial diamond is synthesized from the powder of natural diamond under certain conditions. Basic idea is to convert graphite, the carbon source material, into diamond while applying high enough temperature and pressure. In the HPHT method, pressures of several gigapascals (GPa), e.g. 5.5 GPa, and temperatures around 1300 - 1600 °C are used to grow diamond under conditions like those in the Earth's crust [16]. Under these conditions it is more likely to obtain diamond rather than graphite. The phase diagram shows that graphite is the most stable form of carbon at atmospheric pressure, however, at high pressures, above 5 GPa, temperature 1300-1600 °C diamond becomes more stable. Sp^3-carbon is more stable at high pressure, high enough temperature overcomes activation barrier required for rearanging sp^2 into sp^3. If temperature is too high graphite may form, so HPHT controls the conditions to mantain diamond growth. Within the Earth, diamond forms at pressure of 5.5-8 GPa and temperature in range of 1000-1400 °C at 140-240 km in-depth [17]. HPHT technology produces small diamond crystals of diameter a few millimetres and is thus limited in application [16]. It is the most produced form of diamond.

An alternative to HPHT is diamond synthesis in its metastable regime, namely chemical vapour deposition (CVD). Here, diamond is grown from a hydrocarbon gas mixture. In this process usually 99% of hydrogen H_2 and 1% of methane CH_4 are used as a gas source [18]. In the initial growth phase, carbon atoms form crystallites on the substrate material and then grow to form a continuous diamond film. This technique can be used for fabrication of both polycrystalline and single-crystal structures [19]. Unlike HPHT, the CVD process does not require high pressures as the growth occurs typically at pressures under 27 kPa. Even though HPHT diamond crystals are of high-quality, the CVD techniques allow diamond to be deposited in the form of thin films over large areas and on various materials [20]. Moreover, CVD diamond can be deposited on substrates of different shapes [21]. This approach cannot be realized by either natural or HPHT diamond. Figure 1.6 shows the differences between the two growth methods and their impact on the final shape of the crystal.

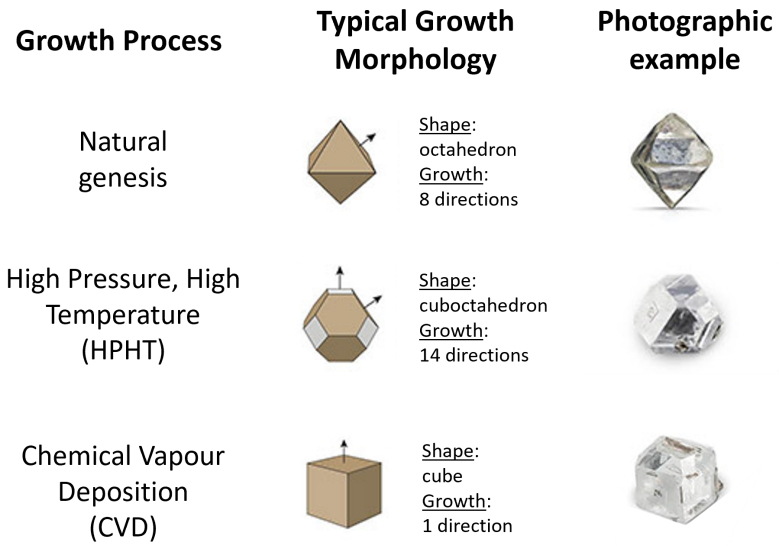

FIGURE 1.6: Different diamond growth processes and their typical morphologies. However, by changing the CVD conditions, the diamond morphology can be cubic, octahedral, cubo-octahedral, triangular, etc., based on [22].

Thanks to the ability to precisely control impurity levels and tailor the electronic and optical properties of the diamond, CVD has emerged as the preferred diamond growth technique for variety of applications. The well known properties of its extremely high hardness (Vickers hardness of 10000 $kgmm^{-2}$) and high refractive index (2.4), resulted in diamond being primarily used in the jewellery and cutting and drilling industries. Optically, diamond samples grown by CVD have the widest wavelength transmission spectrum known in material science (from UV to FIR). Thus, diamond makes a suitable substrate for integrated photonic devices that operate over a wide wavelength spectrum. UV–vis-NIR region has been used to create diamond windows and lenses for optical systems, the mid-IR transparency allowed for applications in molecular sensing and astro-photonics, and the far-IR transparency (up to THz regime) allowed for applications in bio-imaging, Far-IR astronomy imaging, security screening and Terahertz waveguides for imaging applications [23]. Moreover, diamond's high thermal conductivity (2000 WmK^{-1}), which is 5 times that of copper and 100 times higher than typical optical materials, result in the use of diamond in thermal management for high power devices and radiation detectors.

Moreover, CVD diamond components are highly resistant to chemical corrosion, which makes them suitable for use in harsh environments. Their bio-inertness allows for applications in bio-sensing [24], medical devices [25], and lab-on-chip technologies [26]. Diamond also provides exceptional resistance to scratches and breakage. The intrinsic nitrogen concentration in diamond is crucial for applications related to nitrogen-vacancy (NV) magneto-optical properties, such as high fluorescence, single-photon generation, the ability to read the spin state using optical methods [27–29].

In general, there are two main grades of CVD diamond used in laser writing, namely electronic grade (Type Ia) with about 5 ppb nitrogen and

optical grade (Type IIa) with about 100 ppb nitrogen. For applications that require dense ensembles of NVs, HPHT-grown diamond (Type Ib) with nitrogen concentrations of 100 ppm is recommended.

1.6 Methods of introducing dopants into diamond

Apart from defects occurring naturally or during diamond growth, damage of the diamond lattice may be caused by post-processing methods, namely ion implantation, neutron or electron irradiation [30] or laser writing [31].

1.6.1 Ion implantation

Ion implantation introduces impurities (ions) into the near surface region of any solid, including diamond and graphite. This process causes microscopic and macroscopic modifications in diamond that impact the chemical and physical properties of the sample. This method possesses high positional accuracy and is commonly used [32]. During ion implantation, highly energetic ions are bombarded on to the target sample. Their energy often exceeds the binding energies of the atoms of the target material, here carbon, which leads to displacement of the host atoms. This damage is undesired, however, there are several post-implantation techniques that diminishes the unwanted effects of ion implantation, e.g. annealing. The main change in diamond structure due to implantation is the breakage of sp^3 diamond bonds, which results in formation of sp^2 graphite bonds. Moreover creation of vacancies and carbon interstitials that assist throughout the whole ion implantation proces may disrupt the metastable equilibrium of the diamond phase. When energy, in the form of heat or kinetic energy is delivered to the system (lattice atoms), there is always a possibility that diamond may transform into the thermodynamically stable form of carbon, i.e. graphite. Structural modifications like graphitisation lead to changes of the properties of diamond, e.g.

electrical conductivity and density. Therefore, it is important to transform material structure in a controllable and precise way. Depending on the application, the ion implantation procedure allows controllable incorporation of dopant atoms into semiconductors with respect to their concentration and depth. The implantation depth is determined by the energy of the incoming ions. The ions with the highest energy can penetrate around a micron into the material [33, 34]. Nonetheless, highly energetic ions generate more damage to the material resulting in a loss of lateral positional accuracy [32] . On the other hand, ions of lower energy stay closer to the surface of the material, reaching depths of around 1 nm. Diamond with shallow dopants finds application in, for example, magnetic sensing [35]. Lattice vacancies or dislocations are formed when the energetic ions pass through the material. There are three ways in which an incident ion can dissipate energy within the diamond, namely Rutherford scattering, knock-on atoms and ionisation [36]. The Rutherford process comes from direct ion-ion scattering and subsequent displacement of a carbon atom into an interstitial state. Knock-on displacements occur when a fast-moving displaced carbon causes further lattice damage of the material. The final way ions can dissipate energy is in the form of ionisation by generating electron-hole pairs in the diamond. It was observed that if the initial ion energy is too high, i.e. above 100 keV, graphite material is formed [32]. Additionally, a large concentration of substitutional atoms create strain in the structure. Therefore, to provide accurate introduction of dopants the ion implantation takes place under specific conditions, andunder specific implantation energy and fluence [37].

1.6.2 Irradiation

Another method to introduce disorder into the diamond lattice is, for example, irradiation with high energetic particles and neutrons. This technique

causes collision displacements, i.e. energy transfer from incident neutrons to material atoms, that result in changes in the distribution of material atoms and its properties. This is called neutron irradiation damage [38]. Usually, the higher the energy of the neutrons, the greater the irradiation damage. Carbon is an interesting material to study structure transformation, for example the graphite to diamond transition. Thanks to the optical experiments conducted on single crystal diamond exposed to ion irradiation of an energy of a few MeV, the radiation effects were observed, namely the transition from diamond to graphite structure, and accordingly the decrease in the mass density [39]. Figure 1.7 shows the process of formation of NV centres, starting from nitrogen irradiation of diamond [40].

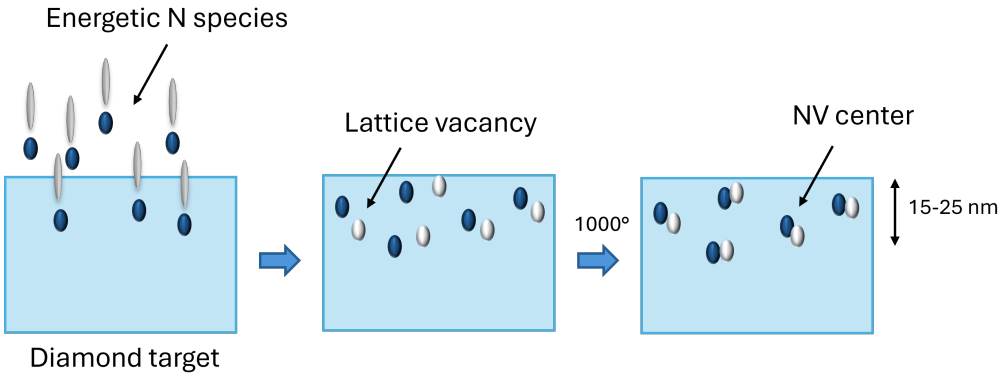

FIGURE 1.7: Schematic picture of irradiation of diamond by ^{14}N and generation of NV centres. Energetic N species enter diamond, then they are incorporated within the lattice and finally after thermal processing form NV centres (grey elements were drawn to indicate fast movement of energetic species), based on [40].

When diamond is exposed to high energy particles (e.g. electrons, neutrons, protons, ions) or photons (e.g. γ-rays) carbon atoms can be displaced from the lattice and produce vacancies and interstitial atoms. Upon annealing where interstitials and vacancies are mobile, they can migrate in the lattice and form intrinsic (e.g. V2) or extrinsic (NV) complexes. The study of extrinsic defects in diamond led to development of more advanced technologies to introduce defects in a more governable and accurate manner.

1.6.3 Laser writing

Laser writing enables more precise defect incorporation in different types of material, compared to the methods mentioned above. The availability of such technology is crucial, especially in the research area of colour centres in diamond and application of NV centres in quantum computing [41]. This technology enables fabrication of localised defects by laser writing in a diamond structure, and is a promising prelude to the novel defect engineering techniques for quantum technologies. It is of particular importance since NV centres exhibit atom-like properties that are required in quantum computing. NVs have an electron which is isolated from the lattice, which means that a certain electronic state information can be stored and maintained in the NV even at room temperature. Therefore, in quantum information, NVs may be treated as basic units called qubits [42]. Due to this finding, diamond was announced as a perfect substrate for spintronics and quantum technology, resulting in development of manufacturing of a new generation of quantum devices that use individual colour centres.

1.6.4 Patterning diamond

Patterning of diamond for electronic devices requires controllable and reproducible methods. Knowing that diamond possesses unique chemical inertness and hardness, the removal of surface material without damage is required. Thiss been successfully accomplished by dry etching processes, including plasma etching, ion beam etching and reactive ion etching (RIE). These techniques have been applied for fabrication of uniformly etched diamond structures for photonic devices, e.g. micro-electrochemical systems (MEMS). Moreover, prototypes of diamond devices have been demonstrated,

e.g. diamond cold cathodes [43], field effect transistors [44], MEMS [45], optical diffractive elements, and diamond micro lenses [46]. Patterning the surface of diamond was also demonstrated by laser processing, e.g. excimer laser etching [47]. Moreover, nanosecond pulsed lasers manifest the ability of micromachining [48] and even cutting the diamond [49]. These examples show that lasers are ideal for processing delicate and extremely hard materials. For instance, diamond, which is the hardest material known, can be drilled, cut, and patterned by laser machining technology. Ultrafast lasers, e.g. 500-fs pulsed lasers, surpass the ability of other laser systems offering multiple advantages, i.e. lack of lateral thermal damage, precision, and cleanliness of the abricated surface.

Therefore, this report focuses mainly on the diamond defects created by ultrafast laser technologies, in particular, direct laser writing (DLW). This novel technique is considered an effective way to induce defects into diamond structure. The important factor is that DLW enables generation of microstructures at both the surface and the subsurface of a transparent material. DLW is a new and emerging method that can transform diamond technology through effective machining inside crystals. This process serves different purposes, vacancy creation, graphitisation, and local annealing, just to name a few. Thus, the further development of this technique is required. Such research on DLW in diamond, supported by adaptive optics, leads to better understanding and improving of existing technology. Here, adaptive optics is applied to correct for aberrations in the laser beam caused by imperfections in optical components or variations in the refractive index of the material being processed. By adjusting the shape or phase of the laser beam, adaptive optics systems can compensate for these aberrations in real-time, resulting in improved precision and resolution of the fabricated structures.

Moreover, DLW technique possesses the potential to be applied in interdisciplinary studies, including surface processing, sensing, quantum information, biomedicine, etc.

1.7 Conclusions

Owing to its extreme properties, diamond has a high industrial value and thus is a favourable material for interdisciplinary technologies. Moreover, the amount of chemical impurities and thus the properties of diamond can be easily manipulated when produced in the laboratory environment. The development of CVD diamond synthesis allowed scientists to control the purity of the material, obtain larger areas of diamond, and utilize its properties. Both CVD and HPHT methods enable control of diamond growth, including the concentration of impurities, that influence material properties, and hence the final performance of the diamond devices. Diamond synthesis in laboratory conditions has reduced the costs of the material, and diamond wafers of 120 mm diameter can be deposited. Currently, CVD diamond has found applications in machining and tribology (e.g. cutting tools), photonics (e.g. optical components for lasers), electrochemistry (e.g. electrochemical sensors) and the semiconductor industry (e.g. heat sinks) [50], just to name a few. Additionally, there are still areas of science where properties of synthetic diamond might find their use, for instance quantum technology and high-power electronics. Thus, today's demand for diamonds is mostly satisfied by laboratory grown diamonds.

Chapter 2

Laser processing in transparent materials

2.1 Introduction

Ultrafast lasers have been initially developed over half a century ago and became the state of the art of the current research and development. Lasers in the femtosecond, picosecond and nanosecond time regimes have been applied to modify and characterize different materials. In comparison with nanosecond pulsed lasers, the ultrafast ones are distinguished by their high peak intensities and their interaction with materials on a timescale shorter than the creation of attice disorder and heat conduction. These characteristics enable ultrafast lasers to perform very precise and controlled modification of structure of the material. Currently, laser processing technology is used in diamond to generate individual defects (e.g. colour centres), graphitic microstructures, and surface structuring (nanoablation). This chapter aims to outline the nature of ultrafast lasers, and provide examples of material processing and methodology, namely direct laser writing and laser machining in transparent materials, such as diamond. The principle and importance of adaptive optics to support the laser writing processes is also discussed

here. This chapter introduces various examples of applying laser writing for diamond functionalization. However, research presented in this thesis concentrates mainly on laser writing of graphitic microstructures that find application in electronic and photonic devices, e.g. electrodes for radiation detectors.

2.2 Ultrashort pulsed lasers

In the context of laser classification, lasers are categorized based on their operational mode, which can be either continuous or pulsed. In the case of continuous-wave (CW) lasers, the emitted light operates continuously, maintaining a constant amplitude throughout a time duration. For continuous-wave operation, the population inversion of the gain medium needs to be continuously replenished by a steady pump source. In some lasing media, such as Ruby laser, nitrogen lasers this would be impossible, while for others it would mean pumping the laser at very high powers that could eventually destroy the laser. Lasing media that require short-lived excited states or high power densities for inversion (e.g., excimers, nitrogen, ruby, and free-electron lasers) are typically unsuitable for continuous-wave operation. Consequently, such lasers must be run in pulsed mode. CW lasers typically exhibit a narrow wavelength bandwidth. Initially, CW lasers utilized laser dyes to cover broader spectral regions, particularly within the visible spectrum. Over time, the spectral coverage of CW lasers expanded, reaching into the infrared (IR) region along with the advancement of solid-state materials. Although dye lasers dominated the field in earlier times, they have been nearly completely replaced with powerful and efficient diode-pumped solid-state lasers.

In contrast, pulsed laser light emission means that the optical power is delivered in pulses of a specified duration at a particular repetition rate. The mode-locking procedure enables emission of laser light in the form of time limited pulses [51]. The first ultrafast laser was a helium-neon laser operating in nanosecond pulse regime, built in 1964 [52]. Currently, the most popular lasers are picosecond and femtosecond ultrashort pulsed lasers, used in a variety of research applications. The ultrashort laser pulses are considered to have a uniform phase across the collimated laser beam and a uniform pulse front (contours of constant intensity within the pulse). A common example of a femtosecond laser is Ti:sapphire, which is used as a tunable laser medium.

Ultrafast lasers are characterised by several parameters, i.e. pulse duration, which is the time between the start and the end of a pulse (short pulse durations are on the order of picoseconds, femtoseconds or attoseconds), peak power, which occurshen the intensity reaches its maximum value (minimum power is usually 0 W), and the bandwidth (or linewidth), which means the width of the optical spectrum of the output. It is possible to calculate the peak power of a laser beam by dividing the energy in each pulse by the duration of the pulse (also known as pulse width). Ultrashort pulses with few-femtosecond pulse durations can have very large bandwidth, for example tens of terahertz. Moreover, ultrafast lasers have higher peak intensity than CW lasers as the mode-locking technique significantly increases the peak power of ultrafast lasers.

2.2.1 Mode locking techniques

An ultrafast laser comprises an optical cavity containing two mirrors and a material, referred to as a gain medium, positioned between these mirrors.

When light enters the cavity, it oscillates between the mirrors, being amplified with each passage through the active medium as a result of stimulated emission. Stimulated emission of pumped energy occurs when an excited atom in the gain medium is stimulated by an incoming photon to emit another photon of the same wavelength and phase. One of the mirrors is partially transparent, permitting a portion of the light to exit the cavity after each cycle of propagation within it. Laser emission has a spectral bandwidth Δv, which is usually defined as a full width at half maximum (FWHM) of the Gaussian curve (see figure 2.1).

As the light confined in the cavity reflects multiple times, the radiation of the laser is represented in the form of cavity modes of certain resonance frequency. The mode spacing is defined by the round-trip time inside the cavity, and represents the frequency difference between each mode, δn. The frequency difference between each mode is described by the following equation,

$$\delta n = \frac{1}{T_{RT}} = \frac{c}{2L} \tag{2.1}$$

where T_{RT} is the cavity round-trip time, c is the speed of light and L stands for the optical length of the cavity.

Mode-locking techniques are introduced to obtain ultrashort laser pulses in a regular pattern with a fixed phase relationship between the modes. The presence of the mode-locking device ensures that pulse parameters, such as pulse energy, pulse duration, spectral bandwidth, etc., do not change after each completed round trip. Figure 2.2 represents a temporal profile of the mode-locked laser emission.

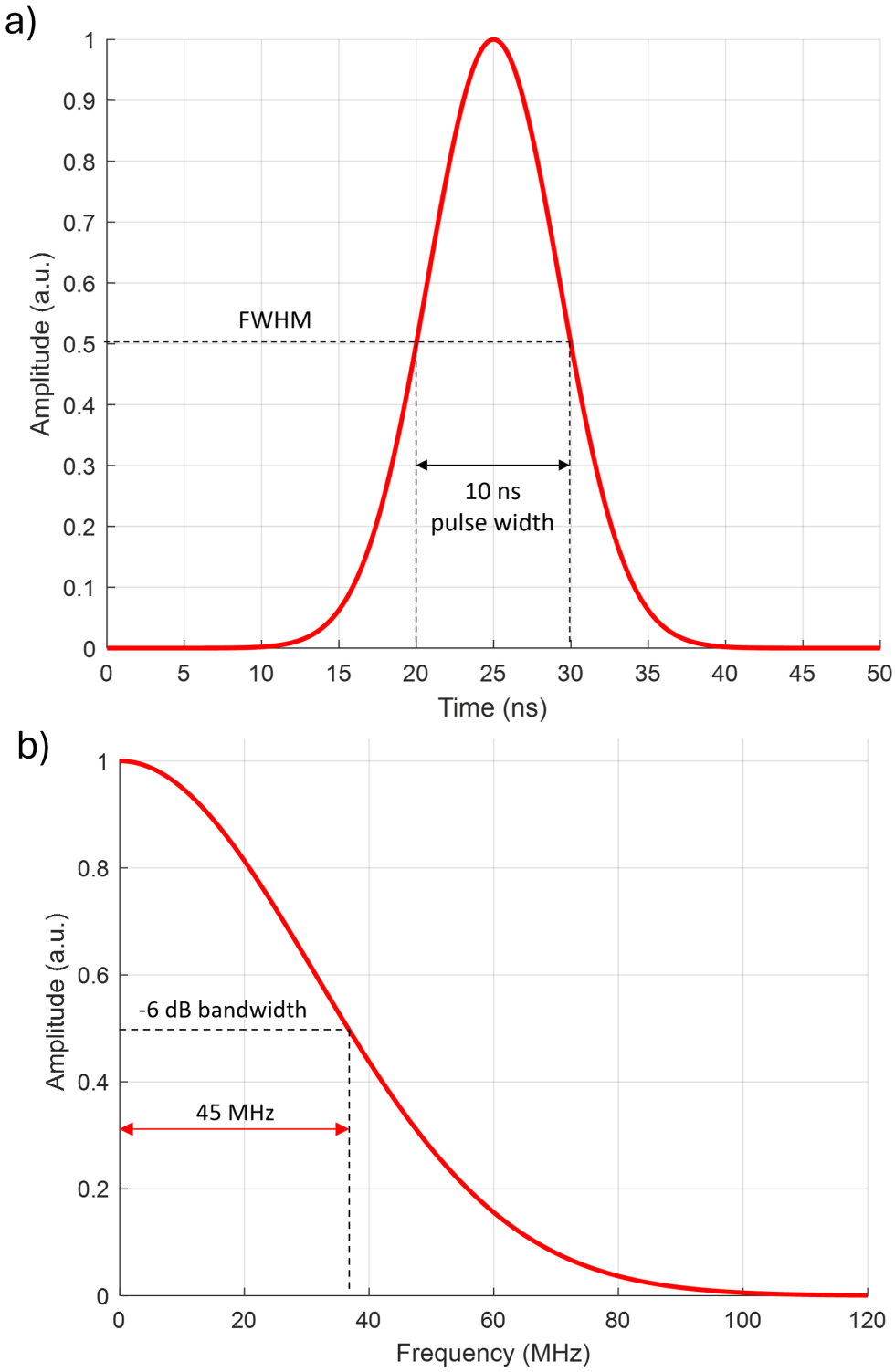

FIGURE 2.1: An example schematic of (a) Gaussian temporal distribution of a pulsed laser with FWHM pulse width of 10 ns and (b) -6 dB bandwidth of the pulsed laser corresponding to apulse width of 10 ns, based on [53].

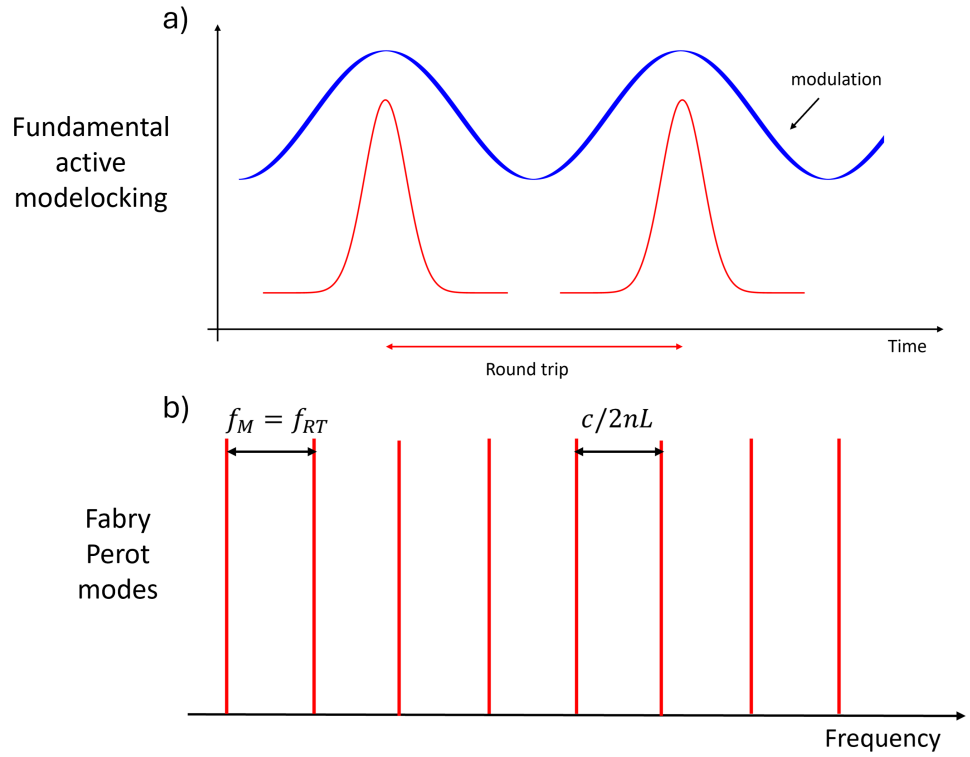

FIGURE 2.2: Fundamental modelocking in a) time and b) frequency domain. Modelocking in time domain corresponds to an active modulation that is synchronised to the round-trip time of the pulses. In the frequency domain, this corresponds to a modulation that is equal to the mode spacing, i.e., the round-trip frequency (f_{RT}), based on [54].

Two types of mode locking can be distinguished, namely active and passive mode locking. Active mode locking involves periodic modulation of either the resonator losses or the round-trip phase, and can be performed by placing, for example, an acousto-optic or electro-optic modulator into the laser cavity. Modulation synchronized with the resonator round trips results in generation of ultrashort pulses (usually picosecond pulses). Passive mode locking can be achieved by implementing a saturable absorber into the laser resonator. A saturable absorber is a device that exhibits intensity-dependent transmission. Ideally, a saturable absorber absorbs low-intensity light and transmits high-intensity light. This process is repeated as the light oscillates in the cavity and the passive mode locking is automatically synchronized with the round trip frequency. Therefore, the passive mode locking is also

known as self-mode-locking. Compared to active mode locking, the passively mode-locked laser generates pulses with a shorter pulse duration [55].

During this research a Newport Spectra Physics Ti:sapphire laser with 100 fs pulse duration, 790 nm wavelength with passive mode locking and Light Conversion, Pharos 8SP emitting 200 fs pulses at a wavelength of 515 nm were used. A more detailed description is presented in chapter3.

2.3 Direct laser writing

Direct laser writing (DLW), also known as multiphoton lithography or direct laser lithography, is a laser-based method used for introducing modifications into a material structure. Although the direct laser writing can be performed in either nanosecond (ns) or picosecond (ps) regimes, femtosecond lasers (fs) provide multiple advantages, such as lack of lateral thermal damage, high precision and cleanliness of fabricated surface.

In case of femtosecond laser machining, the optical energy is transferred to the material by laser induced optical breakdown, where a proportion of electrons are excited across the bandgap, and can subsequently transfer energy to the lattice, causing structural damage. DLW with ultrafast lasers offers precise three dimensional (3D) microfabrication inside transparent materials through a non-linear process, which means that the light is absorbed within the transparent sample by multi-photon absorption or tunelling ionization [56, 57]. The femtosecond laser pulses generate large peak electric fields, of the order of 10^9 V/m, which is required for non-linear absorption to occur. Non-linear absorption processes require femtosecond pulsed lasers with very high intensities, and the only location that has sufficient

electric field density for this to occur is within a tight focal volume, which ensures high three-dimensional resolution of fabrication. Features of micrometre scale and smaller may be fabricated within different materials, including glass and diamond. Here, the short pulse duration is crucial, as all the pulse energy is delivered to the laser focus in a timescale shorter than that required for thermal diffusion of the absorbed energy. The laser writing procedure is illustrated in figure 2.3.

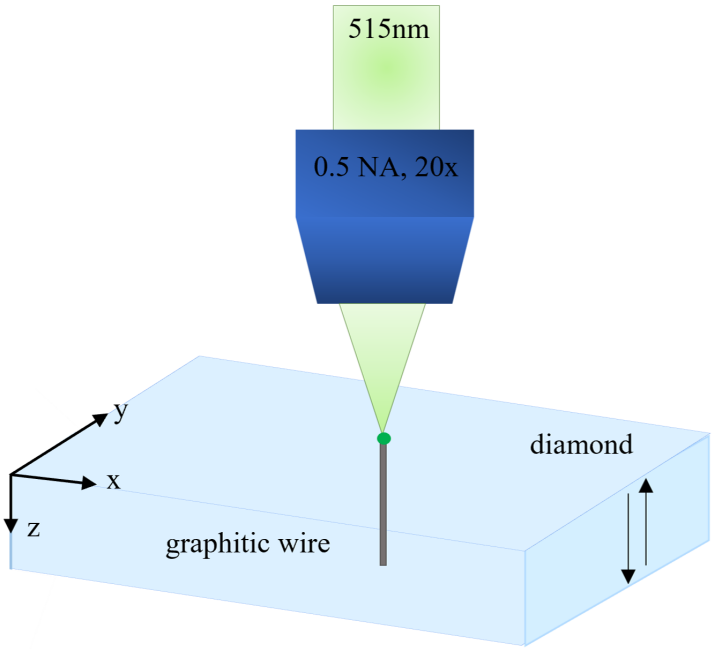

FIGURE 2.3: Schematic of laser writing of graphitic columns.

Upon femtosecond pulse irradiation, the semiconductor material experiences several regimes of excitation and relaxation before coming back to its equilibrium state. The four regimes include carrier excitation, thermalization, carrier removal and thermal and structural effects.

Continuously growing demand for more advanced devices to meet data capacity requirements in communications made femtosecond laser writing an attractive technique to fabricate integrated photonic systems. Features of micrometre scale and smaller may be fabricated within different transparent

materials without any modification to the surface or surrounding regions. Femtosecond laser pulses directly induce refractive index changes in transparent dielectric materials, and when the sample moves along with the laser beam a refractive index profile like in a buried waveguide can be produced [58]. Laser writing of waveguides in bulk glass enhances manufacture of three-dimensional photonic devices. The main characteristic of the waveguide is that they, as the name suggests, guide light. They define the spatial region where the light can propagate. There are many examples of generating waveguide devices in different type of glasses [59–61] and polymers [62, 63]. Optical waveguides have also been demonstrated in different types of crystals, i.e. $LiNbO_3$ [64, 65], Nd:YCOB [66], ZnSe [67], Nd:YAG [68]. The laser writing approach is easier compared to conventional surface waveguide fabrication by alternative processes [69].

Another application of fs-laser micromachining is to support fabrication of magnetic field sensors [70]. Here, the laser system was used to write an interferometer design into silica glass. Aerospace and petrochemical industries require pressure sensors that can work at high temperature, e.g. 500°C. Currently, the main sensor material applied in such conditions is silicon, but that, unfortunately, does not last long in that environment. Thus, silicon carbide (SiC), which is nearly as hard as diamond, has been proposed as a promising candidate to replace silicon detectors. It was already demonstrated that laser micromachining silicon carbide could fabricate high temperature pressure sensors [71]. The excellent properties of SiC, e.g. its resistance to thermoplastic deformation, makes it a perfect candidate for sensing devices in harsh environments. Diamond exceeds SiC performance [9] and is considered as a candidate material for sensing devices applied in extreme conditions [72, 73].

Apart from laser writing of 3D optical waveguides and microstructures in bulk transparent materials, laser micromachining finds application in cell biology [74]. It was demonstrated that femtosecond laser pulses enable non-invasive intercellular ablation of individual organelles in living cells [75]. Recently, scientists from the University of Southampton demonstrated a new approach of ultrafast laser writing in order to pattern silica glass with anisotropic nanograting structures with negligible transmission losses [76]. The resulting birefringent modifications allowed fabrication of ultra-low space-variant birefringent optical elements with high thermal and chemical durability along with high optical damage threshold. These elements can allow the formation of vector beams (beams of light containing structured polarisation) or other optical elements relying on polarisation modulation and can be applied for high power lasers. They are also used for optical data storage, providing high capacity data archiving with unlimited lifetime at room temperature and thermally stable up to 1000°C [77].

One particular example of ultrafast laser machining is ablation, which is removal of material from the surface. This process occurs when the laser fluence of the laser exceeds the ablation threshold of the target material. In case of femtosecond interaction, the laser pulse duration is much shorter than electron cooling rate [78]. At high laser fluences, the energy from the surface leads some of the surface to melt and evaporate resulting in an ablation plume. It is possible to achieve laser-induced periodic surface structuring (LIPSS) in this kind of environment [79]. For fs-lasers processing, the LIPSS consists of periodic nano- and micrometre- scale features [80–82]. It was already observed that femtosecond lasers can damage even the hardest known materials [82, 83]. Ablation is a destructive process and is one of the easiest ways to cut and scribe hard materials, and is hence applied across different industries.

2.4 Graphitisation

At room temperature and atmospheric pressure, diamond is a metastable material. However at high temperatures, usually at 1000–1600 °C, it can transform into graphite. Graphitisation of diamond refers to the transformation of diamond into graphite, which is possible upon implantation of ions, during postimplantation annealing or when high-energy laser irradiation is applied. This conversion leverages distinct physical properties of diamond and graphite, i.e. diamond is an excellent insulator with high thermal conductivity and hardness, while graphite is a good electrical conductor. Diamond graphitisation occurs not only by high-temperature annealing but also by novel methods that enable fast graphitisation, for example graphitisation under laser treatment [84–86], which is the main point of this thesis. The atomistic simulation of the diamond (111) surface y Wang et al. [87] shows that the diamond-to-graphite transition occurs along different pathways, depending on the length of the pulse of the laser. When using nanosecond laser pulses or longer, electrons excited by the laser can reach thermal equilibrium with the lattice over the pulse duration, resulting in thermal disordering or surface melting. In this case, the graphitisation front propagates vertically into the bulk layers, leading to the formation of diamond-graphite interfaces after the laser treatment. However, when the laser pulse duration is reduced to the femtosecond range (200-500 s), structural changes on the surface can occur within a few hundred femtoseconds. This rapid transformation is significantly faster than the usual time scale of lattice dynamics, and is thought to be driven by hot electron plasma excited by the intense femtosecond-laser pulse [88, 89]. Here, graphitisation of the surface occurs layer by layer and results in a clean diamond surface after ablation. Upon the interaction between energetic plasma and diamond, defects start to occur in the lattice by the atom displacement, causing the random formation of amorphous carbon

clusters. Finally, graphitisation of diamond starts at high enough temperatures [90]. When a high-energy laser is focused onto a diamond surface, it generates localized heating that can raise the temperature of the diamond to above its graphitisation point (around 1700°C). At these temperatures, the diamond's crystal structure, composed of sp^3-bonded carbon atoms, begins to rearrange into the sp^2-bonded structure characteristic of graphite.

Typically, an experimental consists of a high-power laser system (e.g. Yb or Ti laser) to irradiate the diamond sample. The laser beam is focused onto the diamond using high numerical aperture (NA) objectives, which allow for high-resolution patterning. The sample is mounted on a precise translation stage that enables control over movements and patterning. Real-time monitoring systems such as optical microscopes and spectrometers, are employed to observe the process and adjust parameters. Laser parameters are very important in controlling the graphitisation process. The wavelength of the laser affects the absorption efficiency of the diamond, with shorter wavelengths generally being more effective. Short pulse duration in ultrafast femtosecond lasers provides high precision, minimizes thermal diffusion and collateral damage to surrounding areas. Another important parameter is repetition rate, higher rates can lead to cumulative heating effects that facilitate the graphitisation process. Furthermore, the quality of the diamond itself significantly impacts the efficiency of graphitisation. Synthetic diamonds, either CVD or HPHT grown or HPHT are often used in these experiments because of their controlled purity and defect levels. The crystallographic orientation and intrinsic defects of the diamond can influence laser fabrication, affecting the uniformity and quality of the resulting graphite.

Recent studies have demonstrated the potential applications of laser-induced graphitisation of diamond in various fields. In photonics, this technique is used to create waveguides and photonic circuits [91], leveraging the

contrasting optical properties of diamond and graphite to guide and manipulate light effectively. In electronics, the combination of conductive graphite and insulating diamond can be used to fabricate advanced electronic components, such as diodes [92]. In sensing applications, the robustness and chemical stability of graphitised diamond make it suitable for developing highly sensitive and durable sensors [93]. Additionally, the precise control over nitrogen-vacancy (NV) center placement in diamond via laser processing opens new possibilities in quantum computing and communication [94].

Aside from writing defects for quantum applications, laser writing can also provide a stronger fabrication regime for micro-graphitic modifications [95], [96]. The interesting fact here is how the choice of laser processing components and parameters affect the nature of graphitic-like structures. Figure 2.4 shows examples of laser-written structures given different processing parameters, where using higher NAs resulted in smoother and continuous laser-written graphitic wires.

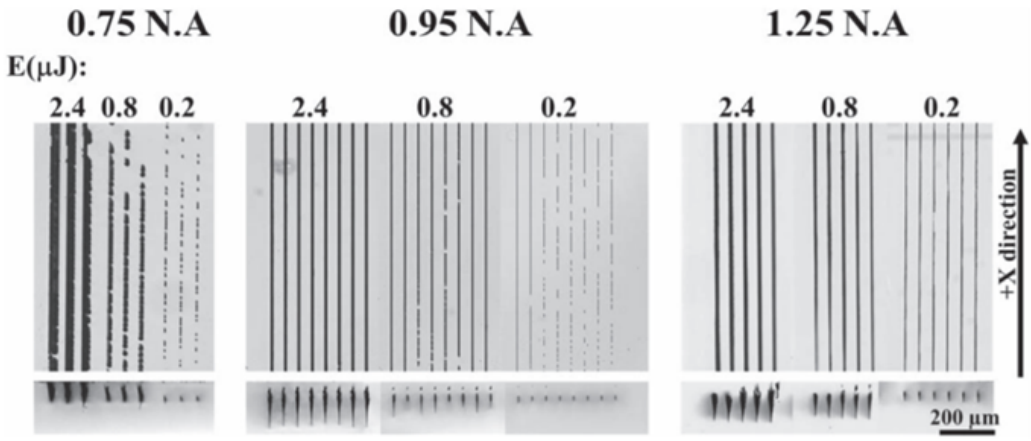

FIGURE 2.4: Microscopic images of the graphitic structures laser written in the bulk of diamond by varying processing parameters, using 0.75 NA, 0.95 NA and 1.25 NA focusing objectives (50 μm depth). The laser writing scan speeds (from left to right) in every energy set of 0.75 NA are 0.05, 0.2, 1 mm s^{-1}. Laser writing speeds for 0.95 NA are 0.2, 0.5, 1 and 5 mm s^{-1} (written along $+x$ and $-x$ directions (left to right), with x direction parallel to 110 crystallographic direction). For 1.25 NA scan speeds are 40, 50, 20, 5 and 2 mm s^{-1}, taken from [63].

The ultrafast lasers enable non-thermal transition from sp^3 phase to graphitic sp^2 phase. At normal temperature and pressure, 20 °C (293 K) and 0.10 MPa, the stable phase of carbon is graphite, but diamond is metastable, thus its conversion to graphite is negligible. However, at temperatures above about 4500 K, diamond rapidly converts to graphite. Rapid conversion of graphite to diamond requires pressures well above the equilibrium line: at 2000 K, a pressure of 35 GPa is needed [26]. Since carbon has no liquid phase at atmospheric pressure, no molten material is generated. Figure 2.5 shows the carbon phase diagram that indicates diamond transformation into graphite.

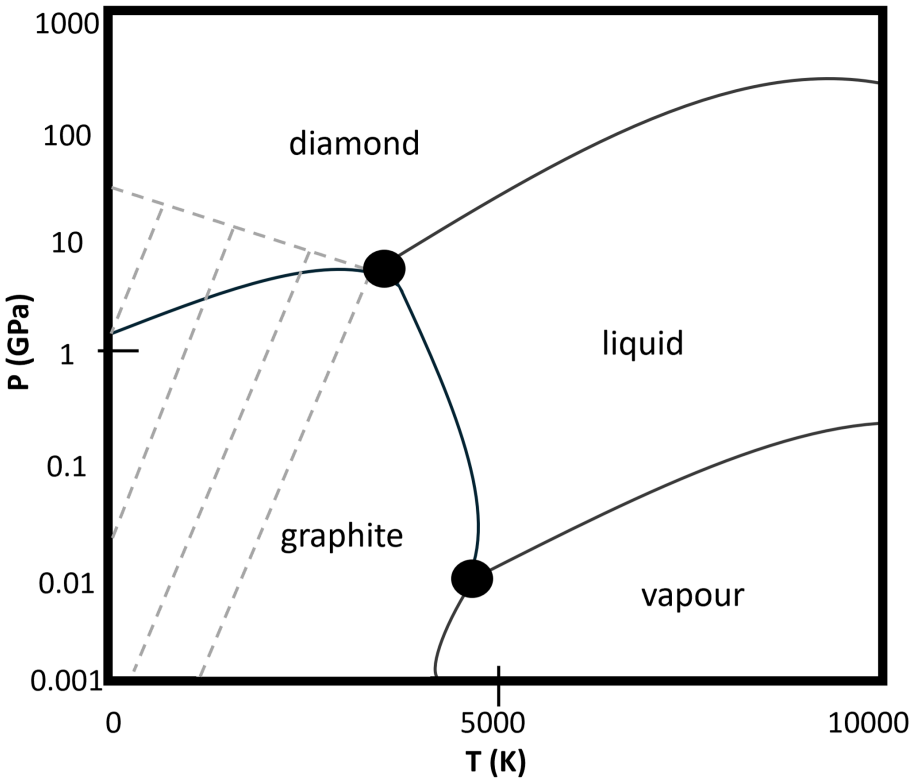

FIGURE 2.5: Carbon phase diagram, which shows the carbon state with respect to varying temperatures and pressures. It indicates conditions under which one phase is metastable. The phase boundary between graphite and diamond for temperatures below 4000 K is a wide coexistence area indicated by the grey stripes, based on [97].

2.5 Different types of laser-written devices in diamond

Although, diamond is the hardest common material, it can be drilled, cut and patterned by laser machining technology. Ultrafast lasers with sub-picosecond pulse duration offer multiple advantages, such as lack of lateral thermal damage, high precision, and cleanliness of fabricated surface. Direct laser writing (DLW) with ultrafast lasers offers precise three-dimensional (3D) microfabrication inside transparent materials through a non-linear process by multi-photon absorption or tunnelling ionization [56], [57]. Features of micrometre scale and smaller may be fabricated within different transparent materials without any modification to the surface or surrounding regions. DLW can be applied to functionalize diamond by modifying its lattice structure [98], [99] and at higher intensities introduce micro-graphitic inclusions through breakdown of the diamond lattice [100], [101]. Such controllable and precise structural modifications offer great promise for diamond technology through effective machining inside crystals.

The development of advanced materials with tailored properties has been a subject of intense research in various fields. One such material that has gained significant attention is synthetic diamond. Synthetic diamond possesses exceptional mechanical, thermal, and electrical properties, making it an attractive material for a wide range of applications, including electronics, optics, and cutting tools. One of diamond's notable properties is its low electrical conductivity. However, carbon also has a common allotrope that is indeed conductive, namely graphite. Hence, diamond offers the possibility of accommodating electrical circuits, if it can be locally changed into graphite. Researchers have explored various methods to introduce graphitic structures into diamond, thereby enhancing its electrical properties. Laser

writing has emerged as a powerful technique for modifying both surface and subsurface of synthetic diamond, enabling the generation of graphitic structures. Laser fabrication on synthetic diamond offers unprecedented control over the material's properties, opening up new avenues for the development of advanced devices and systems. It has been demonstrated that laser assisted methods enable writing of individual defects in diamond at selected locations and with high positioning accuracy [102]. For example, generation of vacancies in diamond samples with nitrogen content followed by thermal annealing, is a first step for formation of the coherent colour centres, i.e. NV centres, for quantum photonics.

2.5.1 Electrical devices

Another example presents laser writing of graphitic electrodes for diamond detectors [103, 104]. As a result, laser processing has attracted interest due to potential generation of 3D electrical circuitry and its advantage over other conventional methodologies [90, 105, 106]. Currently, electrical devices created in materials such as silicon are used for radiation detection. However, diamond is more resistant to radiation and exhibits higher thermal conductivity than silicon. These properties, including temperature tolerance, chemical inertness and ability to detect different types of radiation, make diamond an attractive detector material for harsh environments, e.g. nuclear-power-station monitoring and oil-well logging [107]. Some scientific experiments require focused beams of X-rays, which are usually produced by highly energetic electrons in synchrotrons. To support the analysis of the beam, a prototype of an X-ray diamond detector has been already reported [108]. The aim of this device is to simultaneously measure the position, profile, and flux of an incident beam. The illustration of the prototype device is in figure 2.6.

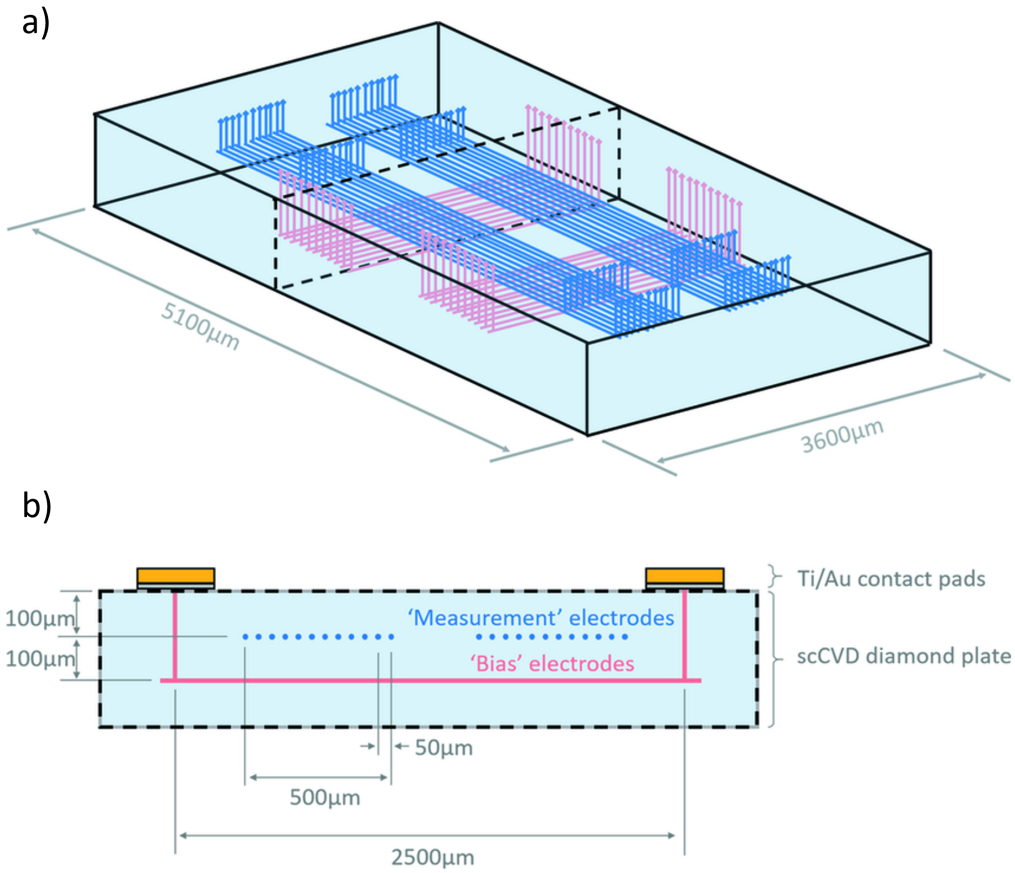

FIGURE 2.6: a) A schematic (not to scale) of the graphitic wire-layout inside a diamond plate and b) the cross-sectional image of the fabricated detector. Presented are embedded graphitic wires together with vertical columns that are used to transport the charge to the surface pads, taken from [109].

To obtain the above structure a short, 200 fs, pulsed laser, focused to micron-sizes using high NA lenses, assisted by adaptive optics aberration correction to graphitize wire paths inside bulk diamond was used. This kind of pixel detector was fabricated by laser writing two separate and mutually perpendicular arrays of graphitic wires, that are located beneath the surface of a diamond plate. The advantage of this detector is that the intensity, position, and shape of an X-ray beam can be well monitored. Single crystal CVD diamond detectors are essential as non-destructive diagnostic tools for the operation of synchrotron beamlines [110]. For that reason, it is crucial to functionalize diamond for sensing applications, e.g. laser writing of graphitic

structures. Furthermore, the conductive graphitic structures beneath the surface of the diamond give better control over wire geometry, i.e. its 3D geometry. In order to bring this technology to life, comprehensive studies need to be performed, which form the motivation for the research in this thesis.

2.5.2 Optical Waveguides

It was already demonstrated that it is possible to laser write optical waveguides [111] and other graphitic structures [84, 112] in diamond. The laser fabrication parameters, i.e. wavelength, intensity and pulse energy can be adjusted with respect to a chosen defect of interest. Figure 2.7 illustrates the laser writing procedure and the fabricated waveguides within the diamond bulk.

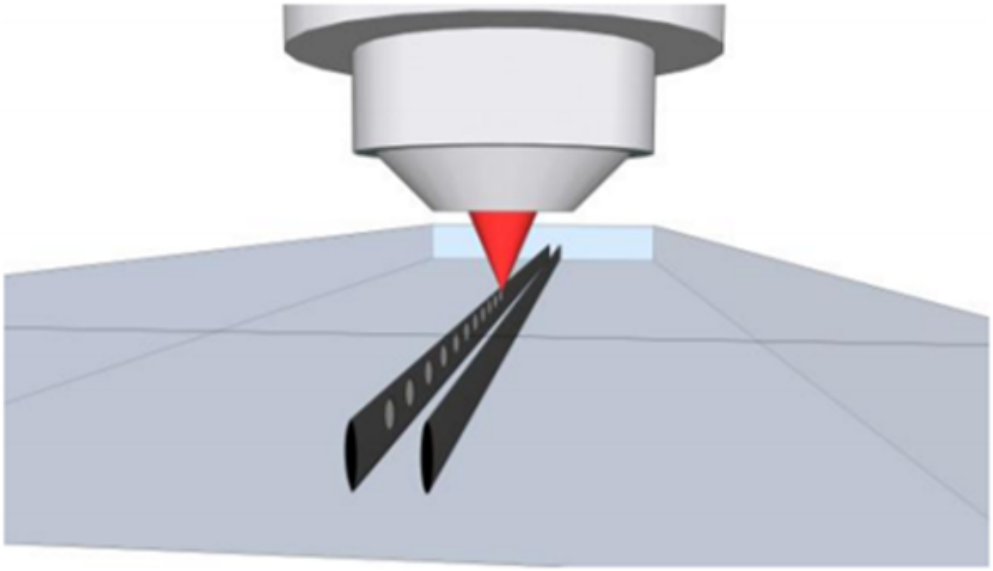

FIGURE 2.7: Femtosecond laser-writing procedure and laser-written waveguides in bulk diamond, taken from [113].

Three-dimensional waveguides in the bulk of diamond are manufactured using ultrafast laser fabrication. High intensities in the focal volume of the laser cause lattice breakdown. As a result, diamond is transformed into a

graphitic phase leading to a stress-induced refractive index change in neighboring regions. Waveguides consist of the region of increased refractive index, compared to the surrounding medium (also called cladding). In case of diamond, the laser-generated graphitic-like modifications enable light propagation. Due to the lower density of the sp^2 phase, compared to that of sp^3, a strong localized stress is generated within the surrounding diamond, which can act as an optical waveguide. It is possible to fabricate type II and type III waveguides [111], which means that they support propagation of either one or two polarization states, respectively.

2.5.3 Advanced applications and innovations

Ultrashort laser pulses are used to modify the structure of a material. Moreover, this technology is being used as a tool for product protection, namely security laser marking. One of the examples is to fabricate diffraction-based security features, e.g. holograms [114]. Another idea is surface marking on the girdle of diamond gemstones to identify or personalize jewellery. This idea is currently used by the Gemological Institute of America (GIA). However, there is a risk that the security features written on the surface may be easily polished off or be replicated on counterfeit stones. Small laser marks written beneath the surface of diamonds offer increased resilience to polishing, providing a significant improvement in the security of diamonds when compared to surface marking. These engravings can be performed by laser systems built at Opsydia, that specializes in commercially available laser technology to implement practically invisible structures, or identifiers, on the surface of or within transparent materials without compromising their integrity. The resolution of these marks created in the bulk of the material is much higher than current surface laser marks and so can be made much smaller, while still being visible under sufficient magnification.

2.6 Adaptive optics for aberration correction

Femtosecond laser writing requires focusing of the laser beam with a high NA objective lens inside the transparent material. The femtosecond pulses diminish the heat distribution and allow precise, highly localized at the focus, structure modifications. Focal volume confinement of the structural change enables precise machining of complex structures in 3D. However, apart from imperfections or misalignment of the optical system, the size of the light-matter interaction volume is defined by diffraction effects. It is said that an optical system with a resolution close to its theoretical limit is 'diffraction limited'. This phenomena was discovered in 1873 by Ernst Abbe, who observed that light of a wavelength λ that travels in a medium of refractive index n converges to a spot of angle θ and makes a spot of radius r, the minimum resolvable distance,

$$r = \frac{\lambda}{2n\sin\theta} = \frac{\lambda}{2NA} \tag{2.2}$$

where $n\sin\theta$ is the so-called numerical aperture, NA. This phenomena is known as Abbe's Diffraction Limit [115].

Currently, the intensity of the best focused light of a circular aperture is defined by an Airy function, also known as an Airy disk. The Airy pattern intensity is a result of diffraction theory, which in the focal plane of an objective lens can be approximated to a two-dimensional Fourier transform of the light incident on the pupil. In the x-y focal plane (lateral focal plane), the distance between two first intensity minima can be specified as follows:

$$d_{x,y} = \frac{1.22\lambda}{NA} \tag{2.3}$$

The above formula defines the lateral size of a perfect focal spot. Correspondingly, the axial (z axis) size of the focal spot is described by:

$$d_z = \frac{4n\lambda}{NA^2} \tag{2.4}$$

However, the approximate equation is valid for low NA. A more accurate expression in terms of NA is presented below:

$$d_z = \frac{2\lambda}{(n - \sqrt{(n^2 - NA^2)}} \tag{2.5}$$

Both results were obtained based on derivation of Fourier optics and trigonometric relationship, which represents light propagation through a lens [116]. From Fourier theory, it possible to calculate the light intensity in the focal plane of the lens. Here, the lens acts in a way such that the focal plane of the lens displays the far-field Fraunhofer diffraction pattern of the objective lens aperture. Figure 2.8 presents the schematic of optical system Fraunhoffer diffraction approximation with an example of Airy disc and intensity distribution, where equation 2.3 describes the first minimum.

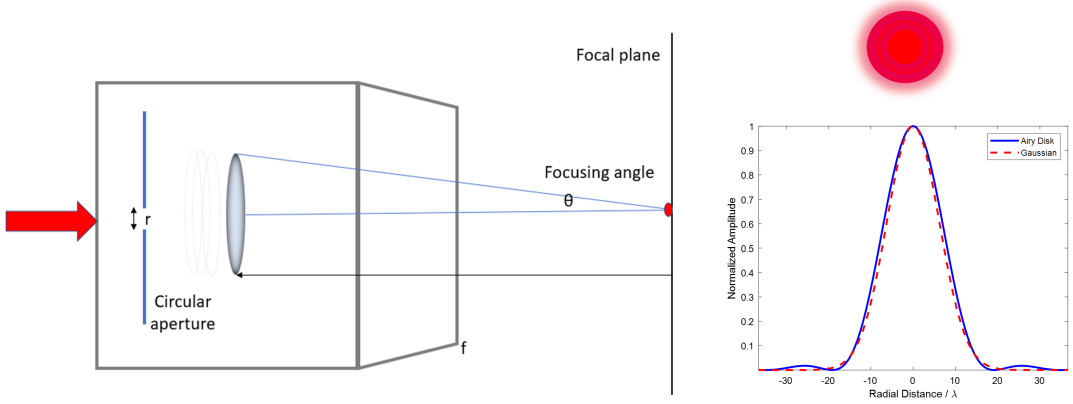

FIGURE 2.8: Optical system Fraunhoffer diffraction approximation. Schematic includes Airy disc and intensity distribution.

The successful fabrication of sub-surface microstructures is limited by spherical aberrations that occur when focusing onto a specimen with refractive index different to the immersion medium of the focusing objective lens, e.g. oil or air. A particular example is a depth-dependent spherical aberration as a result of refraction of light rays at the specimen interface. The spherical aberration results on a loss in resolution and power efficiency of fabrication. It has been demonstrated that a characteristic elongation of the focal intensity limits the generation of desired features [117]. Thus, control over the focal point is required to eliminate any optical aberrations. Figure 2.9 presents a schematic diagram of the phase aberrations arising from the lens.

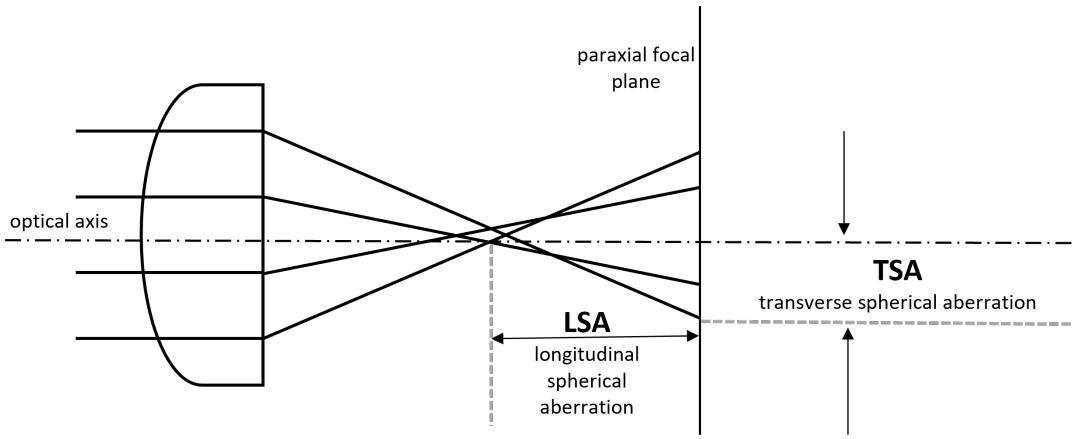

FIGURE 2.9: Schematic of spherical aberrations arising from the lens, based on [118].

The phase ϕ of the light as a function of position within the back focal plane (pupil plane) of the objective lens can describe the light-matter aberrations. The aberrated phase function in the pupil of the objective lens can be written as [119]:

$$\phi_{SA}(\rho) = \frac{-2\pi d_{nom}}{\lambda}(\sqrt{(n_1^2 - NA^2\rho^2)} - \sqrt{(n_2^2 - NA^2\rho^2)}) \qquad (2.6)$$

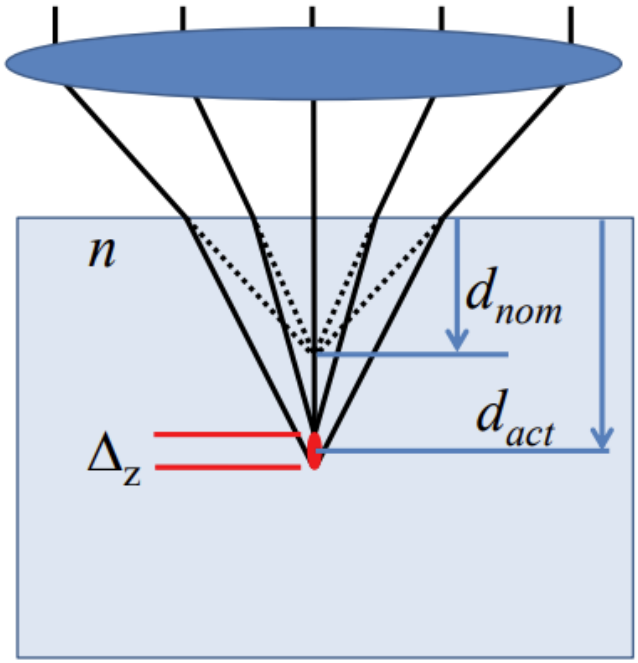

FIGURE 2.10: Schematic of focusing geometry showing the refraction of rays at the interface between two media of different refractive index, d_{nom} being the nominal depth within the sample and d_{act} is the actual depth, Δ_z is extent of the focus.

where λ is the wavelength of the light, ρ is the normalised pupil radius of the objective lens, n is the refractive index of the sample and d_{nom} is the nominal depth within the sample (see figure 2.10), assuming that the objective lens operates in air (n=1). Equation 2.6 describes spherical aberration as a result of the refractive index difference between the immersion medium of the objective lens (n_1) and the specimen (n_2). It is a very common aberration that occurs when light is focused into material through planar interface of two different refractive indices. It is worth highlighting, that even a small mismatch between the refractive indices may lead to significant spherical aberrations.

Phase aberrations can also be described by Zernike polynomials, orthogonal functions that can describe surface shapes and quantify wavefront aberrations in mirrors and lenses of a circular shape. Zernike polynomials correspond to different aberrations, for example astigmatism, coma, and spherical aberrations [120].

This approach assumes that light propagates through an inhomogeneous refractive index material. Figure 2.11 graphically represents the most common Zernike modes. The lower order Zernike modes such as piston, tip, tilt and defocus have negligible effect on the focusing mechanism. The aberrations that are corrected during the laser-writing procedures include coma, astigmatism and spherical.

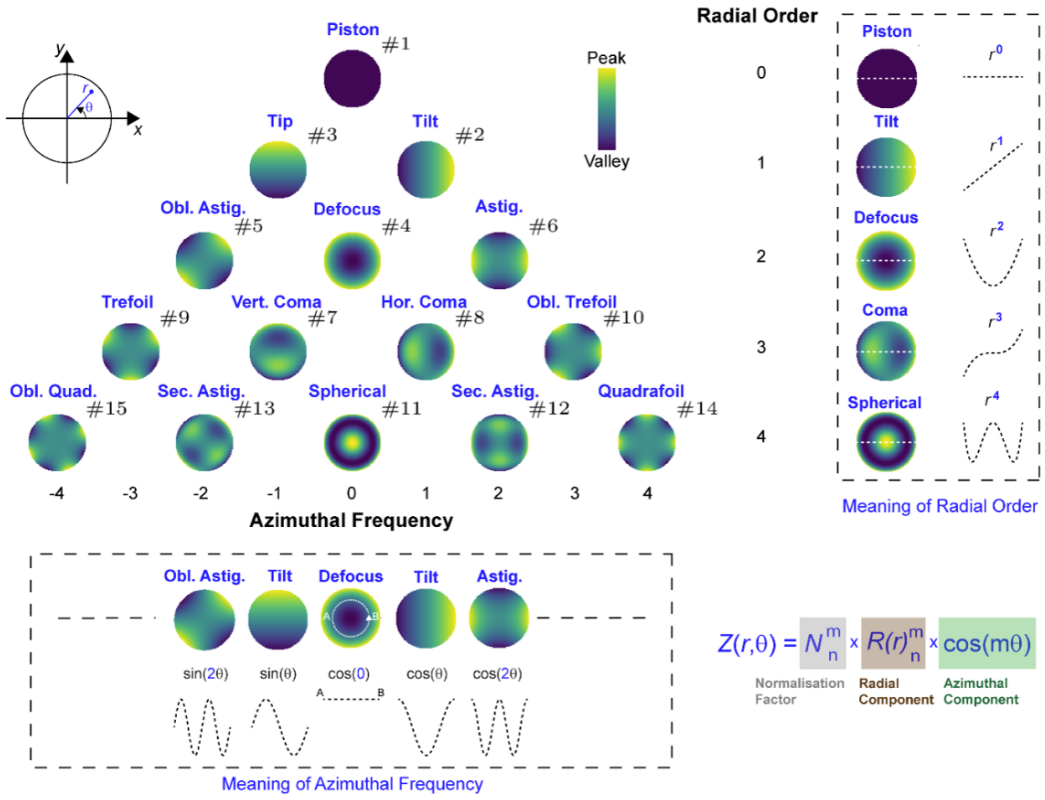

FIGURE 2.11: Graphical representation of Zernike modes, taken from [121].

It was already demonstrated that adaptive optics elements have supported ultrafast laser systems in various experiments, for instance for resolution enhancement in multiphoton microscopes [122] and manipulation of temporal pulse distribution [123]. An adaptive optics instrument can compensate for the depth-dependent spherical aberration by introducing a phase profile on an incident wavefront. The phase profile needs to be equal and opposite to the aberration caused by mismatch of refractive indices at the sample surface. This requires so-called adaptive-optics instrumentation, i.e.

a membrane deformable mirror (DM) or liquid-crystal spatial-light modulator (SLM), enabling precise fabrication of microstructures embedded within transparent materials. A deformable mirror provides a continuous phase distortion with large amplitude, but has a low number of actuators. On the contrary, an SLM benefits from a larger number of pixels, but its maximal modulation depth is typically limited to 2π radians. Figure 2.12 shows a schematic of a liquid-crystal spatial-light modulator.

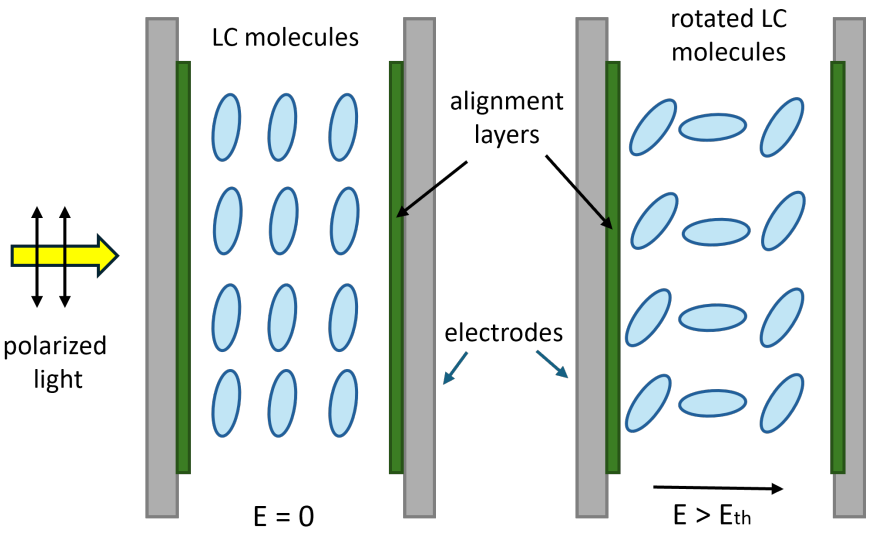

FIGURE 2.12: Schematic of liquid crystal SLM in ON and OFF states, LC: liquid crystal, E_{th}: threshold of the electric field amplitude, based on [124].

The SLM used in this research is a parallel-aligned liquid-crystal SLM that is used to compensate phase aberrations generated in the optical system. This SLM uses Liquid Crystal (LC) on Silicon technology, where liquid crystal is controlled by an applied voltage, resulting in a change of refractive index of the LC. Thus, the wave front of the reflected laser light can be modified. The performance of the SLM is controlled by software. Here, the liquid crystal modulates only the phase of light without any changes in polarization or intensity. Figure 2.13 presents the resolution of laser-focal intensity distribution, without and with, an adaptive-optics element, namely SLM.

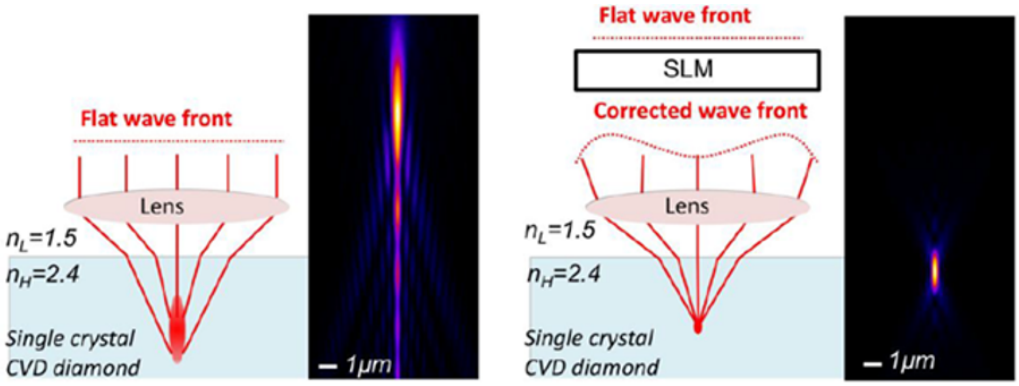

FIGURE 2.13: Example of correction of laser focal intensity distribution 50 µm in the diamond. Without any correction, the focus is elongated (left) but drastically improves with use of a spatial light modulator, SLM, that compensates optical aberrations that occurred during laser processing, taken from [94].

The SLM removes spherical aberration caused by light propagation through the air-diamond interface. The SLM is positioned on objective lens and changes the direction of the beam. There is no flat wave front after SLM. Moreover, the choice of lens numerical aperture is crucial, as the higher the NA the bigger the focusing angle, which results in shorter elongation in the z-axis. The advantage of laser systems equipped with adaptive-optics elements is that they can generate precise modification in substrate structures, even if there is a big refractive index mismatch between both the sample and the immersion medium. For example, 1.4 NA oil lens (n=1.52) laser fabrication in diamond (n=2.42). Figure 2.14 shows a result of laser fabrication in diamond before and after aberration correction.

The laser processing system may employ different objective lenses for different applications. For example, during laser machining at the surface of the diamond, usually an air lens of NA=0.5 is used. Here, the appearance of aberrations is not expected, as there is no refractive index mismatch. For subsurface modifications an oil immersion lens (NA=1.4) is preferable. The reason for this choice is that the oil burns before surface fabrication. In order to fabricate deep structures within the material it is required to flip the sample, as the fabrication with an oil lens is limited to around 200 µm in depth.

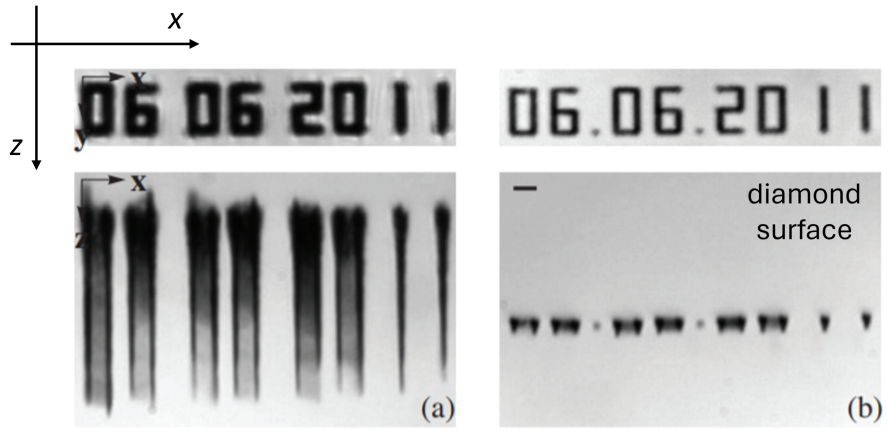

FIGURE 2.14: Laser fabricated structures a) without and b) with aberration correction, taken from [125].

In case of vertical fabrication, sometimes there is is a gap between the sub-surface structure and the surface, therefore the air lens is applied to connect the wire with the surface of the material. Figure 2.15 shows graphitic wires generated beneath the surface of diamond (80 µm deep).

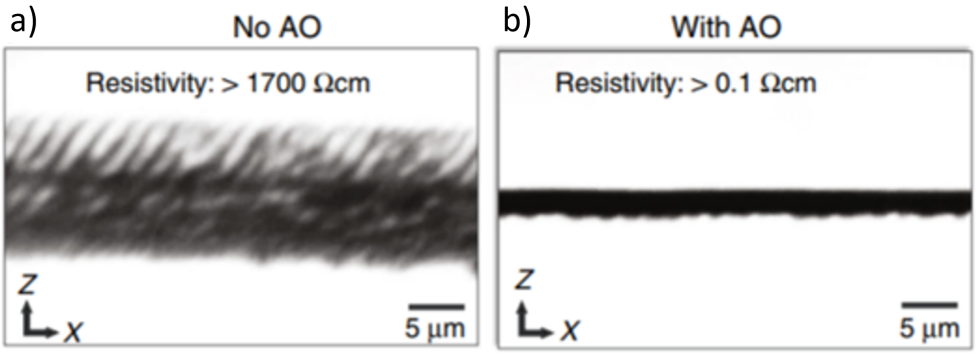

FIGURE 2.15: Graphitic wire fabricated a) without aberration correction and b) with adaptive optics element, taken from [112].

It was demonstrated that the resistivity of the fabricated wire drops drastically when aberrations are compensated by adaptive-optics (AO) instrumentation [112]. As long as adaptive optics compensates for aberrations that occur during laser processing within the substrate and tailors the focal intensity distribution, ultrafast laser machining becomes a promising method for fabrication of advanced three-dimensional structures.

2.7 Conclusions

The current need for high-power devices makes femtosecond laser machining an attractive technology in interdisciplinary research. Direct laser-writing has been demonstrated to be a powerful tool in the structural modification of transparent materials, which have promising applications in quantum computing, sensing and photonics. Furthermore, ultra-fast laser micro-machining of transparent materials has many advantages over other fabrication methods. First, due to the tight confinement of the focal volume, it is possible to fabricate well localised, permanent and complex three-dimensional structures on a sub-micron scale. Even though the laser-fabrication system suffers from aberrations, they can be compensated by implementing adaptive-optics elements. It was already proven that aberration correction significantly improves characteristics of laser written structures inside diamond. Moreover, it ensures that all the structural modifications happen in the laser focal area, meaning that the rest of the material remains unchanged. Second, this technology enables fabrication of different structures inside transparent materials without the necessity of using cleanroom facilities. Direct laser-writing enables fast and simple modification of the material, which makes it a favourable method for device prototyping. The main advantage of this technology is that it can be applied to a variety of materials and adjust to customised applications. However, this thesis concentrates predominantly on laser writing of graphitic electrodes inside synthetic monocrystalline CVD diamond, which has a potential application in radiation sensing. Thus, the aim of this project is to investigate the process of laser writing of graphitic structures followed by optical and electrical characterization including the evaluation of measured resistivity. Moreover, analysis of birefringent induced structure modifications is required to estimate the stress distribution. Most of all, it is crucial to choose the fabrication parameters, because as reviewed

in the literature, different sets of parameters lead to different results.

Despite the promising advancements, challenges remain. Achieving uniform graphitisation over large areas and complex patterns is difficult, and there is a need for further research to enhance the precision and scalability of the process. Advanced laser systems, hybrid fabrication techniques, and comprehensive theoretical models are areas of ongoing investigation to address these challenges and unlock the full potential of diamond graphitisation.

Chapter 3

Experimental methods

3.1 Introduction

The aim of this chapter is to describe the experimental set-ups used throughout the rest of the thesis. This chapter will begin with a description of common fluorescence characterisation techniques used throughout the thesis. This information is partly repeated in Chapter 5, however due to the unique application of the confocal fluorescence microscope found within that chapter the repetition is useful. Additionally, this chapter will cover non-optical experimental aspects of the research performed, such as information on diamond samples and annealing.

3.2 Ultrafast laser machining

In this study, graphitic structures were laser written inside diamond samples. Direct Laser-Writing techniques enabled the introduction of three-dimensional (3D) structural modification within the crystal of interest. Two laser writing systems have been used in this research, namely PHAROS and SOLSTICE.

3.2.1 Laser-Writing System SOLSTICE

This section describes the experimental setup and process used to generate conductive graphitic structures. Figure 3.1 gives a schematic diagram of laser system Solstice.

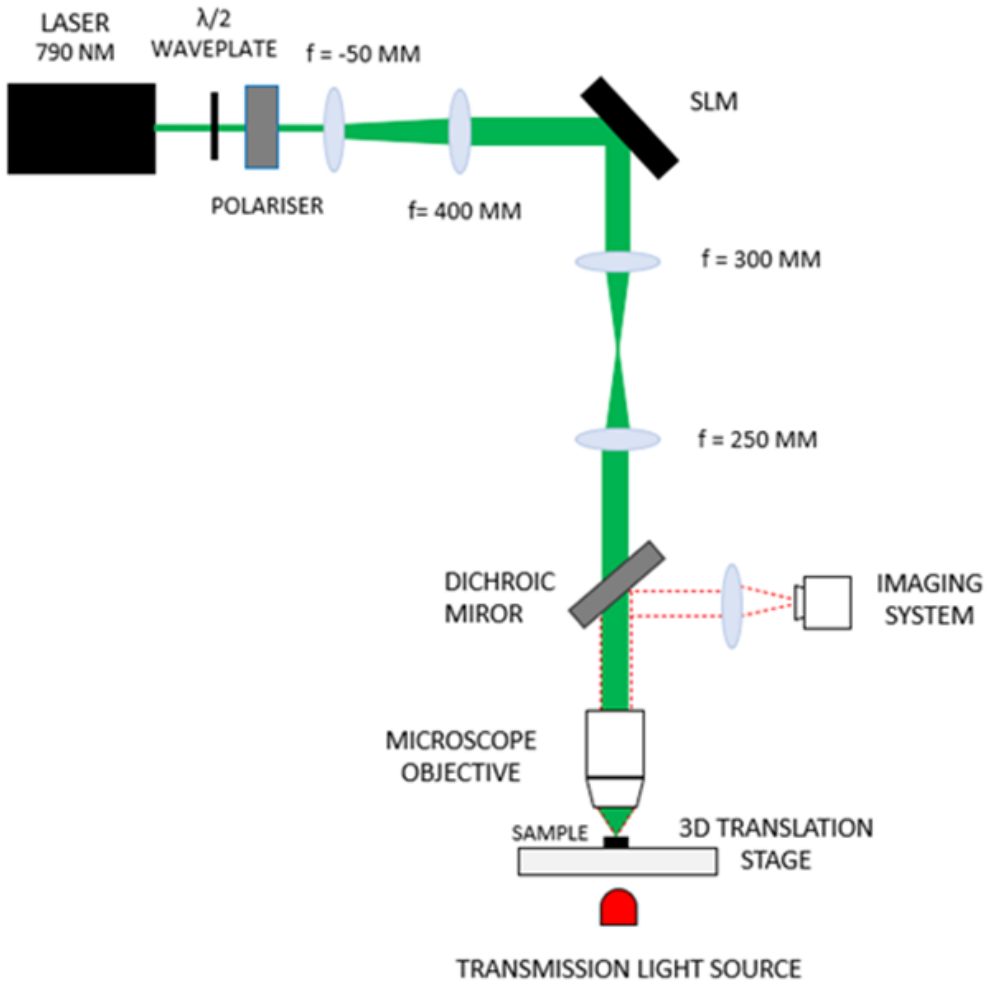

FIGURE 3.1: Schematic of laser system SOLSTICE, with spatial light modulator (SLM) and red LED as a transmission light source.

The experimental setup consisted of different optical components. The near-infrared Ti-Sapphire Solstice femtosecond pulsed laser operated at 790 nm, pulse repetition rate 1 kHz, pulse duration 250 fs. A femtosecond laser emited optical pulses on the order of a picosecond or less, i.e. ultra-short pulses, which is desired in this experiment. Compared to conventional

laser techniques, femtosecond-laser machining provided high peak irradiance with minimal thermal effects. Moreover, short pulses were required for multiphoton interactions, i.e. nonlinear absorption. The laser beam was expanded onto a liquid-crystal phase-only spatial light modulator (SLM) (Hamamatsu X10468), which was in turn imaged in a 4f configuration on to the back aperture of an objective lens (Zeiss 20$\times$ 0.5NA). Basically, the femtosecond laser beam went through the telescopic lens, which was responsible for its expansion. Later, it reached the processing optics aided by adaptive-optics components and eventually hit the dichroic mirror. The role of dichroic mirror, also known as a colour filter, in this example was to transmit the infrared beam for fabrication, but reflect a red LED light into the camera for imaging of the sample. Then, the laser beam traveled via an objective lens and interacts with the sample placed on a viewing stage. When in focus, the high electric field lead to a non-linear absorption resulting in the breakdown of the diamond lattice.

Since material modification took place at the focal volume, 3D microstructures might be fabricated simply by translating the sample with respect to the laser propagation using computer-controlled motion stage. The diamond samples were mounted on precision translation stages (Aerotech ABL10100, ANT95) and were imaged during fabrication with a transmission optical microscope. Here, the stages moved with respect to certain parameters indicated in the software, to support generation of continuous damage tracks, which might be electrically conductive.

A red LED illuminated transmission microscope was used to provide an image of the sample during fabrication. The transmitted red light was collected by the imaging system, which enabled visualization of the sample. In this study a single crystal CVD diamond sample (3×3×0.25 mm) was used, and micro graphitic structures were generated on both surface and the bulk

of the diamond. The focusing objective used in creation of defects below the surface was an oil objective with numerical aperture (NA) equaled to 1.4 (Olympus 1.4NA 60× oil lens). The laser system with the oil lens had tight focusing which allowed low energies (20 nJ - 70 nJ). Surface fabrication of the contact pads do not require as high intensities, so a lower NA, air lens was used for ease of fabrication.

3.2.2 Laser-Writing System PHAROS

Surface fabrication and laser writing of vertical structures (structures that go through the whole thickness of the sample) within a iamond wafer was performed by laser-writing system PHAROS. The graphitic tracks were produced using an Yb:KGW laser (Light Conversion Pharos SP-06-1000-pp) with a central wavelength of 515 nm, pulse duration 250 fs and various repetition rates, ranging from 100 Hz to 1 MHz, focused with a 0.5 NA air-based objective lens (Zeiss 20×0.5NA) for the vertical wires. Figure 3.2 shows a schematic diagram of the laser-processing system used for surface and subsurface modifications of CVD diamond samples.

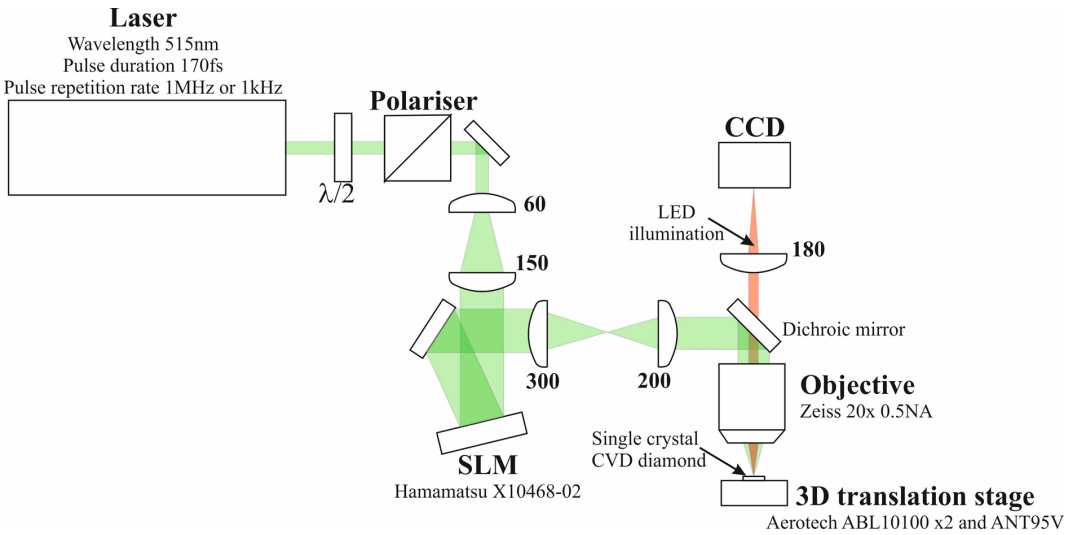

FIGURE 3.2: Schematic of PHAROS laser-writing system, the numbers in bold next to each lens denote the focal length of that element.

This setup consisted of different adaptive-optics components to control the laser during machining. First, the laser beam passed through a rotatable half-waveplate and a polarizer, which enables power control. The beam was expanded and directed at a phase-only liquid-crystal spatial-light modulator SLM (SLM, Hamamatsu X10468) was used to adaptively correct in real-time for optical aberrations related to refraction at the diamond interface. The laser beam was imaged in 4f configuration onto the back of a microscope objective lens (Zeiss 20×, 0.5 NA). The laser beam could be focused down to a diffraction-limited spot size inside the diamond of refractive index of 2.4. The diamond sample was placed onto three dimensional precision translation stages (Aerotech ABL10100 (x,y); ANT95-3-V (z)). The graphitic vertical columns were laser fabricated by focusing the laser on the rear side of the diamond wafer and drawing the laser focus through the thickness of diamond wafer to the top side. The diamond sample was illuminated from underneath by a red LED. A dichroic mirror separated the LED illumination from the laser before passing through a tube lens onto a CCD. This procedure formed a microscope to allow real-time imaging of the diamond sample during fabrication.

3.2.3 Laser writing of graphitic columns

The Pharos laser system was used to fabricate the so-called all-carbon devices. Here, the whole device was generated by using only one laser fabrication system. Figure 3.3 represents the fabrication steps involved in the laser processing, presenting a schematic architecture that allows straightforward testing of electrical properties of graphitic columns.

First, vertical graphitic columns were fabricated by focusing the laser on the back surface of the diamond to seed the graphitisation, and then translating away from the lens to draw the graphitisation through the thickness

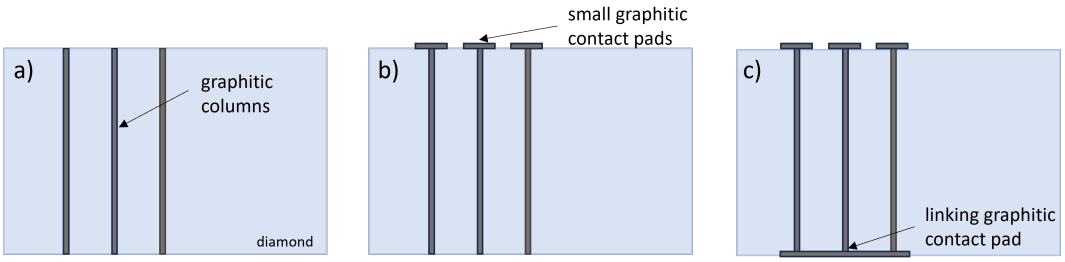

FIGURE 3.3: Schematic of laser writing of a) graphitic columns, b) small graphitic contact pads and c) linking graphitic contact pads. This design was used for a straightforward all-carbon device.

of the sample. The graphitisation occurs at the surface first as the breakdown threshold is lowest. This sp^2 material then absorbs energy from subsequent laser pulses, creating more sp^2 material. The columns were fabricated at different pulse energy in each row, while the repetition rate and translation speed were kept constant at 1 kHz and 10 µm/s, respectively. Adaptive aberration correction ensured diffraction-limited performance at each depth. Secondly, small graphitic contact pads of area 50 µm × 50 µm were fabricated on the top diamond surface over each column. Finally, the sample was flipped over, and larger contact pads were laser written on the opposite surface. The long contact pads (dimension 250 µm × 50 µm) were fabricated in the same way as the small pads and acted as a base electrode to connect a set of graphitic columns that had been fabricated with identical parameters. All surface contact pads were fabricated at optimised parameters of 30 µm/s of translation speed, pulse energy 100 nJ and repetition rate of 10 kHz, with a raster step size of 1 µm. The pattern used for this investigation consisted of three graphitic columns in a row, all fabricated at the same pulse energy.

3.3 Characterisation techniques

Different material characterisation techniques were applied throughout this research. Thanks to these techniques both the optical and electrical properties of CVD diamond and its graphitic modification have been studied.

3.3.1 Two-probe station

The electrical behaviour of the laser-written graphitic columns was examined by two-probe station measurements. Figure 3.5 illustrates the idea of the two-probe station characterisation. After successful laser fabrication of graphitic structures, two tungsten probes with 10 µm tips were micro-positioned to contact the small pads on the top surface of the diamond. The electrical testing investigated the relation between laser-fabrication parameters and d.c. electrical resistance of the graphitic wires. A source Measurement unit (Keithley 2450 SourceMeter) measured the current-voltage relationship for the wires, using a voltage ramp of -50 V to +50 V at 5 V steps.

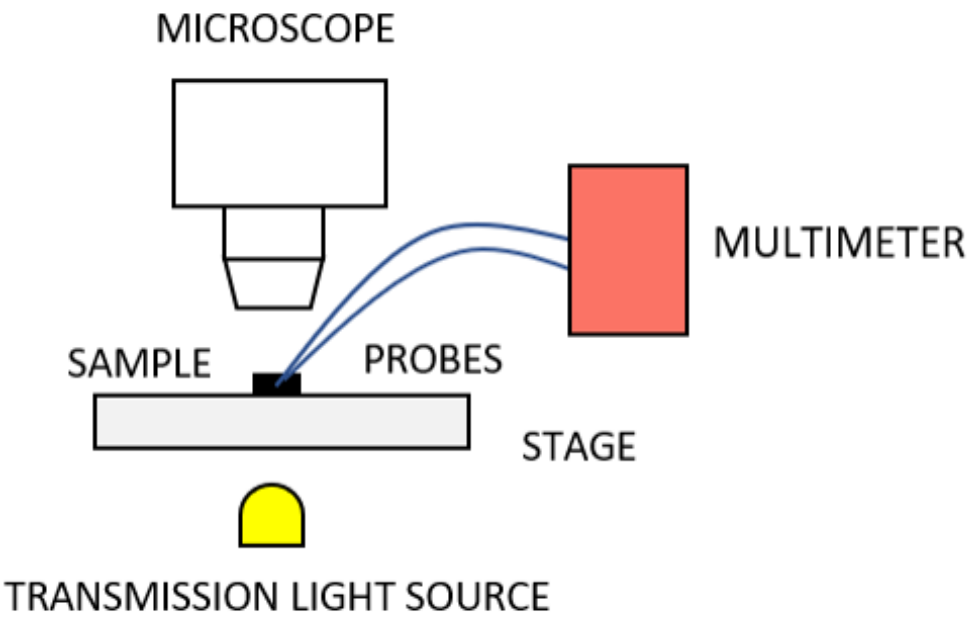

FIGURE 3.4: Schematic diagram of two-probe station electrical characterisation tool.

It is worth highlighting that the design of an all-carbon device enabled a straightforward measurement of resistances of the parallel columns that were linked by the large graphitic contact pad that served as a base electrode. The final resistance outcome contained then, not only the resistances of the graphitic wire, but also all the linking resistances that partially came

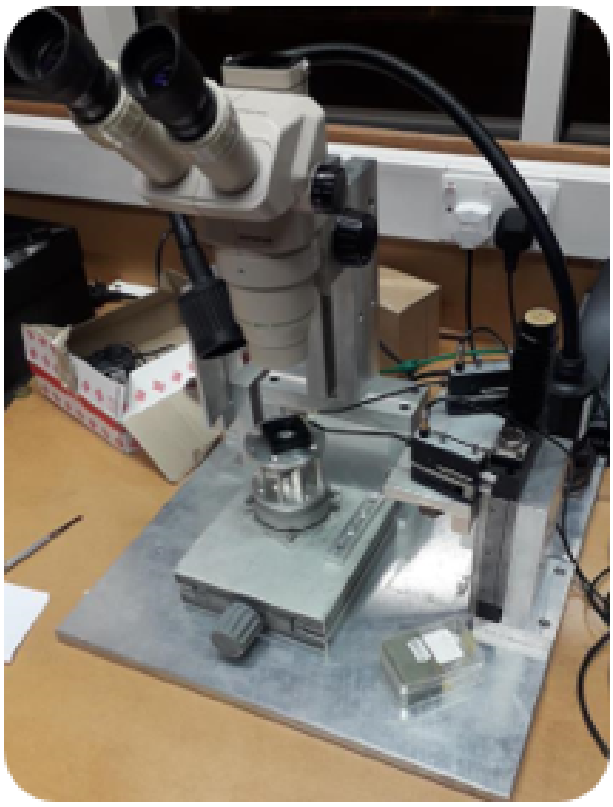

FIGURE 3.5: Picture of two probe station electrical characterisation tool.

from the contact pads. A modified version of electrical characterisation was proposed, where the bottom of the diamond sample was coated with silver paint (Agar Silver Paint, G3691) allowing a direct measurements of the chosen graphitic column. Here, one probe was placed on silver paint that worked as a base electrode and the second one was positioned at the top of the graphitic contact pad.

3.3.2 Raman Spectroscopy

Raman spectroscopy is a characterisation method that helps identifying the composition of a material. This technique can detect molecular vibrational states of different materials. By focusing a laser beam onto a sample, the light interacts with molecular vibrations, resulting in scattered light at varying frequencies. Most of the scattered light retains the same frequency as the laser, which is known as Rayleigh (elastic) scattering. However, a portion of

the light shifts in frequency due to excitation to higher or lower vibrational states, known as Raman (inelastic) scattering (see figure 3.6).

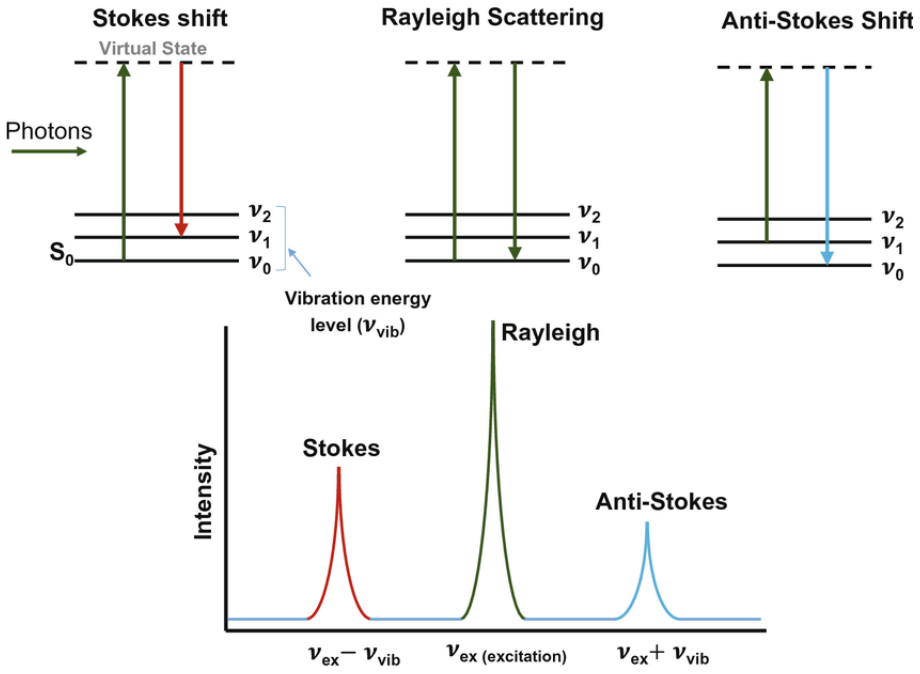

FIGURE 3.6: Schematic diagram of electronic levels involving Stokes, Rayleigh and Anti-Stokes scattering and corresponding Raman spectra, taken from [126].

In this experiment all photoluminescence measurements were performed on a dispersive HORRIBA Raman/PL spectrometer, which operates based on the principles of Raman scattering and photoluminescence detection. Raman spectroscopy is used to identify molecular vibrations and chemical compositions, while photoluminescence (PL) detects the re-emission of light from a material after absorbing photons. Optical characterisation was performed at room temperature. Figure 3.7 illustrates the basic idea of spectrometry.

In the Raman system, a focused laser beam interacts the sample, exciting its phonons. The scattered light is collected and analyzed by a spectrometer, which separates it based on its wavelength. By detecting the shift in frequency of the scattered light, the system generates a Raman spectrum,

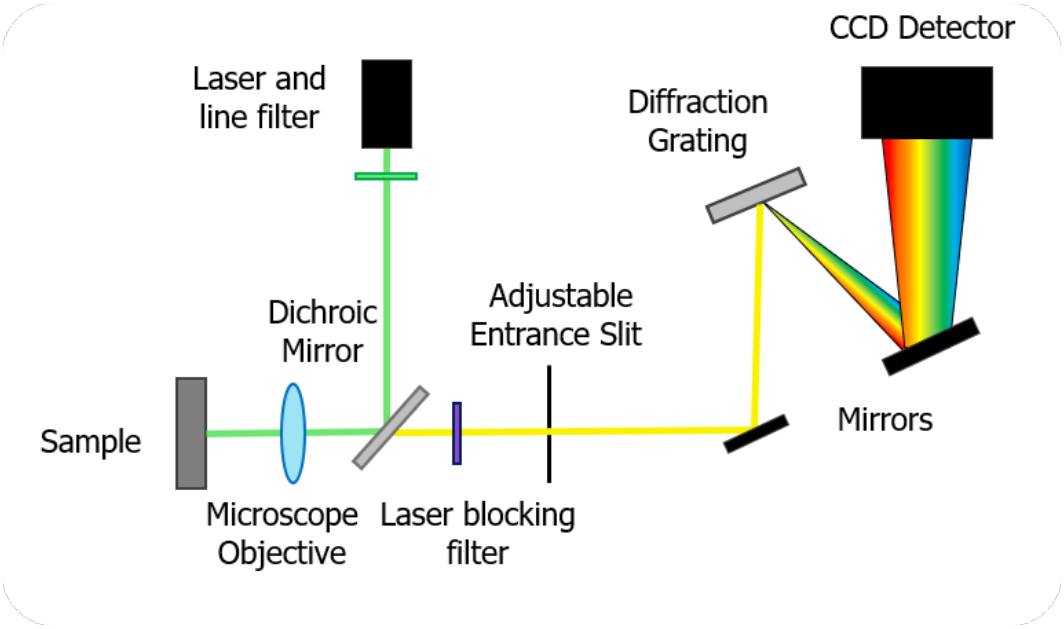

FIGURE 3.7: Schematic diagram of laser Raman spectrometer.

which helps identify molecular components of the material. All measurements were performed in the following manner, the point of choice at the sample was scanned with the Raman spectrometer ($\lambda = 532$ nm) and all the data points were analysed with Matlab2023b software.

In this research, Raman spectroscopy was applied to detect different carbon states. Single-crystal diamond consists of sp^3 bonds, whereas graphite is characterized by sp^2 bonds. Thus, Raman spectroscopy was applied to distinguish these two allotropes. The most characteristic diamond peak exhibits a Raman shift at 1332 cm^{-1}, whereas Raman shift of around 1600 cm^{-1} is associated with graphite (also known as the G-peak). The higher the content of graphite, the higher the intensity of the G-peak. Therefore, Raman spectroscopy was used to investigate the quality of laser-written graphitic columns and graphitic contact pads.

3.3.3 Scanning Electron Microscopy (SEM)

To investigate the quality of laser fabricated wires, usually transmission electron microscopy was applied. However, in order to see how the structure looks like at a smaller than a micrometer scale, Scanning Electron Microscopy (SEM) was applied. This type of microscopy uses a focused electron beam instead of visible light to scan the sample and image very small structures, including even at the nm scale. The electrons interact with atoms in the sample and collect information about the surface topography and sample composition. Here, the highly energetic electron beam is scanned in a raster scan manner across the sample. In most common cases, the secondary electrons emitted by atoms excited by electron beam or backscattered electrons are detected. The detected number of electrons, hence, signal intensity is linked to specimen topography. As a result, magnified images of structural modification can be detected. Secondary electrons (produced by elastic scattering) have low energies, thus they escape only from the top nanometres of sample surface. On the contrary, the backscattered electrons are the primary beam electrons that are reflected from the sample via inelastic scattering and they emerge from deeper parts of the specimen. Secondary electrons are mostly used to provide topographical information about the sample whereas backscattered electrons provide more information about chemical composition of the material [127]. Figure 3.8 illustrates the electron-matter volume in the SEM.

SEM imaging was used to characterize the topography of graphitic structures laser fabricated at the surface of diamond. Both contact pads and the graphitic columns were examined by SEM.

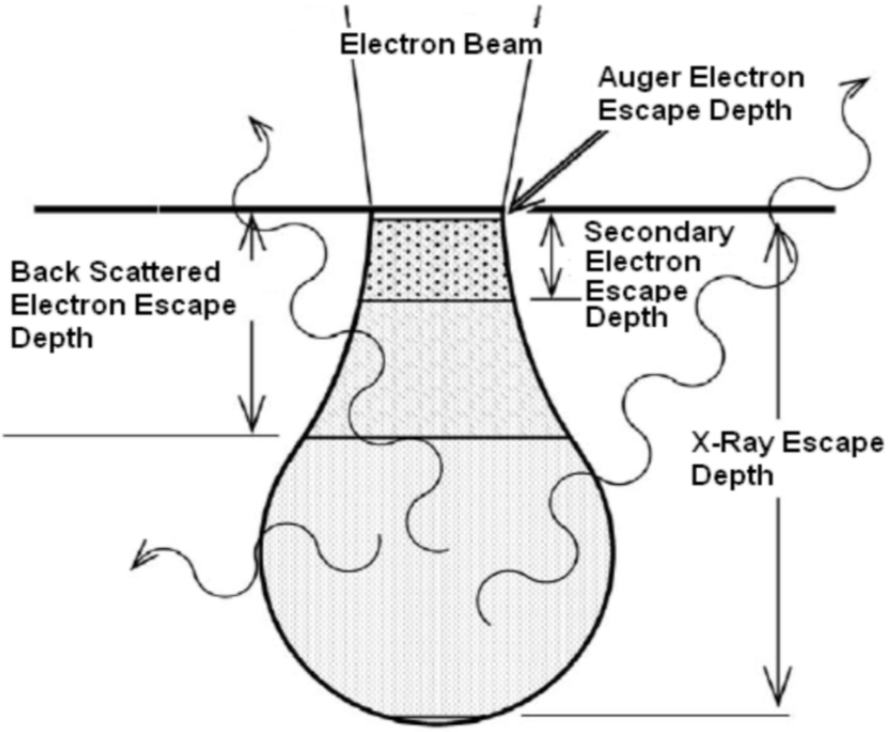

FIGURE 3.8: Electron-matter interaction volume, taken from [128].

3.3.4 Transmission Electron Microscopy

Transmission Electron Microscopy (TEM) was applied for high resolution images. After successful laser fabrication of graphitic columns within the diamond wafer, the sample was prepared for TEM characterisation. A thin layer of diamond sample (including graphitic content) was cut out of the main substrate using the Focused Ion Beam (FIB) lift-out method (see figure 3.9).

The thin plates were extracted from the centre of each laser incident point from the rear (initiating) side. The thin diamond plates were 15 µm long by approximately 5 µm deep with a thickness of around 70 nm. Figure 3.9 shows the schematic diagram of this procedure. All TEM characterisation was performed in Cadiz by Pilar Vilar and Daniel Araujo.

Electron-microscope observations were carried out using two pieces of FEI equipment. Specifically, High resolution transmission electron microscope (HRTEM) and scanning transmission electron microscope (STEM)

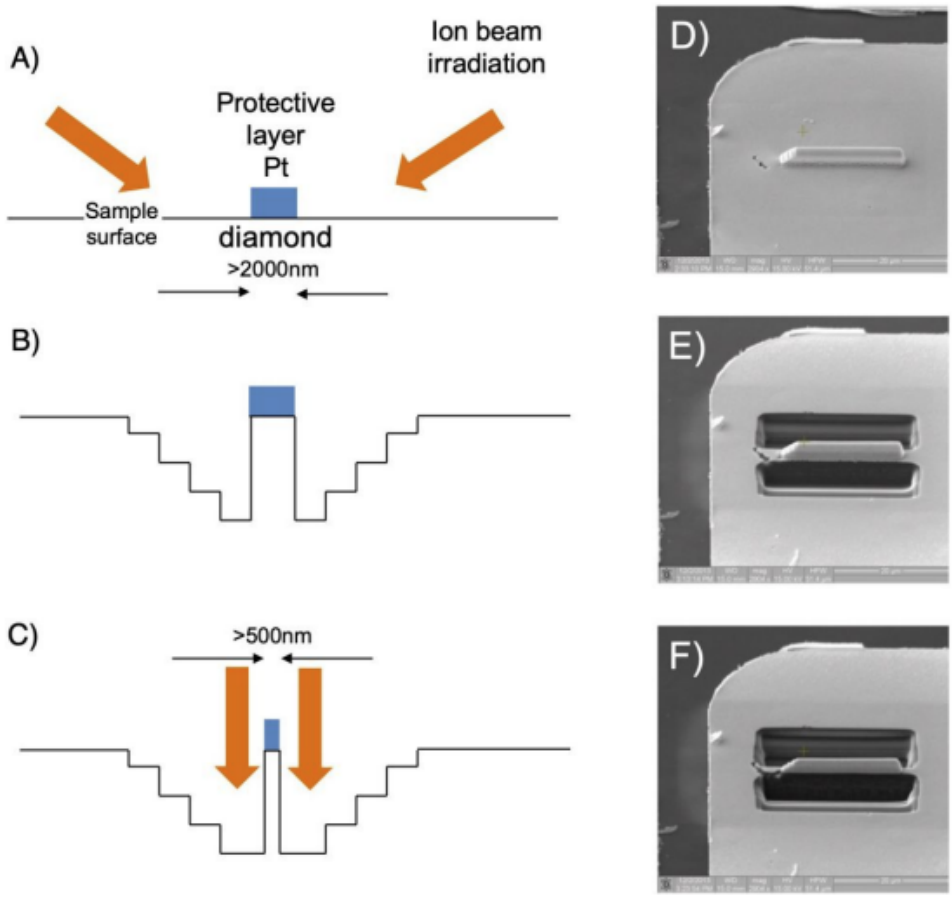

FIGURE 3.9: Lift out methodology. A) A protective layer is applied over the region of interest. Focused ion beam irradiation is used to remove diamond material from the sample either side of the region of interest to create the structure seen in (B). (C) Further vertical ion beam irradiation is applied to this down the sample wafer, taken from [92].

studies were performed using a Talos F200X, and HRSTEM studies were carried out using a Cubed Titan Themis 60-300. Both electron microscopes are equipped with a high-brightness XFEG gun, and the last one also is equipped with a double correction system (Cs-DCOR) for probe and image. All of the electron microscopy experiments were run with200 keV as the electron acceleration voltage. Velox software was used to process TEM micrographs.

Chapter 4

Writing electrodes in diamond

4.1 Introduction

As seen in Chapter 2, ultrashort pulsed laser writing has become established as a technique for fabricating high-quality microstructures inside transparent materials. The direct laser-writing process facilitates transition of diamond into graphitedue to the high intensities in the focal volume of the laser followed by diamond lattice breakdown. This method was developed to generate high-quality electrically conductive graphitic structures on both the surface and below the surface of the diamond. Laser-written graphitic channels that pass through a diamond wafer find application as electrodes in diamond radiation detectors and diamond electronic devices. Thus, chapter 4 depicts the surface and sub-surface laser-writing processes in the diamond bulk. Here, both electrical and optical results of laser-written column electrodes through a diamond wafer are included. Moreover, an optimized all-carbon device is demonstrated for rapid prototyping. A study on the electrical performance of laser fabricated devices is presented supported by Raman spectroscopy.

4.2 Surface structuring

Direct laser writing is used to functionalize synthetic diamond samples by introducing permanent modifications into the diamond structure. Due to this method, changes can be introduced in a precise and controllable manner. The ultrafast laser pulses can be used to introduce periodic patterns on the surface that are much smaller than the laser wavelength. For example laser-induced periodic surface structure (LIPSS) has been used to tailor the surface of synthetic diamond. It was found that this technique enables fast patterning in a controllable manner. Here, the topographic changes depend on the material itself along with the laser wavelength λ, number of applied laser pulses N, the angle of incidence θ and polarization state of electric field [129]. Figure 4.1 shows the example of LIPSS on the diamond surface.

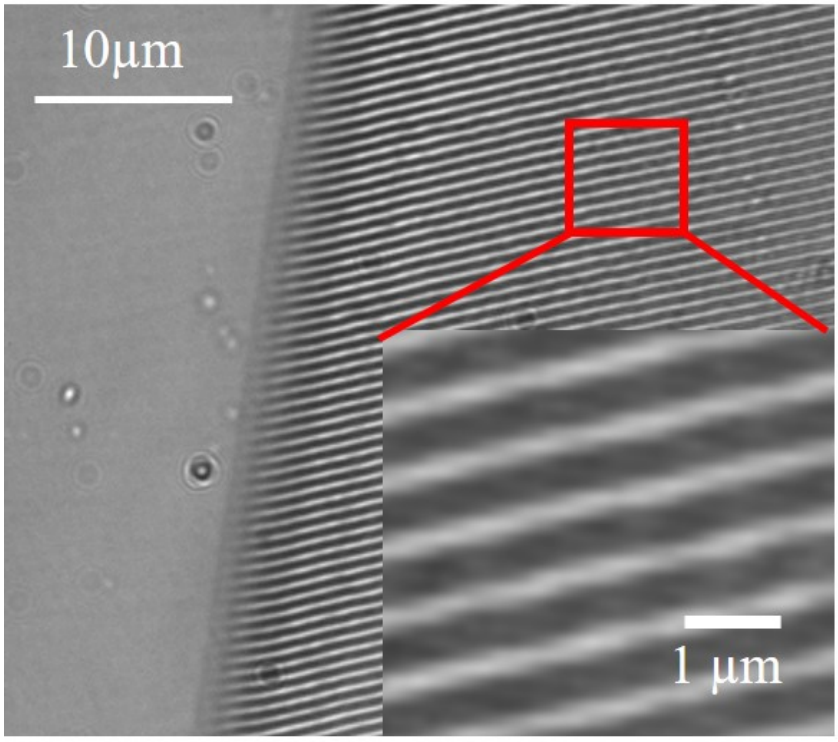

FIGURE 4.1: Example of LIPSS fabricated in diamond.

Here, two different types of LIPSS were tested, namely high spatial frequency LIPSS (HSFL) < $\lambda/2$ and low spatial frequency LIPSS (LSFL) with period > $\lambda/2$ were studied. It was found that the surface modifications, i.e. height and periodicity, are strongly related to the laser processing parameters, such as number of pulses or fluence. LIPSS was applied to tailor optical properties of diamond providing regular and precise patterns of high quality diamond anti-reflection (AR) coatings. The findings demonstrate a large potential for the production of high quality diamond photonic surfaces with tailored characteristics in a simple and reliable way. However, this method can be also utilized in other semiconductor materials and different areas of research [62].

For example, high power lasers are used to introduce graphitisation of diamond also known as metastable modification of carbon [130]. Contrary to thermal heating, here a thin graphitic layer has no time to oxidise and remains on the diamond surface [131], resulting in changes of both optical and electrical properties of the material. Moreover, laser ablation is an efficient method for precise microstructuring the diamond surface. Kononenko et al., have already demonstrated the relationship between laser pulse duration and thickness of laser induced graphitic layer on the diamond surface [132]. The material ablation can happen in both short pulse (ns) and ultrashort pulse (< 10 ps)) regimes. In the case of ultrashort pulses, the material interaction happens at the electron level, where the heat conduction occurs after the end of each laser pulse duration. Hence, the thickness of the graphitic layer is proportional to the absorption properties of graphite. In contrary, longer pulses lead to material heating up, resulting in melting and evaporation [133]. It was reported that for 200 ns laser pulse duration, the graphitic layer may reach 1 µm thickness [132].

During this research the impact of laser writing parameters on the graphitic layers on the surface of the diamond sample was examined. Here, a short-pulsed laser beam was focused on the top surface of the diamond, where the graphitic structures were fabricated. Thanks to ultra short pulses, all the energy is delivered to the laser focus in a timeframe shorter than thermal diffusion of the absorbed energy. High intensities in the focal volume of the laser cause lattice breakdown, and as a result diamond is transformed into a graphitic phase [133]. The graphitisation is confined to the laser structures, which can be electrically conductive [134, 135].

Different laser writing parameters have been studied in order to optimize the laser processing technique for high-quality electrically conductive graphitic structures on the surface of the diamond. The laser fabrication system PHAROS was used in this study (see Chapter 3). The sample used for this examination was a single-crystal CVD diamond from Element Six, Ltd., with dimensions 3 mm × 3 mm ×0.3 mm, a 100 top face and 1 ppm nitrogen concentration. Figure 4.2 presents a microscopic image of successful fabrication results of sixteen graphitic contact pads (dimension 250 µm × 30 µm) that were generated in various environments. Table 4.1 shows the laser-writing parameters applied for processing of these graphitic contact pads.

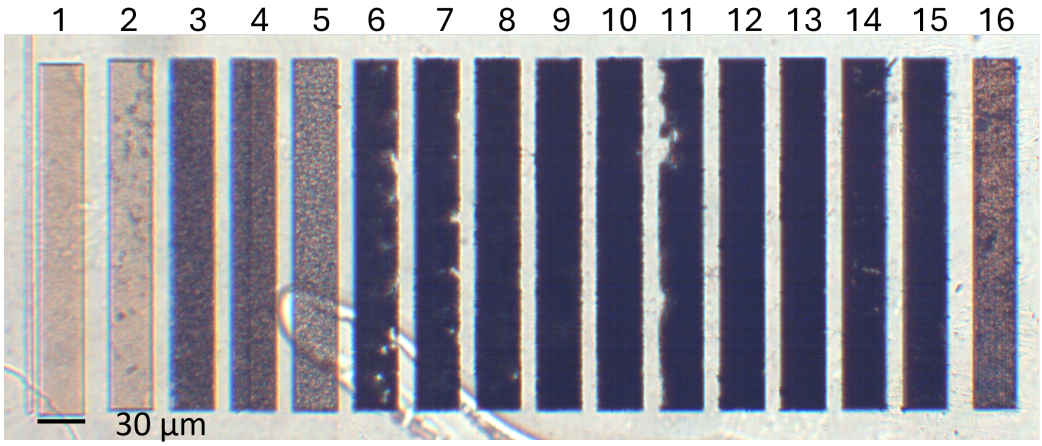

FIGURE 4.2: Microscopic picture of laser written contact pads (1-16).

Fabrication parameters		
Number of contact pad	Pulse repetition rate	Pulse energy (nJ)
1	1 kHz	0.3
2		2.73
3		7.53
4		14.61
5		35.05
6	10 kHz	0.3
7		2.73
8		7.53
9		14.61
10		23.85
11	100 kHz	0.3
12		2.73
13		7.53
14	1 MHz	1.22
15		4.84
16		0.3

TABLE 4.1: Laser fabrication parameters for contact pads (1-16).

As presented in the optical microscope image in figure 4.2, the contact pads reveal the diverse nature of their structure, that is the consequence of using different laser-writing parameters. Each of 16 contact pads was generated using different pulse energies and repetition rates. Pulse energies are always measured by averaging over lots of pulses, effectively taking a power reading and dividing by the repetition rate. This approach helps to investigate the optimal set of parameters in order to achieve a homogeneous, graphitic and conductive layer. It was demonstrated that laser processing leads to either ablation of the diamond surface or generation of a graphitic layer. Different translation speeds have been used for this experiment, 50

µm/s for contact pads: 1, 2, 3, 4, 5, 16; 30 µm/s for contact pads 6, 7, 8, 9, 10, 11, 12, 15 and 10 µm/s for 13, 14. The quality of the fabricated contact pads was examined under the optical microscope and the electrical performance was characterized by a two-point probe station measurement, which is described in more details in the previous chapter. The pattern used for this investigation and choice of dimensions enabled straightforward testing of their electrical properties simply by placing the sample on the stage and positioning two tungsten probes with 10 µm tips on the laser modified area on the top surface of the diamond. The digital multimeter (Fluke 23) delivering a constant dc current of 1 µm measured the resistance of the graphitic contact pads. Thus, the probing test examines the conductivity of the microfabricated graphitic structures. To conduct this measurement, the contact pads were designed to be long enough to prevent the testing probes from touching each other, in this particular sample, they are of 30 µm × 250 µm. Figure 4.3 shows the results of the resistance of these graphitic structures.

As demonstrated, there is no clear tendency depicted in figure 4.3. The probing test was repeated five times in order to check whether the measured values are reliable and trustworthy. Some of the contact pads did not provide any electrical response, presumably because only small pockets of sp^2 were generated with little connectivity between them. Furthermore, it seems that the values of electrical resistance are not stable, most likely due to testing problems. It was also observed that the location of the probes, i.e. whether they are at the edges or closer to centre of the contact pad, impacts the final outcome. Nonetheless, it was observed that for the contact pads numbered 6-13, the electrical resistance values do not fluctuate much. What is more, these structures appear optically darker than the others, which might suggest good graphitic structure.There is also a relationship that the higher

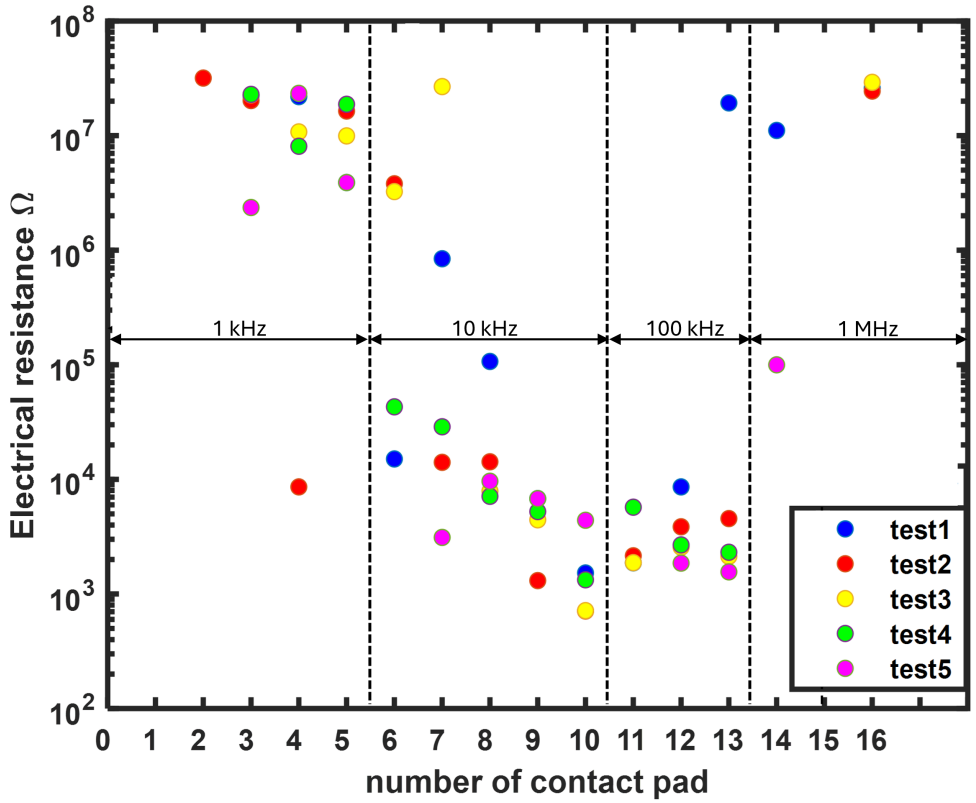

FIGURE 4.3: Conductivity results of the laser fabricated contact pads.

pulse energy used, the lower the electrical resistance (e.g. contact pads 7-13). The study on optimization of laser-writing parameters was performed for graphitic structures laser written inside the diamond bulk. For the sake of laser processing of graphitic contact pads on the surface of the diamond sample, the repetition rate of 10 kHz and translation speed of 30 µm/ s were chosen.

4.2.1 SEM study

SEM was used to study the topography of the graphitic structures laser written on the top surface of the diamond. The laser writing of the surface contact pads was achieved by raster scanning of the laser beam with a 1 µm step. Although the optical microscope images of contact pads (see fig.4.2) present quite homogeneous structures, SEM reveal more details. Figures 4.4 and 4.5

present the topography of the graphitic contact pads under 4.3k and 10.6k magnification, respectively. The laser written graphitic-like structures now appear permanent and rough compared to the surrounding diamond material.

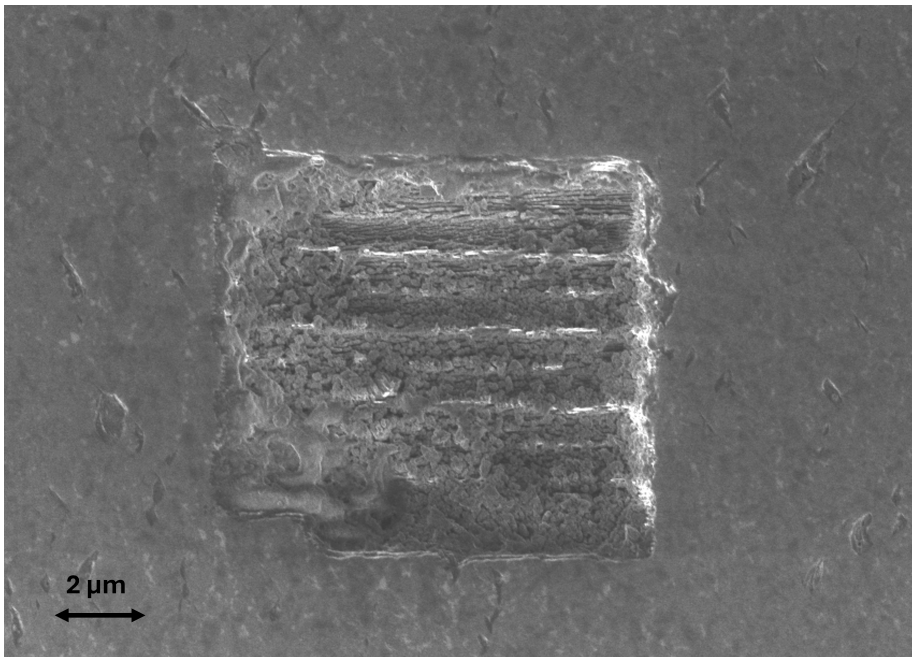

FIGURE 4.4: SEM image of a laser-written graphitic contact pad on the top surface of CVD single-crystal diamond, 4.3k magnification.

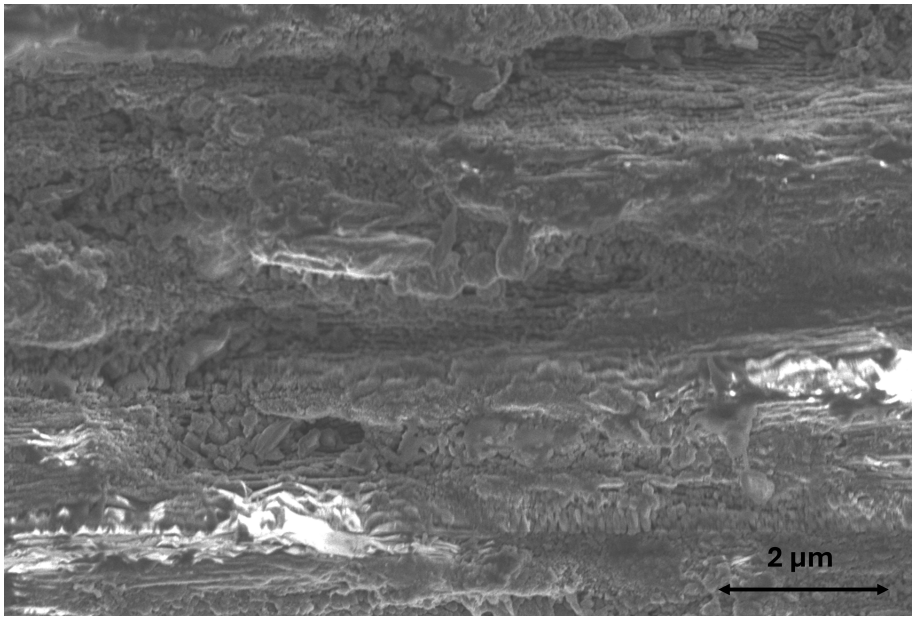

FIGURE 4.5: SEM image of a laser-written graphitic contact pad on the top surface of CVD single-crystal diamond, 10.6k magnification.

SEM imaging showed that even though the laser-fabricated structures are continuous, they are not homogeneous. Images under high magnification reveal the complexity of the laser induced modifications.

4.3 Subsurface fabrication

Femtosecond laser micromachining has opened opportunities for both surface and bulk modification of diamond. Laser processing supported by adaptive-optics systems enables precise and accurate modification of a material's structure. It was already demonstrated that direct laser writing helps to generate a variety of three-dimensional structures of different geometries inside the bulk of diamond [112]. One of the examples includes introducing graphitic tracks inside the diamond bulk for waveguiding purposes [91, 136, 137]. Moreover, this technology is also applied to create atomic-scale defects (e.g. nitrogen vacancies) for quantum technology applications [94, 138, 139].

This next section focuses mostly on laser processing inside the diamond wafer and optimization of laser-writing parameters, which are crucial for a successful fabrication of conductive electrodes. The horizontal graphitic wires were laser written in the subsurface of diamond sample using different parameters settings. They were fabricated with the Solstice laser system using an oil objective lens (1.4 NA) to reduce the aberrations at the interface (more details in Chapter 3).

Figure 4.6 presents the microscopic image of the laser-written graphitic structures. These horizontal wires were connected to the surface by graphitic pillars and graphitic contact pads.

Figure 4.7 shows a microscopic image of few graphitic pillars that were laser written through the diamond bulk by the PHAROS laser system (see Chapter3) at various laser parameters. Both translation speed and pulse

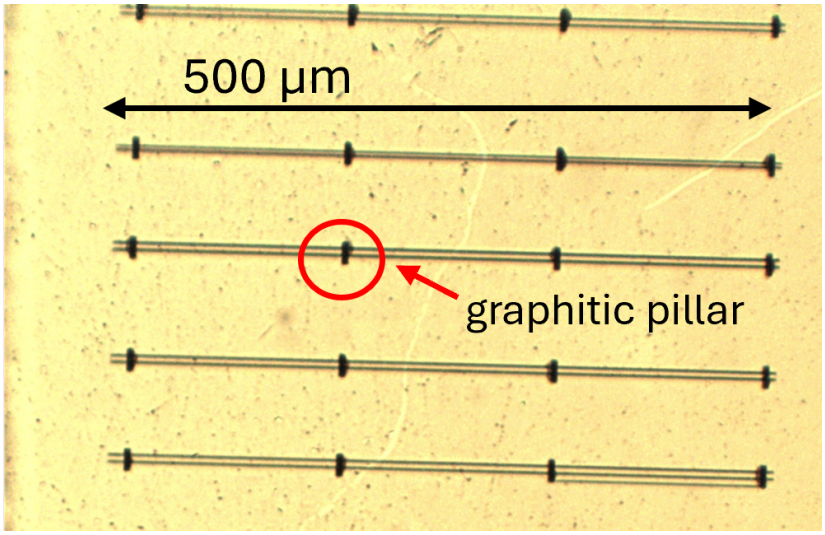

FIGURE 4.6: Microscopic picture of horizontal graphitic structures embedded 10 µm in the diamond sample. The vertical graphitic pillar connect the horizontal wire to the surface.

energy were kept constant, however, the repetition rate was different for each pillar. Devices were fabricated on electronic-grade single-crystal CVD diamond substrates.

Optical analysis of graphitic structures at the polished side of diamond was performed. Figure 4.7 depicts the longitudinal profiles of laser-written graphitic structures, viewed here through the polished side of the sample.

This study proved the importance of choice of laser parameters. It was observed that there is no continuous graphitic structure at 100 Hz (D), as the delivered laser dose is too low. Thus, no electrical conduction was seen. In this case, random graphitic points are present throughout the laser fabrication path. The graphitic structures laser written at 1 kHz (C) and 10 kHz (B) look optically similar, being dark, which suggests efficient diamond-to-graphite conversion. The most surprising result happens at 1 MHz (A), where the graphitic-like column is continuous but less distinguishable optically. One may deduce that there is less graphite present compared to the previous examples. For better understanding of the characteristics of the

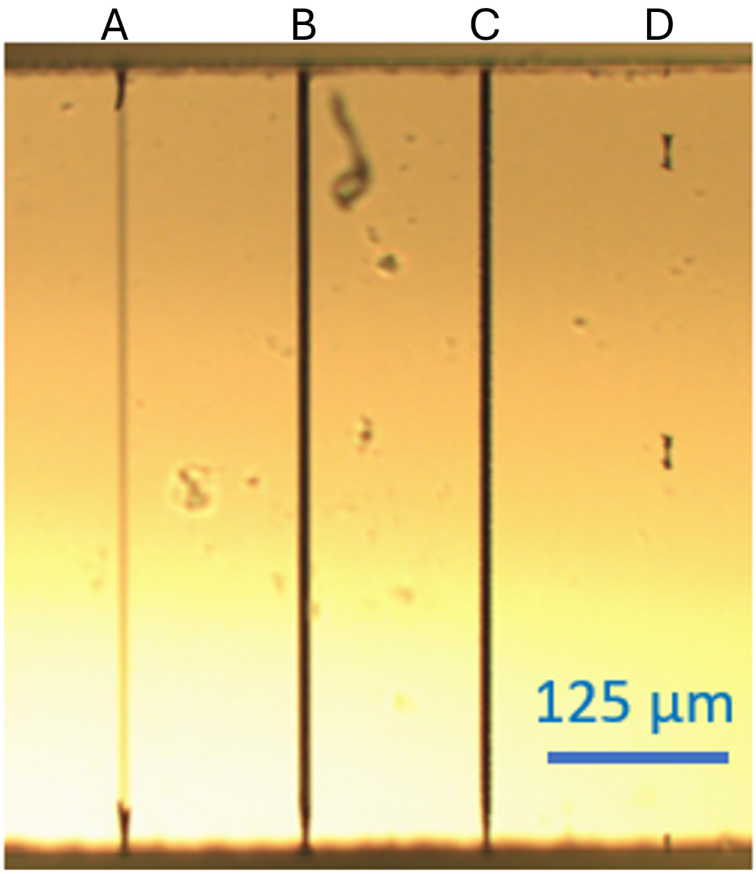

FIGURE 4.7: Microscopic image of laser-written graphitic columns on the polished side of a CVD polycrystalline diamond sample. They were fabricated with 10 µm/ s of translation speed, 144 nJ pulse energy and various pulse repetition rates, from the left: 1 MHz, 10 kHz, 1 kHz and 100 Hz.

laser-written graphitic wires inside the diamond wafer, TEM and SEM studies were carried out. The results of TEM study are discussed in section 4.8.

4.3.1 SEM analysis

SEM images were taken of the chosen graphitic structures laser written in diamond bulk. Figures 4.8 and 4.9 present the pictures of the heads of the chosen graphitic columns from the non-seeding surface (opposite to the seeding surface). It was demonstrated that the structures possess circular-like shapes and that a certain degree of roughness accompanies all of them. Under higher magnification it is noticed that even though the structure goes through the

wafer, there is a crater-like imperfection around the wire. This information is important for any further post processing.

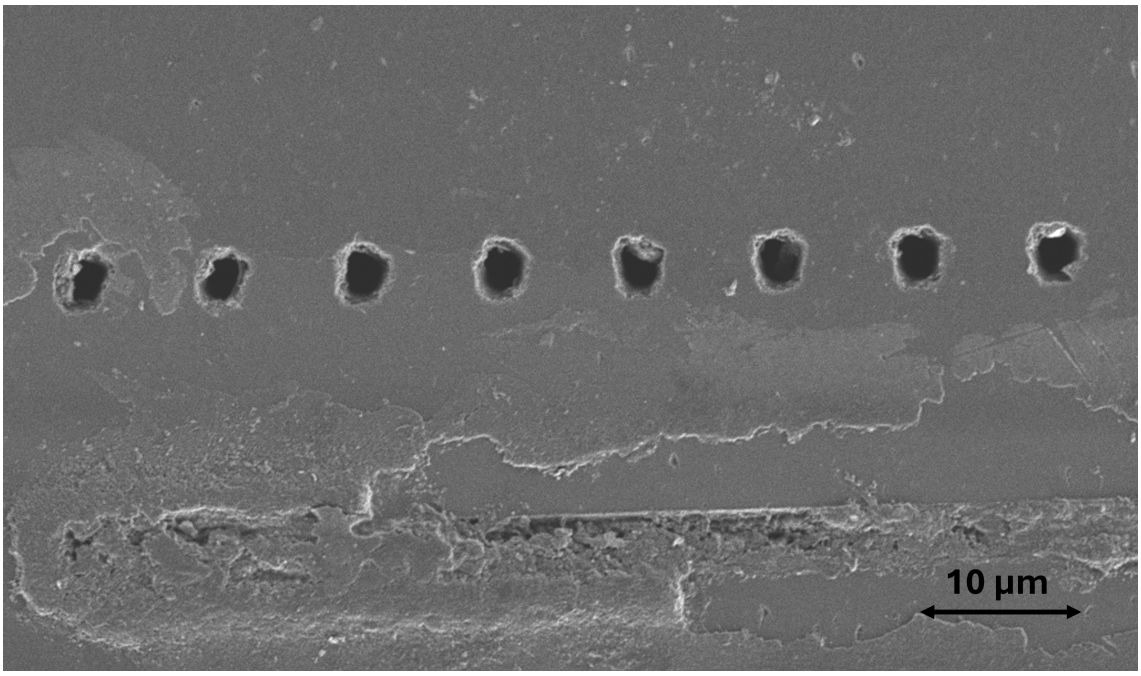

FIGURE 4.8: SEM image of a heads of laser-written graphitic wires on the top surface of CVD single-crystal diamond, 1.44k magnification.

SEM was performed to examine the topography of the laser-written graphitic columns. Here, the images were taken from the top surface of the diamond sample. It has been demonstrated that a circular shape was obtained for all the wires. The diameter of the chosen head of a graphitic column has been measured as 3.3 µm. Knowledge about the topographical characteristics on the top of the sample may enhance any further post processing.

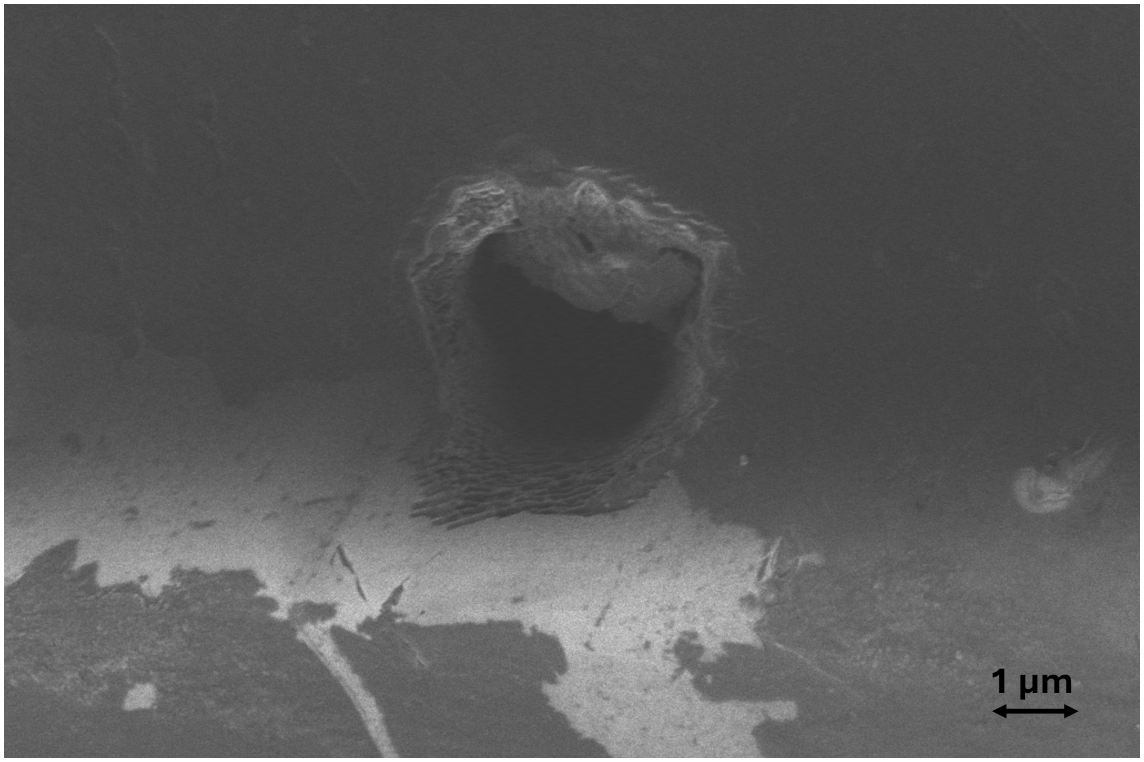

FIGURE 4.9: SEM image of a head of laser-written graphitic wire (diameter 3 µm) on the top surface of CVD single-crystal diamond, 8.77k magnification.

4.4 All-carbon device for rapid testing

A prototype of an all-carbon device has been designed for straightforward electrical testing. Figure 4.10 presents a schematic diagram of laser writing of graphitic structures inside diamond.

Here, the laser-writing system PHAROS was used to introduce structural modifications within the diamond wafer (see Chapter 3). The sample was a single-crystal CVD diamond from Element Six with dimensions 3 mm × 3 mm × 0.3 mm, a 100 top face and 1 ppm nitrogen concentration.

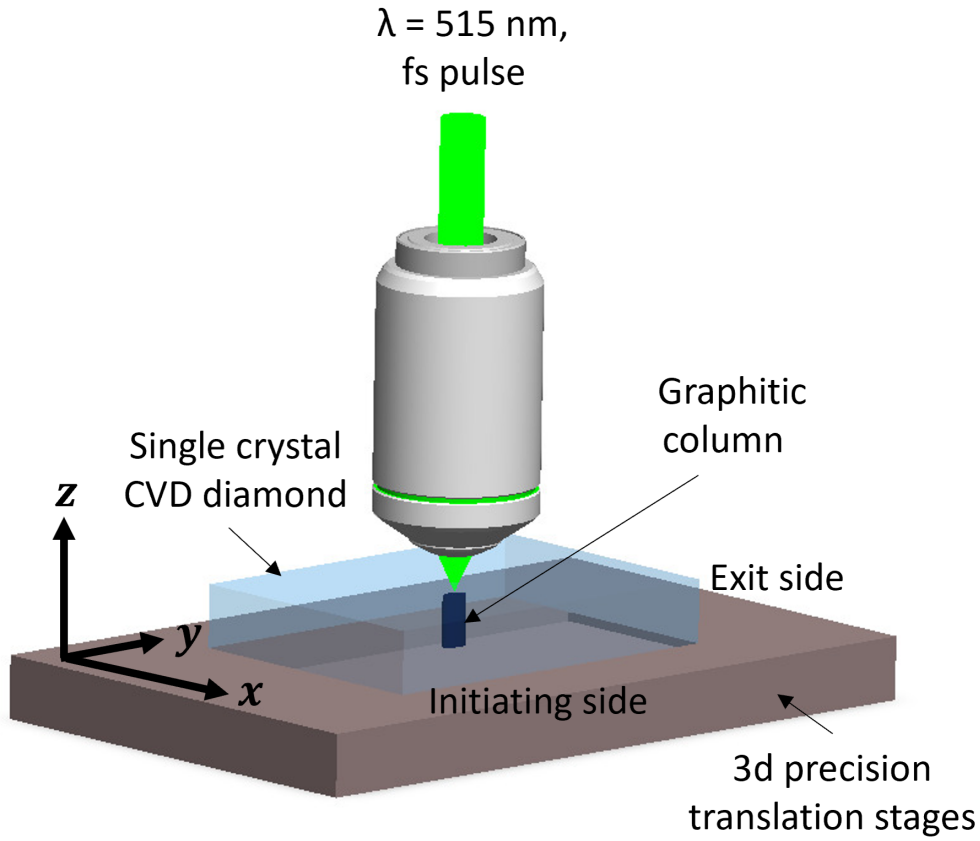

FIGURE 4.10: Schematic diagram of laser writing of graphitic structures.

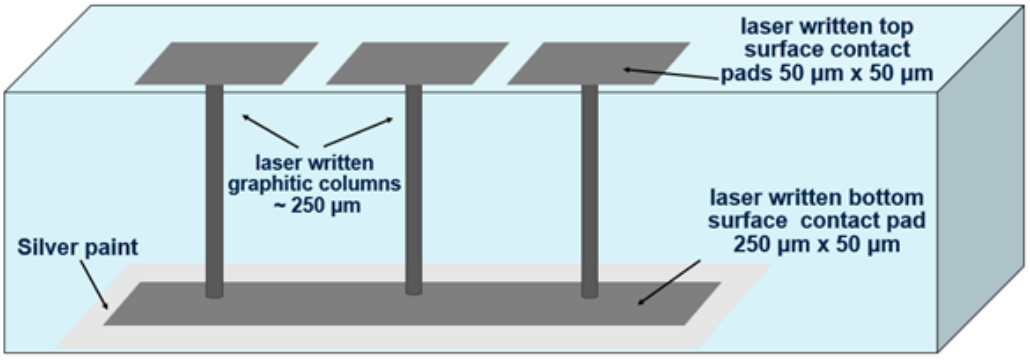

FIGURE 4.11: Schematic diagram of laser-fabrication procedure of graphitic wires of length of ~ 250 µm and diameter of ~ 5 µm . Firstly, the columns were generated throughout the sample thickness. Secondly the graphitic contact pads were fabricated on the diamond surface each side at a time. Finally, the sample was examined electrically as an all-carbon device. Finally, the bottom of the sample with large contact pads was coated with silver paint and the sample was re-tested to probe individual columns.

Figure 4.11 presents the architecture allowed for straightforward testing of the electrical properties of the laser-written graphitic columns, by placing electrical probes on the small contact pads on the top surface of the diamond, without any additional procedures such as surface metallisation. This permits a rapid cycle of fabrication and testing on a single sample, for optimisation of the laser process parameters. To ensure reliability of the testing process, the back side of the sample with the large contact pads was finally coated with a silver conductive paint (Agar Silver Paint, G3691), to allow analysis of the properties of single columns. The understanding of correlation between laser-fabrication parameters and electrical properties of graphitic structures is crucial for fabrication of novel diamond devices.

After successful laser fabrication, the sample was analysed both optically and electrically. The quality of fabricated contact pads and structures was examined under the optical microscope and the electrical properties were measured by a two-point probe-station measurement (see Chapter 3). Figure 4.12 shows the microscopic images of the laser-written graphitic structures.

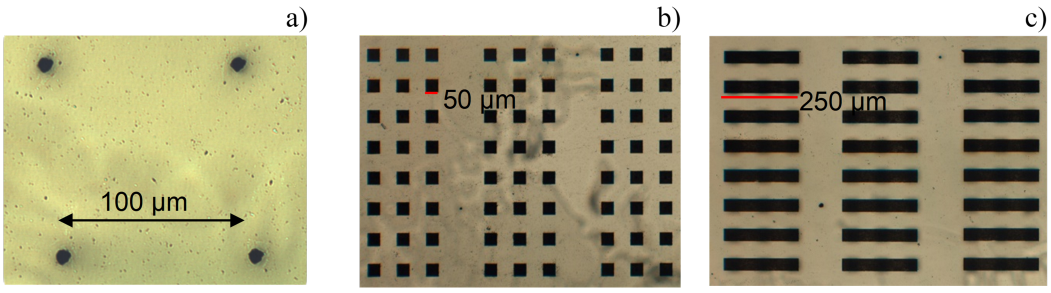

FIGURE 4.12: Microscopic images of laser-written graphitic structures a) top of the graphitic column, b) small and c) large graphitic contact pads

Figure 4.13 presents the two-probe measurement that was used to examine the electrical properties of the laser-written graphitic columns. The electrical testing investigated the relation between laser-fabrication parameters and d.c. electrical resistance of the graphitic wires. Two tungsten probes

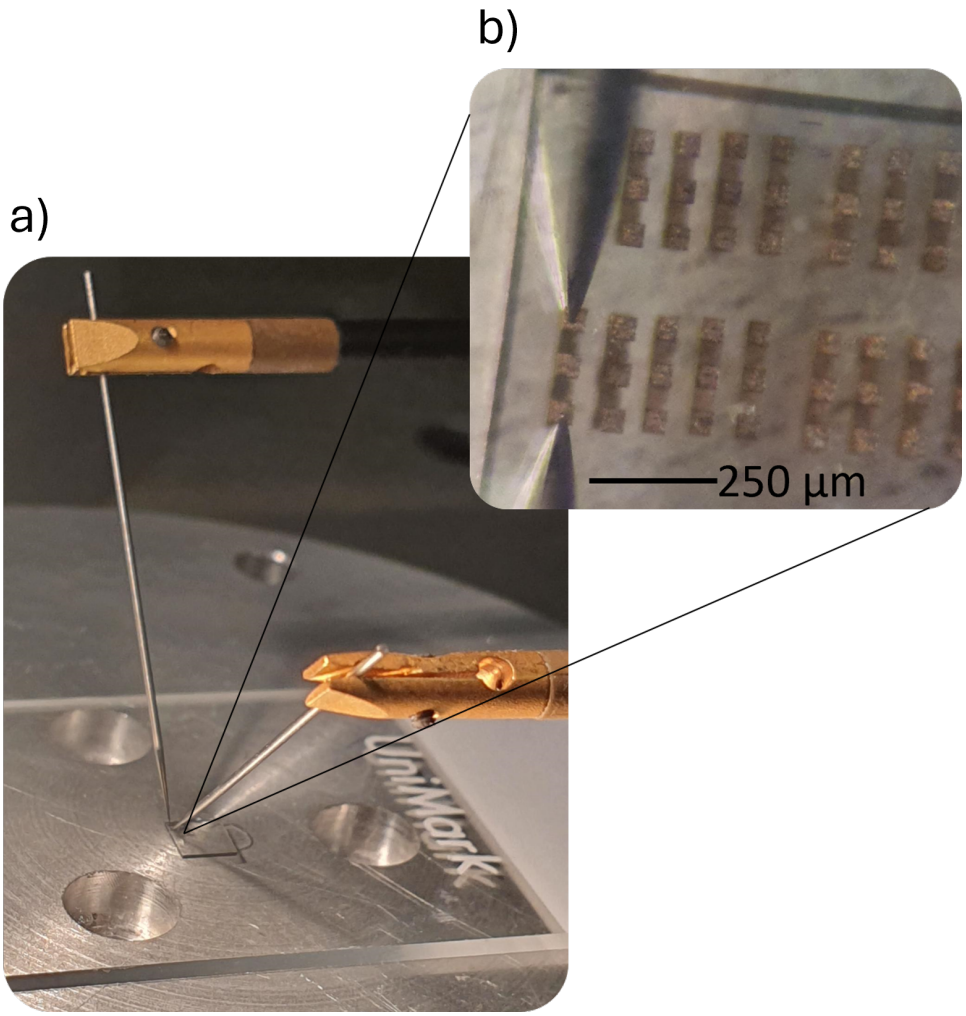

FIGURE 4.13: Picture of the two-probe station. a) Two probes touching the diamond sample. b) The probes contacted the laser-written graphitic pads, that linked the graphitic column with the two surfaces of the diamond.

with 10 µm tips were micro-positioned to contact the small pads on the top surface of the diamond. A Source Measurement unit (Keithley 2450) measured the current-voltage relationship for the wires, in a voltage ramp of -50 V to +50 V at 5 V resolution. Several tests demonstrated that only fabrication with optimized laser parameters generated wires showing measurable ohmic conductivity with the linear IV curve with no barrier potential [135].

Tests were conducted for two environments, firstly one for the native all-carbon device without any additional coating. The connection between probes on the small contact pads on the top surface of the diamond (figure

4.13b) thus measured the resistance of the two columns traversing the wafer in addition to the contact resistance from the graphitisation at the top and bottom surface. Finally, to verify the reliability of the test procedure, a silver paint layer was added to the bottom surface to create a common ground-electrode for contact with one of the probes, thus allowing analysis of individual graphitic columns by probing single pads on the top surface (see figure 4.11).

It is shown that the laser-fabricated graphitic columns exhibited ohmic behaviour. Their electrical properties were investigated by two-probe station measurements and proved that the columns exhibit ohmic behaviour. However, it is worth highlighting that their resistance drops on average by a factor of 2, as expected, when the silver paint is applied as a common base electrode. The layer of silver eliminates the additional link resistances, resulting in a direct measurement of the resistance of a single graphitic column. The resistances were examined by discrete measurements at different laser fabrication powers (from 100 nJ to 350 nJ) as shown in figures 4.14 and 4.15.

Finally, resistance has been calculated and the outcome is presented for two scenarios, one all carbon native device and one with an additional layer of silver paint. Figure 4.16 presents the obtained results. Both examples were laser written with the same processing parameters. The two-probe station method was applied to analyse this device. The first set of measurements was taken without any supplementary material, however, silver paint was used to create a common base electrode in the latter. It was observed that both sets of results present similar behaviour, namely the resistance drop with the increase of the laser pulse energies. For pulse energies higher than 309 nJ a spike in resistances is noticed. Here, resistance for a laser pulse energy of 340 nJ is higher than that for 350 nJ.

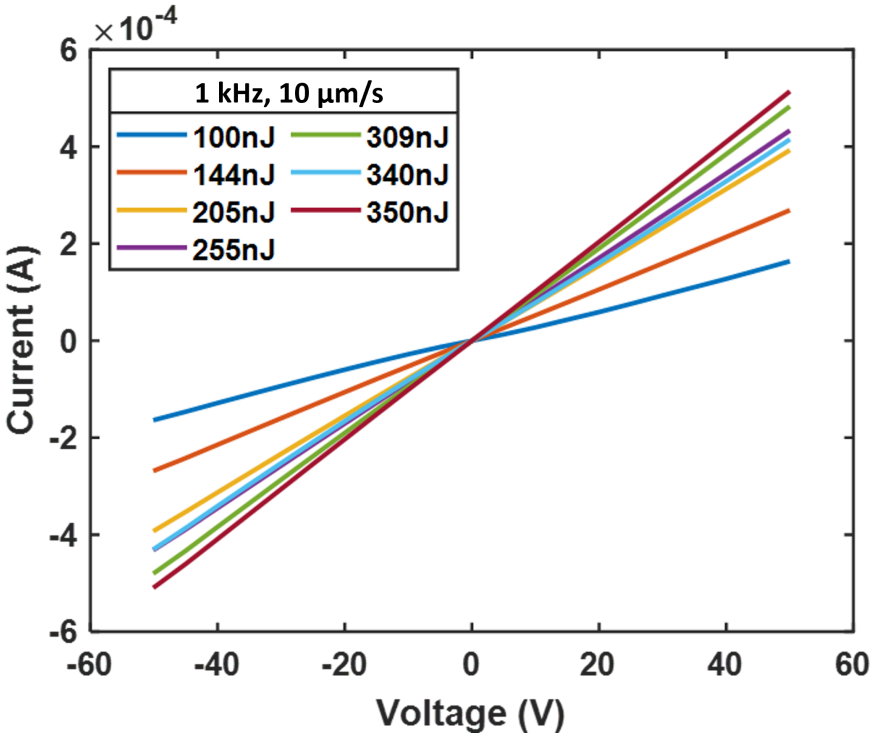

FIGURE 4.14: Ohmic behaviour of laser-written graphitic wires without any additional coating.

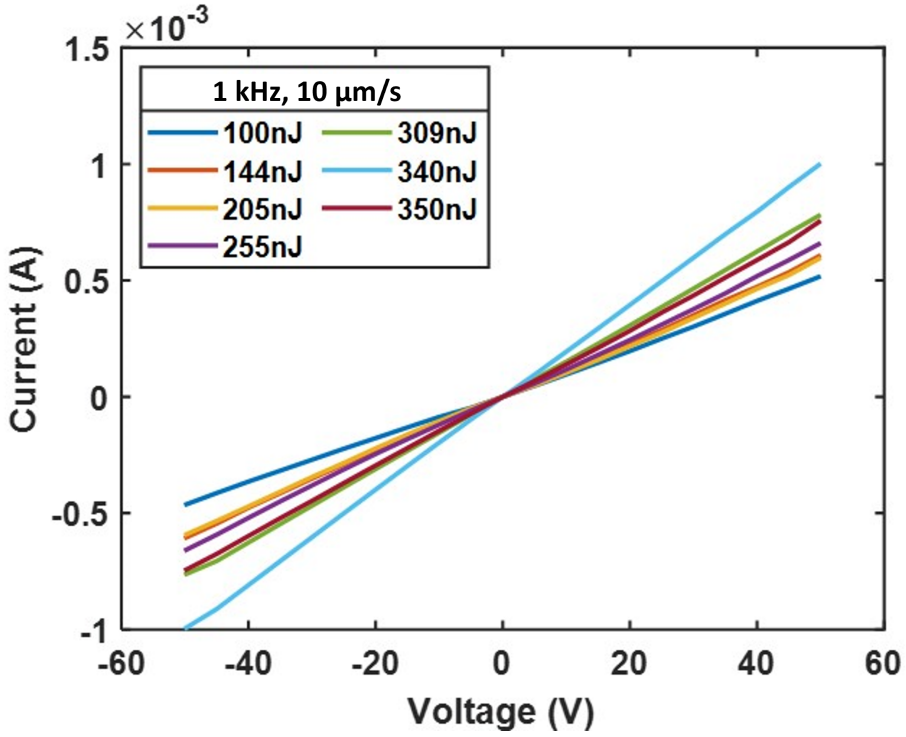

FIGURE 4.15: Ohmic behaviour of laser-written graphitic wires with an extra layer of silver paint.

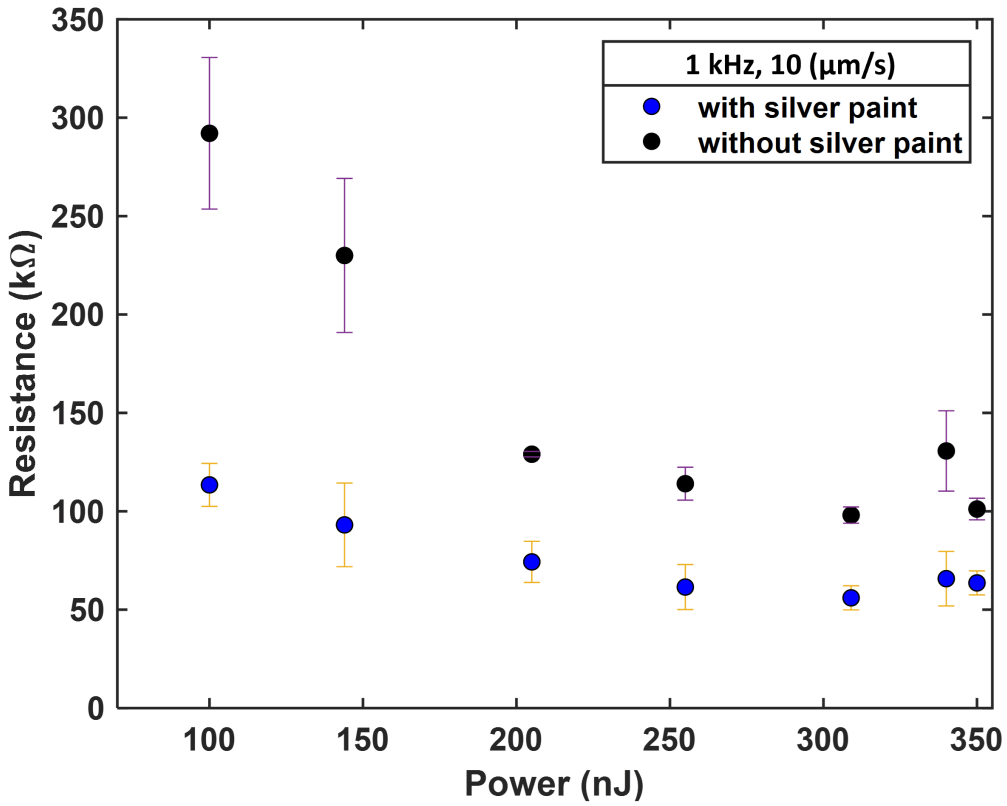

FIGURE 4.16: Resistance of laser-fabricated graphitic columns, comparison between the results with and without silver paint.

4.5 Optimization of laser processing parameters

It was already shown that the choice of laser-writing parameters is crucial for a successful fabrication. Therefore, further study was performed for a better understanding of the laser-writing process and how optimize the laser writing parameters for conductive graphitic wires. Figure 4.17 shows the current-voltage relationship for graphitic columns fabricated at a fixed pulse energy of 144 nJ and translation speed of 10 µm/s but different repetition rates. It was demonstrated that the pulse repetition rate had a significant impact on electrical properties of the generated structures. Surprisingly, only narrow fabrication window with linear ohmic conduction, ranging from 200 Hz to 2kHz, was shown. The insets in figure 4.17 present the low current data

at higher resolution. They proved that there is no conduction seen for repetition ratesf 100 Hz and 10 kHz, whereas at 5 kHz there is a barrier potential at 15 V [135] before conduction.

Figure 4.18 shows the conduction for wires fabricated at pulse repetition rate (PRRs) of 1 kHz with different laser pulse energies from 100 nJ to 350 nJ. The conduction shows a weaker dependence on pulse energy than PRR, with higher-pulse-energy wires yielding slightly higher current for a given voltage. For laser pulse energies above the fabrication threshold at 1 kHz and 500 Hz, the conduction was linear in all cases and there was no evidence of a barrier potential, presumably since the system was well corrected for aberration [135].

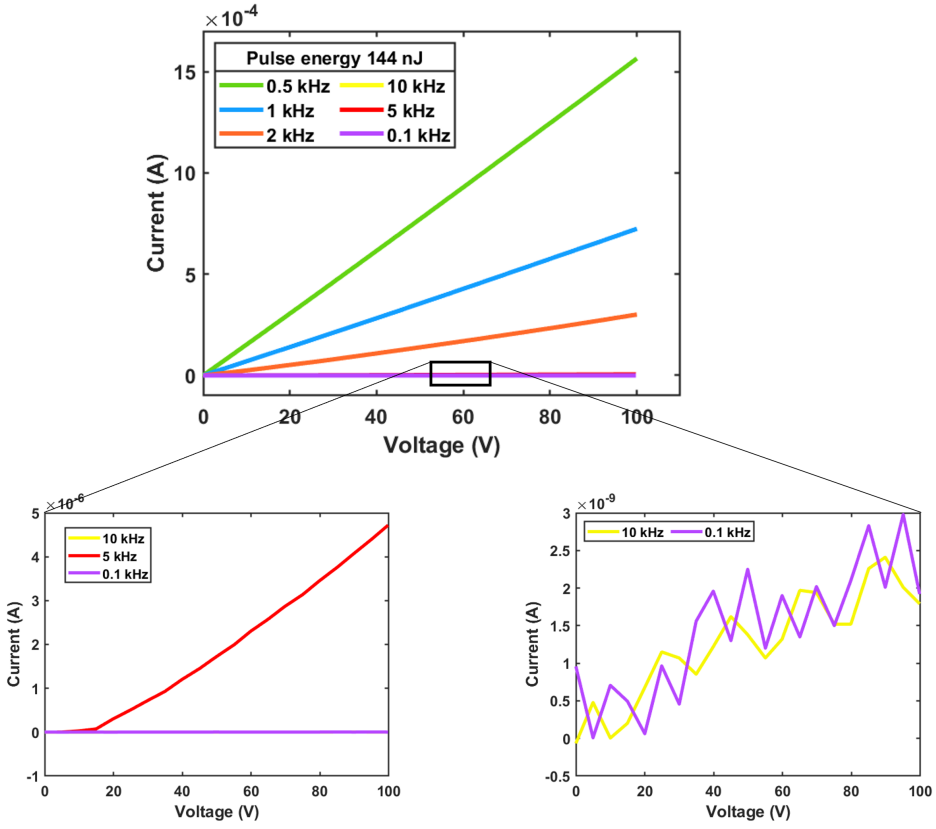

FIGURE 4.17: Current-voltage relationship of laser-written graphitic columns generated at fixed pulse energy and translation speed but at different pulse repetition rates. Insets show data for selected PRR on a magnified current scale.

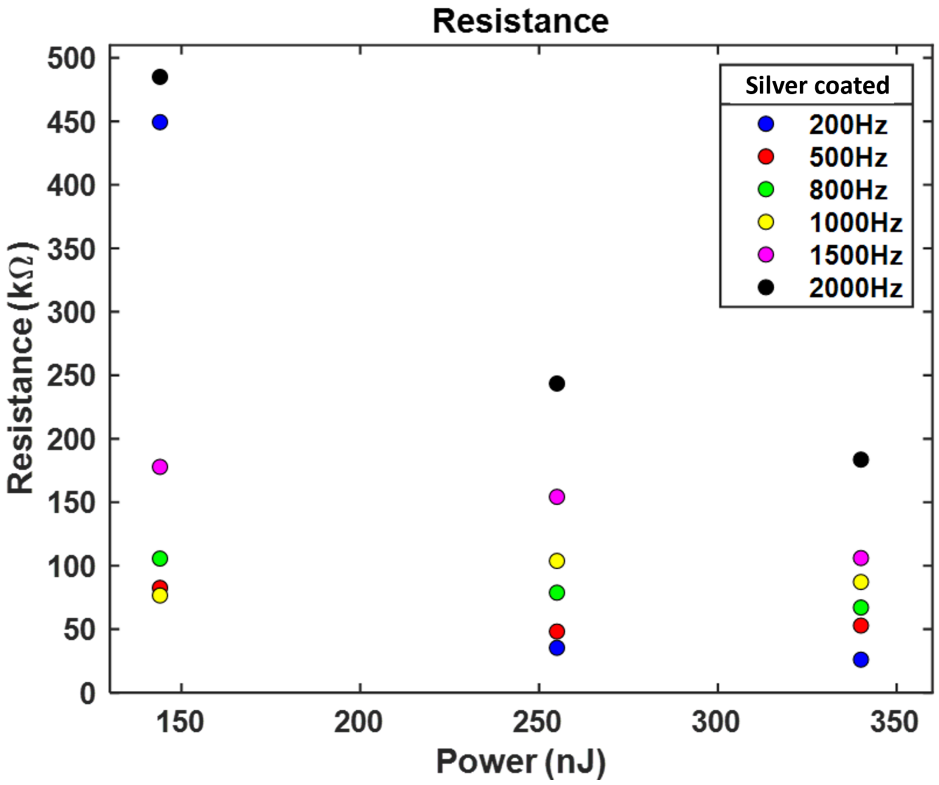

FIGURE 4.18: Resistances of laser-written graphitic columns and different repetition rates.

A clear tendency of increasing column resistance with increasing repetition rate was observed for all fabrication energies. These results are presented for a small fabrication window of 200 Hz to 2 kHz. Moreover, impact of translation speed at a fixed repetition rate of 1 kHz was examined and the findings are presented in figure 4.19.

There is a clear tendency that the resistances of the graphitic columns decrease with the higher translation speed. However, for high fabrication pulse energy (340 nJ), only wires fabricated at translation speed up to 35 µm/s demonstrated ohmic behaviour. For those fabricated faster than 35 µm/s there was no conductive electrical response at all. Resistance below 50 kΩ could be obtained by laser machining at 30 µm/s using either 144 nJ or 255 nJ of pulse energy. Here, with lowest resistance values of 32 kΩ was obtained at pulse of 255 nJ and speed of 45 µm/s.

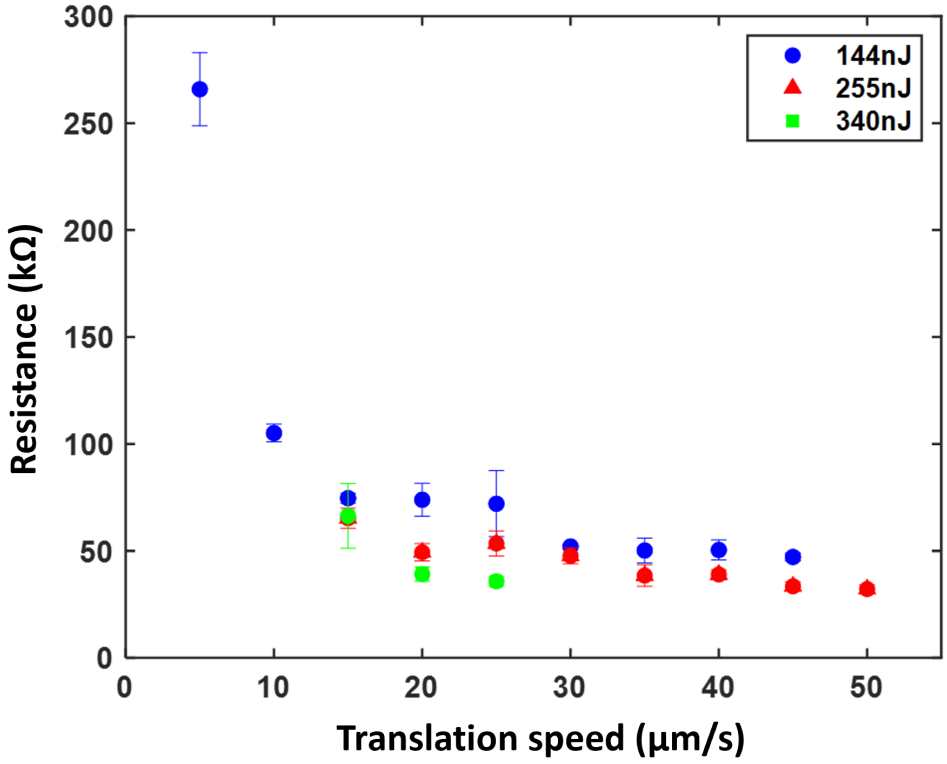

FIGURE 4.19: Relationship between electrical resistance of the graphitic columns and laser-writing parameters, here, with constant pulse repetition rate, 1 kHz, and different pulse energies and translation speeds.

Another important concept when looking at the column resistance values is the 'axial dose'. Here, it was defined as the number of pulses incident per unit micrometre along the writing direction.

$$\text{dose} = \frac{\text{pulse repetition rate (PRR)}}{\text{translation speed}} \tag{4.1}$$

The importance of dose was was performed based on a set of graphitic columns fabricated at a pulse energy of 144 nJ with both constant PRR (1 kHz) while translation speed was varied, and constant stage speed (10 µm/s) while PRR was varied. The obtained results are presented in figure 4.20.

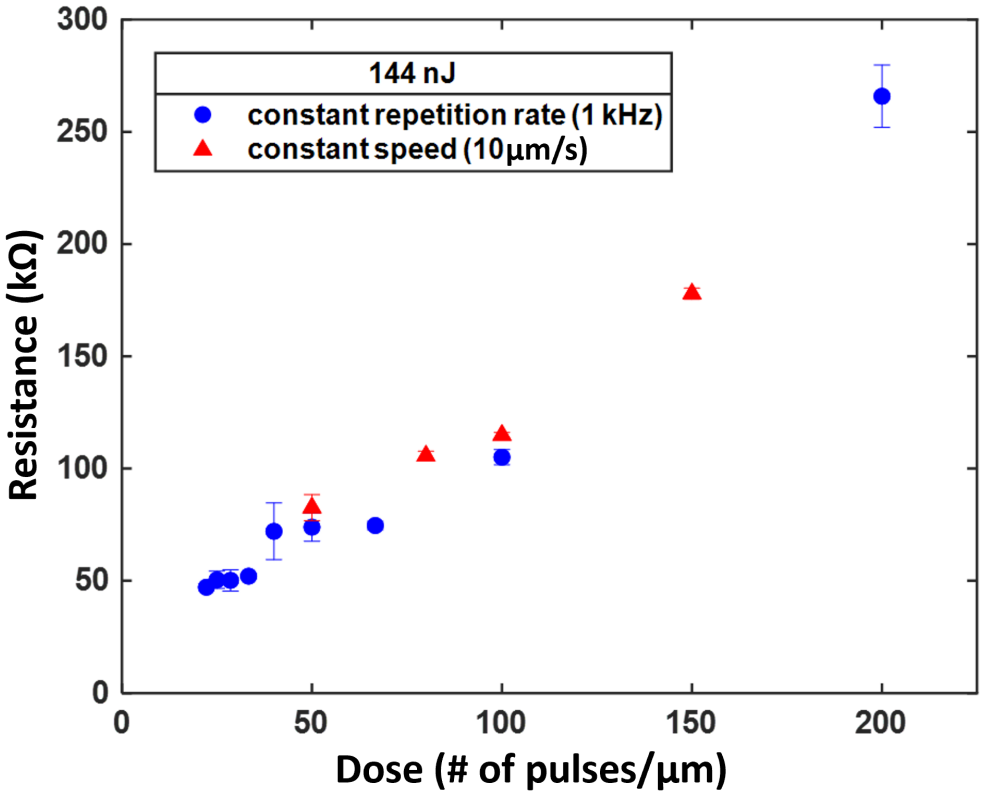

FIGURE 4.20: Relationship between dose and resistances at fixed pulse energy (144 nJ), here in two environments, at constant repetition rate and at constant speed.

It has been determined that values of resistance increase along with the increase in dose. Additionally, a clear tendency was recognized in the data for resistance values presented as a function of laser dose, whether repetition rate or translation speed were kept constant. Thus, laser dose is an important parameter when fabricating graphitic electrodes.

Finally, the resistivity of the fabricated graphitic columns was estimated based upon optical measurements of their cross-sectional areas. The diameter of the wire at the top surface of the diamond (the exit side) was calculated based on measurements taken in a transmission optical microscope. Figure 4.21 displays values of both resistivity and radius of graphitic columns fabricated at different repetition rates and at different pulse energies.

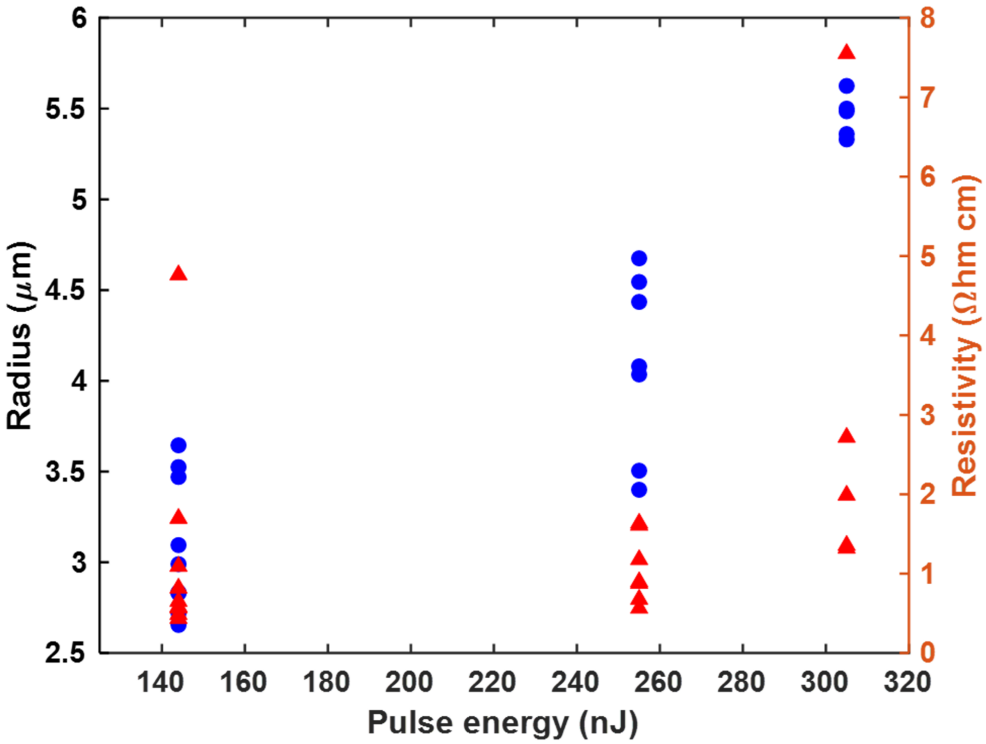

FIGURE 4.21: Relationship between resistivity at different pulse energies.

It was noticed that the diameter of measured column increased with the increase of both pulse energy and repetition rate. The increase of the column diameter results in increased effective resistivity. Resistivity in the range less than 1 Ωcm, as typical for such columns, is achievable for many settings with lower pulse energy and lower PRR. However, resistivity is not the most ideal criteria for describing graphitic columns. High-resolution electron microscopy imaging has shown that the internal structure of such columns consists of a complex network of sp^2 and sp^3 carbon bonds (more details in section 4.8). Furthermore, controlling the cross-sectional area of the columns during fabrication is not straightforward, making it challenging to use as a reliable parameter. Therefore, resistance of graphitic column becomes the primary criterion for evaluating the laser fabrication process, where we have shown that the laser dose is a critical parameter.

4.6 Wires oriented in different crystallographic directions

Another approach that was examined during this project was performance of laser-written graphitic wires at different geometries. Here, the graphitic wires were fabricated at different angles in the diamond, starting from 5° to 45° relative to the surface normal. Figure 4.22 illustrates the idea behind laser processing at different angles. It has recently been shown that laser written graphitic wires can show different conductivity based on orientation within the diamond [134], where wires along (110) direction had higher conductivity than those along (100) direction. Thus it is important to investigate wires written in different directions. Also so we can fabricate more complicated devices with wires in any direction.

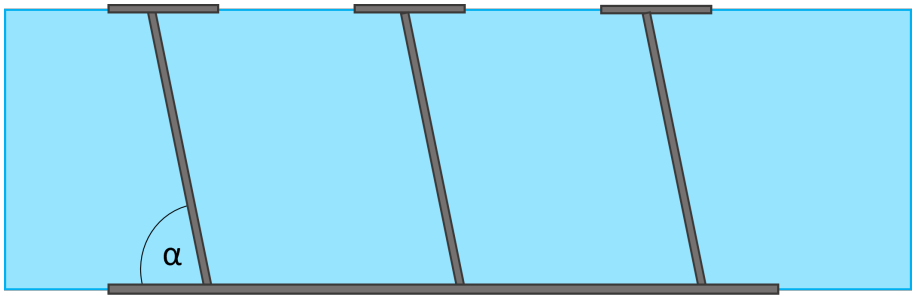

FIGURE 4.22: Schematic of laser writing of graphitic structures at different geometries, where α refers to the angle between the surface of the diamond and graphitic wire.

In this experiment, two different designs were investigated. The first one included laser writing of graphitic wires at different orientations in the (100) crystal plane, whereas the second example consisted of graphitic wires laser written in different orientations in the (110) crystal plane. More details are depicted in figure 4.23. The diamond lattice features different fracture characteristics in different crystal directions, so exploring wire orientation relative to crystal orientation is important.

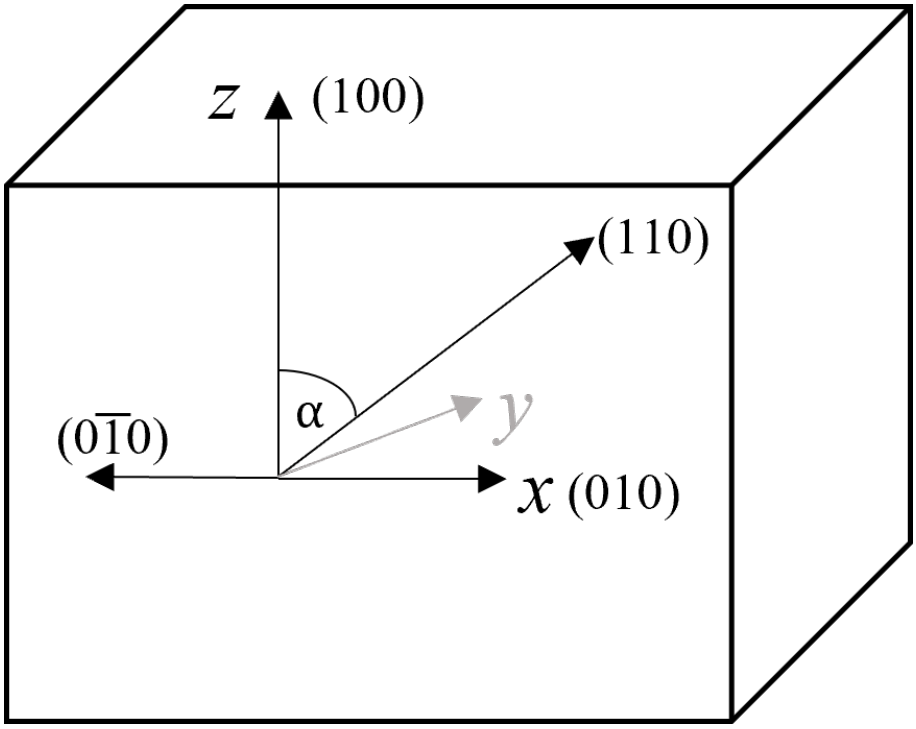

FIGURE 4.23: Schematic diagram of laser writing of graphitic structures ain different directions relative to the diamond crystal.

Wires were written with the Pharos laser system (Chapter 3) at a pulse repetition rate of 1 kHz, speed of 10 µm/s and pulse energy of 250 nJ at different angles to surface normal as described above. Figure 4.24 shows a transmission optical microscope image of the entire diamond chip following the laser processing, while Figure 4.25 shows a magnified image of wires in the (100) crystal plane, and Figure 4.26 shows a magnified image of wires in the (110) crystal plane. After successful fabrication of graphitic wires, small graphitic contact pads were generated to enable direct electrical measurements. The long contact pads linked three wires of each set to independent devices. Procedure was maintained the same as in those in the case of all-carbon devices (see figure 4.10). However, in this case, the dimensions of graphitic contact pads were chosen with respect to separation distances between diagonal graphitic structures, thus they differ in sizes, from 40 × 50 µm to 120 × 40 µm (see figure 4.27).

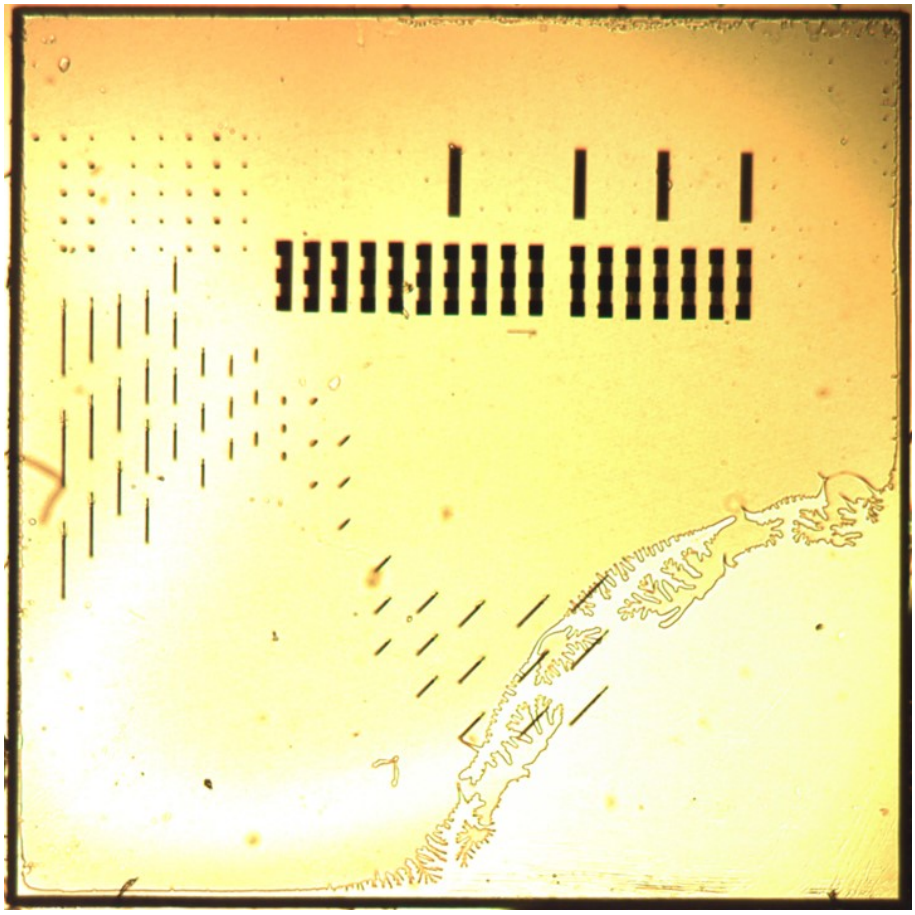

FIGURE 4.24: Transmission microscope image of diamond chip showing laser-written wires at various angles to the surface normal.

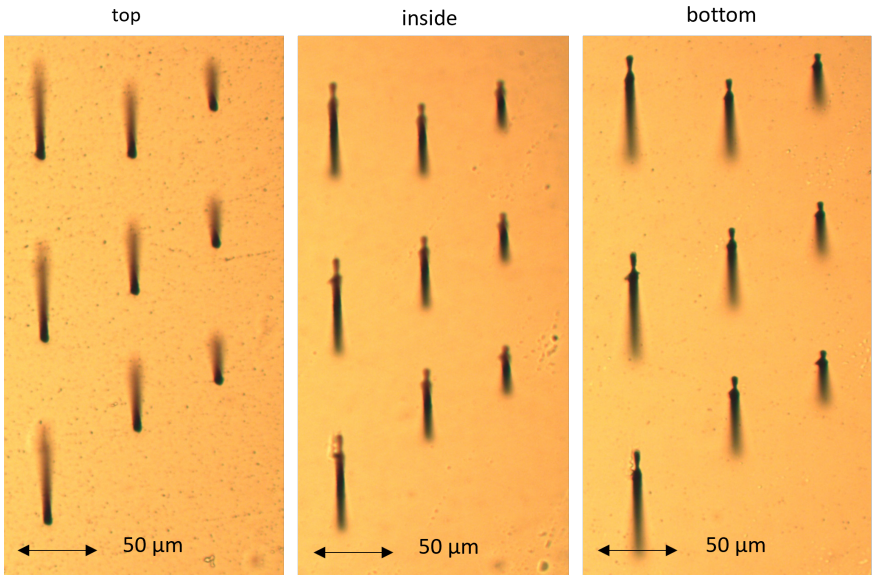

FIGURE 4.25: Transmission microscope image of diamond chip showing laser-written wires at various angles within the 100 crystal plane. Images show the wires at top surface, inside the diamond and focused at bottom surface.

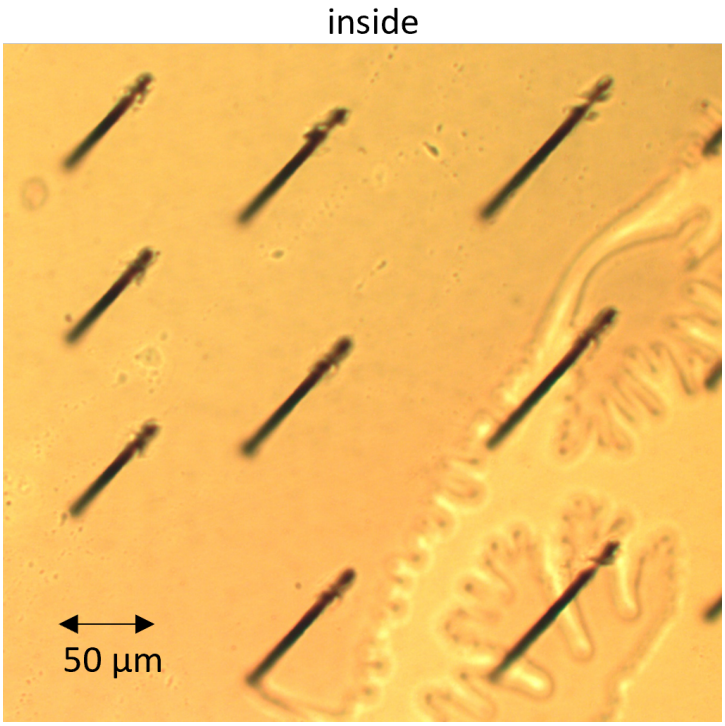

FIGURE 4.26: Transmission microscope image of diamond chip showing laser-written wires at various angles within the 110 crystal plane. Images show the wires when focused inside the diamond.

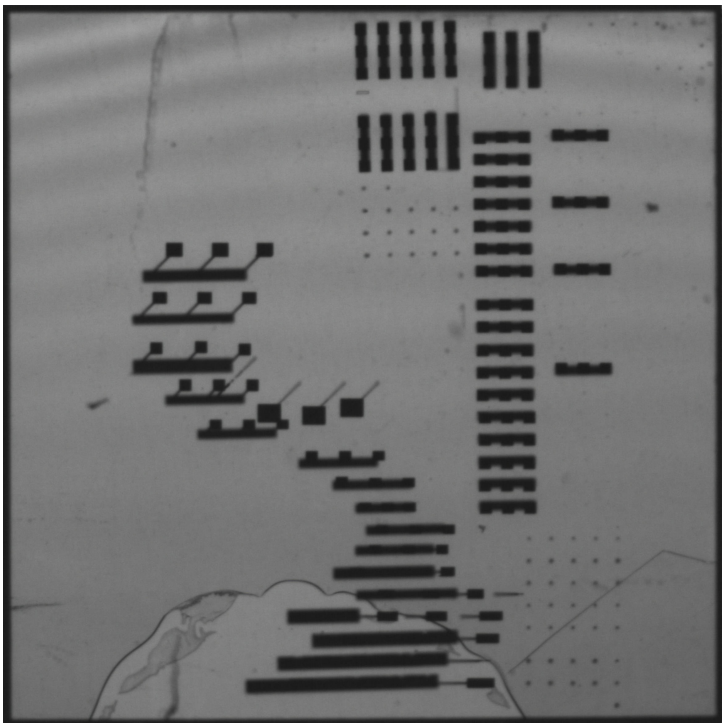

FIGURE 4.27: Microscopic image of diagonal graphitic wires covered with graphitic contact pads.

The bottom side of the sample was covered in silver paint (Agar) and the electrical characterization was performed for these devices. Figures 4.28 and 4.29 present the current-voltage relationship at different angles for both fabrication at different angles in (100) and (110) crystal planes respectively.

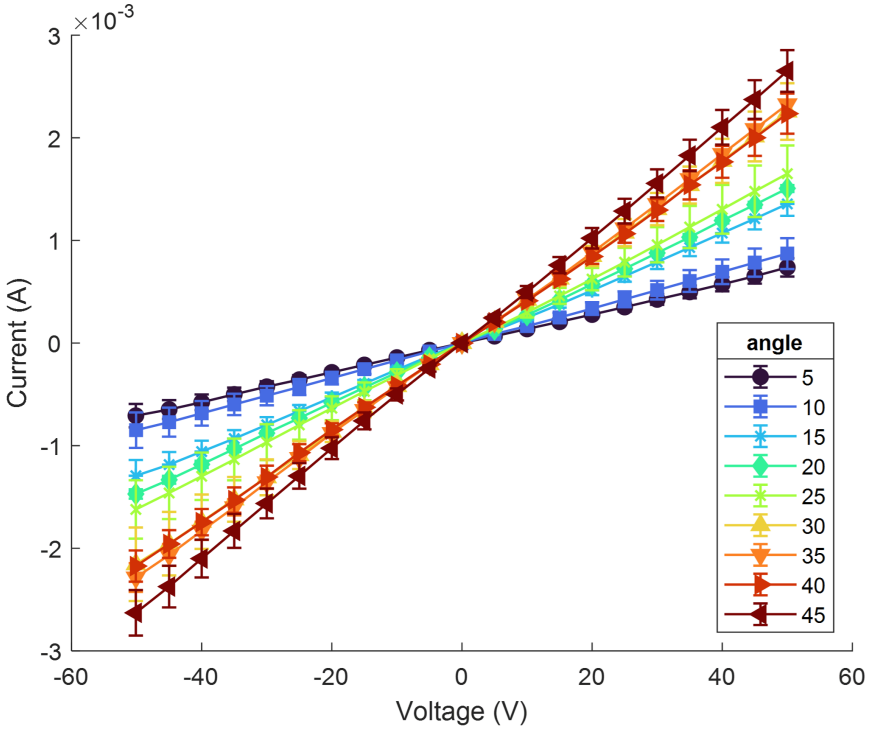

FIGURE 4.28: Current-voltage relationship of graphitic wires with respect to different angles of fabrication, from 5° to 45° in (100) crystal plane.

Both figures show Ohmic behaviour for two different scenarios. However, only characterisation of diagonal wires fabricated from 5 to 30 degrees was successful in the (110) crystal plane. For angles bigger than 30° the IV curves were very noisy and disrupted.

Finally, the resistances of these graphitic microstructures have been calculated. A basic fit was applied in order to extract resistance values. This procedure was used for all IV-curves, as depicted in figures 4.30 and 4.31, and all of them have expressed linear ohmic behaviour, with negligible error.

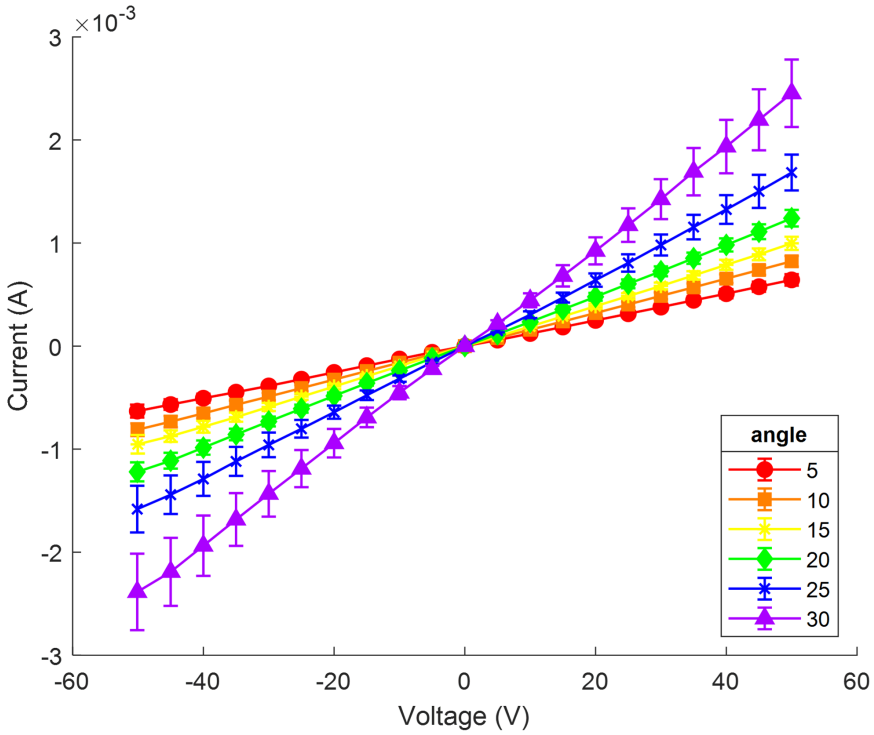

FIGURE 4.29: Current-voltage relationship of graphitic wires with respect to different angles of fabrication, from 5° to 30° in (110) crystal plane.

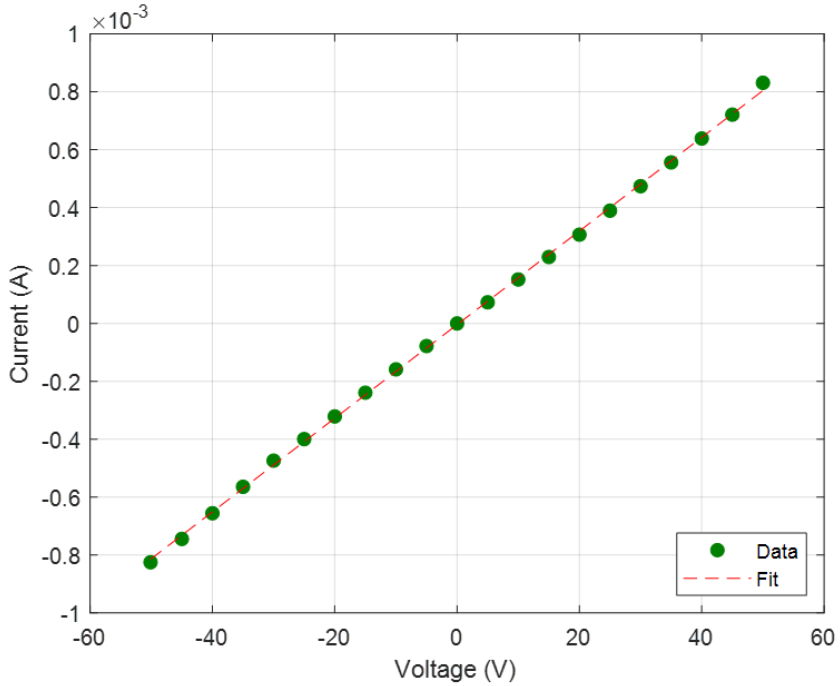

FIGURE 4.30: Current-voltage relationship with a basic fit for a chosen fabrication orientation, here in (100) plane at 5°. Resistance (R) equals 61.84 kΩ and the best fit factor r^2=0.9996.

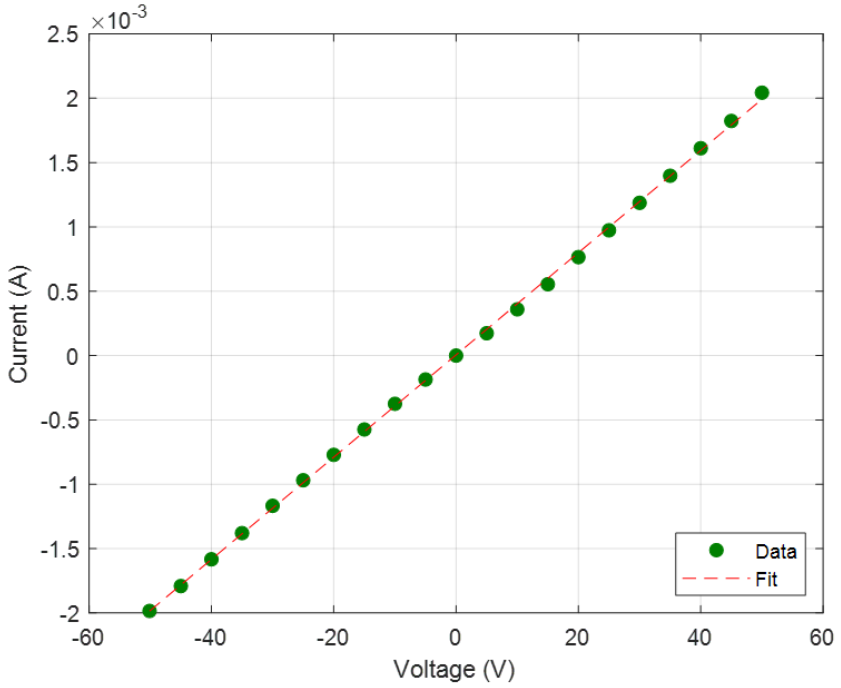

FIGURE 4.31: Current-voltage relationship with a basic fit for a chosen fabrication orientation, here example in (110) plane at 30°.Resistance (R) equals 25.17 kΩ and the best fit factor r^2=0.9996.

Comparison between two cases is presented in figure 4.32. Both approaches exhibit similar behaviour, namely the resistances drop as the angle of diagonal wire increases. Resistances of wires fabricated in the (110) plane have a very linear relationships, however there is a quite sharp drop in resistance value at 15° for those fabricated in (100) plane.

It is initially surprising that the measured wire resistance drops as the angle of the wire increases. As the angle increases, the length of wire increases as can be seen in Figure 4.33, so we might expect the resistance to increase. However, it is worth noting that the laser focal spot is asymmetric due to the limited numerical aperture of the focus. Figure 4.34 shows that if there is asymmetric focal spot moving at an angle relative to the optic axis, the effective cross-sectional area is traced out increases. Therefore, whilst the length of wires increases we can also expect the wire cross-sectional area to increase. Therefore, it is also possible for wire resistance to drop due to the

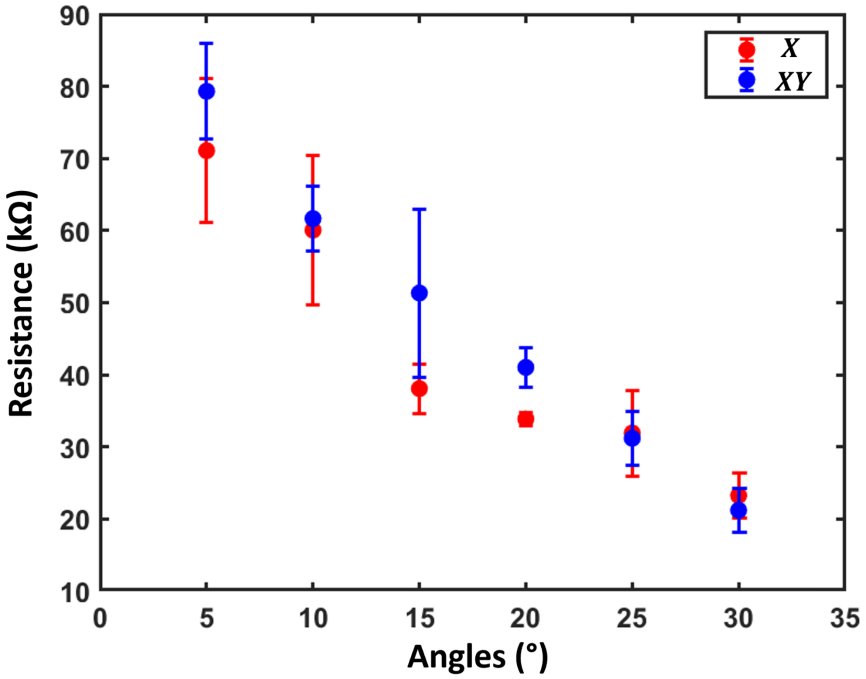

FIGURE 4.32: Resistances of graphitic diagonal wires with respect to angle of fabrication, from 5 ° to 30°.

greater cross-section of conductive material, regardless of any effect related to crystal orientation.

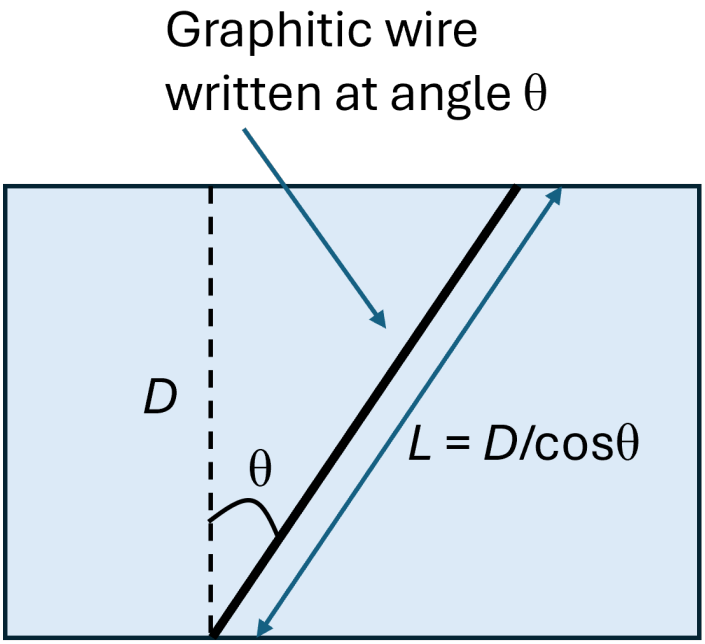

FIGURE 4.33: Schematic diagram of diagonal wire in diamond wafer.

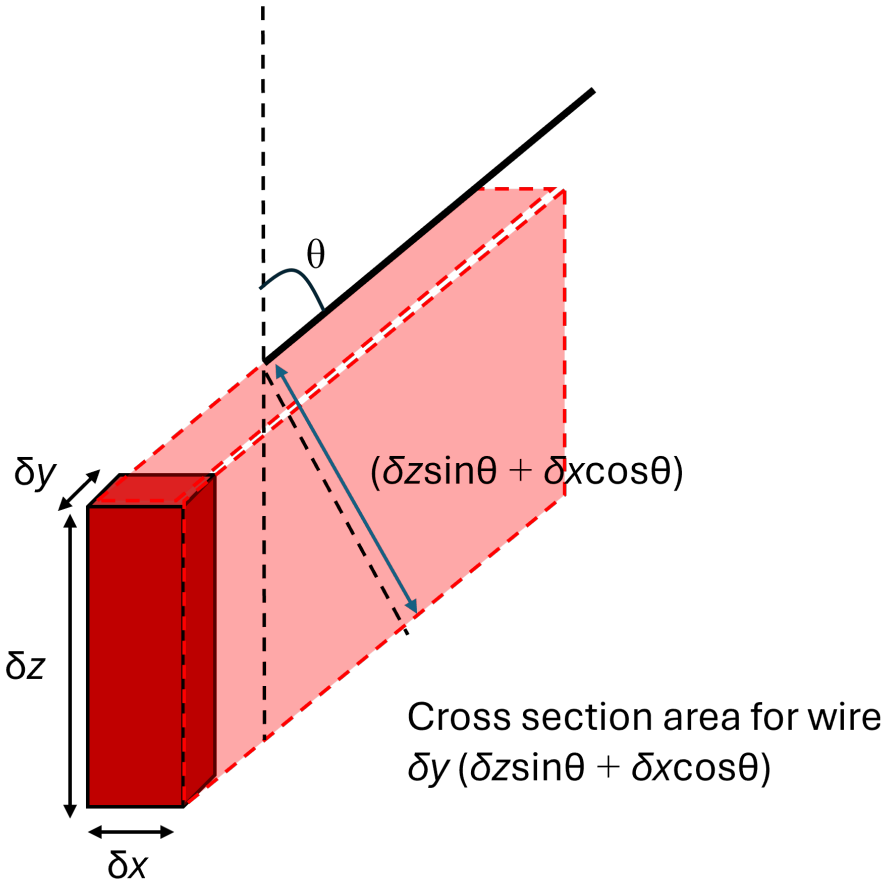

FIGURE 4.34: Elongation of the laser focus can create wires with greater cross section area when writing at angles other than normal.

With reference to Figures 4.33 and 4.34, a formula we can derive a formula to predict the wire resistance at different angles in the substrate as:

$$R = \frac{\rho L}{A} = \frac{\rho D}{\cos\theta \delta_y (\delta_z \sin\theta + \delta_x \cos\theta)} \tag{4.2}$$

where R is the resistance, ρ is the conductivity, L is the length and A is the cross-sectional area. D denotes the substrate thickness, while θ gives the wire angle relative to the surface normal. $\delta_y x$, δ_y and δ_z give the laser focal dimensions along respective axes. This simple geometric relationship is used in figure 4.35 to fit the data. It can be seen that the equation describes the experimental data well.

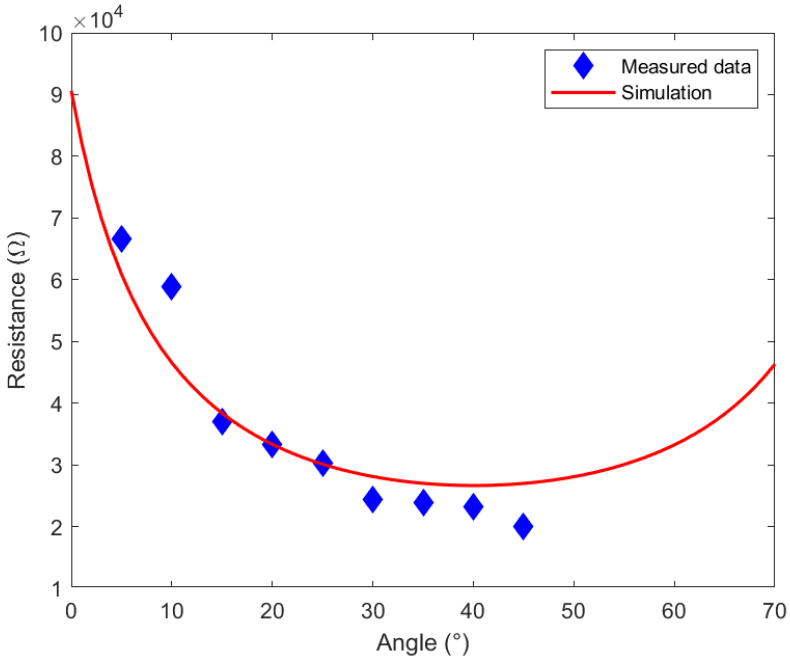

FIGURE 4.35: Comparison of the measured data and the simulated data for wires in (100) crystal plane. Simulation calculated with respect to Equation 4.2.

This study has confirmed that the graphitic microstructures can be successfully generated at different orientations within diamond crystal. Moreover, they have maintained their conductive properties. Resistances of this structures have dropped with respect to increasing angle of deviation from the optical axis. Knowing that resistance is proportional to the relationship between length and area of the structure it would be expected that their resistance values would increase along with their length. Even though, the graphitic wires were longer for bigger angles, their resistances kept decreasing. This is due to the increased cross-section traced out by the asymmetric laser focus. A simple geometric relationship is used to provide a good fit to the data. There is little difference between wires fabricated in (100) plane and (110) plane indicating that wire geometry and laser parameters are more significant than crystal orientation for wire conductivity.

4.7 Raman analysis

Raman analysis was performed to examine the presence of graphite in the laser-written structures (see Chapter 3). This study has investigated the behaviour of both sp^3 and sp^2 peaks and its relationship with respect to different laser-fabrication conditions. Firstly, the measurement of a reference sample was taken, namely a chosen area of unprocessed CVD crystal diamond sample was scanned. Figure 4.36 presents the obtained results.

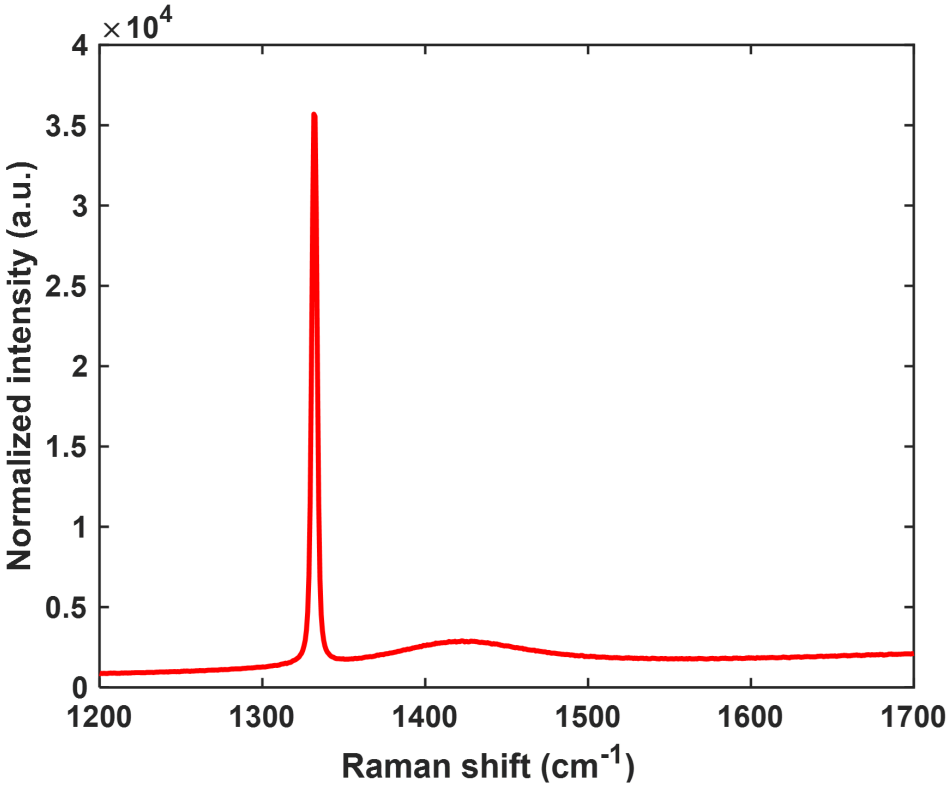

FIGURE 4.36: Raman spectrum of CVD single-crystal diamond.

Here, the sp^3 peak is very distinguishable at a Raman shift of 1332 cm^{-1} that confirms the sample is diamond. However, laser-written graphitic columns were also present in this CVD single-crystal diamond sample. They were generated by PHAROS laser system (see Chapter 3) to characterize optically graphitic content within the fabricated microstructures. Figure 4.37 shows the microscopic image of the laser-written graphitic structures, in this

case only columnar graphitic wires were fabricated through the diamond wafer. Here, different laser processing parameters have been applied, the pulse energies were of 144 nJ, 255 nJ and 340 nJ and when the repetition rate was kept constant at 1 kHz, the translation speed varied from 5 µm/s to 50 µm/s. The other set was fabricated at the same pulse energies but here the translation speed was the same and equaled 10 µm/s and the repetition rates varied from 100 Hz to 1 MHz.

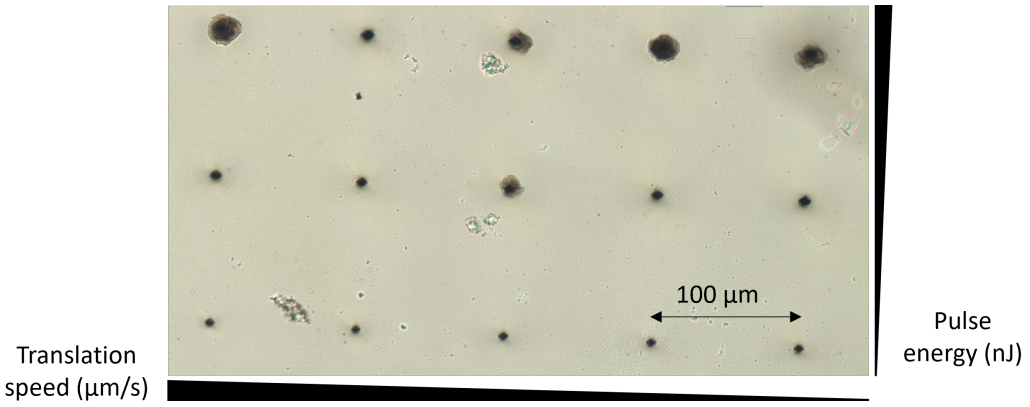

FIGURE 4.37: Microscopic image of chosen laser-written graphitic columns, view from the top. The top row was laser written with a pulse energy of 340 nJ, middle row of 255 nJ and bottom row of 144 nJ. The repetition rate was kept constant, 1 kHz. The translation speed varied, from the left from 50 µm/s to 30 µm/s with a 5 µm/s step.

The spectrometer cursor was placed on the corresponding head of graphitic wire and the scans were performed for the full range of the parameters. Figure 4.38 and 4.39 present the obtained results for fabrication at 255 nJ of pulse energy with varied repetition rate and varied translation speed, respectively.

All spectra of the analysed samples show a vry distinctive diamond peak at 1332 cm^{-1} Raman shift and the secondary peak at 1580 cm^{-1}, that coresponds to a graphitic peak. Here, the graphitic peak is present in all spectra, regardless of the laser-fabrication conditions.

Finally, the Raman spectra of structures fabricated with the most used repetition rates are presented, here the range is 100 Hz, 1 kHz, 10 kHz, 100

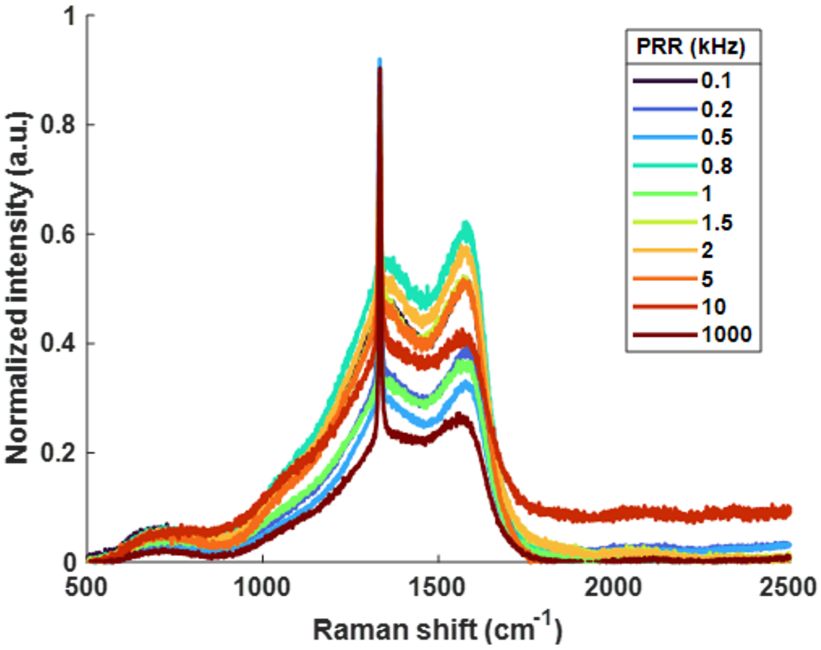

FIGURE 4.38: Raman spectra of graphitic columns fabricated at the same pulse energy, 255 nJ, but for different repetition rates of fabrication.

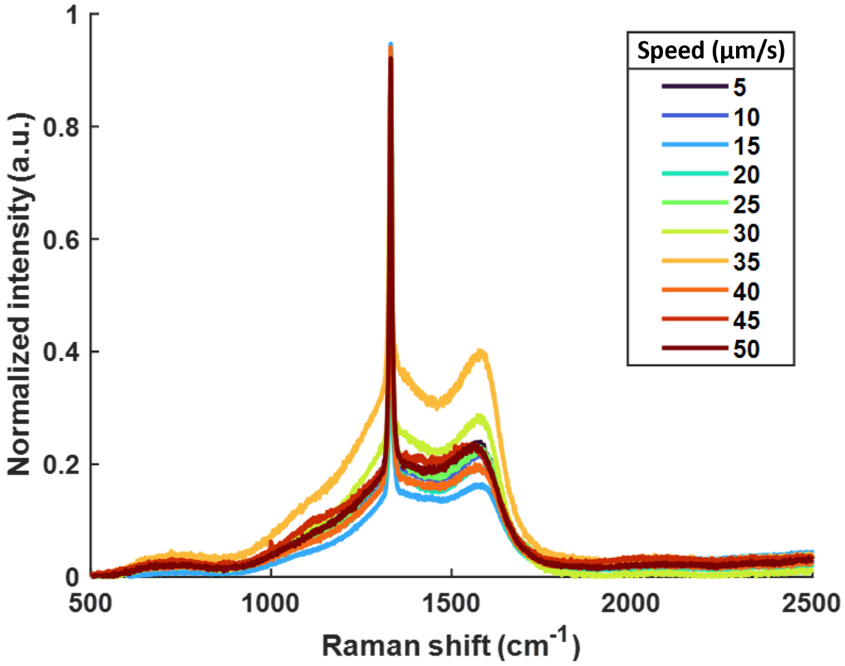

FIGURE 4.39: Raman spectra of graphitic columns fabricated at the same pulse energy, 255 nJ, but for different fabrication translation speeds.

kHz and 1 MHz. Based on figure 4.40 it is seen that the Raman peak at 1332 cm^{-1} describing sp^3 bonded diamond is present for all laser written columns, as expected (more details in section 4.8). In contrast, an sp^2-bonded carbon with a peak at around 1600 cm^{-1} is only present for 1 kHz fabrication.

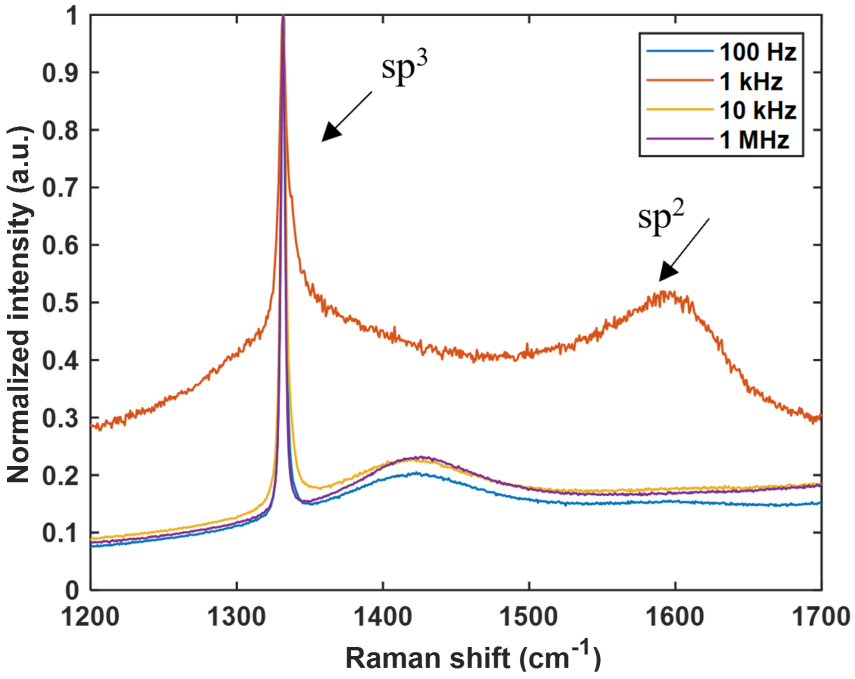

FIGURE 4.40: Raman spectra of graphitic structures laser written at 255 nJ pulse energy, 10 µm/s translation speed, but different repetition rates (measurement performed at the top surface of the diamond sample).

The relationship between sp^2-bonded carbon and sp^3-bonded carbon is presented in figure 4.41.

As described above, a high intensity sp^3 peak was present in all of the spectra (see figure 4.40). However, the intensity of the sp^2-carbon-bonded peak was not repeatable. Even though, the Raman measurements were taken at the top side of the diamond sample at the centre of the laser-written graphitic column, it was demonstrated that they mostly consist of sp^3 carbon.

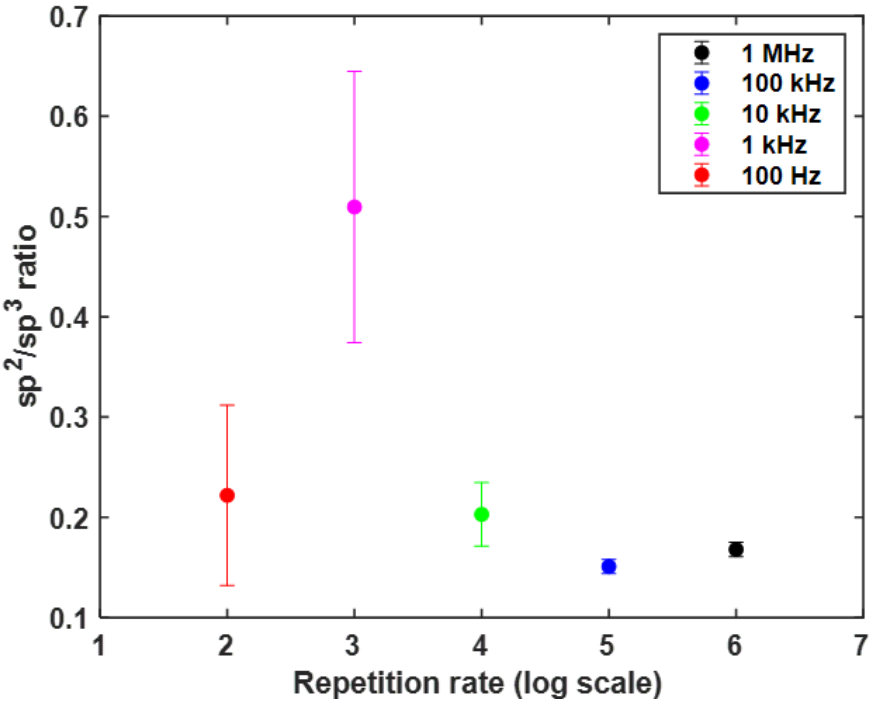

FIGURE 4.41: Relationship between graphite and diamond with respect to different fabrication repetition rates for graphitic structures fabricated at the same pulse energy, 255 nJ.

4.8 TEM analysis

Laser-induced lattice modifications significantly impact the final performance of the device. The hypothetical approach assumes that the generated graphitic structures are not homogeneous and that other nanocarbon features are present, resulting in a stack of graphitic-like clusters spaced out close enough from each other to provide the ohmic behaviour. Figure 4.42 depicts the idea of distribution of graphitic-like content within the area of a graphitic wire. This assumption was examined by high resolution microscopy.

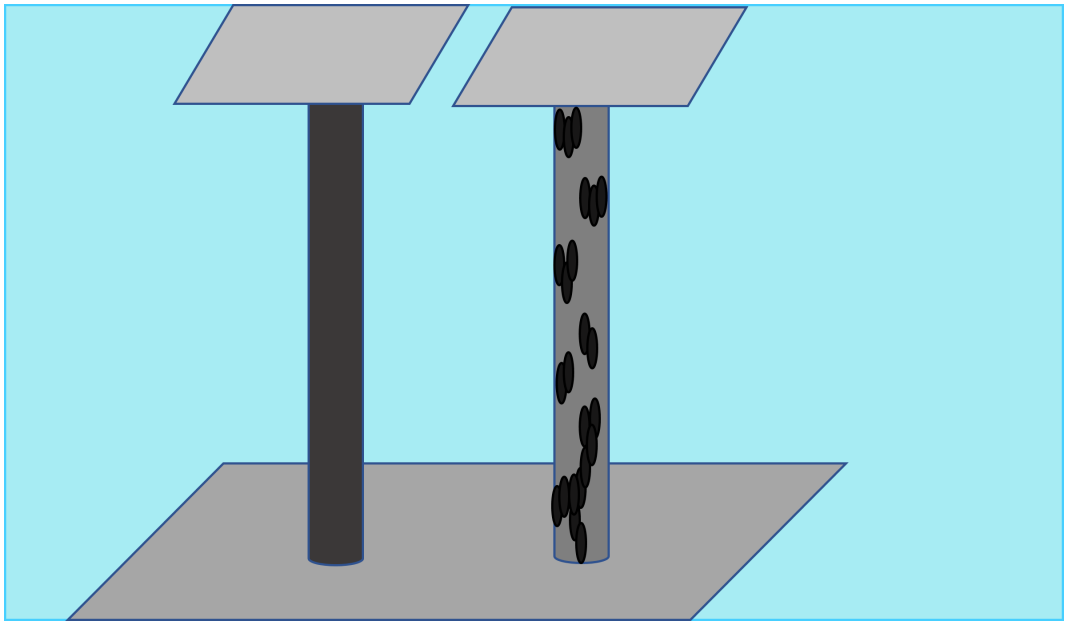

FIGURE 4.42: Schematic diagram of hypothetical dispersion of graphitic-like content inside the area of graphitic wire.

To understand the mechanism for the different conduction properties of the graphitic columns and how they depend on the laser processing conditions high-resolution imaging was performed. TEM was applied to previously described laser-written devices (see figure 5.2) to investigate the laser-induced structural modifications. In the case of the results presented here, TEM imaging has been carried out on the initiating side of the written wire.

Here, high resolution TEM was used to provide depth resolution and better spatial resolution of these sub-surface graphitic structures. Cross-sections of the chosen wire were then extracted by a method known as lift-out. In this example, the thin area of diamond was cut out and then lifted out from the sample and then analysed by high resolution TEM (see Chapter 3). Figure 4.43 shows a TEM image of a chosen graphitic wire laser written at 1 kHz.

TEM image revealed the internal microstructure of laser written graphitic column and proved the presence of structural disruptions in the laser-processed

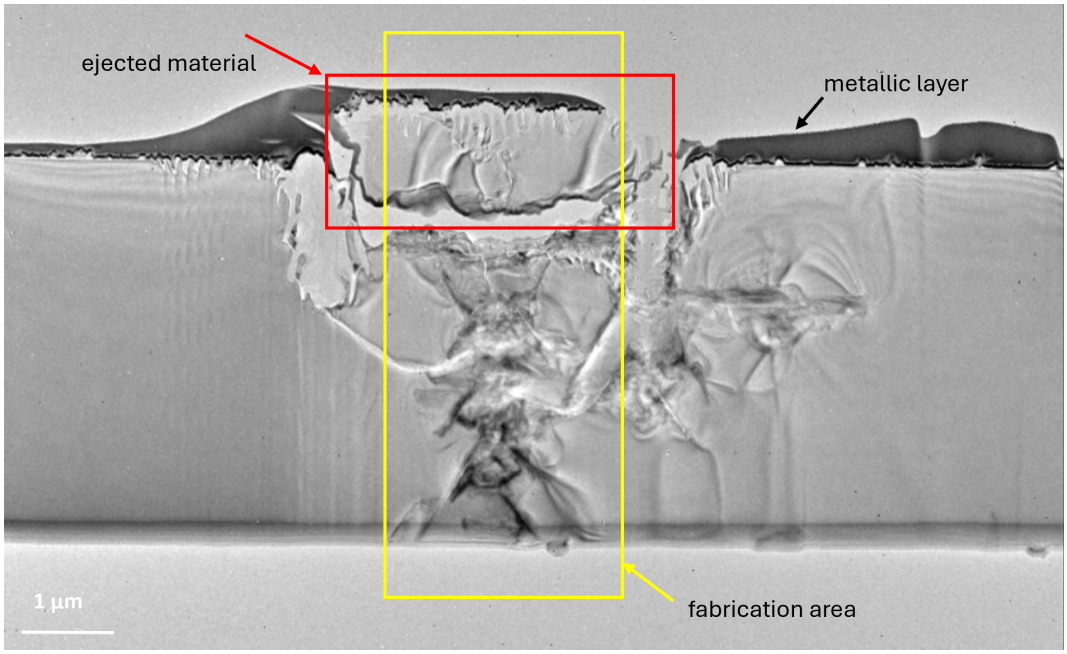

FIGURE 4.43: Cross-sectional TEM image of a graphitic wire laser written at 1 kHz in the diamond bulk (in yellow frame) and the ejected material (in red frame). (The dark material on the top of the image can be disregarded, as it is metal associated with the FIB preparation method.)

area. Here, the light-matter ineraction created the main structure of approximately 1 µm across, which is expected to continue in this manner through the whole thickness of the diamond wafer. The interesting result of laser fabrication was observed at the top of the sample, the area at which laser beam started to interact with diamond. Here, a partial ejection of material in an area greater than the laser beam diameter was seen. Additionally, the laser-written graphitic column contains regions of lattice damage that propagate from the main core structure in [110] directions. These can be seen as the lattice giving way under the buildup of localized pressure along weaker (111) cleavage planes that intersect with the (110) facets. Their irregularity is quite consistent and most of them are of a few hundred nanometres in size, which is below the optical diffraction limit. However, these nanostructures were spaced out close to each other thus the whole graphitic column appeared as a continuous wire when imaged optically.

When a stationary laser spot is focused below the diamond surface, an opaque material begins to spontaneously propagate through the diamond towards the laser [140]. Raman microscopy revealed that this opaque material exhibits a G peak (1580 cm^{-1}), which is characteristic of graphite [141]. As the laser focus moves steadily through the crystal toward the radiation source, the graphitization wave can continue indefinitely, allowing the creation of graphitic wires of any length [101], [142]. These wires are often described as series of distinct wave fronts that overlap enough to support electrical conductivity. The wavefront pattern arises because the volume expansion needed to convert diamond into graphite is restrained by buildup of pressure, which is only relieved when the laser moves to a less pressured area of the crystal. This pattern of wave fronts has been observed in earlier studies and resembles the backbone structure seen under the pulse repetition rate 1kHz (PRR-1k) condition (see figure 4.43).

Another example was also examined with high resolution microscopy. Figure 4.44 reveals the internal microstructure of laser-fabricated column at 1 MHz of pulse repetition rate. Compared to what was presented above, cross-sectional TEM images revealed a totally different structural modification when the laser pulse repetition rate was increased by a factor of 1000. Figure 4.44 showed that there is no connected conductive pathway, only lots of small dots of sp^2 bonded material that are not linked to each other.

The results discussed above provide insight into the electrical properties of the laser-written wires. For wires generated under pulse repetition rate of 1 kHz, the IV characteristics exhibit ohmic behavior, indicating that electrical conduction occurs symmetrically in both positive and negative charge directions with the same resistance. TEM images reveal that, rather than forming a single continuous wire, a complex array of nanocarbon networks

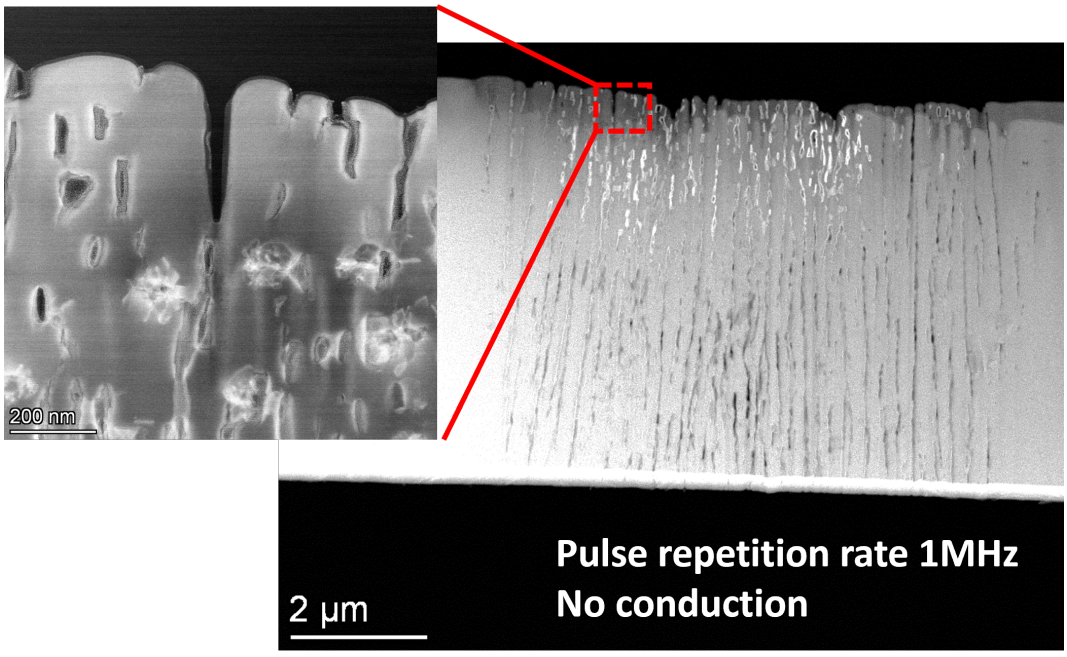

FIGURE 4.44: Cross-sectional TEM image of a graphitic wire laser-written at 1 MHz in the diamond bulk. A spaced out series of sp^2 spots appeared not linked to each other, resulting in no electrical charcteristics.

(NCNs) is produced. These networks were broad enough to be interconnected and contained both graphite-like and graphene-like areas [92], whose presence explained the observed ohmic conductivity. However, under pulse repetition rate of 1 MHz (PRR-1M) conditions the energy delivered to the system is too big to support graphitisation, resulting in formation of a series of disconnected damaged regions. In case of overwriting a PRR-1k wire with PRR-1M (designated PRR-1k1M), the nanocarbon structures characteristic of PRR-1k were also observed in the subsurface region on the laser writing initiation side, but no graphite-like structures were detected deeper within the overwritten structure. Moreover, the resulting junction-like electrical properties were consistently reproducible across multiple locations on the sample as well as on other samples. Even though, a stable 3D junction has been laser fabricated, a further study is still required to understand described mechanisms.

4.9 Conclusions

The direct laser writing enabled fabrication of graphitic structures on both the surface and below the surface of diamond, which were shown to demonstrate ohmic conductivity. An all-carbon device structure was introduced to allow straightforward testing of electrical properties for pairs of laser written graphitic columns without any additional post-processing, e.g. metallization. The method was verified by comparison with results when the sample was coated with silver paint on one surface to provide data from individual graphitic columns. It was shown how the laser parameters used influence the resistance of the laser-written columns, which is important to minimize for novel diamond electrical devices. At the optimized laser-writing environment, graphitic wires exhibited ohmic conduction. Although, these graphitic structures were examined by Raman spectroscopy, it was not a stable characterisation technique for these particular cases, because their results have not been repeatable. The optical analysis form the top view has confirmed presence of modified structures within the sample, however, no notable distinction was observed between the structures created with a single laser pass and those that were overwritten. Optical imaging from the side has revealed more information about graphitic columns laser written at different repetition rates, showing that structures fabricated at low repetition rate were not continous and those fabricated at very high repetition rate were continuous but blurred. It was demonstrated, that the fabrication window is very narrow with respect to pulse repetition rate. Thus, the dose was crucial. Moreover, TEM analyses have revealed more information about features present in the laser modified regions. It has explained why the structures generated with 1 MHz do not conduct but exhibit graphitic content within modified areas. Presumably, higher power pushed fabrication further from the laser

focal volume resulting in worse conversion from diamond to graphite. Nevertheless, TEM was a complex analytical approach and provided details only about the surface region. Therefore, this study creates a good base knowledge and understanding for future fabrication of graphitic electrodes and diamond-based devices that find application in various areas.

Chapter 5

Advanced writing concepts

5.1 Introduction

This chapter introduces the ideas of advanced laser writing of graphitic wires inside the CVD diamond. Based on the all-carbon device, another prototype was fabricated. This approach consists of laser fabication of graphitic columns at a repetition rate of 1 kHz and then overwriting them with an additional laser-beam pass at 1 MHz repetition rate. The overwritten areas were distributed in the area of choice along graphitic columnsand some whole columns were overwritten. Interesting electrical properties were characterised for overwritten structures. Moreover, the optimisation techniques for even more time-efficient fabrication was studied. The parallelisation idea relies on simultaneous fabrication of a number of graphitic wires. This experiment investigates the scenarios of both sequential and holographic laser writing of graphitic columns. Arrays of graphitic columns examined in this study consist of two-by-two columns matrix to six-by-six columns matrix.

5.2 Overwriting graphitic wires

Taking the idea of an all-carbon device (see figure 4.11) another approach has been established. It is seen in Chapter 4 that the laser writing of the graphitic columns is very sensitive to laser pulse repetition rate, which gives inspiration for the new device design. This design consists of areas that were laser fabricated first at pulse repetition rate of 1 kHz to be conductive and with additional laser pass at the repetition rate of 1 MHz, which normally gives no conduction.

For the experiment, the graphitic columns were laser machined in a high-purity single-crystal diamond using the PHAROS laser system described in Chapter 3. The laser was focused down to a spot size of 1 µm on the rear side of the diamond to initialise the graphitic column, the substrate then was translated downward along the optical axis (within [100] crystal orientation) to complete laser writing through the wafer. Here, the laser pulse energy of 120 nJ and sample translation speed of 10 µm/s were kept constant. As seen in Chapter 4, the pulse repetition rate (PRR) was a critical factor determining the electrical characteristics of the laser- written graphitic structures. The fabrication process consisted of three different regimes with different choice of repetition rates, namely 1 kHz and 1 MHz. They are described as PRR-1k (single column written at pulse repetition rate of 1 kHz), PRR-1M (single column written at pulse repetition rate of 1 MHz) and PRR-1k1M (single column written first at pulse repetition rate of 1 kHz, then overwritten with 1 MHz).

Figure 5.1 shows transmission microscope images of the various wires imaged at the top surface. Laser-written cross hairs can be seen in figure, and were processed on the surface of the diamond for accurately aligning the wire for subsequent analysis in TEM (as described in Chapter 4). From the

top view, there is little obvious difference between the laser-written wires in different regimes. It was already discussed that the graphitic columns show different electrical conduction properties. However, the optical images of the column's 'head' are similar, with a column diameter of 5 to 6 µm. Dimensions of the diameter of laser-induced graphitic columns were significantly larger than the focused laser spot (1 µm in diameter).

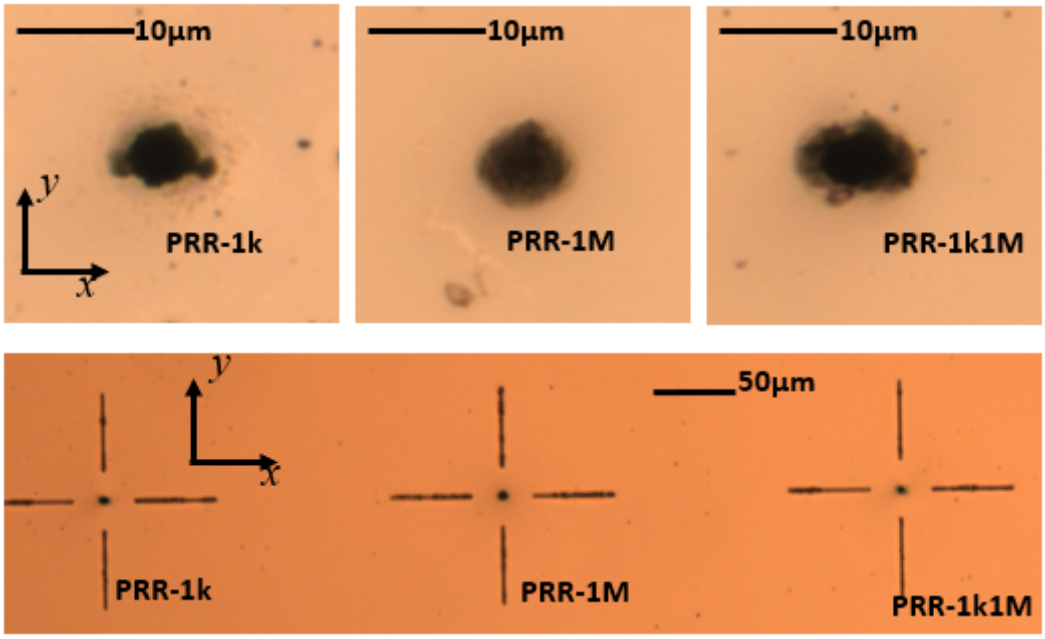

FIGURE 5.1: Optical micrographs showing the initiating side of each graphitic column.

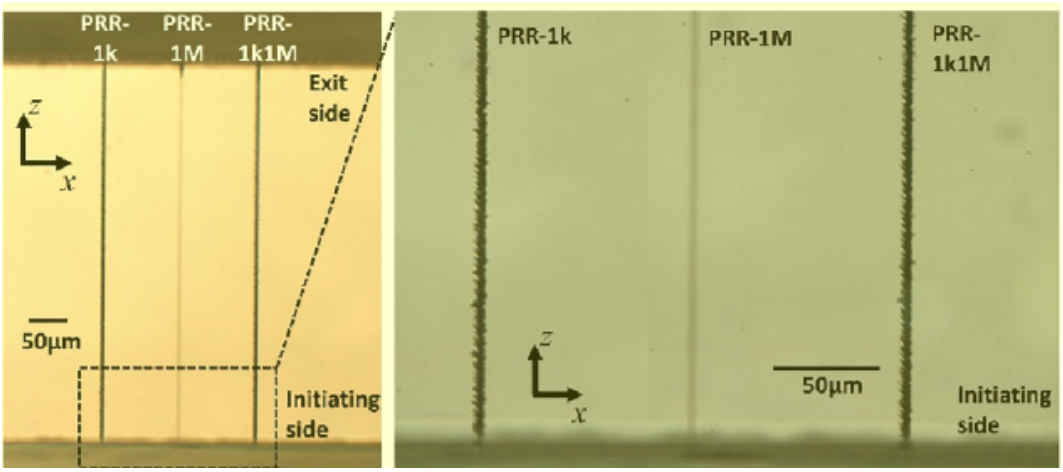

FIGURE 5.2: Optical micrographs of cross-section of graphitic wires laser-written through the thickness of the single-crystal diamond plate.

Figure 5.2 shows the microscopic images of the same laser-written graphitic structures viewed from the side of the single-crystal diamond sample (through the polished surface) that were generated using different fabrication conditions. The differences in structural modification are now clearly observed. Only those columns that were laser written firstly with repetition rate of 1 kHz show graphitic content within the microstructure. The laser written column at PRR-1M is optically distinct, being lighter in colour and smoother, compared with the latter two. However, optically, the structure with overwrite PRR -1k1M looks very similar to that without PRR-1k.

Additionally, the electrical analysis was performed for three different laser writing regimes. First samples were coated with layers of titanium, platinum and gold to give ohmic conduction connection to the laser written wires. The metal was then patterned, as seen in figure 5.3, to give connection to single wires. The metallisation work was done through collaboration with Callum Henderson at University College London.

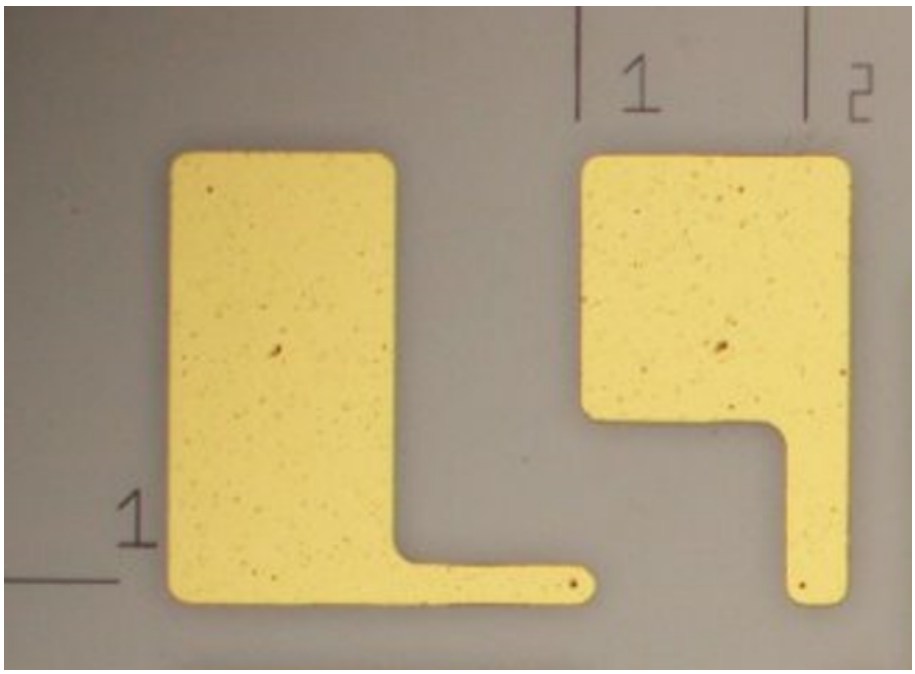

FIGURE 5.3: Optical micrographs showing the initiating side of each graphitic column after metallisation.

Figure 5.4 shows current voltage relationships for the PRR-1k and PRR-1M scenarios. Ohmic behaviour is seen for the graphitic column fabricated with PRR-1k, however, in case of PRR-1M fabrication, the structure became insulating. This is consistent with findings presented in Chapter 4. Furthermore, the hybrid configuration was generated by initially forming the graphitic column with a single pass of the laser at 1 kHz PRR and then overwriting it at 1 MHz PRR. As a result, semiconducting properties were obtained and showed a diode-like behaviour, which is depicted in figure 5.5. An asymmetric barrier potential was formed, i.e. it conducts at voltages greater than +25 V but does not conduct at all up to -80 V. This is very unusual and exciting behaviour for an all-carbon device.

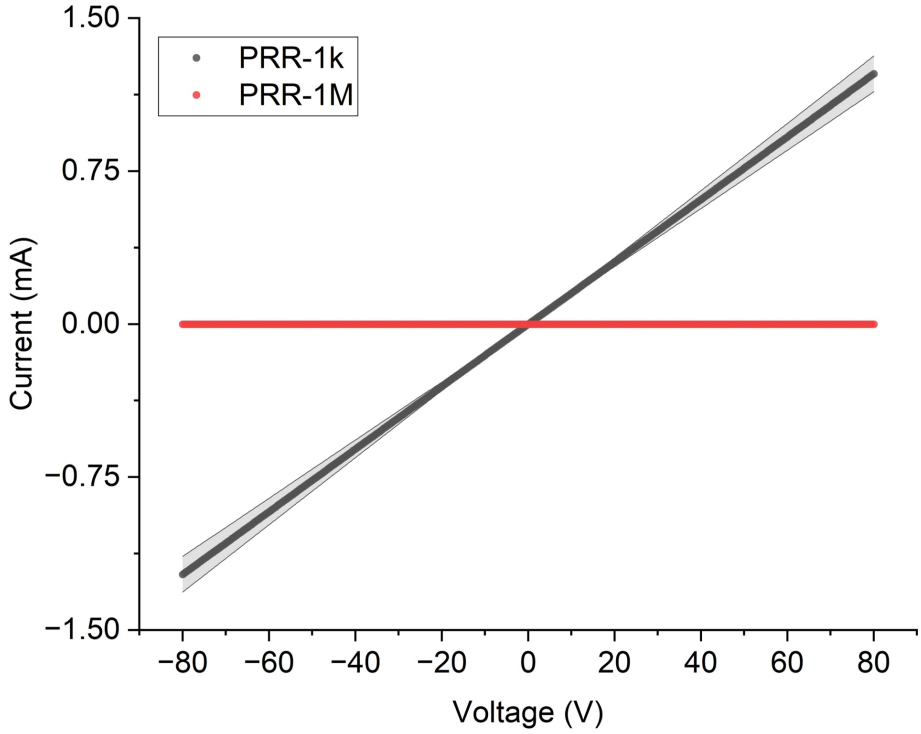

FIGURE 5.4: Current-voltage relationships for graphitic columns depending on the laser pulse repetition rate used for fabrication, PRR-1k and PRR-1M. Ohmic conduction is seen for PRR-1k while insulating characteristics are observed for PRR-1 M example. Figure courtesy of Callum Henderson, UCL.

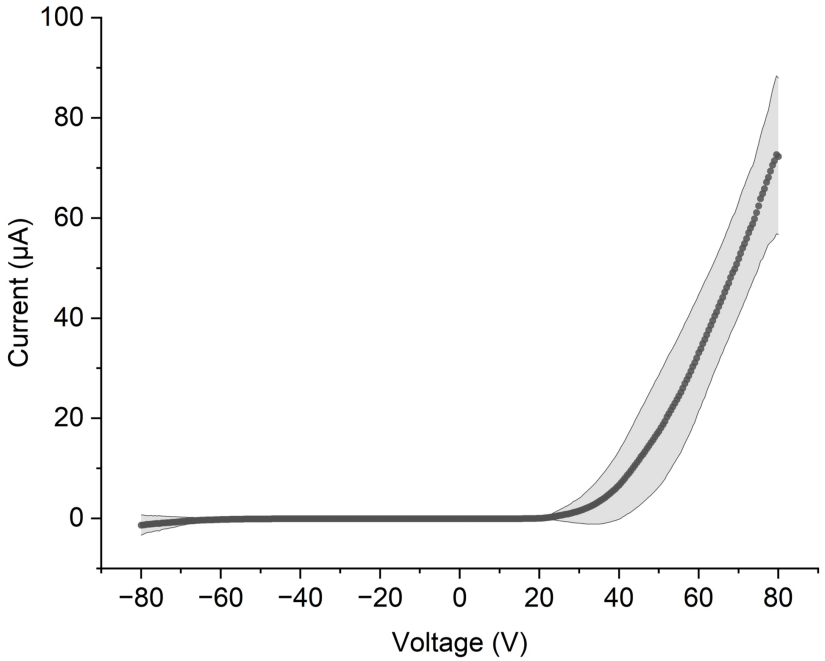

FIGURE 5.5: Nonlinear diode-like behaviou seen for a hybrid laser write strategy, where the graphitic columns were initially formed with a PRR of 1 kHz and then overwritten at 1 MHz (PRR-1k1M). igure courtesy of Callum Henderson, UCL.

It was found that the order of the overwrite is important. If the graphitic wire was firstly generated at 1 MHz and then overwritten with at 1 kHz, the resulting structure did not conduct at all. Even though the other wires were generated at PRR-1k and PRR-1k1M, respectively, they seemed optically indistinguishable (Figure 5.2). Therefore, the imaging at higher spatial resolution is necessary to investigate the characteristics of the generated modifications to try to see why they lead to different electrical behaviour. This was done via transmission electron microscopy in Ref [92]. It was found that asymmetry in the breakdown of the diamond lattice based on process direction could maybe explain asymmetry in conduction. Furthermore, it was seen that the ordering of the graphite layers next to the diamond interface was different compared to the PRR-1k scenario. This is the subject of further work to understand the exciting underlying reason for unusual conduction characteristics.

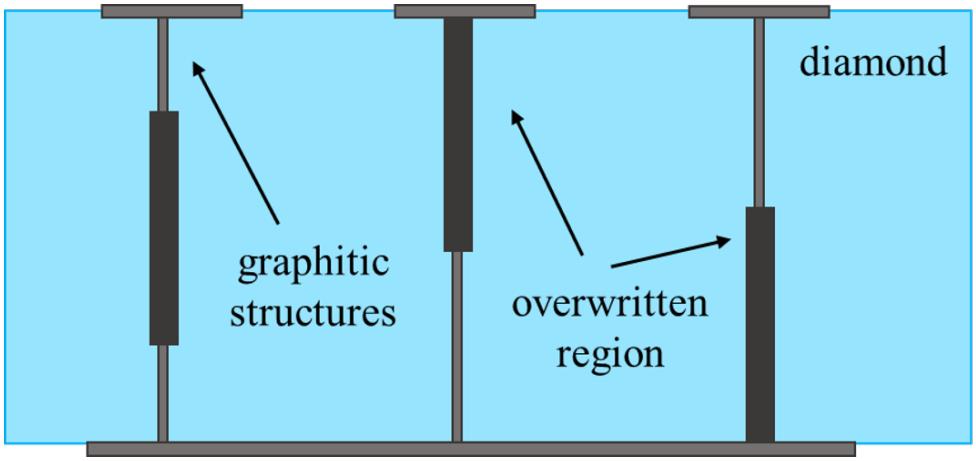

FIGURE 5.6: Schematic diagram of graphitic columns overwritten at the chosen regions.

A further study was devised to explore the origin of the asymmetric barrier potential. Figure 5.6 introduces a schematic diagram of this idea. In general, the architecture of the new device stays the same as for all-carbon devices, with the only difference being that, here, some of the areas of graphitic wire are overwritten with an additional laser-fabrication scan. In this case, devices consisted of two columns per row and there were five rows fabricated (see figure 5.7).

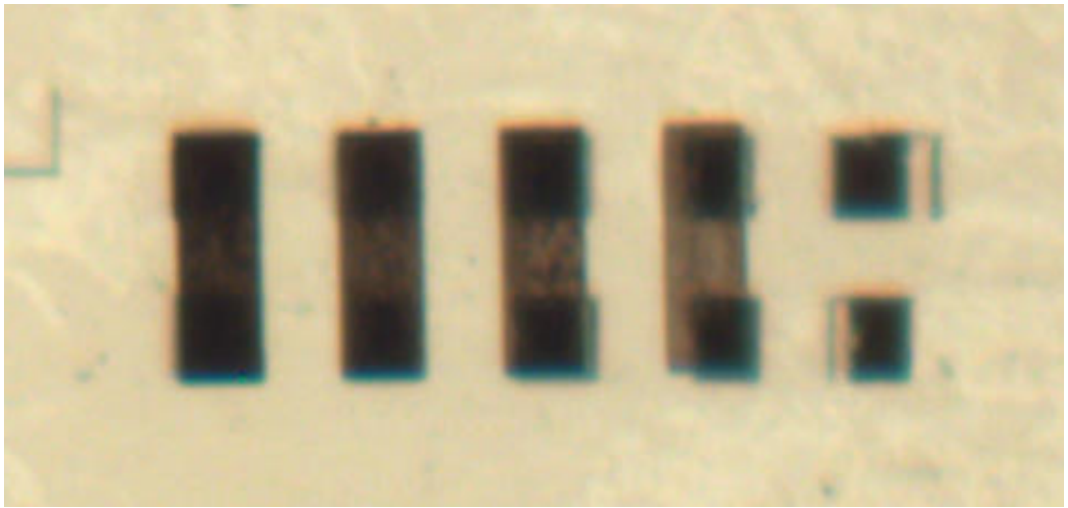

FIGURE 5.7: Microscopic image of laser-written graphitic columns with overwritten elements, here covered with graphitic contact pads. This design consists of five pairs of columns.

All five pairs were first laser written with single scan with pulse repetition rate of 1 kHz, translation speed of 10 µm/s at pulse energy of 255

nJ. Rows 2 to 5 consisted of graphitic columns with overwritten elements. The whole columns were overwritten in row number 2. Halves of graphitic columns in row 3 were overwritten, from the focus point at the rear side of the diamond sample toward the middle of the column. Row number four also consist of graphitic wires that were overwritten in half, here from the middle of the column towards the top side. Graphitic columns in row number five were overwritten in the middle, here the laser was focused at one quarter of the wire length from the rear side of the diamond. It is worth highlighting that the overwriting scan was conducted from the bottom of the diamond sample towards the top side of the sample. There was only one scan applied for each fabrication idea. The reason for the study was to examine whether the origin of the asymmetric barrier potential is related to the surface or bulk effects, and whether there is difference for the seed and exit side of the wire.

5.3 Holographic writing

This research presents a way of optimizing the laser-writing procedure of graphitic columns. It has already been demonstrated that the conductive properties of graphitic column can be tailored with respect to laser-processing parameters. However, all these results were presented for sequential laser writing of graphitic columns, namely single column by column. An alternative approach could be laser writting of several columns simultaneously. Figure 5.8 presents a schematic diagram of this idea and the microscopic image of laser fabricated columns from the top view. In order to have multiple columns laser written simultaneously, a holographic mask has been implemented to the laser-processing system (see figures 5.9 and 5.10). This enables many columns to be written at the same time to speed up fabrication process and think about scaling for larger devices.

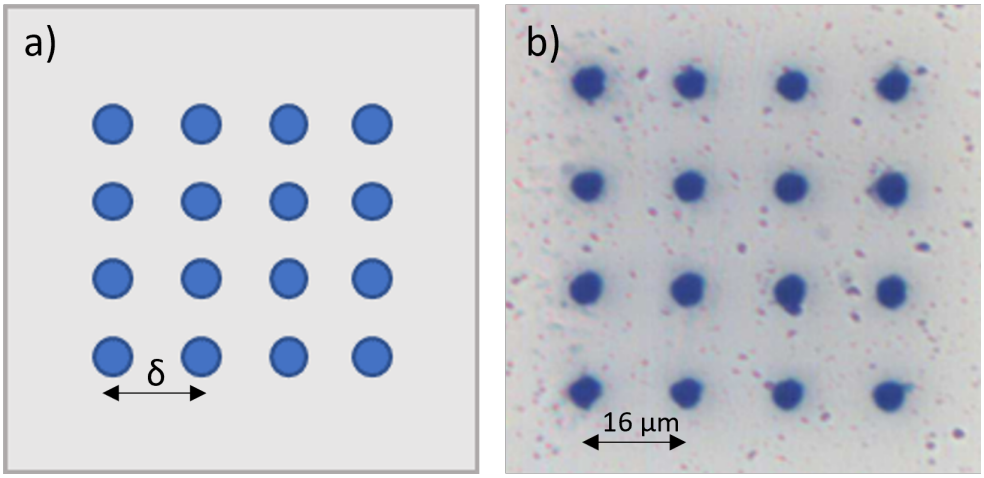

FIGURE 5.8: a) Schematic diagram of holographic approach to laser writing of graphitic columns. Here, δ is the distance between the graphitic columns, which is kept constant within the matrix. Scenarios with variable distances between columns have been fabricated. b) Microscopic image of laser-fabricated graphitic wires (top view). Distance between the columns in this matrix equals 16 µm.

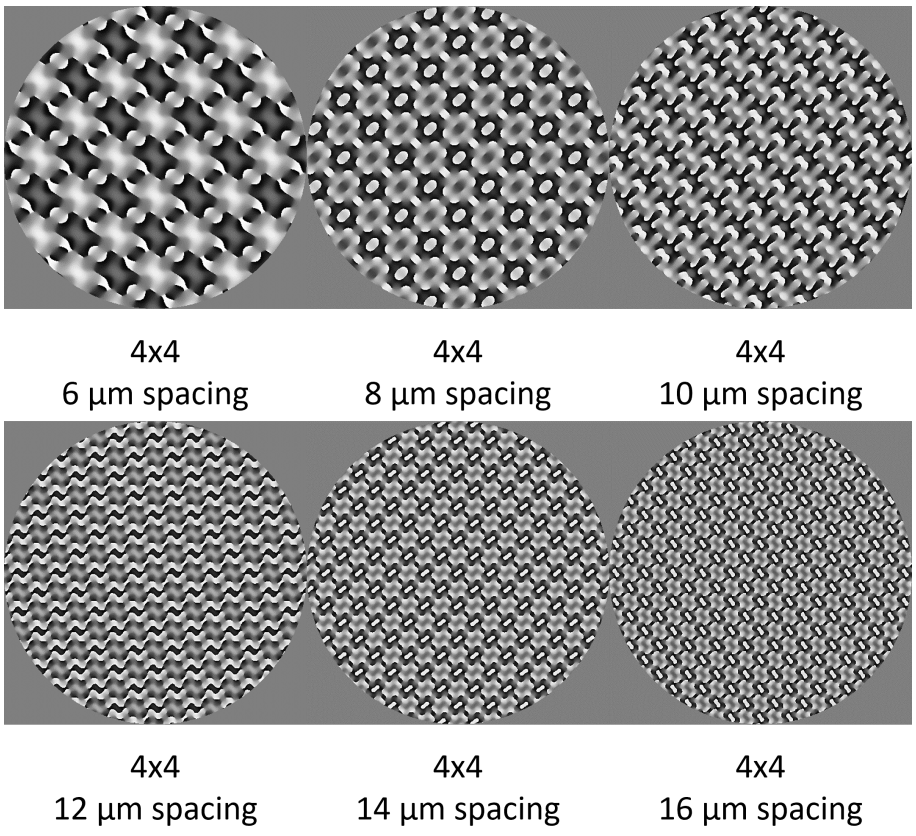

FIGURE 5.9: Example of a holographic mask applied to a liquid-crystal spatial-light modulator with respect to spacing, 4×4 refers to a matrix of columns to be laser written, in this case it was 16 columns.

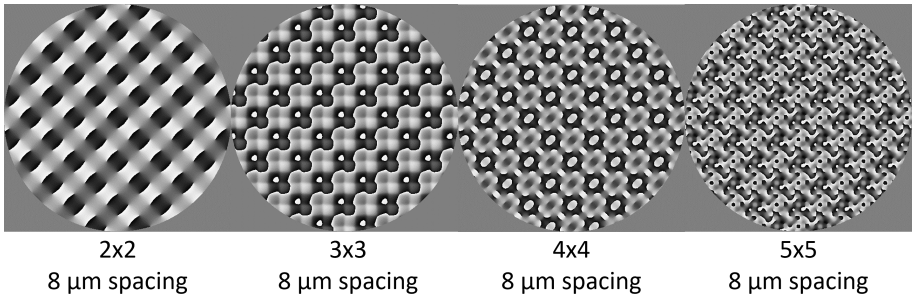

FIGURE 5.10: Example of a holographic mask applied to liquid crystal spatial light modulator with the same spacing of 8 µm but different column arrays, for example 2×2, 3×3, 4×4, 5×5.

An adaptive hologram displayed on a liquid-crystal spatial-light modulator enabled simultaneous fabrication of multiple graphitic wires and correction for aberrations associated with refraction at the air-diamond interface [125]. As a result, arrays of graphitic columns were laser written with a single scan through the thickness of the diamond, which optimized their fabrication time. Holograms displayed on the SLM were generated using a weighted Gerchberg-Saxton algorithm [143]. Different holograms were generated for a square lattice of 2×2, 3×3, 4×4, 5×5, and 6×6 foci. The aim of this research was to explore how the device performance scaled with the degree of parallelisation. Supplementary holograms were generated for a 4×4 lattice of points with different spot spacing δ from 6 µm to 16 µm. Additionally, the spherical aberrations were continuously updated during fabrication based on feedback from the vertical translation stage.

Electrically conductive graphitic columns were laser written through wafers of single crystal CVD diamond with a thickness of 300 µm (Element Six, nitrogen content < 1 ppm) using the Solstice laser fabrication system (see Chapter 3).

This study shows results of two different fabrication scenarios, namely structures fabricated with a single laser focus and with a focal array for parallel fabrication. Graphitic columns were laser written following the scheme

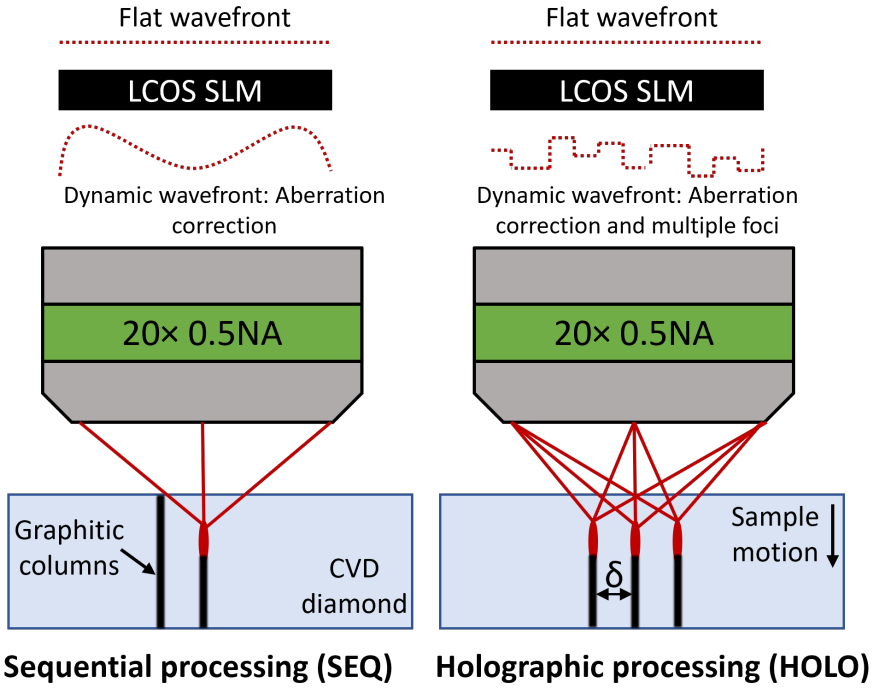

FIGURE 5.11: Schematic of laser-writing procedure of graphitic columns through the thickness of a diamond wafer. The laser wavefront was modulated by a SLM to correct for aberrations induced by refraction at the diamond surface or to additionally generate multiple foci.

depicted in Figure 5.11, which shows a schematic diagram of the laser-writing procedure used in both sequential (SEQ) and multi-spot fabrication (HOLO). Here, the laser was initially focused on the rear surface of the diamond wafer to seed the graphitic column. The diamond sample was then translated vertically down at a constant speed of 10 µm/s to build the graphite up through the thickness of the wafer. Arrays of columns were generated with the multi foci generated by the hologram. Additionally, an identical array was then generated using a single laser focus which fabricated each column consecutively. Arrays were fabricated at two different laser pulse energies (either 200 nJ or 400 nJ per focus) were used to fabricate the arrays. This means that, for example, for a 2×2 holographic array the total pulse energy was either 800 nJ or 1600 nJ. Figure 5.12 presents microscopic image of single-crystal diamond sample with laser written graphitic columns (top view).

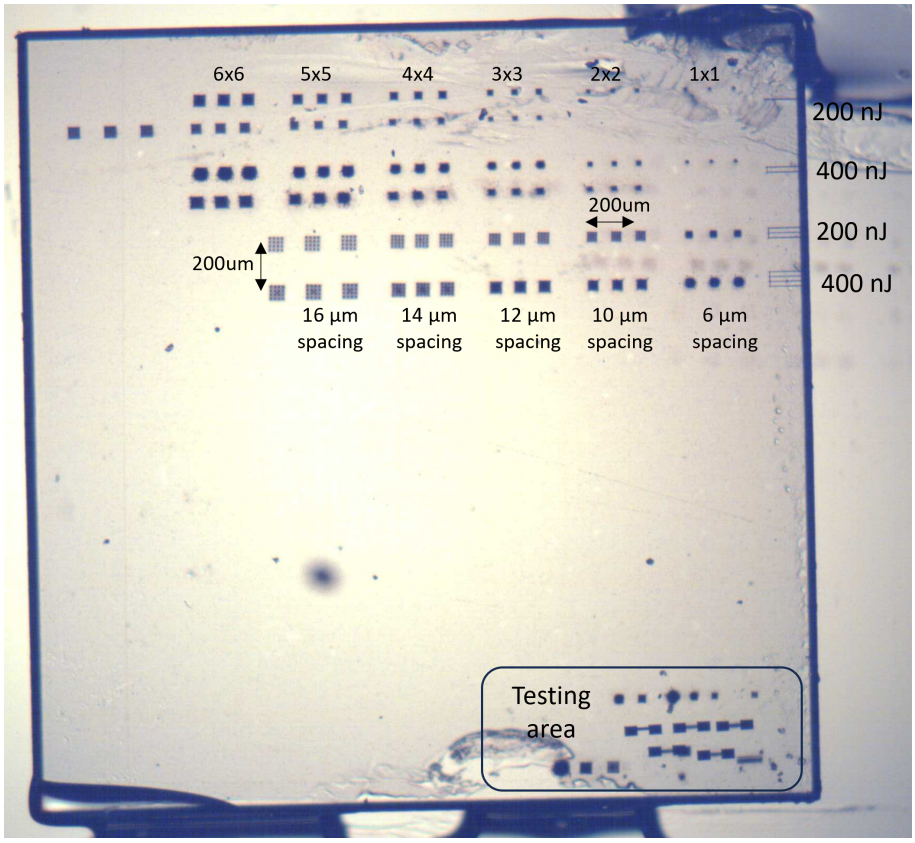

FIGURE 5.12: Microscopic image of the graphitic wires fabricated both sequentially and holographically at two different laser pulse energies (200 nJ and 400 nJ). From the top: first and third rows were written in a single scan using hologram, second and fourth rows were written with single spot generating each column in the array sequentially. Single columns were only fabricated in first and third rows. First four rows present different size spot arrays at fixed spot spacing (2×2, 3×3, 4×4, 5×5 and 6×6), whereas rows five and six show 4×4 hologram array with different spot spacings (from 6 μm to 16 μm). Right bottom corner includes the testing area.

Transmission microscopy was used to examine the laser-written graphitic structures. Figure 5.13 depicts exemplary microscopic images of laser written arrays of 3×3, 4×4 and 5×5 columns generated in two different manners. Interestingly, arrays of graphitic columns fabricated sequentially and holographically differ in image. It was observed that at small spacing distances and due to high power, cracks started to occur in case of sequential fabrication (see figure 5.13 b) and 5.13 c)). This occurrence could be related to high stress induced during the laser-writing process of short-spaced arrays of graphitic columns.

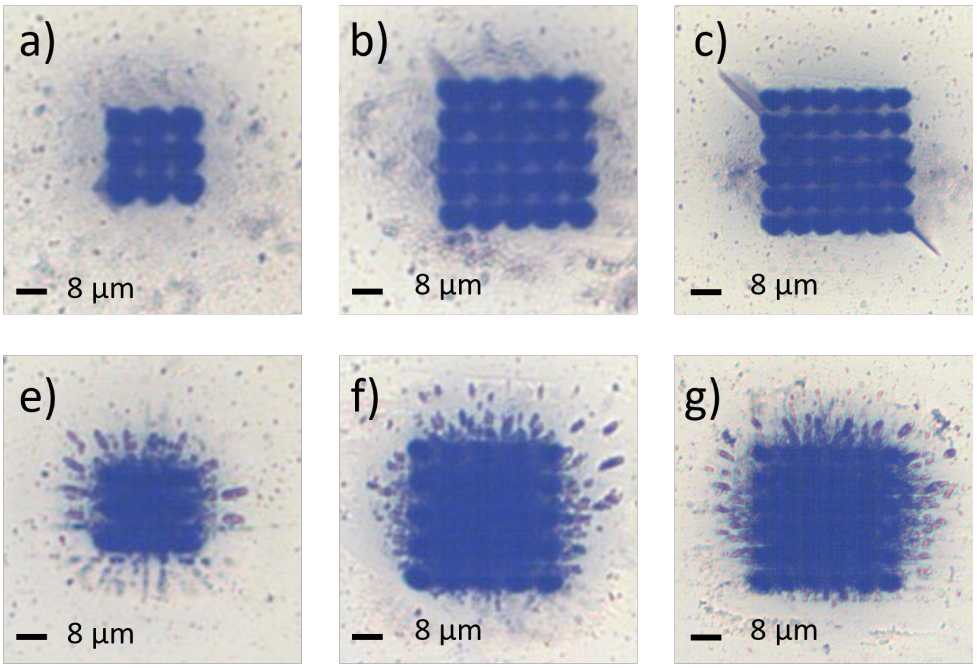

FIGURE 5.13: Example microscopic images of graphitic wires fabricated both sequentially (a, b, c) and holographically (e, f, g). All arrays were fabricated at 400 nJ. Spacing of all arrays is the same and equals 8 µm.

Moreover, images were also taken on a polarising optical microscope to investigate strain-induced birefringence within the sample. Figure 5.14 depicts crossed-polar images of chosen arrays of laser-written graphitic columns. The level of birefringence depicted on theseimages can be used to estimate the ress induced in the diamond sample due to the graphitisation process [144], [145]. Significant stress was noticed for all of the arrays. However, images indicate that more stress is present arround the SEQ arrays in comparison with the equivalent HOLO arrays. This can suggest a greater lattice disruption and introduction of more sp^2-bonded material, resulting in better conductivity for the SEQ laser-written columns.

After imaging, arrays of graphitic columns were covered by laser-written graphitic contact pads. This procedure enabled linking all the columns of the array. Figure 5.15 presents the diamond sample with generated graphitic contact pads.

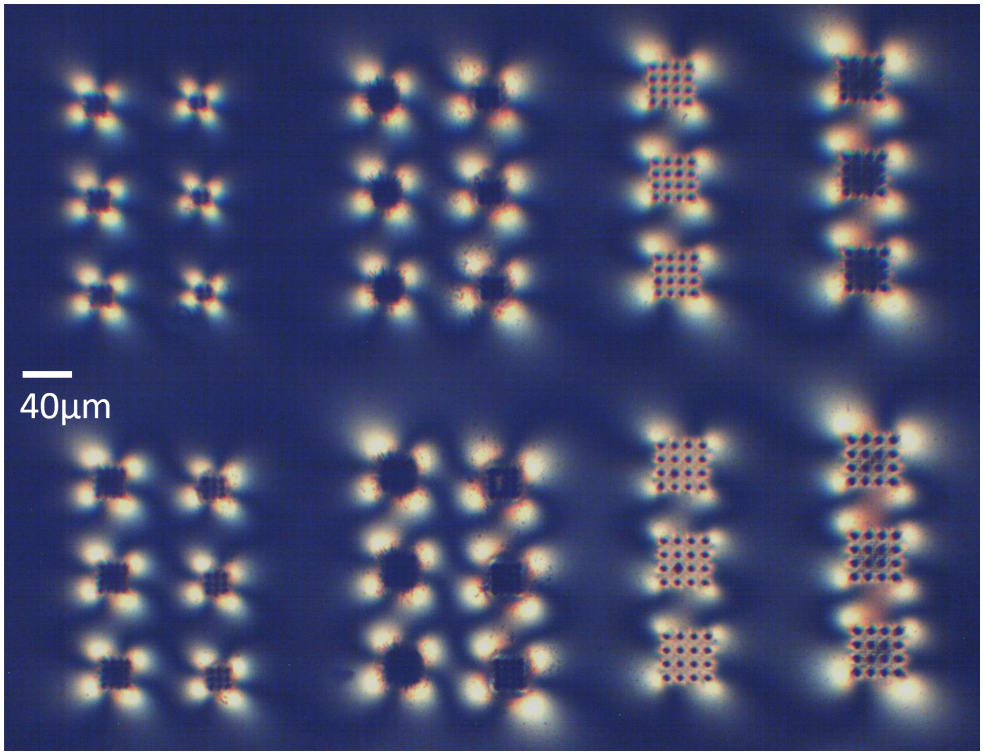

FIGURE 5.14: Example image of the graphitic columnar arrays taken by polarising optical microscope.

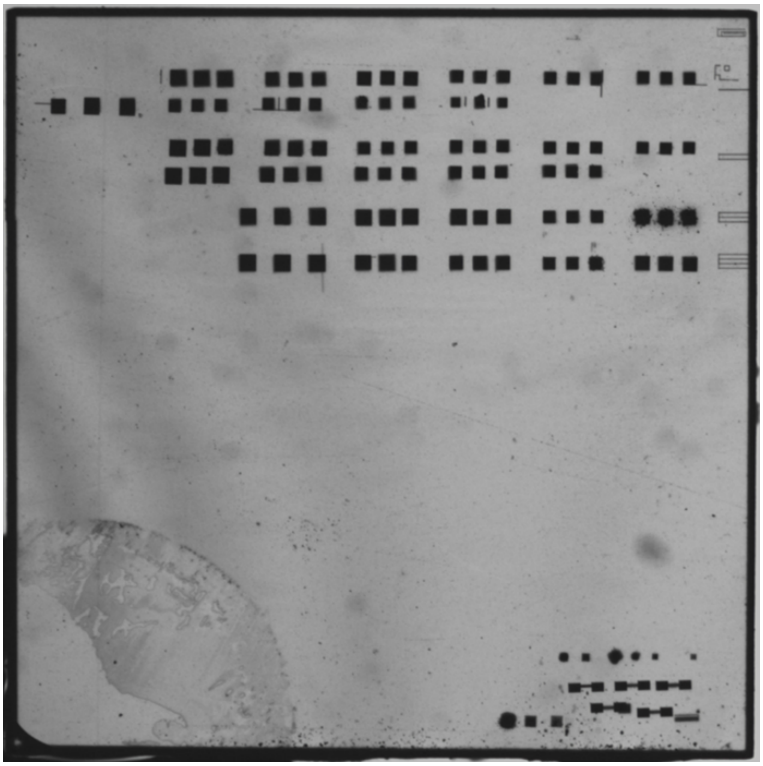

FIGURE 5.15: Microscopic image of columnar arrays of graphitic wires covered by graphitic contact pads. Here, dimensions of contact pads were adjusted to the dimensions of the arrays.

All contact pads were laser written on one of the diamond surfaces at pulse energy of 100 nJ, repetition rate of 10 kHz and translation speed of 30 µm/s. In order to characterize them electrically, the other surface of diamond was coated with silver paint (Agar G3691) to create a blanket electrode, which enabled direct measurements. Electrical testing of the dc current-voltage relationship of each array were taken by two-probe station measurement. Here, 10 µm tungsten tips were probe between a graphitic contact pad on the top surface and the silver electrode on the lower surface. A Keithley 2450 sourcemeter was used and all the measurements were taken between $\pm$50 V in 5 V steps.

The current-voltage relationships for arrays of different sizes fabricated holographically are depicted in figure 5.16. Figure 5.17 shows current-voltage relationships of arrays of different sizes fabricated sequentially. All arrays presented at figure 5.16 and 5.17 were generated at a laser pulse energy of 200 nJ per focus.

The current-voltage relationships for arrays of different sizes fabricated holographically are depicted in figure 5.18. Figure 5.19 shows current-voltage relationships of arrays of different sizes fabricated sequentially. All arrays presented at figure 5.18 and 5.19 were generated at a laser pulse energy of 400 nJ per focus.

It can be seen that for both fabrication methods, as the size of the focal array increases, the maximum current increases as well. It was expected as there is a greater number of conductive pathways in larger arrays. The current-voltage relationship is linear for all arrays, and indicates ohmic conduction. The sequentially fabricated arrays were observed to perform better, presenting higher maximum current when compared with the equivalent holographic array. It was also noted that in HOLO case, the maximum

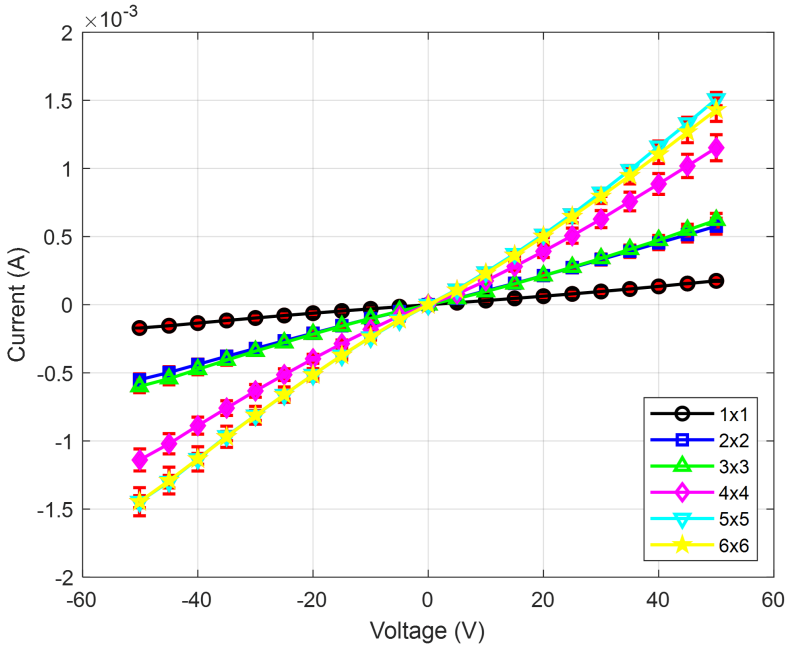

FIGURE 5.16: Current-voltage relationships from the laser-written graphitic columnar arrays, for different array sizes. The laser-write pulse energy was 200 nJ per focus. Here, the arrays were laser written in a single scan of the sample using a holographically generated focal array.

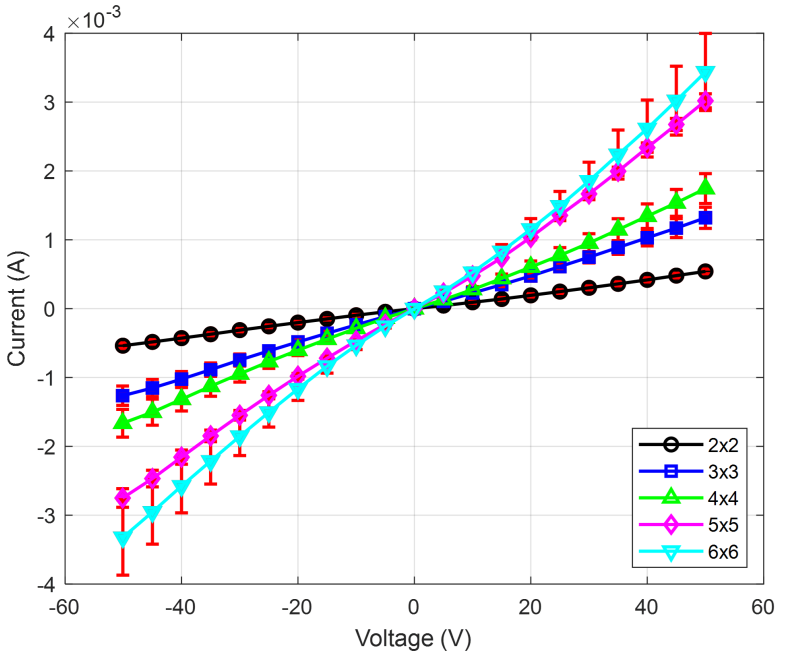

FIGURE 5.17: Current-voltage relationships from the laser-written graphitic columnar arrays, for different array sizes. The laser-write pulse energy was 200 nJ per focus. Here, the arrays were laser written sequentially, i.e. a single focus was used to write each column in the array.

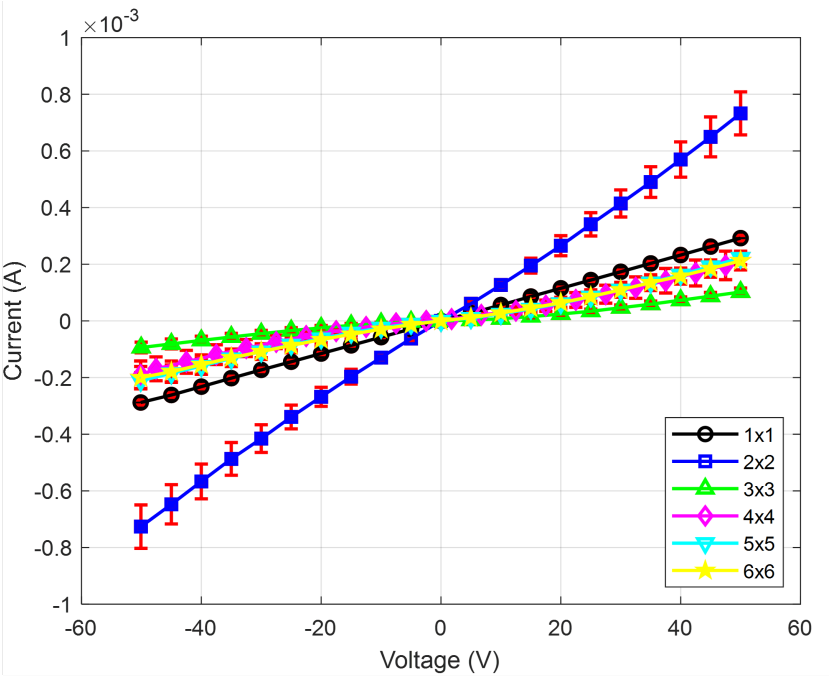

FIGURE 5.18: Current-voltage relationships from the laser-written graphitic columnar arrays, for different array sizes. The laser-write pulse energy was 400 nJ per focus. Here, the arrays were laser written in a single scan of the sample using a holographically generated focal array.

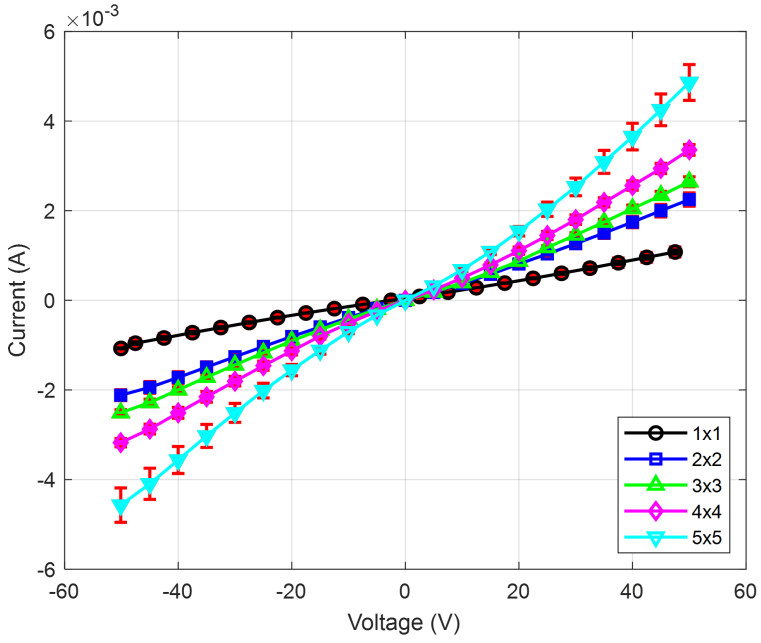

FIGURE 5.19: Current-voltage relationships from the laser-written graphitic columnar arrays, for different array sizes. The laser-write pulse energy was 400 nJ per focus. Here, the arrays were laser written sequentially, i.e. a single focus was used to write each column in the array.

current does not always increase with an increase in the array size. For example, 2×2, 3×3 arrays are similar while the 5×5 array appears to show more conductivity than the 6×6 array.

For the fabrication with laser pulse energy of 400 nJ per focus, there is a difference in behaviour between the HOLO and SEQ processing methods (see figure 5.18 and figure 5.19. The current-voltage relationship for the SEQ arrays exhibits the same tendency as those at lower pulse energy, where maximum current increases along with the size. However, for the HOLO arrays, whilst the 2×2 array displays an improvement in conductivity, all other arrays show maximum current lower than of just a single column (1×1), despite being written with a total pulse energy that is raised by as much as an order of magnitude and supposedly a much higher graphitic cross-section. Moreover, the HOLO arrays bigger than 2×2 exhibit a current that is no longer purely linear with applied voltage and symptomatic of a symmetric barrier potential [135] (see figure 5.20).

Resistance values were extracted from the I-V plots from Figures 5.16, 5.17, 5.18 and 5.20 by using a basic linear fit to the data. Three separate devices were fabricated for each setting and repeat measurements were taken to establish error bars. For arrays exhibiting a barrier potential (only those fabricated with 400 nJ HOLO), resistance values were ascertained by a linear fit to data points outside of the barrier voltage window (see figure 5.21).

Figure 5.22 shows the effective total resistance of each array while figure 5.23 plots the average resistance per column for each array. It was shown that for 200 nJ HOLO arrays it was possible to reduce the resistance of the vertical graphitic columns using a holographic fabrication process. Even though these resistances drop, they are not at the same level as for arrays written sequentially. However, the fabrication is done within a single scan and hence

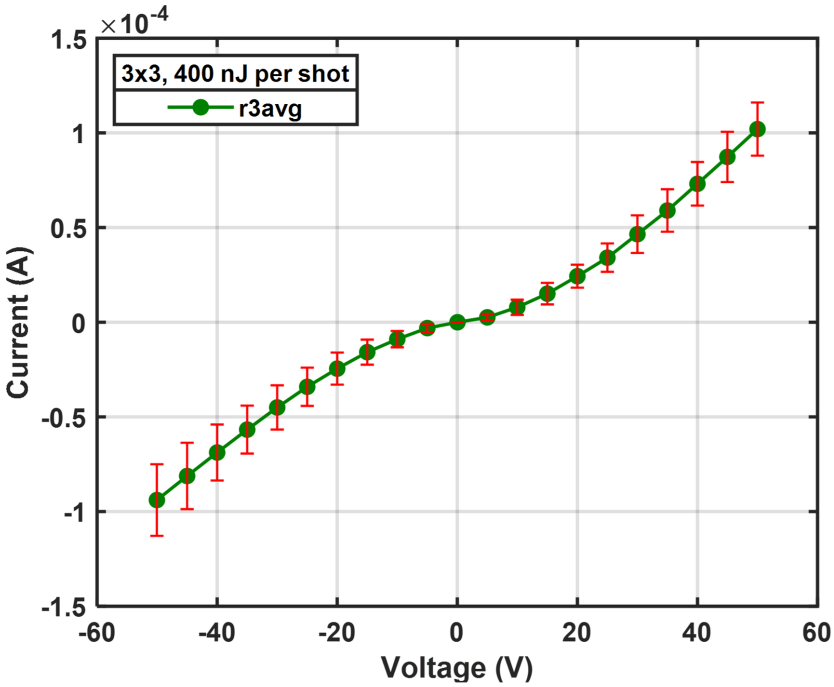

FIGURE 5.20: Current-voltage relationships from the laser-written graphitic columnar 3×3 array. The laser-write pulse-energy was 400 nJ per focus. Here, the arrays were laser written in a single scan of the sample using holographically generated focal array.

the processing time be significantly reduced. The holographic technique has some limitations, for example for the higher pulse energy of 400 nJ per focus the fabrication breaks down and produced results are inferior to those with a single scan and single focus. This method of fabrication was highly repeatable with small error bars (less than 5%) for the resistance. However, the holographic fabrication at 400 nJ was much more variable, indicating problems with the holographic processing at higher pulse energies. Nevertheless, by appropriate choice of pulse energy and array size, the holographic technique allowed fabrication of highly conductive structures with reduced processing time.

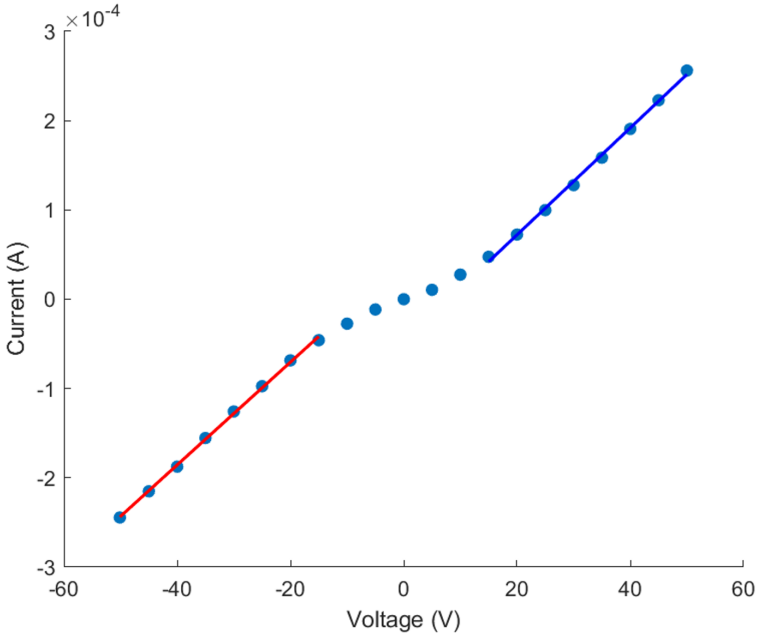

FIGURE 5.21: Current-voltage relationships from the laser-written graphitic columnar 4×4 array. The laser-write pulse-energy was 400 nJ per focus. Here, the arrays were laser written in a single scan of the sample using holographically generated focal array. Basic fit was applied to the first and last 8 data points. The resistance of the first 8 data points (red line) equals 173.5 kΩ and of the last 8 data points equals 166.9 kΩ. As a result the averaged resistance equals 170.3 kΩ.

It was analysed that the average resistance per column in an array seemed to always grow with the array size, regardless of the fabrication technique (see figure 5.23). For the sequential laser fabrication, this could be related to a growing amplitude aberration. Here, existing graphitic columns may disturb part of the laser focus cone for the other columns in an array (see Figures 5.24 and 5.25). Moreover, graphitic structures generate a compressive stress in the surrounding diamond, which may affect laser writing process as the latter graphitic structures were fabricated in pre-stressed material. The average resistance per column rises more rapidly as a function of array size for the holographic process, even though the amplitude aberrations were considered negligible in this case. Nevertheless, there may still be effects associated with stress-accumulation in the diamond, although these

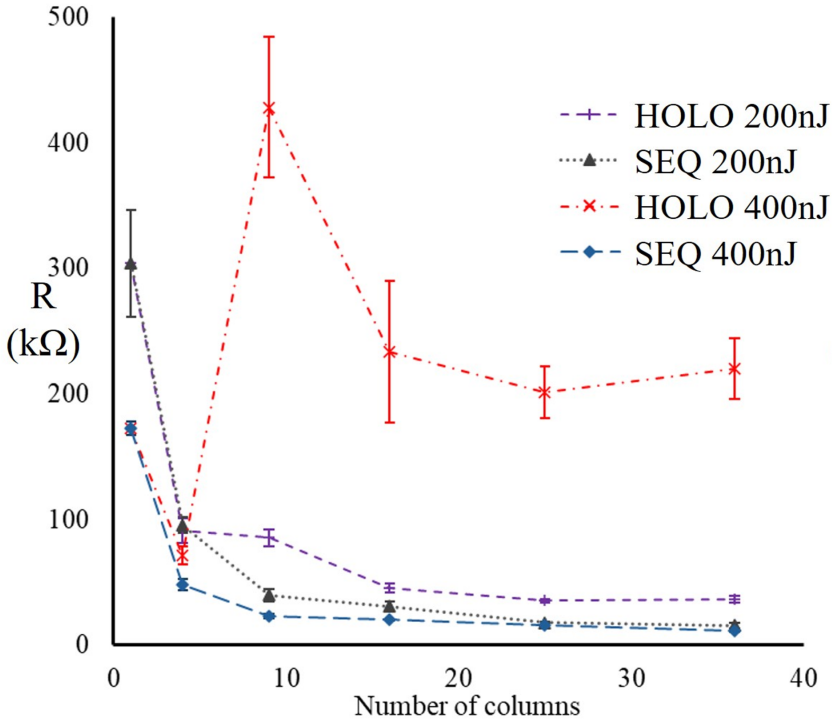

FIGURE 5.22: Different array resistance as a function of column spacing. Graphitic columns were laser written at pulse energies of 200 nJ and 400 nJ.

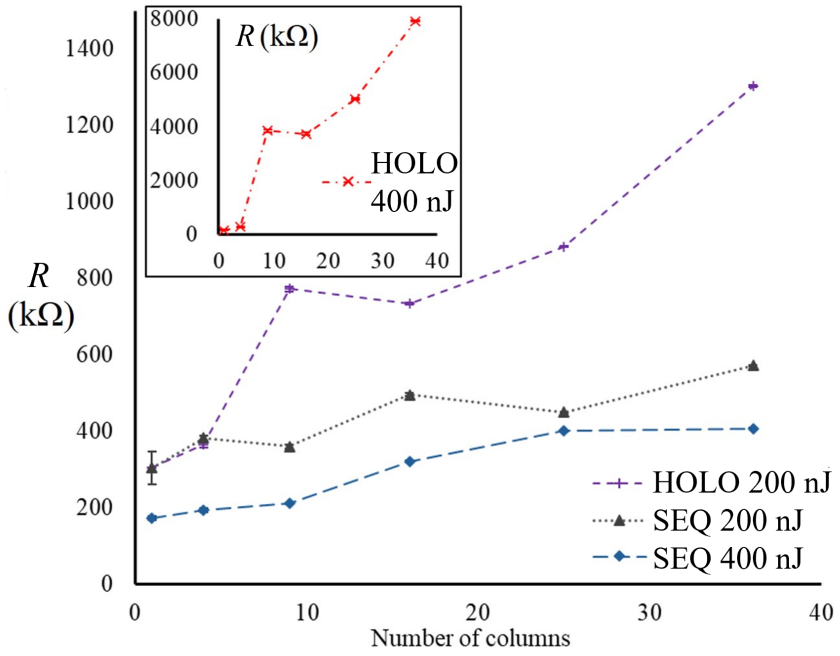

FIGURE 5.23: The average resistance per column in each array as a function of number of columns, for both holographic and sequential fabrication.

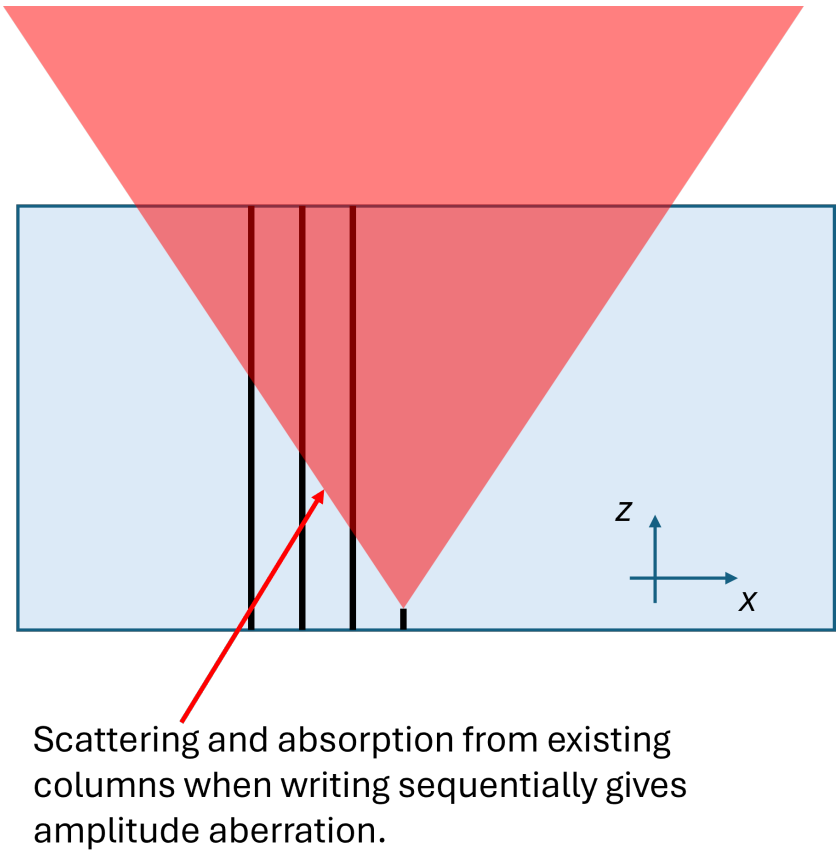

FIGURE 5.24: Amplitude aberration arising from sequential laser writing of closely spaced graphitic columns.

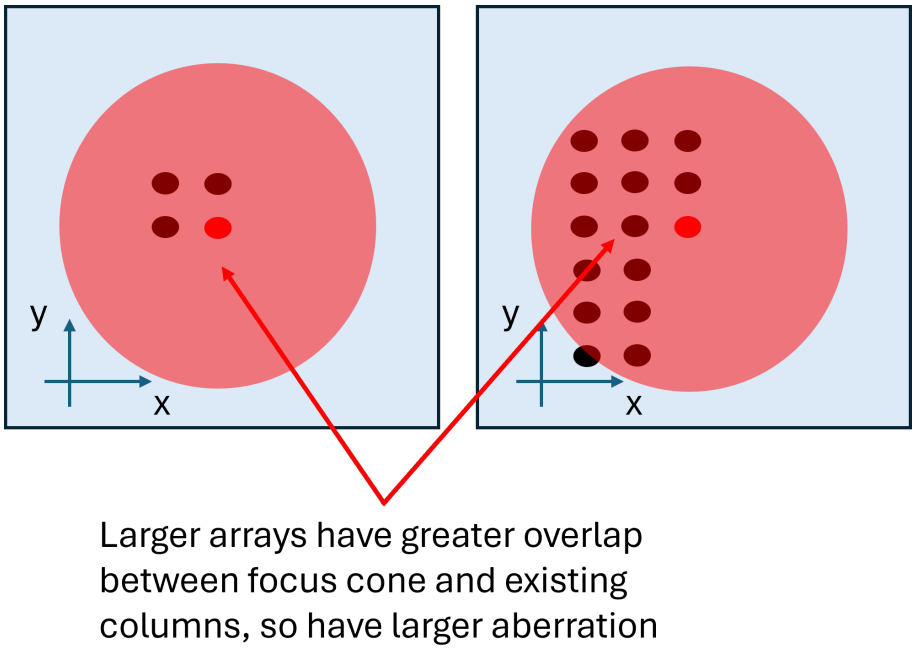

FIGURE 5.25: The amplitude aberration in SEQ laser writing becomes worse for larger arrays of graphitic columns.

would be slightly different in nature than for the sequential fabrication process. Another aspect was that it was more likely that, as the array size increased, the hologram became less efficient at distributing the laser energy to the focal array and resulting in increasing non-uniformity across the array, which impedes the fidelity of the laser-induced graphitisation. This is supported by analysis of transmission microscope images of the arrays (see figure 5.29). Here, the SEQ arrays showed clear definition of the columns in the array. In case of holographically written arrays there is much evidence of surface graphitisation between column locations confirming the existence and influence of the stray light. Especially, at the higher pulse energy of 400 nJ per focus, this stray light disturbed the laser fabrication of the graphitic columns near the top surface of the diamond, resulting in increase of resistance per column and development of a barrier potential.

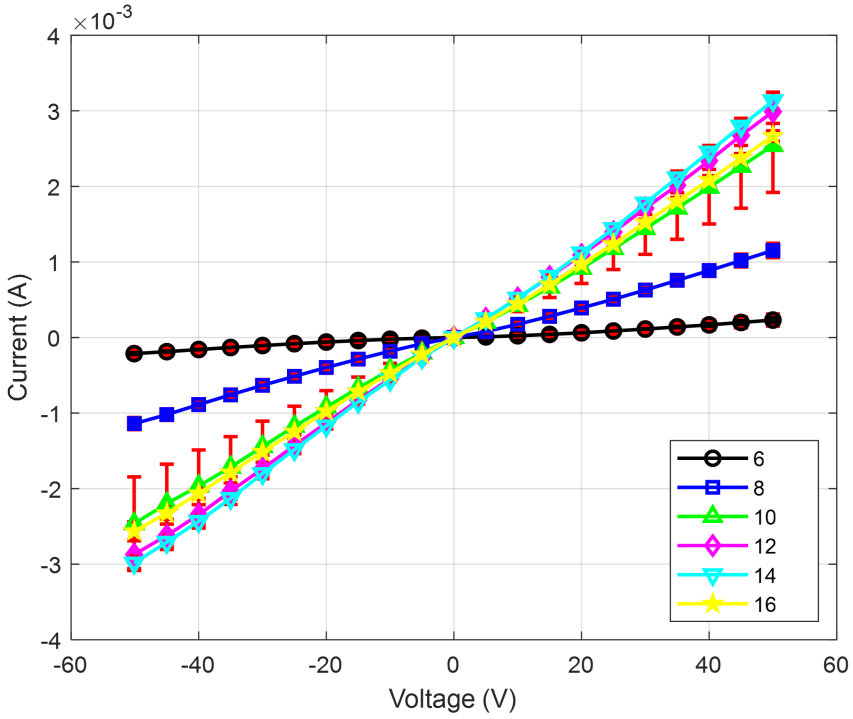

FIGURE 5.26: Current-voltage relationships from the laser-written graphitic columnar 4×4 arrays at different spot spacings, varied from 6 µm to 16 µm. The laser-write pulse-energy was 200 nJ per focus. Here, the arrays were laser written in a single scan of the sample using holographically generated focal array.

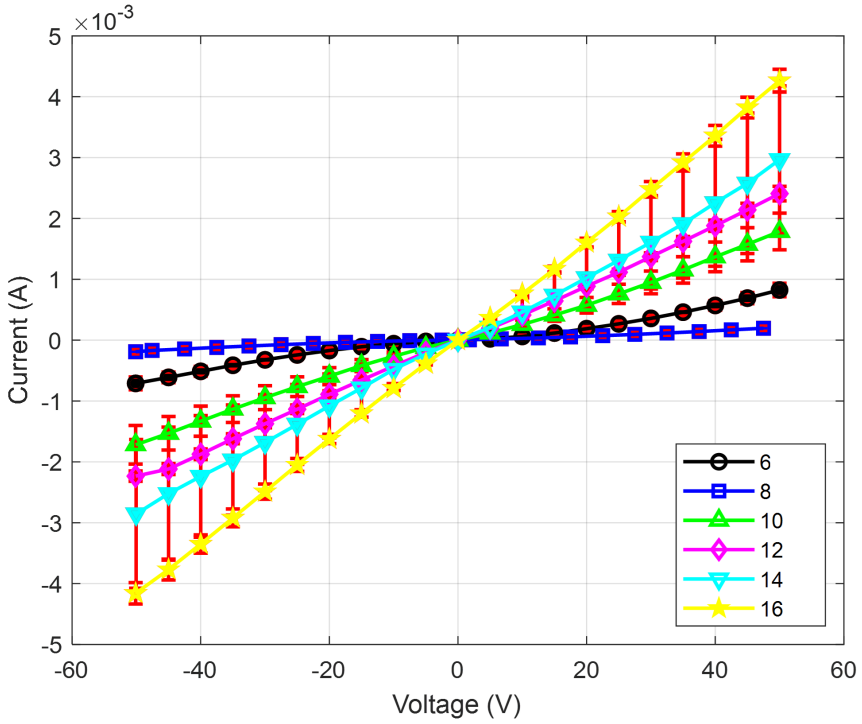

FIGURE 5.27: Current-voltage relationships from the laser-written graphitic columnar 4×4 arrays at different spot spacings, varied from 6 µm to 16 µm. The laser-write pulse-energy was 400 nJ per focus. Here, the arrays were laser written in a single scan of the sample using holographically generated focal array.

The influence of the spot spacing in a focal array when implementing holographic processing was also studied. Figure 5.26 and figure 5.27 present the current-voltage relationships for pulse energies of 200 nJ and 400 nJ, respectively. Both figures present plots for a range of different 4x4 arrays with varied centre-to-centre spacings, from 6 µm to 16 µm. For smaller column spacing, e.g. 6 µm, the current-voltage relationship is not linear. In this case, the IV curve indicates a barrier potential and reduced maximum current. For column spacings above 10 µm, the current-voltage relationship becomes linear and the maximum current increased. In general, the current-voltage characteristics are independent of the column spacing at higher separations, which is expected since there is the same number of columns and the same pulse energy per column. This is clearly presented in figure 5.28 where the overall array resistances approach a uniform value at larger spacing.

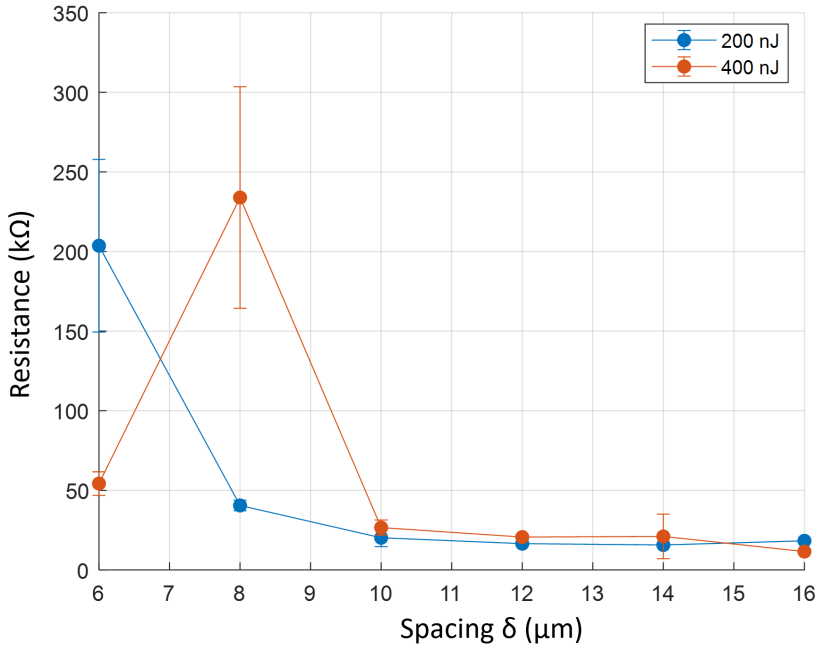

FIGURE 5.28: Different array resistance as a function of column spacing. Graphitic columns were laser written at pulse energies of 200 nJ and 400 nJ.

Figure 5.29 presents transmission microscope images of arrays with different spacing between columns. It was noticed that individual columns cannot be clearly distinguished in arrays with small spot separationsf 6 µm. The cross-talk between the fabrication process may have resulted in poor electrical performance. On the other hand, at higher spacings, each graphitic column was well defined and there was a corresponding improvement in electrical conduction (see figure 5.28).

It was also observed that the choice of columnar spacing might depend on the pulse energy. For instance, there was still some evidence of cross-talk in the optical processing for the 400 nJ 16 µm array which did not occur in the 200 nJ counterpart. Furthermore, a column spacing of 8 µm appeared problematic for fabrication at a laser pulse energy of 400 nJ but not 200 nJ per focus. Due to the limited diffraction efficiency of the SLM for high-spatial-frequency phase patterns and the broadband nature of the ultrashort laser pulses, it was not possible to examine larger column spacings [146].

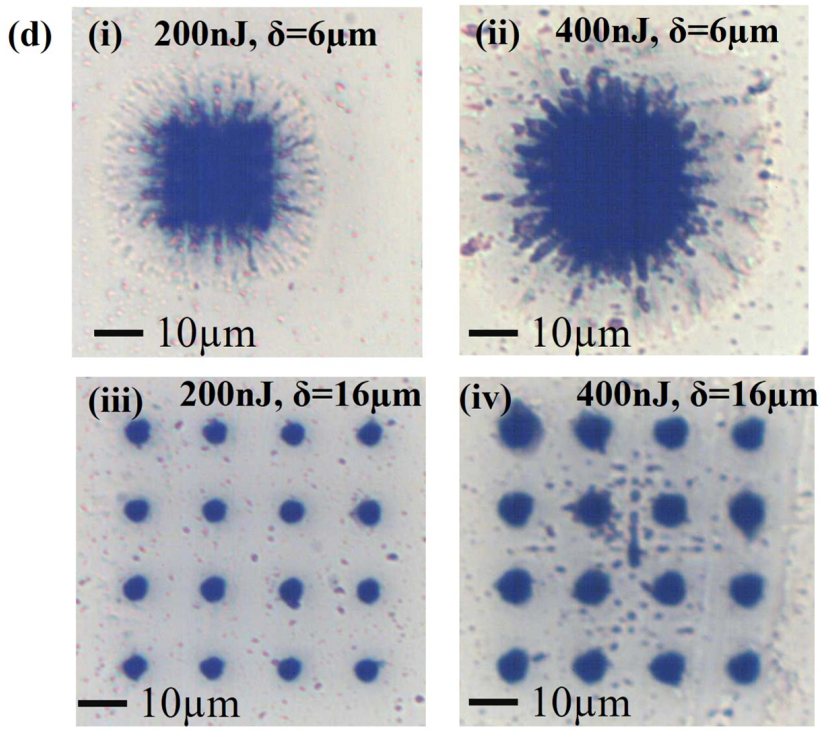

FIGURE 5.29: Microscopic images of graphitic column arrays with different spacing.

5.4 Conclusions

This chapter summarizes the advanced techniques used in laser fabrication and characterization of novel diamond devices.

The first part described the overwriting technique and discussed its potential application in fabrication of diodes. Both optical and electrical examination has revealed different properties of graphitic structures that were laser written under different processing conditions. The current voltage relationship of graphitic wires laser-written at PRR-1k exhibited an ohnmic behaviour, the PRR-1M proved the structure to insulating and the overwritten column (PRR-1k1M) presented a diode-like behaviour. The ability to laser write conductive, semiconductive and insulating 3D wires within a diamond substrate was demonstrated, and showed the potential for all-carbon systems for electronics and other types of devices. However, there is still further

study required to understand the complexity of these processes.

The second part of the study focused on the use of holographic laser processing to reduce the fabrication time of conductive graphitic columns in diamond wafers. It was discussed that the laser-processing time could be shortened by parallelizing the process through the use of computer-generated holograms, which create multiple focal points from a single lens, allowing different parts of the device to be fabricated simultaneously. Additionally, the study found that the choice of spot spacing, array size, and laser-ulse energy significantly affects device performance. The results were compared to traditional sequential processing, showing that by carefully optimizing these design parameters, highly conductive graphitic structures can be produced in a shorter time. The current-voltage relationship of both scenarios has expressed the ohmic behaviour, and the calculated resistance had linear tendency in both cases, where the resistance values were similar. Although multi-spot fabrication had been previously studied conceptually, this work demonstrated its practical application in device manufacturing. The findings have potential implications for improving laser processing in diamond and other material devices.

Chapter 6

Birefringence and stress analysis

6.1 Introduction

In its pure form, diamond is optically isotropic and not birefringent. However, strain in diamond induced by impurities makes the structure anisotropic and birefringent [147]. Laser-writing technology precisely introduces structure modifications that lead to stress in the diamond crystal structure and result in a change of refractive index. Sometimes, transformations of the material generate stress fields that modify diamond's properties. The stress fields formed due to laser graphitisation can be used to create optical waveguides inside the diamond [111]. Moreover, direct laser-writing procedures enable fabrication of graphitic wires within the diamond. These graphitic modifications are used to enhance electronic diamond devices, and the analysis of stress generated in the sample could possibly provide more information about the quality of the laser-written microstructures. Thus, this chapter focuses on characterisation techniques of stress induced by laser processing.

6.1.1 Diamond sample

Laser writing of microstructures inside a diamond sample not only modifies the diamond crystal structure but also induces stress in the surrounding diamond during the graphitisation process. These characteristics can be used to enhance the properties of novel graphitic devices, for example waveguides. In order to investigate the properties of birefringence as a result of stress-accumulated in the diamond, sets of graphitic columns were laser written in a single-crystal diamond wafer. The whole sample consists of series of laser-written vertical microstructures (see figure 3.3) of different lengths. The purpose of structuring the sample this way was to divide the sample with respect to different sets of parameters (see figure 6.1), including the length of the modification, pulse energy and optical elements, and observe their impact on the final outcome of laser machining. In order to analyse birefringence, a couple of sets of various subsections were selected, which are presented in figure 6.2. The imaging was performed accordingly.

6.2 Imaging techniques

The stress analysis relies on analysis of polarimetric images that reveal birefringence of the microfabricated structures. Once the changes in the refractive index are known, it would be possible to estimate the stress distribution. In this experiment, the optical properties of the sample were investigated by two types of polarimetry, namely Metripol polarimetry [148] and Mueller matrix polarimetry [149]. Metripol microscopy helps to obtain quantitative birefringent data in the form of images within a matter of seconds. This technique requires two parallel light faces to pass through the sample of a known thickness (d). The birefringent colours observed between crossed polarizers indicate the level of retardation. An exemplary image of diamond is shown

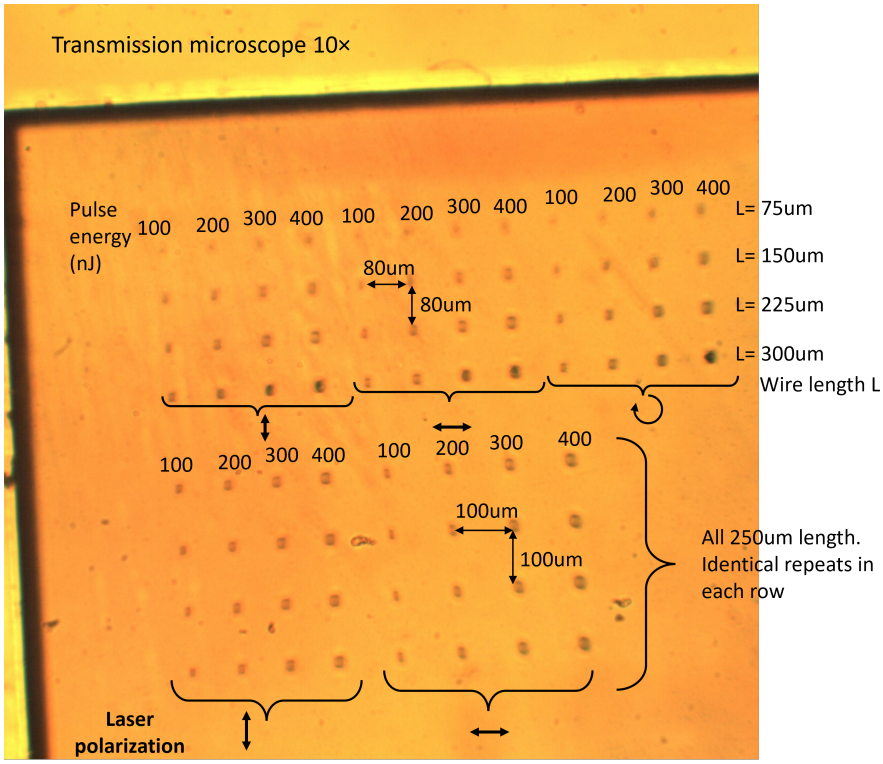

FIGURE 6.1: Transmission microscopic image of the laser-fabricated microstructures in one of the samples. L represent the length of the wire that varies along the subsections, from 75 µm to 300 µm. The laser-writing procedure was repeated for different laser pulse energies.

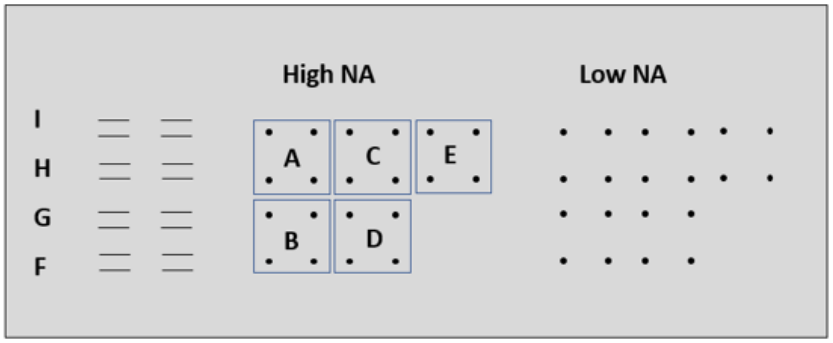

FIGURE 6.2: Illustration of the subsections of the investigated sample. Laser-written graphitic columns are present in sections A-E, and sections F-I consist of laser-written graphitic waveguides. Both high and low numerical apertures (NA) were used in this experiment.

in figure 6.3.

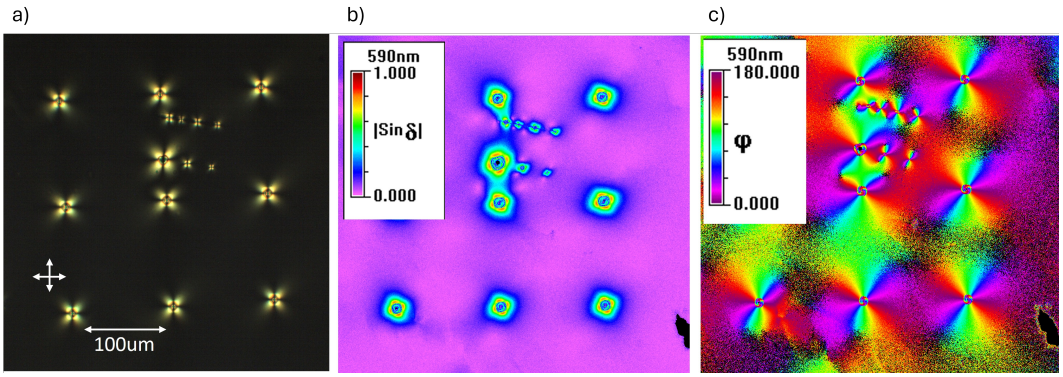

FIGURE 6.3: a) Diamond between crossed polarisers (as indicated by white arrows), where the colours indicate birefringence. The dark lines passing through each column are due to the orientation of the polarisers. Quantitative birefringent imaging techniques (like Metripol) give details on b) retardance and c) orientation, credit to Patrick Salter.

The phase shift of the light (η) is described by the equation below:

$$\eta = kd\delta n = \frac{2\pi}{\lambda}\delta nd \tag{6.1}$$

Here, λ length, d corresponds to the thickness of the sample, which establishes the path length of the birefringent material. The Metripol's signal output that is expressed sinusoidally, $|\sin(\eta)|$. The birefringence, which is the refractive index difference for orthogonal polarizations (Δn=n_e - n_o, where e refers to extraordinary and o refers to ordinary axis) generates phase retardance, described as (δnd). Here, the real part of the refractive index is described as a ratio of the speed of light in the investigated material and the speed of light of vacuum. The imaginary part of refractive index is described by the absorption coefficient in anisotropic materials, both the real and imaginary parts of refractive index depend on thevpolarization of light.

Mueller matrix microscopy is a technique for investigating anisotropic properties of the refractive index e.g. in biological tissues [147]. Figure 6.4 presents a schematic diagram of the polarimetric microscope built by Dr Chao He.

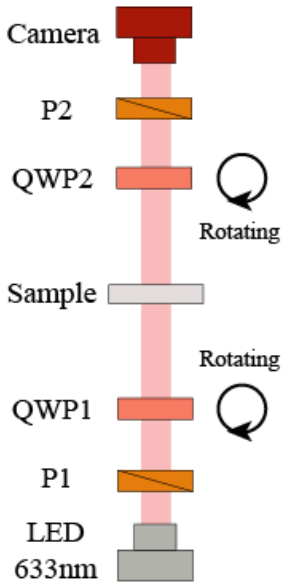

FIGURE 6.4: Schematic diagram of Mueller matrix microscope, here QWP stands for quater-waveplate, P is a polarizer, LED means light emitting diode, credit to Chao He.

Here, two quarter-wave plates (QWP1 and QWP2) rotate out of phase to each other. One rotates by every 6° and the other by every 30°. Once the sample is located on the stage, the position of the uarter-wave plates changes and the polarimetric images are taken. This technique uses multiple images, all together 30 images for each measurement, with illumination of varying polarisation to create a map of magnitude of retardance (η) and the fast-axis orientation at each point of the image. The process repeats with respect to the number of structures to be investigated. The birefringent images of the fabricated microstructures were taken using a birefringent imaging system. Stress distribution was estimated based on analysis of polarimeter images. Retardance is proportional to the birefringence that is proportional to the difference between principal stresses. The magnitude of birefringence in principal coordinates is:

$$\delta n = \frac{1}{2}(n_0^3 q_{iso}(\sigma_{max} - \sigma_{min})) \tag{6.2}$$

q_{iso} stands for piezo-optical coefficient, which for diamond equals 0.301 $\times$ 10^{-12} Pa^{-1} [148], σ_{max} is the maximal stress value, σ_{min} is the minimal stress value and n_0 is the refractive index of diamond. The polarimetry technique does not provide separate information on principal stresses, but the difference can be estimated by the following equation:

$$(\sigma_{max} - \sigma_{min}) = \frac{\lambda}{\pi d n_0^3 q_{iso}} \eta \tag{6.3}$$

The wavelength used for imaging was 633 nm, n_0 is the refractive index of diamond and d is the length of the laser fabricated wire. Although, this form of polarization imaging enables collection of information required for further stress analysis, it is still not complete. For example, the depth of field is unknown, which might result in a limited information of the laser written microstructure.

6.3 Stress-induced birefringence from graphitic structures

6.3.1 Polarimetric results for high and low NA

For the sake of stress analysis I have chosen examples that were fabricated with high (NA=1.4) (see figure 6.5) and low (NA=0.5) numerical aperture (see figure 6.6). Once the birefringent data were computed, it was interesting to see how the profiles of the retardance of the fabricated structures look. In order to obtain more information, the MATLAB R2020a software was developed to obtain the profiles of investigated quantities. Firstly, the birefringent images were generated, followed by choosing a desired microstructure, then the cross-sectional profiles were extracted. Every profile was extracted in a

clockwise manner and taken by every 10°. The results of the chosen samples are presented below.

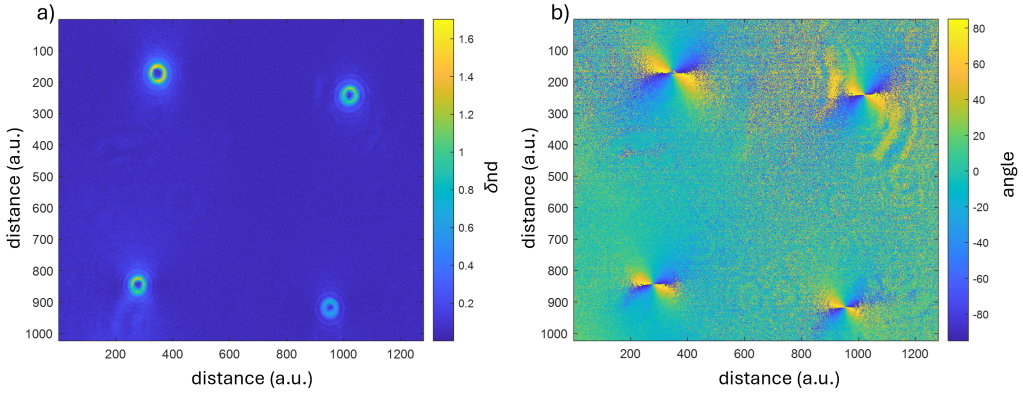

FIGURE 6.5: a) Birefringent image of microstructures written into diamond sample with high numerical aperture (1.4 NA). The top line consists of graphitic wires of length of 100 µm and the bottom-line wires have 75 µm. The left and right column were fabricated with 50 nJ and 25 nJ pulse energy, respectively. b) The orientation of the fast-axis of a radial distribution.

In general, there is a similarity in the results obtained for structures fabricated with both low and high numerical aperture. However, in case of laser fabrication with low NA aperture, the structures have the same forms but different diameter and higher value (see figure 6.6a). Figure 6.6b represents the fast axis orientation of a radial distribution. It is shown that the stress distribution around the wires is radial.

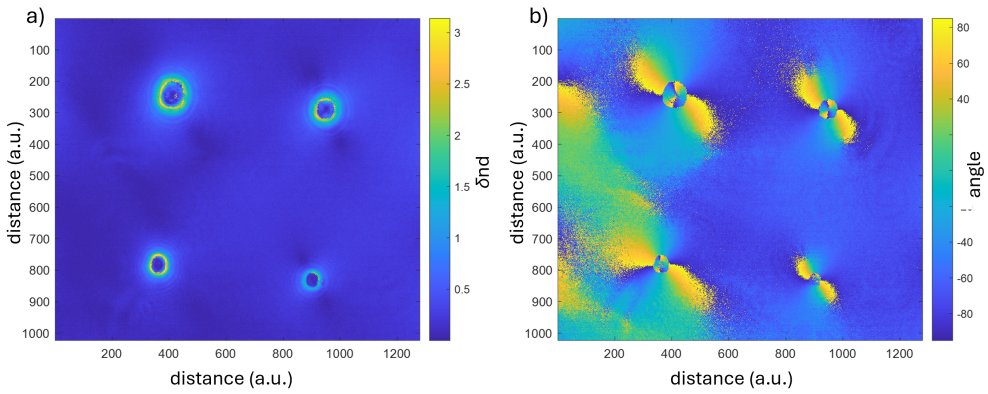

FIGURE 6.6: a) Birefringent image of microstructures written into diamond sample with low numerical aperature (0.5 NA). The bottom line consists of graphitic wires of length of 75 µm and the bottom-line wires have 150 µm. The left and right column was fabricated with 200 nJ and 100 nJ pulse energy, respectively. b) Orientation of the fast-axis of a radial distribution.

The retardance profiles and their average retardance profile are exhibited in figure 6.7 and figure 6.8. Here, the retardance data consist of data points taken at a radius of 7.5 µm, starting from the centre of the circle. Different profiles were taken in order to investigate the influence of various numerical aperature.

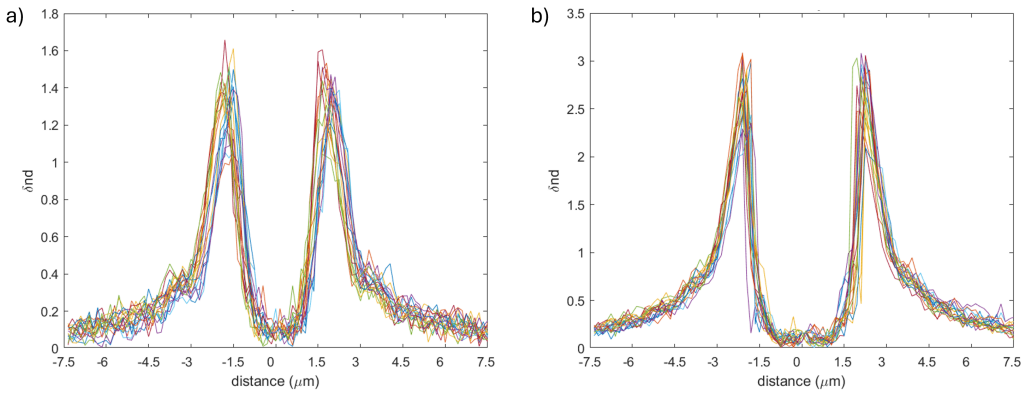

FIGURE 6.7: The profiles of retardance of the chosen microstructures fabricated with high NA (a) and low NA (b

It is clearly visible that the lines are pretty smooth, and the graphs show low retardance in the middle, which is due to the high absorbance in this region leading to low light levels. It results in most of the stress induced modifications being present outside the fabricated microstructure, which is highlighted as a ring shape structure. The radius of laser-fabricated defect changes with respect to the optical system of fabrication. When high NA instrumentation is applied, the radius of the defect is smaller.

The shape of the retardance profiles remains similar for both cases, however, the main noticeable difference is that the retardance peaks reach higher values for the microstructures fabricated with lower NA, compared to those of high NA. Finally, the retardance peaks of the chosen structures were examined. Figure 6.9 presents their relation, together with length of the wires and pulse energies used during fabrication.

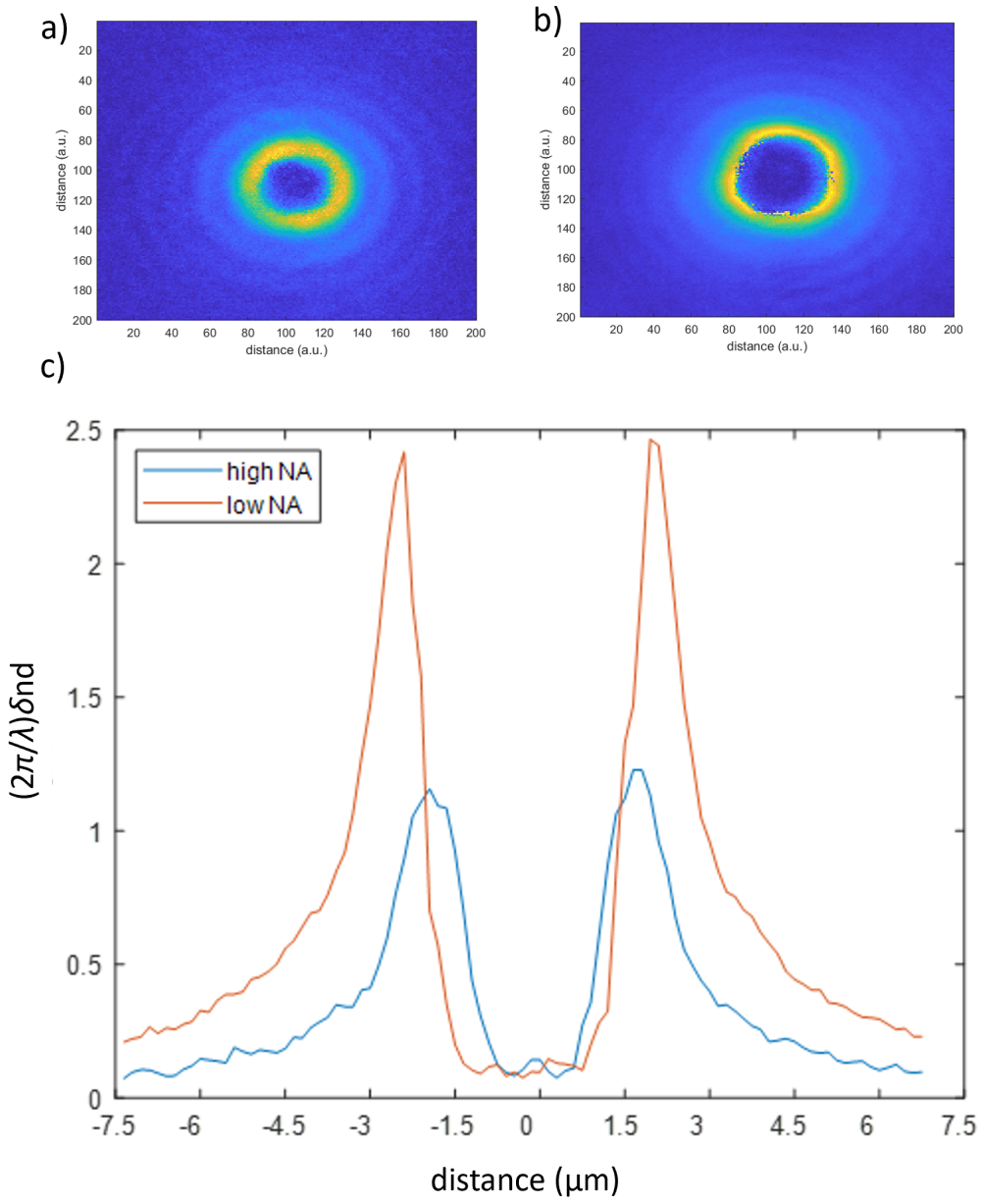

FIGURE 6.8: The profiles of retardance of the chosen microstructures fabricated with high NA (blue) nad low NA (red).

6.4 Measurements of laser-induced stress

These data were examined by two techniques, namely polarimetry and cross-polar microscopy. The following analysis presents results obtained by these two methods.

It is known that $(2\pi/\lambda)\delta nd$ varies with respect to the length of the wire

and corresponding pulse energy. The tendency is that the longer the wire and the higher pulse energy, the higher the retardance. However, this rule does not apply to the wires of 50 µm (see figure 6.9). It was proven by analysis of the polarimetry images that the retardance of the 50 µm wire is higher than those of 75 µm and 100 µm.

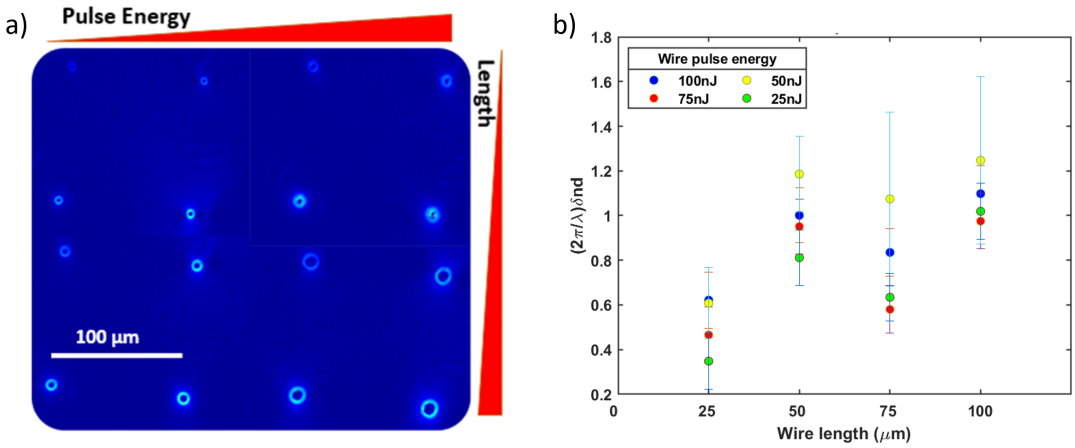

FIGURE 6.9: a) Polarimetric images of the microfabricated structures. b) Retardance peaks of the wires with respect to the wire lengths.

These results are quite surprising, thus further research using the polarimetric analytical tool is required along with limiting the imperfections of the optical system itself. The depth of field is not known and it may appear that the focal spot used for taking birefringent images does not cover the whole length of the graphitic wires, resulting in misleading information about its retardance. What is more, the polarimetric findings do not correlate to those based on crossed-polar analysis. Based on analysis of crossed-polar images, it was observed that high pulse energy, regardless of wire length, generates higher stress, which is depicted by more intense petal-shaped patterns around the graphitic points on the surface (see figure 6.10), which was expected also for the results of polarimetry measurements. The crossed-polar microscopic image was divided into four sections with respect to the wire length, while the image intensity was analysed corresponding to the pulse energy. It was found that the highest intensity peaks are present for the

longest modifications that were laser written with the highest pulse energy. The intensity of crossed-polar images was analysed in ImageJ software and the obtained results are presented in figure 6.10b) .

Eventually, the crossed-polar and polarimetry microscopy provided qualitatively different results. However, the crossed-polar images were taken with a 0.3NA lens and the polarimeter used 0.5NA. Thus, it is expected to see a greater depth of field of the crossed polar image, and as a result, a more accurate representation of the whole structure. Moreover, the depth of field is also related to the illumination, where there is more control with a commercial widefield microscope, than possible in home-built version.

Along with laser writing of graphitic waveguides, again it is demonstrated that higher pulse energy induces stronger graphitisation (see figure 6.11). It was noticed that higher pulse energy provides a more homogeneous graphitic structure, resulting in continuous and non-disruptive lines. The quality of the raphitic structure is evaluated based on optical analysis.

The birefringent colours observed between crossed polarizers indicate the level of retardation (see figure 6.12).

Graphitic waveguides laser-written in diamond, as presented in figure 6.11, can precisely guide light, which makes them suitable for applications in integrated photonics circuits in telecommunication.

6.4.1 Improved measurement

The experiment was repeated with a new design. Here, six rows of nine wires of different lengths (from 10 µm to 50 µm) were laser written vertically in the bulk of diamond. None of them went through the sample, and they were shorter when compared to the previously analysed wires. These

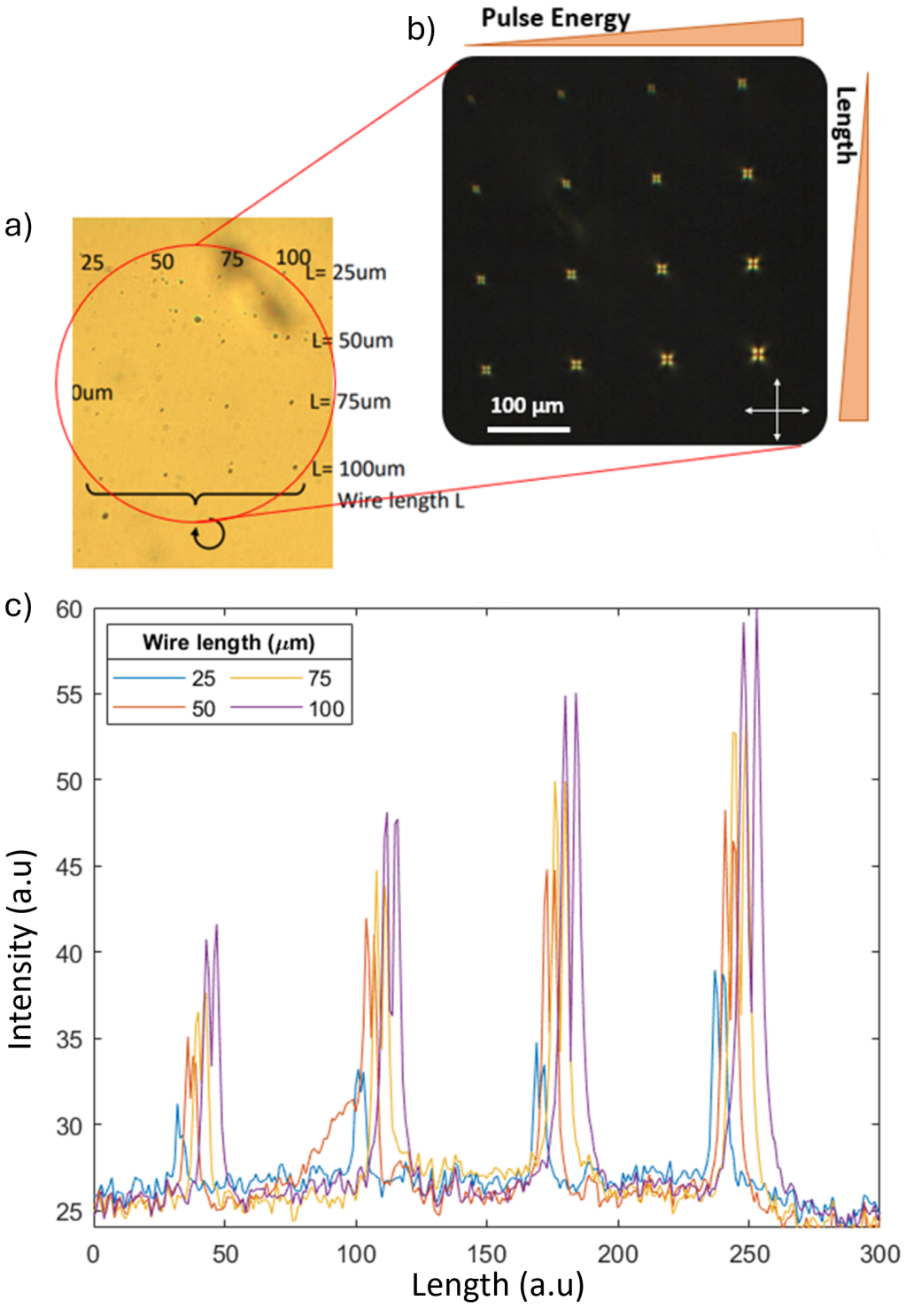

FIGURE 6.10: a) Transmissive microscopy image of laser-fabricated wires and b) cross polar microscopic image of laser fabricated wires. c) Intensity profiles of crossed-polar microscopic images of laser-fabricated structures analysed with respect to wire lengths and laser pulse energy.

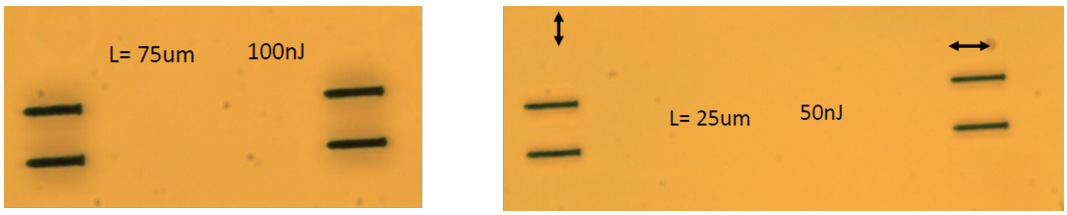

FIGURE 6.11: Transmissive microscopy images of laser fabricated waveguides.

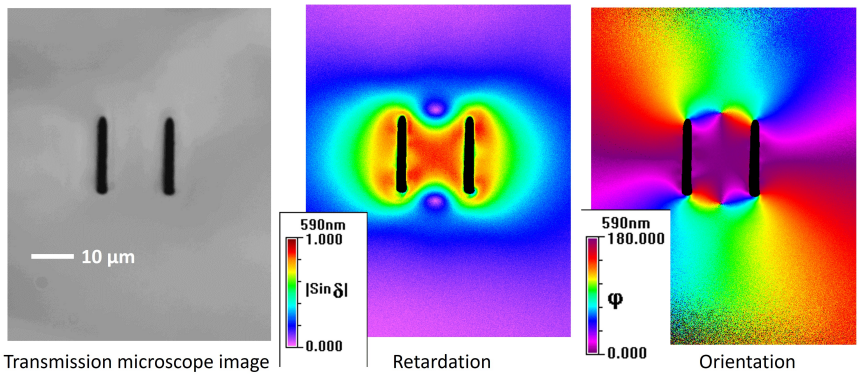

FIGURE 6.12: Retardance of laser-written graphitic waveguide.

structures were analysed by crossed-polar microscopy and polarimetry microscopy. The obtained results are presented in figure 6.13 and figure 6.14.

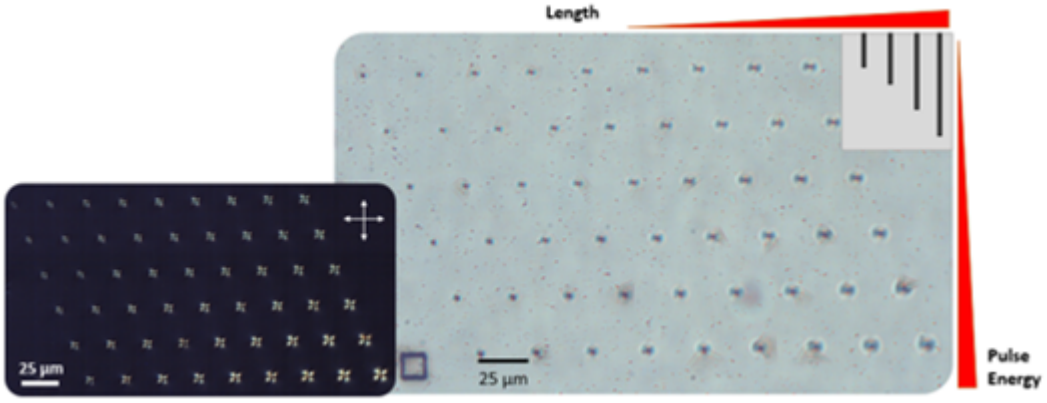

FIGURE 6.13: Crossed-polar microscopic image and transmission-microscopy image of laser written structures.

As presented in figure 6.13, the intensity of the birefringent patterns reflects the fabrication environment applied during laser writing. Here, longer wires generated with the higher pulse energy exhibit higher birefringence.

The polarimetric image was taken with objective lens of 0.5NA and lower magnification (M=20x). Therefore, it was possible to collect the whole

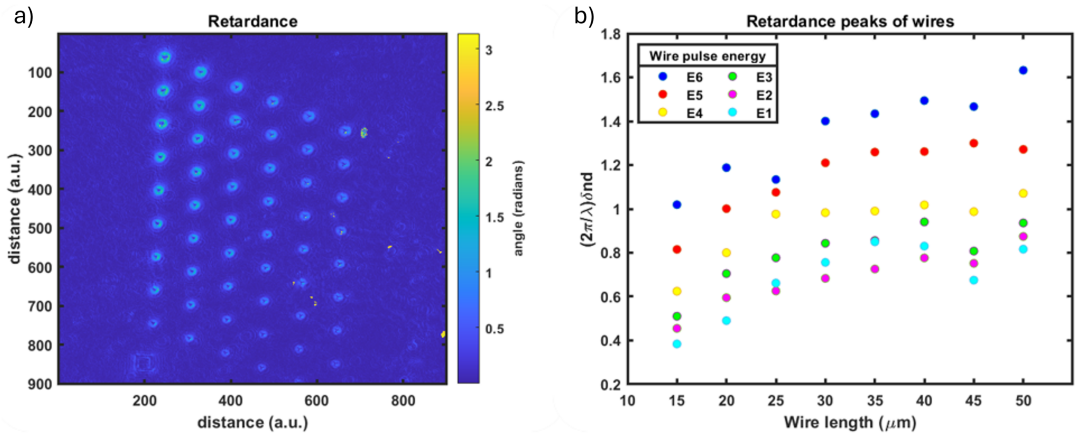

FIGURE 6.14: a) Polarimetric image of retardance of laser-fabricated structures (0.5NA, M=20x) and b) averaged retardance peaks with respect to pulse energy and length of wires.

set of microstructures on one image. This attempt eliminated the need of moving the stage in order to take picture of another microstructure, resulting in no focus modification. Subsequently, the average retardance was analysed and it is noticed that the behaviour of the averaged retardance peaks with respect to pulse energies and microstructure lengths is more linear than in the previous example, and corresponds to the results of crossed-polar microscopy. Additionally, the importance of focal position was evaluated. The position of the best focus position was established optically, by estimating the best focus point of the centre of the structure by eye, and afterwards it was decided which stage position provided the best image. It was demonstrated that the stage position impacts the shape of the analysed structures, which leads to different retardance peak values. Figure 6.15 depicts how the polarimetric image changes with respect to change of stage position, i.e. focus modification.

In general, it was found that the system is sensitive to any change of the stage position. It was noticed that a movement of few µm results in huge discrepancies between the final outcomes, based on analysis of retardance peaks. Here, all the measurements were taken consistently with respect to

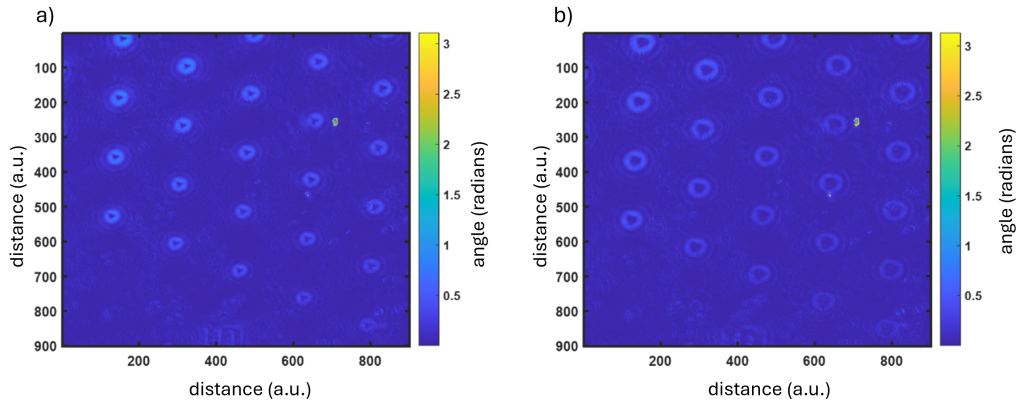

FIGURE 6.15: Polarimetric images of retardance (M=20x) with the best focus (a) and at defocus (b).

the visual optimisation discussed above. Therefore, it is crucial to further investigate the performance of the system, bearing in mind that stress analysis consists of several steps including experimental measurement and data analysis, that may introduce an error. Finally, the stress of the microstructures was calculated, based on the measured retardance (see figure 6.16).

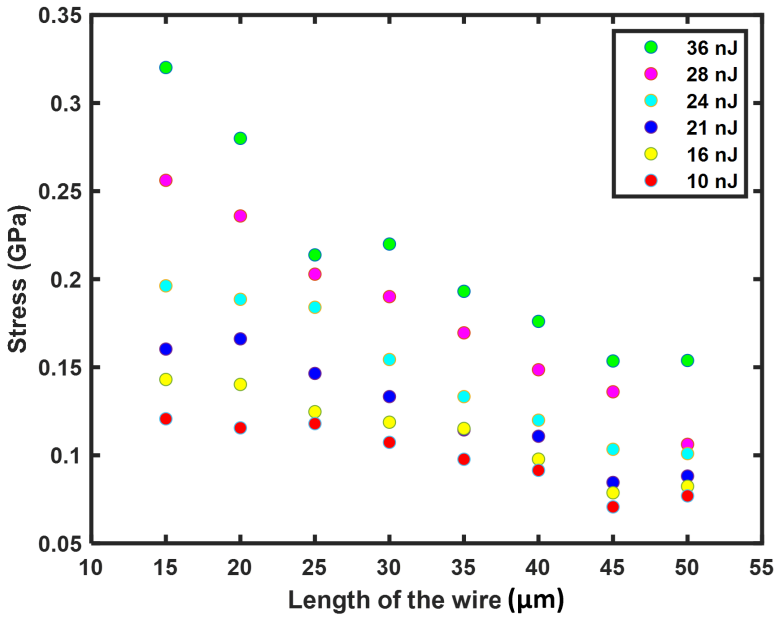

FIGURE 6.16: Stress values of the microfabricated structures according to their lengths and fabrication parameters.

It was observed that the laser-induced stress values are influenced by the properties of the generated structures. Based on the analysis of retardance peaks of these structures, the lowest stress was achieved for the long wires (45 µm) and the lowest powers. However, for the wire 50 µm long there is a slight increase of stress for the first three pulse energies compared to the 45 µm wire. Additionally, the values obtained at the highest pulse energy are very similar for both 45 µm and 50 µm wires. However, there is further study required for better understanding of laser-induced stress in single-crystal diamond.

6.5 Conclusions

Structural modifications in a diamond lattice lead to strain, resulting in birefringence. In this study, direct laser writing was applied to introduce graphitic microstructures of different lengths inside the single-crystal diamond bulk. The laser induced birefringence was characterised by both crossed polar microscopy and Mueller Matrix polarimetry. This experiment indicates that the highest retardance occurs for the longest wires fabricated at the highest powers. Moreover, for the pulse energy of 10 nJ, 16 nJ, 21 nJ and 28 nJ there is a linear trend for the wires lengths from 15 µm to 35 µm. In case of 45 µm wire, the retardance drops and raises up again for the 50 µm wire. Surprisingly, there is a tendency that the stress values decrease with respect to the length of the wires. Furthermore, it was also demonstrated that the choice of the best focus position impacts the final retardance values. Here, the polarimetric microscopy was used for imaging, meaning that scanning of 30 images contributed to the final ratardance outcome. In this experiment a 0.5 NA lens was used. The other limitation of this technique might be the fact that some graphitic structures were out of the depth of field of the objective lens, leading to the distortion of the stress values.(It was assumed that the stress values

will be constant for each pulse energy, regardless of the length of the wires.) This investigation shows that high pulse energies lead to high stress values, however, a previous study shows that the resistance of the wires drops significantly. These results have direct implications for optimizing various diamond based devices. Further study and optimization of analytical tools is suggested for a better understanding of strain-induced stress in diamond.

Chapter 7

Devices in diamond

7.1 Introduction

The laser-written graphitic modifications of diamond structure formed a basis for further post-processing methodology with potential application in electrical devices and radiation sensors. The direct laser-writing technique enabled precise crystal modifications in both surface and subsurface of the diamond, resulting in the presence of graphite-like material. Introduction of graphite in optimized and controllable conditions implemented the electrical properties within the diamond bulk. It was demonstrated that the laser processing is repeatable and leads to low-resistance devices. Additionally, the understanding of the formation mechanisms underlying graphitisation provides significant technological advancements allowing production of novel devices. In order to use the extreme properties of diamond, some laser processing was applied to diamond samples. Two technology areas are described in this chapter, namely graphitic modifications in diamond for radiation sensing and power electronics.

7.2 Radiation detectors

Radiation detectors are exposed to extreme conditions, for example like those encountered in nuclear reactors or high-energy physics experiments. Currently, silica (silicon dioxide) is most common material applied for radiation sensing devices [150]. However, diamond radiation sensors have gained increasing attention in recent years due to their remarkable performance in high-radiation environments[151]. Diamond not only surrpasses the characteristics of silica and other semiconducting materials (see Chapter 2) but also offers several advantages that make it an ideal choice for advanced radiation sensor applications. For example, diamond can withstand high levels of radiation without degradation in performance. Additionally, diamond has a wide bandgap (5.5 eV) compared to silica, which results in lower noise levels and better signal-to-noise ratios. Therefore, diamond sensors can operate effectively at room temperature, without the need for complex cooling systems, making them more efficient and cost-effective for long-term use. The wide band gap also provides diamond with a high threshold for ionizing radiation, enabling precise detection of high-energy particles with minimal interference. Moreover, diamond ensures efficient heat dissipation, which is crucial in harsh environments, as diamond reduced the risk of overheating.

As a result, intrinsic diamond resistance to radiation damage guarantees longer operational lifespan with consistent accuracy. The basic mechanism of a diamond sensor working principle is presented in figure 7.1.

7.2.1 Pixellated diamond radiation sensors

When radiation interacts with diamond, it generates free charge that can be collected to measure the presence of the radiation. Laser-written graphitic electrodes offer a new architecture to collect charge. Radiation detectors

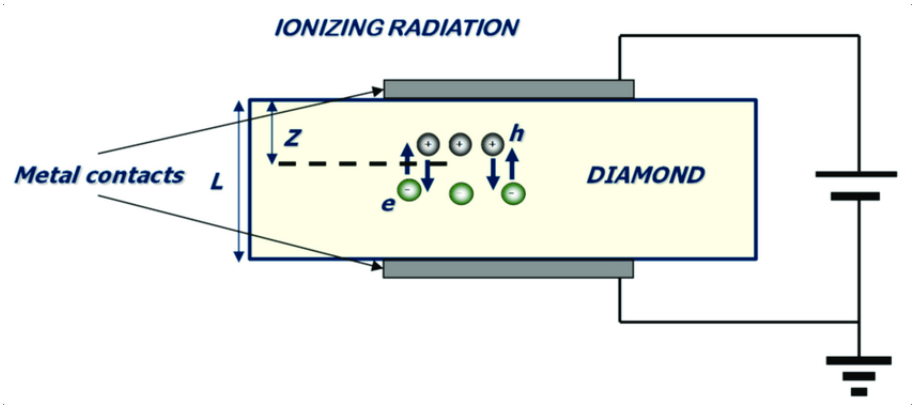

FIGURE 7.1: Schematic of diamond radiation sensor, where L is the width of the diamond sample, e stands for electron, h is the hole and z is the penetration depth of the ionizing radiation.

are important for high radiation environments (like CERN and LHC as described in this chapter) but also have relevance for nuclear reactors and other more practical implementations. This section demonstrates a 3d-pixel detector made for the RD42 collaboration at CERN and tested at CERN. Figure 7.2 presents the schematic diagram of a laser-machined radiation sensor for CERN.

A planar design for radiation detectors is standard. However, this can sometimes require very thin diamond layers which affects the robustness of the device. The 3D design has electrodes in the bulk which can be much closer spaced, reducing the drift distance needed for the charge before collection. It has been shown that the 3D detectors are more resilient to radiation damage than the planar counterpart [152]. The schematic diagram of a planar adiation sensor mechanism is depicted in figure 7.2.

Charged particles or ionising radiation that passes through diamond layer generate electron-hole pairs and lose energy due to scattering. An internal electric field set up by the electrodes causes charge migration, and the charge can then be collected to show theresence of radiation. Pixellation of the detector shows the location of the radiation. Analysis of the charge collected can give information on particle species and energy.

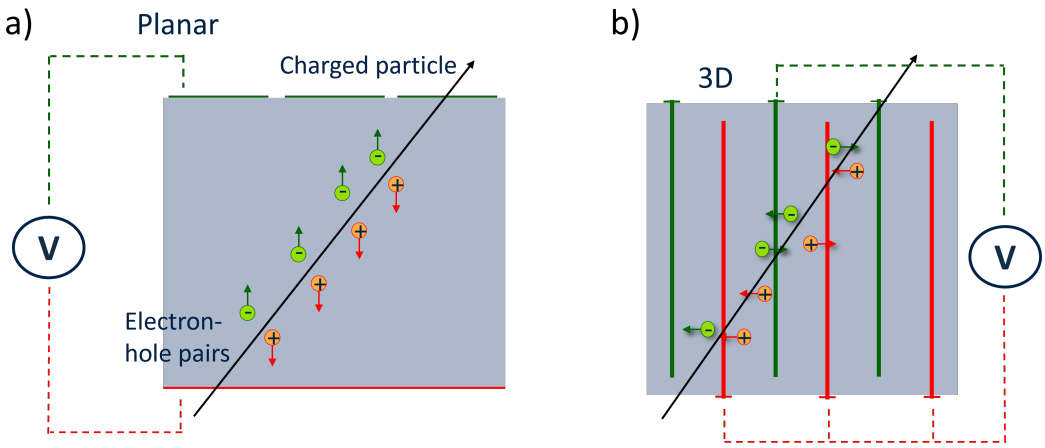

FIGURE 7.2: Schematic diagram of a planar diamond radiation detector (a) and a 3D design with internal wires (b.

Three-dimensional diamond detectors are made by inscribing vertical electrode columns in the bulk of the material. In this work, the electrodes are made by focusing a femto-second laser inside the crystal to create graphitic paths. The processing of the columns has been optimised with dynamic-adaptive optics, using a Spatial Light Modulator (SLM). Control of the processing with an SLM has led to new design features in 3D diamond detectors, such as implementing horizontal electrodes inside the bulk and use of graphitisation in place of conventional surface metal. The thesis demonstrates the applications in the advancements of 3D diamond detector design for specific applications and outlines the motivations for the future viability of full scale 3D diamond devices. Prototype 3D diamond detectors have been designed to meet the specifications for the upgrade of the ATLAS diamond beam conditions that monitor the high luminosity LHC.

All existing 3D detectors tested at CERN comprise purely columnar arrays for the laser-written graphitic electrodes. Additional control over the graphitisation process from high NA focusing and aberration correction allows the option to have both horizontal and vertical graphitic paths inside the diamond substrate [108]. This opens up other possibilities to refine detector designs for the ATLAS experiment (specifically BCM, Beam Condition

Monitor), which has the purpose of monitoring the beam conditions and luminosity very close to the ATLAS interaction point, inside the Inner Detector.

It is expected that by including horizontal wire paths, particularly between bias electrodes, the geometry approaches that of a coaxial wire. This should reduce the volume of the low field regions in the bulk of the diamond as the homogeneity is interrupted in the z direction. A horizontal path connecting electrodes of the same type (bias or sense) are named onwards as a 'cage'.

The internal connections can be on either the bias or sense electrodes. Alternating the cage connections between the two types adds redundancy to both structures and adds more partitioning to reduce low field regions in the detector volume. It is important not to add too many internal connections though, as it raises the device capacitance which is bad for signal retrieval [152]. Structures were fabricated with both cubic and hexagonal 3D cell shapes. The prototypes structures were tested using beams of high energy particles.

Figure 7.3 presents a design of a three-dimensional pixellated radiation sensor that includes graphitic columns within its structure. Graphitic columns were linked with internal horizontal connections, which is referred to as the cage. After laser fabrication of the graphitic structures with respect to the design, the modifications were examined optically in a transmission microscope.

Transmission microscope images were taken at different depths within the diamond layer to check the quality of the laser processing. It has been shown that was possible to laser generate complex three-dimensional graphitic structures to match the design specification from CERN. Figure 7.4 shows the device after metallisation, with layers of titanium, platinum and gold

patterned on the diamond to enable connection to graphitic connectors for charge extraction.

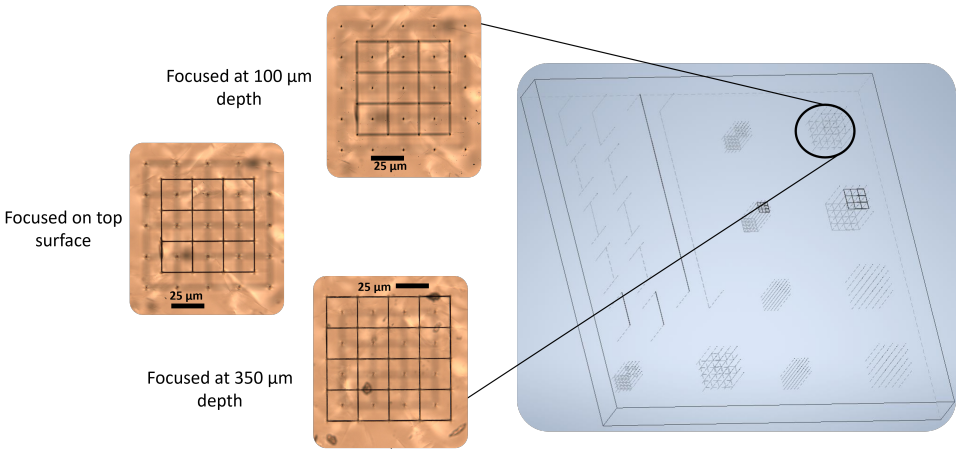

FIGURE 7.3: Schematic design of a 3D diamond radiation sensor with microscopic images focused at different depths within the device, to show horizontal cage structures.

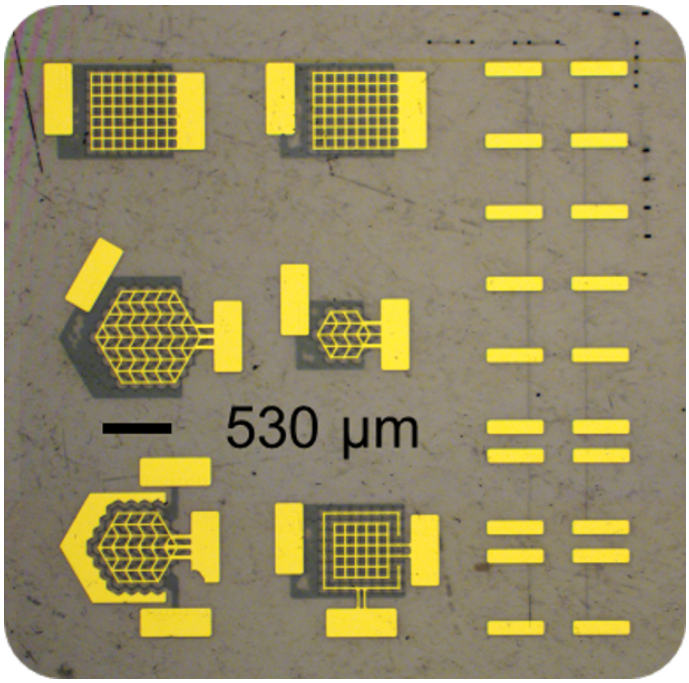

FIGURE 7.4: 3D detector with vertical and horizontal graphitic wires inside the bulk for the RD42 collaboration at CERN, after surface metallisation.

Figure 7.5 presents an image of a diamond radiation-sensing device. The devices have been tested on the SPS CERN test beam with 120 GeV pions and with 4.5 MeV protons at the Ruder Boskovic Insititute in Zagreb. Preliminary data are promising but analysis is ongoing [152].

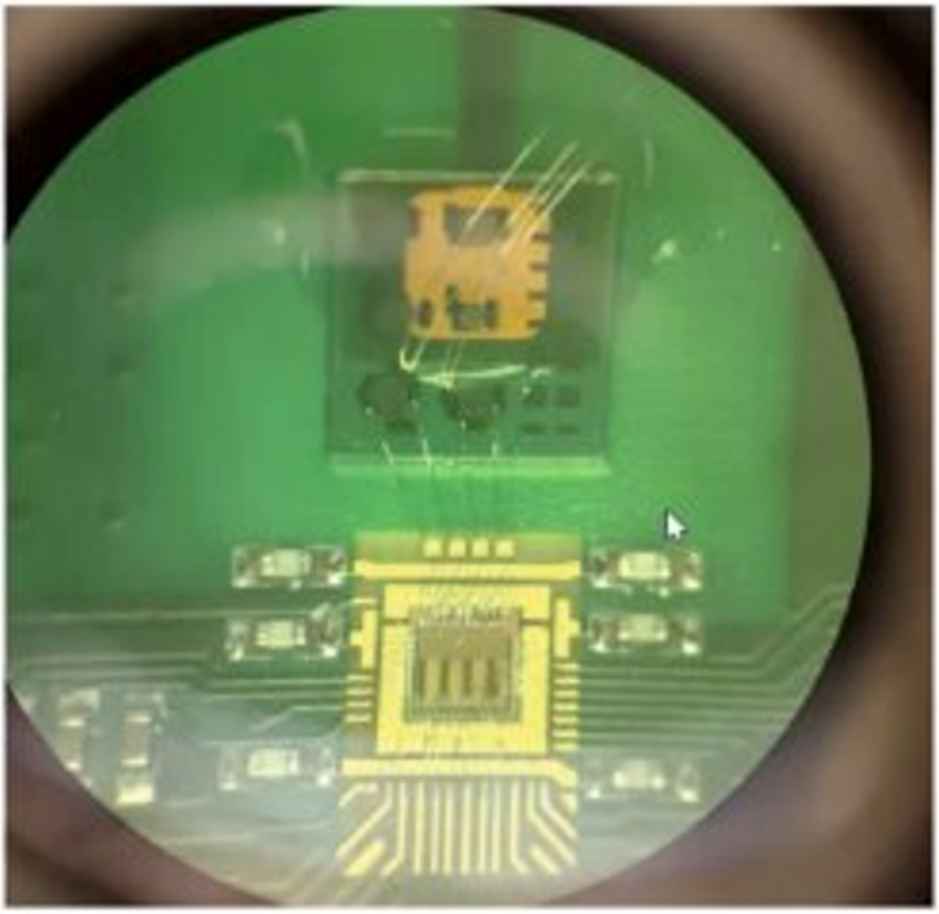

FIGURE 7.5: Picture of prototype diamond 3D radiation-detector device with internal cage bonded in to the CERN CALYPSO electronics, for testing on the CERN test beam.

7.3 Power electronics

As discussed in Chapter 2, diamond has many nice attributes for power electronics, particularly a very large breakdown voltage, very low leakage of charge and good thermal extraction. However, it can be difficult to make devices for power electronics from diamond due to difficulty in doping, as diamond already has a very stable and tight lattice. Laser written structures inside diamond can enable new device architectures, particularly for vertical devices, which can be attractive when dealing with high voltage (in an electrical grid, for example). This chapter demonstrates a novel Schottky diode

device involving laser-written conducting columns within a lightly boron-doped diamond, which has a high blocking ratio. This work was done in collaboration with the research team of Professor Richard Jackman at University College London, and in particular Rebecca Watkins.

7.3.1 Graphitic wire-boron-doped diamond Schottky diodes

Figure 7.6 shows the process flow for the fabrication of the Schottky diode device. The sample was 480 µm thick lightly boron-doped HPHT substrate (boron concentration $\approx 10^{14}$ cm^{-3}). Laser-written columnar wires were fabricated using optimised conditions from Chapter 4, namely translation speed of 10 µm/s, pulse energy of 250 nJ and pulse repetition rate of 1 kHz. Instead of the wires completely crossing the diamond layer, each column stopped short of the top surface, leaving a gap of unmodified diamond. A variety of gaps were studied in the range 2 µm to 10 µm. Also some control devices were made where the laser written wires completely crossed the diamond (i.e. a gap of 0 µm). Each device to be tested consisted of an 8×8 array of identical laser-written columns with 12 µm spacing, to increase the effective graphite conduction paths for each device. This process is shown in Figure 7.6(a).

After laser processing, layers of titanium and gold were deposited on the back (seed) side of the diamond to form an ohmic contact to the laser-written columns (Figure 7.6(b)). Next aluminium was patterned on to the top surface of the diamond above each array of laser-written columns (Figure 7.6(c)). Aluminium is known to give a Schottky diode connection to boron-doped diamond. The diamond is shown in a transmission microscope image in Figure 7.7 after laser processing. Many laser-written devices consisting of 8×8 arrays of columns with different spacing from the top surface are visible. The diamond is next shown in Figure 7.8 in reflection microscopy

showing the sample after metallisation, with patterned aluminium Schottky contacts visible.

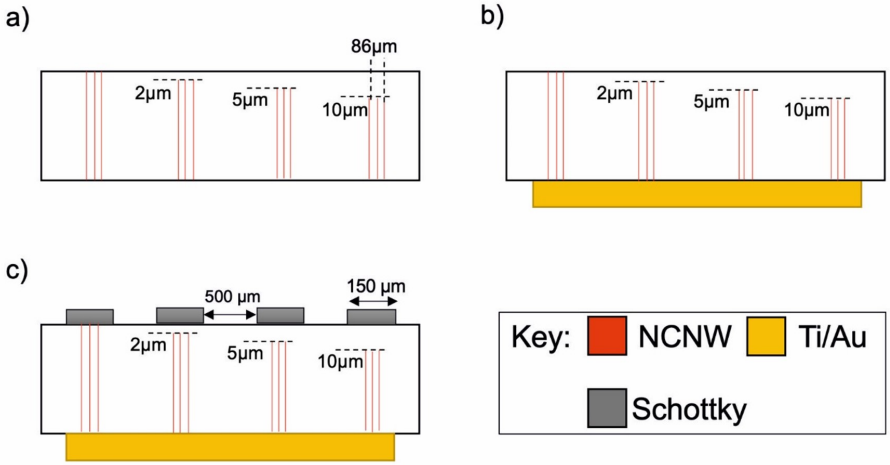

FIGURE 7.6: Process flow for the fabrication of the full Schottky diode device with internal nano-carbon network wires (NCNWs) [153]. Image courtesy of Rebecca Watkins.

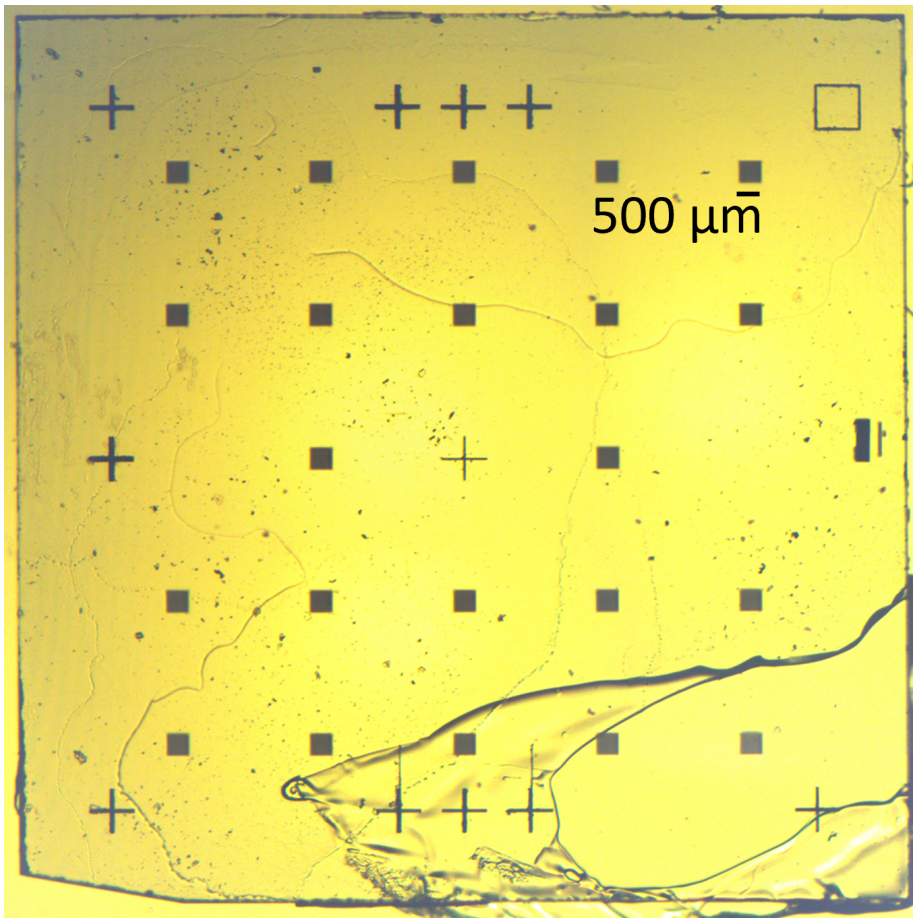

FIGURE 7.7: The boron-doped diamond sample after laser processing, where arrays of laser-written graphitic columns are visible.

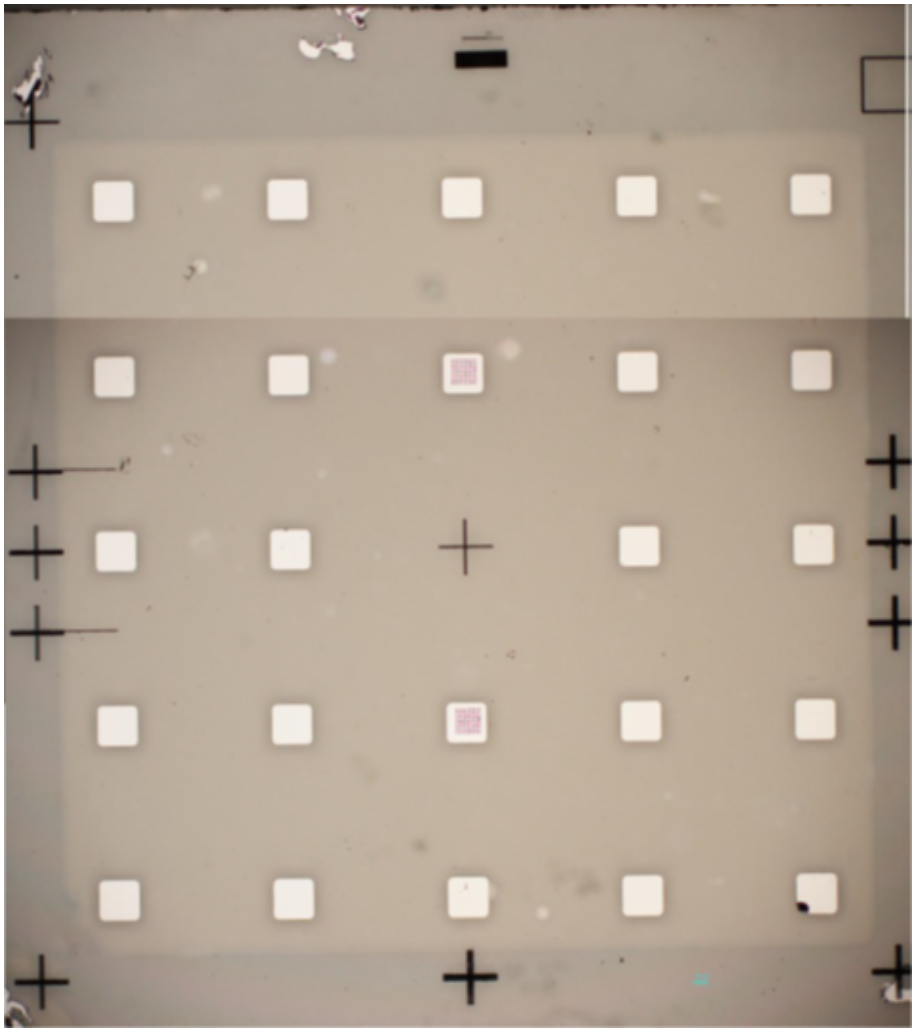

FIGURE 7.8: The boron-doped diamond sample after full process and ready-for-testing. patterned aluminium Schottky contacts visible above each laser-written array of columns.

Figure 7.9 shows current-voltage characteristics for the control device where the laser-written column array completely crosses the diamond sample, with no gap between laser-written wires and the diamond top surface. It can be seen that the current-voltage relationship is largely linear showing ohmic conduction. This shows that the conduction characteristics are defined by the laser-written structures, and are analogous with structures presented in Chapter 4. This important result indicates that the light boron doping of the diamond does not significantly affect the laser process for breaking down the lattice during graphitisation or affect the conduction in the wires. It is

also seen that the aluminium top surface metal contact gives ohmic conduction and not Schottky conduction. Finally, we see that the effective resistance is low at 3.4 kΩ because of the large numbers of columns within an array.

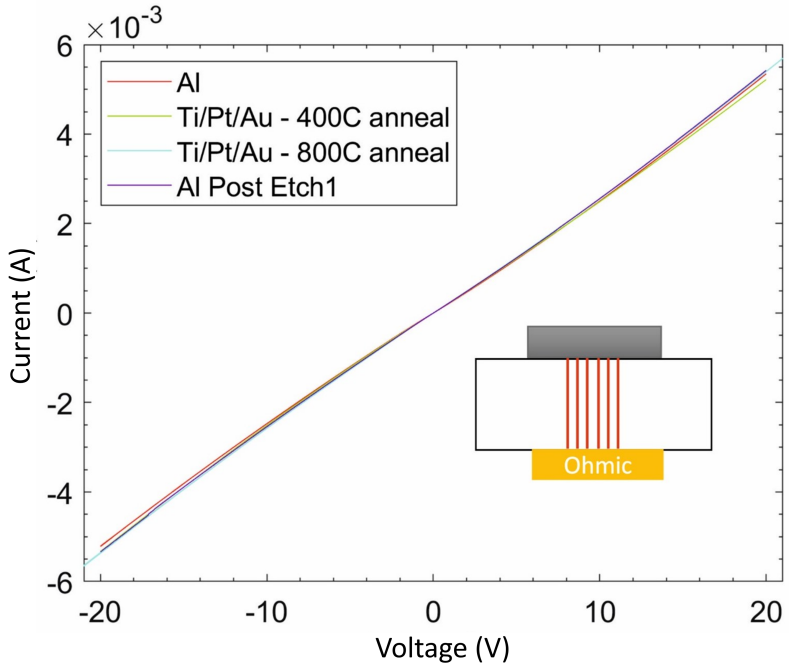

FIGURE 7.9: Current-voltage characteristics of control device where laser-written columns completely cross the diamond sample [153]. Figure courtesy of Rebecca Watkins.

Figure 7.10 shows the current-voltage characteristics of the device with 2 µm, gap between the laser-written wires and the top surface of the diamond [153]. It is seen that this device acts well like a diode, with a strong block to the current at positive voltage whilst conducting at negative voltage. Figure 7.10 also shows the current-voltage characteristics for a conventional device architecture, where there are no laser-written columns and simply boron-doped diamond layer between the ohmic and Schottky electrodes. The laser-written device shows higher current at negative voltage, with some structures in the curve indicating different conduction mechanisms. Surprisingly, the laser-written device also shows lower current than the conventional device at positive voltage. Work is ongoing to explore the reasons for this.

The inset plots the rectification ratio, which is the ratio of current at positive and negative voltage as function of voltage, showing high values at high voltage, as desired.

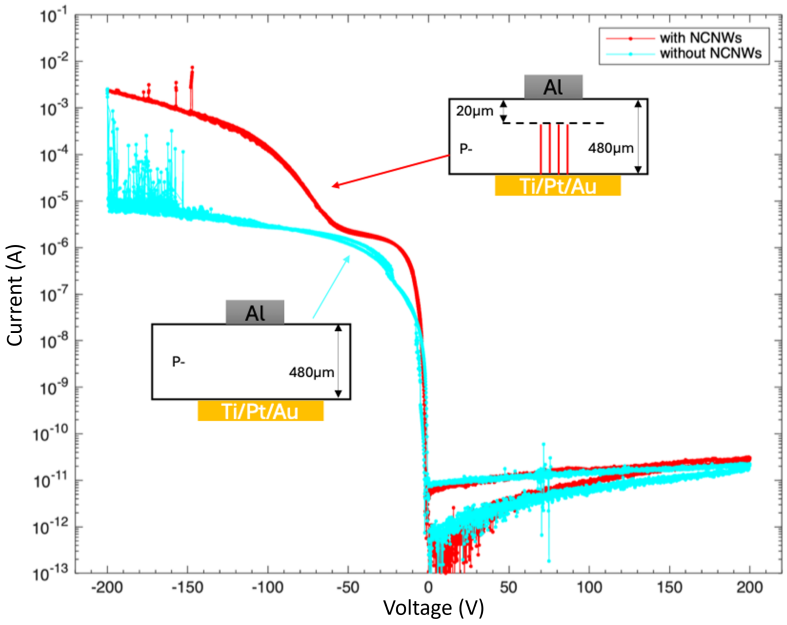

FIGURE 7.10: Current-voltage characteristic for device with array of laser-written wires that stop 2 µm short from top surface of the diamond (red curve: with NCNWs (nanocarbon network wires)). Also shown is the current-voltage characteristic for conventional device architecture with no laser-written wires (blue curve: without NCNWs). Inset shows rectification ratio for laser-written device [153]. Figure courtesy of Rebecca Watkins.

7.4 Conclusions

A lot of results in this thesis have been done on the optimisation of the laser-writing process for fabrication of conductive graphite structures in diamond. It is important that these developments are transferred across to demonstration of improved devices used in applications. In that way, the benefit of the laser-writing optimisation can be realised. In this chapter,two collaborative projects demonstrate devices enabled by the laser writing. New device architectures have been made possible for 3D pixellated radiation detectors, by having horizontal graphite connectors in a cage structure. Preliminary

results are promising and these designs are being further developed with colleagues in the collaboration at CERN. In addition, a new device structure for a vertical Schottky diode in diamond is demonstrated in collaboration with University College London, using laser-written wires in arrays that stop a short distance from the top surface of the diamond. This is also one of the first experiments looking at performance of laser-written conductors inside diamond material doped with boron. The Schottky diode device is seen to perform well and with better characteristics than the conventional device architecture without laser-written wires. This device design shows much promise for applications in power electronics at high voltage, which is the subject of further research.

Chapter 8

Conclusions and Future Work

8.1 Conclusions

This thesis focused on the development and optimization of laser processing techniques to produce novel diamond devices, in particular graphitic electrodes in diamond for radiation detectors and electrical devices. It was demonstrated that development of all-carbon device architecture allowed straightforward optimisation of laser-processing parameters for conductive structures. One of the key benefits of this approach is the ability to assess electrical characteristics immediately after laser processing, without any additional substrate treatment. This allows for the rapid adjustment of laser parameters to achieve the desired conductive properties. A critical finding in this work was the surprisingly narrow range of laser pulse repetition rates, from 200 Hz to 2 kHz, that resulted in the formation of ohmic conductive wires. Moreover, when the repetition rate was increased beyond this range, and even though much higher laser energy was delivered, the resulting structures displayed no conductivity.

Further analysis revealed that conductivity is not solely dictated by the laser pulse-repetition rate. Instead, the speed of the laser-writing process

plays an equally important role. It was demonstrated that the key parameter influencing the formation of conductive graphitic pathways is the laser dose, which was defined as the number of laser pulses per distance. Careful selection of the appropriate combination of repetition rate and process speed resulted in highly conductive structures with reliable ohmic properties.

In this study, various techniques were employed to assess the quality of the laser-written wires, including optical imaging, SEM and Raman spectroscopy. However, none of these methods provided sufficient information to fully evaluate the electrical properties of the wires. While they offered insights into surface morphology and composition, they were unable to reveal the internal structural features critical to conductivity.

It was shown that TEM, on the other hand, proved to be a highly effective method in assessing the internal structure of the laser-processed columns. TEM imaging revealed a clear conductive path through laser-modified lattice for columns written at low repetition rate. These structures displayed sp^2-carbon regions continuous enough for electrical conduction. On the contrary, columns that were laser written at higher repetition rates showed small pockets of sp^2-carbon, but the lack of connectivity between these regions resulted in absence of conduction in these structures.

In general, this study demonstrates that fabrication with appropriate laser parameters can generate reliable ohmic conductors that could pave the way for advanced all-carbon devices. The insights gained from this research, in particular, the role of laser dose and complexity of internal structures, could support future development of electronics based on laser-processed diamond materials.

Moreover, advanced concepts in laser writing were explored, particularly the overwriting techniques. This approach facilitated the creation of

a hybrid structure that merged the characteristics of both low pulse repetition rate (PRR) and high PRR regimes. While previous studies have observed the formation of symmetric barrier potentials, the presence of asymmetric barrier and diode-like behaviour is highly novel. This represents the first demonstration of an all-carbon diode-like device within diamond, which could serve as a critical step towards the realization of vertical all-carbon devices intended for power-electronics applications. The observed asymmetry in the barrier may correlate with the inhomogeneous structural breakdown of the diamond within the low PRR precursor track. TEM analyses suggest a potential reordering of the sp^2 layers at the diamond interface resulting from the overwriting process, indicating an area for further investigation.

Additionally, the study examined the potential of holographic laser writing for device fabrication. For any complex devices that might be made using this technology, it is likely that the entire device will need to be patterned by the laser. Any process that can speed that up is very important. It was demonstrated that a computer-generated hologram displayed onto a spatial light modulator (SLM) can be used to generate multiple laser foci, each one of which can simultaneously machine a column in a single pass of the substrate. It is shown that the choice of the laser pulse energy and spot spacing is very important in the technique being effective. Although the electrical performance of the columns produced by this method was slightly inferior to those fabricated sequentially, even when accounting for amplitude aberrations, resistance values were still within 50% of those achieved through sequential writing. Notably, this reduction in processing time by an order of magnitude holds substantial promise for scaling up device fabrication.

In this research, the stress-induced birefringence around laser-written columns in diamond was investigated using advanced imaging techniques. Two quantitative methods were employed to measure stress, i.e. Metripol

imaging and Mueller Matrix (MM) imaging. These techniques were complemented by simple imaging using crossed polarisers. A new sample was developed to examine stress-induced birefringence with different processing parameters and different column lengths. It was presented that it is important to consider column length and the depth of field of the microscope to accurately assess the stress induced in the crystal. These findings are particularly relevant for development of future photonic devices that rely on birefringence, such as optical waveguides or for analysis of laser written conductive columns.

The chapter on devices demonstrates how fundamental developments in laser-writing techniques and the optimization of fabrication parameters, discussed in earlier chapters, have been applied to create functional devices. Two examples of functional device that were made based on the work in this thesis, in collaboration with others, demonstrate the practical applications of this research.

The first example involves radiation detectors developed as part of the RD42 collaboration at CERN. Advances in the fabrication have enabled new device architectures using a cage for greater reliability through increased connectivity. The results from these devices are promising, indicating the potential for laser-written structures in high-performance applications such as radiation detection.

Secondly, laser-written graphitic structures were used for a Schottky diode device where columns did not fully bridge the diamond wafer. This

requires careful fabrication control, particularly in lightly boron-doped diamond substrates. The device performed better than a control sample without laser-written columns, suggesting that the combination of laser processing and doping levels could be a valuable area for future exploration. Understanding the electrical properties of laser-written columns in substrates with different dopant levels offers a promising direction for optimizing device performance.

8.2 Future Works

Whilst there have been many interesting findings and intriguing results arising from this work, it also raises several new questions and can prompt further study.

First, more work would be valuable to explore how pulse repetition rate influences laser-written structures from different focusing geometries. It is known that higher NA focusing is better for breakdown of the diamond lattice, as high NA oil lenses are typically needed for fabrication of horizontal conductors, like the cage structure in the CERN devices. It should be explored how columns written with different NA (and aberration correction) behave at different pulse-repetition rates. Likewise, more work can be given to see whether the process window, in terms of pulse-repetition rate, is equally small for vertical and horizontal wires in the diamond substrate. Also, recently there have been good demonstrations of laser-written conductive vias using Bessel beams which stretch across the diamond wafer and can create columns without sample movement [134]. It would be very interesting to see if these structures are similarly affected by different pulse-repetition rates.

The overwritten wires that combine processing at different pulse-repetition rates to give an asymmetric barrier potential provide much excitment for future all-carbon electronics. However, the results are still very early and more work is needed. It is important to explore different repetition rates and pulse energies to find optimum conditions to create the diode-like behaviour. It is also needed to better understand where the diode-like behaviour arises. Possibly more TEM analysis or theoretical considerations could give some insight into this. It would be nice to extend work to determine whether it is a surface phenomena that drives the asymmetric barrier potential or whether it is stronger at the surface.

Quantitative birefringent measurements were shown for analysing the stress distribution around wires. It would be good to extend this more towards analysis of photonic structures (i.e. to design and test new photonic structures in diamond, based upon stress induced birefringence). There is much scientific and practical interest in looking at the interaction of stress distribution from nearby written structures. For example, if structures are written which are too large, stress can accumulate and lead to a macroscale cracking of the crystal. Valuable work would be to find whether there are ways to arrange features to manage stress and avoid cracking.

Engineering is about developing solutions that are useful for society. Thus all of the work here is towards manufacturing diamond devices and giving developments in range of applications that can benefit society. It would also be interesting to look at a range of diamond substrates with different doping, for example phosphorus-doped diamond. There are many ways this technology can give better devices and that is important work that must be done.

Bibliography

1. Angelone, M. & Verona, C. Properties of Diamond-Based Neutron Detectors Operated in Harsh Environments. *Journal of Nuclear Engineering* **2,** 422–470 (Oct. 2021).
2. Coe, S. & Sussmann, R. Optical, thermal and mechanical properties of CVD diamond. *Diamond and Related Materials* **9,** 1726–1729. ISSN: 0925-9635 (2000).
3. Zaitsev, A. *Optical Properties of Diamond: A Data Handbook* ISBN: 9783540665823 (Springer, 2001).
4. Bonhaus, J., Borchert, D., Denisenko, A. & Fahrner, W. *Diamond heat spreaders for high power devices with integrated temperature sensors* in *Fourteenth Annual IEEE Semiconductor Thermal Measurement and Management Symposium (Cat. No.98CH36195)* (1998), 139–146.
5. Poltoratskiy, V. *et al.* A novel composite abrasive material of unmarketable natural diamond powder. *Journal of Superhard Materials* **36,** 136–144 (Mar. 2014).
6. Vavilov, V. S. The properties of natural and synthetic diamond. *Physics-Uspekhi* **36,** 1083 (Nov. 1993).
7. Eaton-Magaña, S. & Shigley, J. Observations on CVD-Grown Synthetic Diamonds: A Review. *Gems and Gemology* **52,** 222 (Nov. 2016).
8. Briddon, P. & Jones, R. Theory of impurities in diamond. *Physica B: Condensed Matter* **185,** 179–189. ISSN: 0921-4526 (1993).

9. Kaminski, N. & Hilt, O. SiC and GaN devices – wide bandgap is not all the same. *IET Circuits, Devices & Systems* **8,** 227–236 (2014).
10. Kalish, R. Doping of diamond. *Carbon* **37,** 781–785. ISSN: 0008-6223 (1999).
11. Koizumi, S., Watanabe, K., Hasegawa, M. & Kanda, H. Ultraviolet Emission from a Diamond pn Junction. *Science* **292,** 1899–1901 (2001).
12. Paoletti A. Tucciarone, A. *The physics of diamond* (Netherlands: IOS Press, 1997).
13. Breeding, C. & Shigley, J. The "Type" Classification System of Diamonds and Its Importance in Gemology. *Gems Gemology* **45,** 96–111 (July 2009).
14. Bundy, F. P., Hall, H. T., Strong, H. M. & Wentorf, R. H. Man-Made Diamonds. **176,** 51–55 (July 1955).
15. Balmer, R. *et al.* Chemical vapour deposition synthetic diamond: Materials, technology and applications. *Journal of Physics: Condensed Matter* **21,** 364221 (Aug. 2009).
16. Eaton-Magaña, S., Shigley, J. & Breeding, C. Observations on HPHT-Grown Synthetic Diamonds: A Review. *Gems and Gemology* **53** (Nov. 2017).
17. Shirey, S. & Shigley, J. Recent Advances in Understanding the Geology of Diamonds. *Gems Gemology* **49** (Dec. 2013).
18. Md Nor, R., Suriani, A., K Thandavan, T. M., Rusop, M. & Yahya, N. in, 195–217 (Sept. 2010). ISBN: 978-3-642-14672-5.
19. Komanduri, R. *et al.* Polycrystalline Diamond Films and Single Crystal Diamonds Grown by Combustion Synthesis. *CIRP Annals* **39,** 585–588. ISSN: 0007-8506 (1990).
20. Schwander, M. & Partes, K. A review of diamond synthesis by CVD processes. *Diamond and Related Materials* **20,** 1287–1301. ISSN: 0925-9635 (2011).

21. Kamo, M., Sato, Y., Matsumoto, S. & Setaka, N. Diamond synthesis from gas phase in microwave plasma. *Journal of Crystal Growth* **62,** 642–644. ISSN: 0022-0248 (1983).
22. Tappert, R. & Tappert, M. in (May 2011). ISBN: 978-3-642-12571-3.
23. Harris, D. C. *Properties of diamond for window and dome applications* in *Window and Dome Technologies and Materials IV* (ed Klocek, P.) **2286** (SPIE, 1994), 218–228.
24. Briones, M. *et al.* Diamond nanoparticles based biosensors for efficient glucose and lactate determination. *Biosensors and Bioelectronics* **68,** 521–528. ISSN: 0956-5663 (2015).
25. Narayan, R. J., Boehm, R. D. & Sumant, A. V. Medical applications of diamond particles surfaces. *Materials Today* **14,** 154–163. ISSN: 1369-7021 (2011).
26. Khanna, P. *et al.* Use of nanocrystalline diamond for microfluidic lab-on-a-chip. *Diamond and Related Materials* **15.** Proceedings of the joint 11th International Conference on New Diamond Science and Technology and the 9th Applied Diamond Conference 2006, 2073–2077. ISSN: 0925-9635 (2006).
27. Segawa, T. F. & Igarashi, R. Nanoscale quantum sensing with Nitrogen-Vacancy centers in nanodiamonds – A magnetic resonance perspective. *Progress in Nuclear Magnetic Resonance Spectroscopy* **134-135,** 20–38. ISSN: 0079-6565 (2023).
28. Gorrini, F. & Bifone, A. Advances in Stabilization and Enrichment of Shallow Nitrogen-Vacancy Centers in Diamond for Biosensing and Spin-Polarization Transfer. *Biosensors* **13,** 691 (June 2023).
29. Haque, A. & Sumaiya, S. An Overview on the Formation and Processing of Nitrogen-Vacancy Photonic Centers in Diamond by Ion Implantation. *Journal of Manufacturing and Materials Processing* **1.** ISSN: 2504-4494 (2017).

30. Bayn, I. *et al.* Diamond processing by focused ion beam—surface damage and recovery. *Applied Physics Letters* **99.** 183109. ISSN: 0003-6951 (Nov. 2011).
31. Zukauskas, A. *et al.* Ultrafast laser processing of materials: from science to industry. *Light: Science Applications* **5,** e16133 (Mar. 2016).
32. Haque, A. & Sumaiya, S. An Overview on the Formation and Processing of Nitrogen-Vacancy Photonic Centers in Diamond by Ion Implantation. *Journal of Manufacturing and Materials Processing* **1.** ISSN: 2504-4494 (2017).
33. Aharonovich, I. & Neu, E. Diamond Nanophotonics. *Advanced Optical Materials* **2,** 911–928 (2014).
34. Smith, J. M., Meynell, S. A., Jayich, A. C. B. & Meijer, J. *Nanophotonics* **8,** 1889–1906 (2019).
35. Santori, C., Barclay, P. E., Fu, K.-M. C. & Beausoleil, R. G. Vertical distribution of nitrogen-vacancy centers in diamond formed by ion implantation and annealing. *Phys. Rev. B* **79,** 125313 (12 Mar. 2009).
36. Delgado, D. & Vila, R. Statistical Molecular Dynamics study of displacement energies in diamond. *Journal of Nuclear Materials* **419,** 32–38. ISSN: 0022-3115 (2011).
37. Dresselhaus, M. & Kalish, R. *Ion Implantation in Diamond, Graphite, and Related Materials* ISBN: 9783540549567 (Springer-Verlag, 1992).
38. Wu, Y. & Wu, Y. Neutron irradiation and material damage. *Fusion neutronics,* 91–113 (2017).
39. Karkin, A. E. *et al.* Neutron irradiation effects in chemical-vapor-deposited diamond. *Phys. Rev. B* **78,** 033204 (3 July 2008).
40. Haque, A. & Sumaiya, S. An Overview on the Formation and Processing of Nitrogen-Vacancy Photonic Centers in Diamond by Ion Implantation. *Journal of Manufacturing and Materials Processing* **1.** ISSN: 2504-4494 (2017).

41. Gulka, M. *et al.* Room-temperature control and electrical readout of individual nitrogen-vacancy nuclear spins. *Nature Communications* **12,** 4421 (July 2021).
42. Childress, L. & Hanson, R. Diamond NV centers for quantum computing and quantum networks. *MRS Bulletin* **38** (Feb. 2013).
43. Geis, M. *et al.* Diamond cold cathode. *IEEE Electron Device Letters* **12,** 456–459 (1991).
44. Grot, S., Gildenblat, G. & Badzian, A. Diamond thin-film recessed gate field-effect transistors fabricated by electron cyclotron resonance plasma etching. *IEEE Electron Device Letters* **13,** 462–464 (1992).
45. Ding, G. *et al. Reactive ion etching of CVD diamond films for MEMS applications* in *Micromachining and Microfabrication* (eds Chau, K. H., Parameswaran, M. & Tay, F. E.) **4230** (SPIE, 2000), 224–230.
46. Lee, C., Gu, E., Dawson, M., Friel, I. & Scarsbrook, G. Etching and micro-optics fabrication in diamond using chlorine-based inductively-coupled plasma. *Diamond and Related Materials* **17,** 1292–1296. ISSN: 0925-9635 (2008).
47. Chan, S. S. M. *et al.* The effect of excimer laser etching on thin film diamond. *Semiconductor Science and Technology* **18,** S47 (Feb. 2003).
48. Wu, M., Guo, B. & Zhao, Q. Laser machining micro-structures on diamond surface with a sub-nanosecond pulsed laser. *Applied Physics A: Materials Science & Processing* **124,** 170 (Jan. 2018).
49. Mouhamadali, F. *et al.* Nanosecond pulsed laser-processing of CVD diamond. *Optics and Lasers in Engineering* **126,** 105917. ISSN: 0143-8166 (2020).
50. Gicquel, A., Hassouni, K., Silva, F. & Achard, J. CVD diamond films: from growth to applications. *Current Applied Physics* **1,** 479–496. ISSN: 1567-1739 (2001).

51. Weiner, A. M. in *Ultrafast Optics* 316–361 (John Wiley Sons, Ltd, 2009). ISBN: 9780470473467.
52. Hargrove, L. E., Fork, R. L. & Pollack, M. A. Locking of He-Ne laser modes induced by synchronous intracavity modulation. *Applied Physics Letters* **5,** 4–5. ISSN: 0003-6951 (Nov. 2004).
53. Davis, G., Balasubramaniam, K., Palanisamy, S., Nagarajah, R. & Rajagopal, P. Additively manufactured integrated slit mask for laser ultrasonic guided wave inspection. *The International Journal of Advanced Manufacturing Technology* **110** (Sept. 2020).
54. Wang, F. *et al.* Ultrafast response of harmonic modelocked THz lasers. *Light: Science Applications* **9,** 51 (Apr. 2020).
55. Paschotta, R. *Field Guide to Laser Pulse Generation* ISBN: 9780819472489 (SPIE Press, 2008).
56. Jiang, L. J. *et al.* Femtosecond laser direct writing in transparent materials based on nonlinear absorption. *MRS Bulletin* **41,** 975–983 (Dec. 2016).
57. Beresna, M., Gecevičius, M. & Kazansky, P. Ultrafast laser direct writing and nanostructuring in transparent materials. *Advances in Optics and Photonics* **6** (Sept. 2014).
58. Streltsov, A. *et al.* Laser-written high-contrast waveguides in glass. *Proc SPIE* (May 2009).
59. Miura, K., Qiu, J., Inouye, H., Mitsuyu, T. & Hirao, K. Photowritten optical waveguides in various glasses with ultrashort pulse laser. *Applied Physics Letters* **71,** 3329–3331. ISSN: 0003-6951 (Dec. 1997).
60. Watanabe, W., Asano, T., Yamada, K., Itoh, K. & Nishii, J. Wavelength division with three-dimensional couplers fabricated by filamentation of femtosecond laser pulses. *Opt. Lett.* **28,** 2491–2493 (Dec. 2003).
61. Abou Khalil, A. *et al.* Direct laser writing of a new type of waveguides in silver containing glasses. *Scientific Reports* **7,** 11124 (Dec. 2017).

62. Yamasaki, K. *et al.* Recording by microexplosion and two-photon reading of three-dimensional optical memory in polymethylmethacrylate films. *Applied Physics Letters* **76,** 1000–1002 (Feb. 2000).
63. Zoubir, A., Lopez, C., Richardson, M. & Richardson, K. Femtosecond Laser Fabrication of Tubular Waveguides in Poly(methyl methacrylate). *Optics letters* **29,** 1840–2 (Sept. 2004).
64. Chen, H., Lv, T., Zheng, A. & Han, Y. Directly writing embedded waveguides in lithium niobate by a femtosecond laser. *Optik* **124,** 195–197. ISSN: 0030-4026 (2013).
65. Wang, P. *et al.* Fabrication of polarization-independent waveguides deeply buried in lithium niobate crystal using aberration-corrected femtosecond laser direct writing. *Scientific Reports* **7,** 41211 (2017).
66. Ródenas, A. & Kar, A. High-contrast step-index waveguides in borate nonlinear laser crystals by 3D laser writing. *Optics express* **19,** 17820–33 (Aug. 2011).
67. Macdonald, J. R. *et al.* Ultrafast laser inscription of near-infrared waveguides in polycrystalline ZnSe. *Opt. Lett.* **35,** 4036–4038 (Dec. 2010).
68. Okhrimchuk, A. G., Shestakov, A. V., Khrushchev, I. & Mitchell, J. Depressed cladding, buried waveguide laser formed in a YAG:Nd3+ crystal by femtosecond laser writing. *Opt. Lett.* **30,** 2248–2250 (Sept. 2005).
69. Righini, G. Glass optical waveguides: A review of fabrication techniques. *Optical Engineering* **53,** 071819 (Mar. 2014).
70. Maia, J., Amorim, V., Viveiros, D. & Marques, P. Femtosecond Laser Micromachining of Fabry-Pérot Interferometers for Magnetic Field Sensing. *EPJ Web of Conferences* **215,** 13001 (Jan. 2019).
71. Zhao, Y., Zhao, Y.-L. & Wang, L.-K. Application of femtosecond laser micromachining in silicon carbide deep etching for fabricating sensitive diaphragm of high temperature pressure sensor. *Sensors and Actuators A: Physical* **309,** 112017. ISSN: 0924-4247 (2020).

72. Zaitsev, A. *et al.* Diamond Pressure and Temperature Sensors for High-Pressure High-Temperature Applications. *physica status solidi (a)* **185,** 59–64 (May 2001).
73. Samudrala, G. K., Moore, S. L. & Vohra, Y. K. Fabrication of Diamond Based Sensors for Use in Extreme Environments. *Materials* **8,** 2054–2061. ISSN: 1996-1944 (2015).
74. Watanabe, W., Tamaki, T. & Itoh, K. Femtosecond laser micromachining and biological therapy. *Laser Physics* **18,** 263–269 (Mar. 2008).
75. Shimada, T. *et al.* Intracellular disruption of mitochondria in a living HeLa cell with a 76-MHz femtosecond laser oscillator. *Opt. Express* **13,** 9869–9880 (Nov. 2005).
76. Sakakura, M., Lei, Y., Wang, L., Yu, Y.-H. & Kazansky, P. Ultralow-loss geometric phase and polarization shaping by ultrafast laser writing in silica glass. *Light: Science Applications* **9** (Jan. 2020).
77. Zhang, J., Gecevičius, M., Beresna, M. & Kazansky, P. Seemingly Unlimited Lifetime Data Storage in Nanostructured Glass. *Physical Review Letters* **112,** 033901 (Jan. 2014).
78. Chichkov, B. N. Femtosecond, picosecond and nanosecond laser ablation of solids. *Applied physics.* **63.** ISSN: 0947-8396 (1996).
79. Sipe, J. E., Young, J. F., Preston, J. S. & van Driel, H. M. Laser-induced periodic surface structure. I. Theory. *Phys. Rev. B* **27,** 1141–1154 (2 Jan. 1983).
80. Tull, B. R., Carey, J. E., Mazur, E., McDonald, J. & Yalisove, S. M. Surface morphologies of silicon surfaces after femtosecond laser irradiation. *Mat. Res. Soc. Bull.* **31,** 626–633 (2006).
81. Bonse, J. & Krüger, J. Pulse number dependence of laser-induced periodic surface structures for femtosecond laser irradiation of silicon. *Journal of Applied Physics* **108,** 034903–034903 (Aug. 2010).

82. Sartori, A. *et al.* Laser-Induced Periodic Surface Structures (LIPSS) on Heavily Boron-Doped Diamond for Electrode Applications. *ACS Applied Materials Interfaces* **10** (Nov. 2018).
83. Dumitru, G., Romano, V., Weber, H., Sentis, M. & Marine, W. Femtosecond ablation of ultrahard materials. *Applied Physics A: Materials Science Processing* **74,** 729–739 (June 2002).
84. Neff, M. *et al.* Femtosecond laser writing of buried graphitic structures in bulk diamond. *Appl. Phys. A* **97,** 543–547 (Nov. 2009).
85. Rehman, Z. & Janulewicz, K. Structural transformation of monocrystalline diamond driven by ultrashort laser pulses. *Diamond and Related Materials* **70,** 194–200. ISSN: 0925-9635 (2016).
86. De Feudis, M. *et al.* Diamond graphitization by laser-writing for all-carbon detector applications. *Diamond and Related Materials* **75,** 25–33. ISSN: 0925-9635 (2017).
87. Wang, C. Z., Ho, K. M., Shirk, M. D. & Molian, P. A. Laser-Induced Graphitization on a Diamond (111) Surface. *Phys. Rev. Lett.* **85,** 4092–4095 (19 Nov. 2000).
88. Stampfli, P. & Bennemann, K. H. Theory for the instability of the diamond structure of Si, Ge, and C induced by a dense electron-hole plasma. *Phys. Rev. B* **42,** 7163–7173 (11 Oct. 1990).
89. Van Vechten, J., Tsu, R., Saris, F. & Hoonhout, D. Reasons to believe pulsed laser annealing of Si does not involve simple thermal melting. *Physics Letters A* **74,** 417–421. ISSN: 0375-9601 (1979).
90. Olivero, P. *et al.* Direct fabrication of three-dimensional buried conductive channels in single crystal diamond with ion microbeam induced graphitization. *Diamond and Related Materials* **18,** 870–876. ISSN: 0925-9635 (2009).
91. Sotillo, B. *et al.* Diamond photonics platform enabled by femtosecond laser writing. *Scientific Reports* **6,** 35566 (Oct. 2016).

92. Salter, P. *et al.* Laser Engineering Nanocarbon Phases within Diamond for Science and Electronics. *ACS Nano* **18** (Jan. 2024).
93. Mali, M. *et al.* Latest results from the RD42 collaboration on the radiation tolerance of polycrystalline diamond detectors. *Nuclear Instruments and Methods in Physics Research Section A: Accelerators, Spectrometers, Detectors and Associated Equipment* **1062,** 169202. ISSN: 0168-9002 (2024).
94. Chen, Y.-C. *et al.* Laser writing of coherent colour centres in diamond. *Nature Photonics* **11** (June 2016).
95. Bharadwaj Shivakumar, V. *et al.* Femtosecond laser written photonic and microfluidic circuits in diamond. *Journal of Physics: Photonics* **1** (Mar. 2019).
96. Granados, E., Martinez-Calderon, M., Gomez, M., Rodriguez, A. & Olaizola, S. M. Photonic structures in diamond based on femtosecond UV laser induced periodic surface structuring (LIPSS). *Opt. Express* **25,** 15330–15335 (June 2017).
97. Hofmann, T. *et al.* Evidence for temporary and local transition of sp2 graphite-type to sp3 diamond-type bonding induced by the tip of an atomic force microscope. *New Journal of Physics* **24** (Aug. 2022).
98. Salter, P., Booth, M., Courvoisier, A., Moran, D. & MacLaren, D. High resolution structural characterisation of laser-induced defect clusters inside diamond. *Applied Physics Letters* **111** (June 2017).
99. Kononenko, V. V., Zavedeev, E. V., Kononenko, T. V., Bukin, V. V. & Konov, V. I. Cleavage-Driven Laser Writing in Monocrystalline Diamond. *Photonics* **10.** ISSN: 2304-6732 (2023).
100. Ashikkalieva, K. Laser-Induced Graphitization of Diamond Bulk: The State of the Art (A Review). *Physics of Wave Phenomena* **30,** 1–16 (Mar. 2022).

101. Kononenko, T., Zavedeev, E., Kononenko, V., Ashikkalieva, K. & Konov, V. Graphitization wave in diamond bulk induced by ultrashort laser pulses. *Applied Physics A* **119** (May 2015).

102. Chen, Y.-C. *et al.* Laser writing of individual nitrogen-vacancy defects in diamond with near-unity yield. *Optica* **6,** 662–667 (May 2019).

103. Lagomarsino, S. *et al.* Electrical and Raman-imaging characterization of laser-made electrodes for 3D diamond detectors. *Diamond and Related Materials* **43,** 23–28. ISSN: 0925-9635 (2014).

104. Lagomarsino, S. *et al.* Three-dimensional diamond detectors: Charge collection efficiency of graphitic electrodes. *Applied Physics Letters* **103,** 233507–233507 (Dec. 2013).

105. Lagomarsino, S. *et al.* Evidence of Light Guiding in Ion-Implanted Diamond. *Physical review letters* **105,** 233903 (Dec. 2010).

106. Hiscocks, M. *et al.* Diamond waveguides fabricated by reactive ion etching. *Optics express* **16,** 19512–9 (Dec. 2008).

107. Metcalfe, A. *et al.* Diamond based detectors for high temperature, high radiation environments. *Journal of Instrumentation* **12,** C01066–C01066 (Jan. 2017).

108. Bloomer, C., Rehm, G., Salter, P. & Newton, M. *A single crystal CVD diamond x-ray beam diagnostic with embedded graphitic wire electrodes* in. **2054** (Jan. 2019), 060058.

109. Bloomer, C., Newton, M., Rehm, G. & Salter, P. A single-crystal diamond X-ray pixel detector with embedded graphitic electrodes. *Journal of Synchrotron Radiation* **27** (May 2020).

110. Morse, J. *et al.* Single crystal CVD diamond as an X-ray beam monitor. *Diamond and Related Materials* **16,** 1049–1052. ISSN: 0925-9635 (2007).

111. Courvoisier, A., Booth, M. J. & Salter, P. S. Inscription of 3D waveguides in diamond using an ultrafast laser. *Applied Physics Letters* **109,** 031109. ISSN: 0003-6951 (July 2016).

112. Sun, B., Salter, P. & Booth, M. High conductivity micro-wires in diamond following arbitrary paths. *Applied Physics Letters* **105,** 231105 (Dec. 2014).

113. Bharadwaj Shivakumar, V. *et al.* Femtosecond laser inscription of Bragg grating waveguides in bulk diamond. *Optics Letters* **42** (May 2017).

114. Rößler, F., Kunze, T. & Lasagni, A. Fabrication of diffraction based security elements using direct laser interference patterning. *Optics Express* **25,** 22959 (Sept. 2017).

115. Hecht, E. *Optics* ISBN: 9780321188786 (Addison-Wesley, 2002).

116. Braat, J. & Török, P. *Imaging Optics* (Cambridge University Press, 2019).

117. Salter, P. & Booth, M. Adaptive optics in laser processing. *Light: Science Applications* **8** (Dec. 2019).

118. Bielykh, S., Subota, S., Reshetnyak, V. & Galstian, T. Electro-optical characteristics of a liquid crystal lens with polymer network. *Ukrainian Journal of Physics* **55,** 293–8 (Jan. 2010).

119. Huang, L., Salter, P. S., Payne, F. & Booth, M. J. Aberration correction for direct laser written waveguides in a transverse geometry. *Opt. Express* **24,** 10565–10574 (May 2016).

120. Booth, M. & Wilson, T. Refractive-index-mismatch induced aberrations in single-photon and two-photon microscopy and the use of aberration correction. *Journal of biomedical optics* **6,** 266–72 (Aug. 2001).

121. Hampson, K. M., Antonello, J., Lane, R. & Booth, M. *Sensorless Adaptive Optics* (Oct. 2020). `https://aomicroscopy.org/sensorless-ao`.

122. Marsh, P. N., Burns, D. & Girkin, J. M. Practical implementation of adaptive optics in multiphoton microscopy. *Opt. Express* **11,** 1123–1130 (May 2003).

123. Salter, P. & Booth, M. Adaptive optics in laser processing. *Light: Science Applications* **8** (Dec. 2019).

124. Li, R. & Cao, L. Progress in Phase Calibration for Liquid Crystal Spatial Light Modulators. *Applied Sciences* **9.** ISSN: 2076-3417 (2019).

125. Simmonds, R., Salter, P., Jesacher, A. & Booth, M. Three dimensional laser microfabrication in diamond using a dual adaptive optics system. *Optics express* **19,** 24122–8 (Nov. 2011).

126. Cho, Y. & Ahn, S. Fabricating a Raman spectrometer using an optical pickup unit and pulsed power. *Scientific Reports* **10** (July 2020).

127. Herrero, Y. R., Camas, K. L. & Ullah, A. in *Advanced Applications of Biobased Materials* (eds Ahmed, S. & Annu) 111–143 (Elsevier, 2023). ISBN: 978-0-323-91677-6.

128. Goldstein, J. *et al. Scanning Electron Microscopy and X-ray Microanalysis ISBN: 0306472929* ISBN: 0306472929 (Jan. 2003).

129. Martínez-Calderon, M. *et al.* Tailoring diamond's optical properties via direct femtosecond laser nanostructuring. *Scientific Reports* **8,** 14262 (Sept. 2018).

130. O'Bannon, E. *et al.* The transformation of diamond to graphite: Experiments reveal the presence of an intermediate linear carbon phase. *Diamond and Related Materials* **108,** 107876. ISSN: 0925-9635 (2020).

131. Rothschild, M., Arnone, C. & Ehrlich, D. J. Excimer-laser etching of diamond and hard carbon films by direct writing and optical projection. *Journal of Vacuum Science & Technology B* **4,** 310–314 (1986).

132. Kononenko, V. V. *et al.* Effect of the pulse duration on graphitisation of diamond during laser ablation. *Quantum Electronics* **35,** 252 (Mar. 2005).

133. Komlenok, M., Kononenko, V., Ralchenko, V., Pimenov, S. & Konov, V. Laser Induced Nanoablation of Diamond Materials. *Physics Procedia* **12,** 37–45. ISSN: 1875-3892 (2011).

134. Kuriakose, A. *et al.* Fabrication of conductive micro electrodes in diamond bulk using pulsed Bessel beams. *Diamond and Related Materials* **136,** 110034. ISSN: 0925-9635 (2023).

135. Haughton, I. *et al.* Barrier potential for laser written graphitic wires in diamond. *Diamond and Related Materials* **111,** 108164. ISSN: 0925-9635 (2021).

136. Courvoisier, A., Booth, M. J. & Salter, P. S. Inscription of 3D waveguides in diamond using an ultrafast laser. *Applied Physics Letters* **109,** 031109 (2016).

137. Sotillo, B. *et al.* Visible to Infrared Diamond Photonics Enabled by Focused Femtosecond Laser Pulses. *Micromachines* **8.** ISSN: 2072-666X (2017).

138. Griffiths, B. *et al. Laser writing of colour centres in diamond* in (Jan. 2019), 28.

139. Wang, X.-J., Fang, H.-H., Sun, F.-W. & Sun, H.-B. Laser Writing of Color Centers. *Laser Photonics Reviews* **16,** 2100029 (Nov. 2021).

140. Kononenko, T. *et al.* Microstructuring of diamond bulk by IR femtosecond laser pulses. *Applied Physics A* **90,** 645–651 (Mar. 2008).

141. Shimotsuma, Y. Three-dimensional Nanostructuring of Transparent Materials by the Femtosecond Laser Irradiation. *Journal of Laser Micro Nanoengineering* **1,** 181–184 (Dec. 2006).

142. Shimizu, M. *et al.* Periodic metallo-dielectric structure in diamond. *Opt. Express* **17,** 46–54 (Jan. 2009).

143. Salter, P., Baum, M., Alexeev, I., Schmidt, M. & Booth, M. Exploring the depth range for three-dimensional laser machining with aberration correction. *Optics Express* **22** (July 2014).

144. Jasbeer, H. *et al.* Birefringence and piezo-Raman analysis of single crystal CVD diamond and effects on Raman laser performance. *J. Opt. Soc. Am. B* **33,** B56–B64 (Mar. 2016).

145. Salvatori, S. *et al.* Diamond Detector With Laser-Formed Buried Graphitic Electrodes: Micron-Scale Mapping of Stress and Charge Collection Efficiency. *IEEE Sensors Journal* **19,** 11908–11917 (2019).

146. Jesacher, A. & Booth, M. Parallel direct laser writing in three dimensions with spatially dependent aberration correction. *Optics express* **18,** 21090–9 (Sept. 2010).

147. Mujat, M., Iftimia, N., Ferguson, D. & Hammer, D. Mueller Matrix Microscopy. *Proceedings of SPIE - The International Society for Optical Engineering* **8873** (Apr. 2010).

148. Howell, D. *et al.* Quantifying strain birefringence halos around inclusions in diamond. *Contributions to Mineralogy and Petrology* **160,** 705–717 (Nov. 2010).

149. Wang, Y. *et al.* Mueller matrix microscope: A quantitative tool to facilitate detections and fibrosis scorings of liver cirrhosis and cancer tissues. *Journal of Biomedical Optics* **21,** 071112 (Apr. 2016).

150. Dalla Betta, G.-F. & Ye, J. Silicon Radiation Detector Technologies: From Planar to 3D. *Chips* **2,** 83–101. ISSN: 2674-0729 (2023).

151. Bäni, L. *et al.* A study of the radiation tolerance of poly-crystalline and single-crystalline CVD diamond to 800 MeV and 24 GeV protons. *Journal of Physics D: Applied Physics* **52,** 465103 (Aug. 2019).

152. Porter, A. L. *Development of 3D Diamond Detectors for Particle Physics and Dosimetry* PhD thesis (University of Manchester, 2022).

153. Watkins, R. J. *Diamond Power Electronics and Radiation Detectors* PhD thesis (University College London, 2024).